1981

Tubular solar collector analysis and comparison with flat plate collectors in SDHW applications

Kevin A. Cole

TUBULAR SOLAR COLLECTOR ANALYSIS AND COMPARISON WITH FLAT PLATE COLLECTORS IN SDHW APPLICATIONS

by

Kevin A. Cole

A Thesis Submitted
in
Partial Fulfillment
of the
Requirements for the Degree of
MASTER OF SCIENCE
in
Mechanical Engineering

Approved by:

Prof. Paul H. Wojuid
(Thesis Advisor)

Prof. Wayne Watts

Prof. Robert Des

Prof. Alan H. Nye

DEPARTMENT OF MECHANICAL ENGINEERING
COLLEGE OF ENGINEERING
ROCHESTER INSTITUTE OF TECHNOLOGY
ROCHESTER, NEW YORK

February, 1981

TABLE OF CONTENTS

TABLE OF CONTENTS (contd.)

ACKNOWLEDGEMENTS

This study was funded in part by a grant from the Rochester Gas and Electric Corporation. I would like to thank Mr. Lew Durland for his assistance with the experimental work and data analysis of this work. Thanks is extended to Dr. Alan Nye who contributed the material of Appendix 7, developed the computer simulation model and also assisted in its operation. Mr. Greg Amorese was instrumental in the development of the system control scheme and supplied the material of Appendix 1. Mrs. Margaret Urckfitz is complimented for her preparation of this typeset. Finally, I would like to thank my advisor, Dr. Paul Wojciechowski, for his continual patience and helpfulness at all stages of this work. Without his support, this work would not have been possible.

LIST OF TABLES

LIST OF FIGURES

Figures - Chapter 3

Figures - Chapter 4

Figures - Chapter 5

Figures - Chapter 6

Figures - Chapter 7

Figures - Appendices

LIST OF SYMBOLS

This table is a listing of the most commonly used symbols in this report. Infrequently used symbols are defined in the text.

A_a absorber tube projected area, m^2

A_t aperture area (diameter of outer glass tube x total length of collector tubes) m^2

b fraction of the projected area (unto a plane perpendicular to the direction of beam radiation) of the outer cover tube silvered backing which directly receives radiation over which beam radiation is reflected to the absorber tube, %/100

C_p fluid specific heat, J/kg°C

d absorber tube outer diameter, m

d' inner cover tube outer diameter, m

D outer cover tube outer diameter, m

E eccentricity correction factor for the solar constant (S_c)

F fin efficiency factor

F' collector efficiency factor

F_R collector heat removal factor

$g(\Omega)$ collector tube shading factor

G collector fluid mass flow rate per unit aperture area, kg/hrm^2

h heat transfer coefficient, $kJ/hrm^2°C$

h_s hour angle

H_b beam radiation on a horizontal surface, kJ/m^2hr

H_d diffuse radiation on a horizontal surface, kJ/m^2hr

H_o total extraterrestrial radiation on a horizontal surface, kJ/m^2hr

H_t total radiation on a horizontal surface, kJ/m^2hr

i angle between the sun's rays and the outer normal to the tube lying in the plane formed by the tube centerline and a line collinear with the sun's rays.

I total radiation on a tilted surface, kJ/m^2hr

I_b beam radiation on a tilted surface, kJ/m^2hr

I_d diffuse radiation on a tilted surface, kJ/m^2hr

I_{eff} total radiation over the aperture area which is either directly absorbed or backreflected by the silvered portion of the outer cover tube to the absorber tube, kJ/m^2hr

k_f thermal conductivity, $kJ/hrm°C$

K ratio of diffuse radiation to total radiation on a horizontal surface, length extinction coefficient

K_t ratio of total radiation to extraterrestrial radiation on a horizontal surface

ℓ latitude

L longitude, total length of collector tubes, m

$\dot{M}$ collector fluid mass flow rate, kg/hr

n index of refraction

N_u Nusselt number

P_r Prandtl number

q_g collector net energy gain per unit aperture area, kJ/hrm^2

q_ℓ net energy lost per unit surface area of the outer cover tube, kJ/hrm^2

q_u collector useful energy gain per unit aperture area, kJ/hrm^2

Q_u collector useful energy gain, kJ/hr

Q_s total heat capacity of the storage tank, kJ

Q_{TRAN} rate of heat addition to the storage tank from the tubular collectors, kJ/hr

Q_{AUX} rate of addition of auxiliary energy to the hot water tank, kJ/hr

R_e Reynolds number

S_c solar constant

T_a outside ambient temperature, °C

T_{AMB} ambient temperature of air surrounding storage and hot water tank, °C

T_{CW} water temperature at preheat tank inlet from city supply, °C

T_{INC} collector inlet fluid temperature, °C

T_{IWH} preheat tank water temperature, °C

T_{OUTC} collector outlet fluid temperature, °C

T_{OWH} hot water tank water temperature, °C

U tank loss coefficient, $kJ/hrm^2°C$

U_h overall heat transfer loss coefficient of heat exchanger, $kJ/hrm^2°C$

U_L collector loss coefficient, $kJ/hrm^2°C$

α glass absorptance

β collector tilt angle

η collector efficiency

θ collector tube orientation angle

Γ radiation enhancement factor, I_{eff}/I

$\gamma(\Omega)$ fraction of the aperture area over which beam radiation is reflected to the abosrber tube, %/100

μ absolute viscosity

ρ reflectance

τ transmittance of glass

$(\tau\alpha)_e$ transmittance, absorptance product of the tubular collectors

Ω collector tube orientation angle with respect to the sun

ABSTRACT

A residential solar domestic hot water system utilizing tubular solar collectors is analyzed for climatic conditions typical of various regions of the Northeast. Experimentally determined system parameters are used in analytical simulations to compare the performance of systems using two different flat plate collectors to the system using the tubular type. A cost/benefit analysis is performed to determine the economic feasibility of the various systems.

1. INTRODUCTION

The world and U.S. demand for energy is expected to grow at a slower rate than in the past, and at least during the next decade the world supply of energy is expected to meet this demand [1]. However, the United States is far from being energy independent and now finds itself more dependent on foreign energy supplies than possibly any other time in history. This situation places the country in a vulnerable position and hence, provides the motivation to develop and implement the use of alternative energy sources.

Solar energy is currently attracting widespread interest as one alternative. Applications are being developed through the support of public funds managed and administered by the U.S. Department of Energy and other federal agencies. Many state governments are promoting solar energy utilization. Private groups and corporations are also investing in solar research and development.

Some solar energy technologies currently being developed are direct conversion of sunlight to electricity through solar cells, solar thermal electric power generation, ocean thermal conversion, agricultural applications, and conversion of organic materials to produce fuels. Solar assisted space air heating systems and solar assisted domestic hot water systems however continue to receive the most public attention. Some reasons which account for their popularity are the availability of materials and technology for the construction of the basic components of

these systems, the simplicity of these basic components from an engineering design standpoint, and their cost effective performance when designed and installed correctly.

While these reasons provide a sound basis for the utilization of solar assisted space air heating systems and solar assisted domestic hot water systems in a large number of places and for many system configurations, it is imperative that systems not conforming to previous analysis conditions be evaluated on a system by system basis.

The solar assisted domestic hot water system at Energy House is an example of such a system. Energy House is a thermally efficient, solar assisted heat pump residence located on the campus of the Rochester Institute of Technology. The configuration of the solar assisted domestic hot water (SDHW) system (which is totally independent of the space air heating system) is a two-tank, indirect, internal heat exchanger scheme using a 50/50 water and propylene glycol anti-freeze solution. The system utilizes commerically available tubular solar collectors utilizing a copper conduit absorber enclosed by two glass envelopes. The collectors are non-evacuated. The outer envelope (which is circular and eccentric with respect to the absorber tube) is silvered on the lower half for back reflection of incoming solar radiation onto the absorber tube. The uniqueness of this particular system lies in the combination of its location in the partly cloudy climate of the Northeast and the use of tubular collectors.

The purpose of this work is to perform a thorough analysis of the solar assisted domestic hot water system located at Energy House. The methodology utilized is as follows. First, an analytical model is developed for the tubular solar collectors. To assist in the development of the model, a literature survey of tubular collectors was performed and is presented in Chapter 2. The analysis parallels that of the Hottel-Whillier-Bliss approach for flat plate solar collectors. Certain optical enhancement factors are developed to account for the circular geometry. This analysis is presented in Chapter 4.

Experimental verification of the mathematical model indicates reasonable correlation between theory and experiment under varying insolation conditions. A description of these results as well as the experimental procedures are given in Chapter 5. In order to clearly understand the experimental procedures of this chapter, a description of the system components, the system operation, and the experimental measuring apparatus is given in Chapter 3.

Operational data from the SDHW system and the analytical model are used to calibrate the TRNSYS computer simulation program configured to simulate the experimental system. This is described in Chapters 6 and 7. TRNSYS simulations are compared for both tubular and flat plate systems for meteorological conditions corresponding to partly cloudy Northeastern climates. A cost/benefit analysis based on the present worth method is also given. Chapter 8 outlines this procedure. The results of the analysis are stated in Chapter 9. Conclusions and recommendations are given Chapter 10. Appendices are given at the end of the report.

2. TUBULAR COLLECTOR LITERATURE SURVEY

Information dealing with tubular collectors was found by searching four abstract information files. The four chosen provide a comprehensive summary of available tubular collector information. The Engineering Index (Ei) file was searched from 1970 to 1979, the National Technical Information Service (NTIS) file was searched from 1964 to 1979, the Energy Information Abstracts file was searched from 1971 to 1979 and the Smithsonian Science Information Exchange (SSIE) Current Research file was searched from 1975 to 1979. The searches were performed by computer utilizing the Dialog service which maintains each of the above files online. Dialog is maintained by Lockheed Missiles and Space Company, Incorporated. Some references were found in more than one file, however, they are only counted where the first occur.

Eighteen references were found dealing with tubular collectors in the Ei, all of which dealt with collectors which were evacuated. Of the eighteen, nine dealt with collector analysis exclusively. Both the thermal and optical performance was evaluated. It was generally concluded that by evacuating the collector tubes, the losses from the collectors could be kept at a much lower level than those from a flat plate collector with the same collection area. This occurs because convection losses are negligible when the collector tubes are evacuated. Optical improvement over flat plate design is achieved by utilizing properly designed specular reflectors [2].

One paper discussed the use of evacuated tubular collectors in a two fluid Rankine cycle to generate electricity [3] while another mentioned the use of tubular collectors for domestic hot water use [4]. The remainder of the papers dealt with using the collectors in space air heating systems as well as solar air conditioning systems. Results show that evacuated tubular collector systems are capable of supplying the high temperatures required for solar air conditioning units.

The NTIS file yielded twenty-three references dealing with evacuated tubular collectors. Twelve covered collector analysis only and eleven dealt with their use in space air heating systems and solar air conditioning systems. The conclusions of these papers are similar to those of the Ei search.

Eleven references were found from the Energy Information Abstracts file; four of which dealt with collector analysis and seven which dealt with their use in the two types of systems mentioned above.

Seven listings were found in the SSIE Current Research file. Most research concerning the performance of tubular collectors in systems applications is currently being undertaken at Colorado State University at Fort Collins, Colorado. An integrated solar heating and cooling system at that location which utilizes evacuated tubular collectors is being assessed as to its practicality. The components of the system are: Owens Illinois Liquid evacuated glass tube collectors, ARKLA Lithium Bromide absorption cooling unit (3 ton), cold and hot storage, and non-pressurized water storage.

Research by private corporations is being directed at improving the performance of tubular collectors as well as reducing construction costs. Some companies currently involved are Solaron Corporation of Commerce City, Colorado; Westinghouse Electric Corporation of Pittsburgh, Pennsylvania; and Owens-Illinois Incorporated of Toledo, Ohio.

3. SYSTEM DESCRIPTION

3.1 System Apparatus

A schematic of the forced-circulation, solar water heating system at the Rochester Institute of Technology Energy House is shown in Figure 3.1. The actual layout of the system is shown in plan view in Figure 3.2. Note that the collectors are located on the garage roof. The expansion tank and supportive piping is located in the data lab while the remainder of the system is located in the basement. Since the system is constructed in a region which experiences subfreezing temperatures, provision has to be made to handle the problems caused by this. There are four basic options available:

1. to use an intermediate, non-freezing transfer fluid,
2. to design a piping system which can withstand freezing conditions,
3. to provide adequate heat to the transfer fluid on cold nights to prevent freezing,
4. system draindown when not in operation.

The system at Energy House utilizes option 1, thereby requiring a special non-freezing transfer fluid in winter (water can be effectively used during summer operation, if desired). Because of the presence of a transfer fluid, the system shown in Figure 3.1 has a closed solar energy collection loop as indicated. The remainder of the system is termed the service water side. From Figure 3.1, the closed loop side of the system is composed of the following apparatus:

1. KTA Tubular Collectors - There are 2 KTA Model No. KT4-85 tubular collectors in parallel in the RIT solar water heating system.

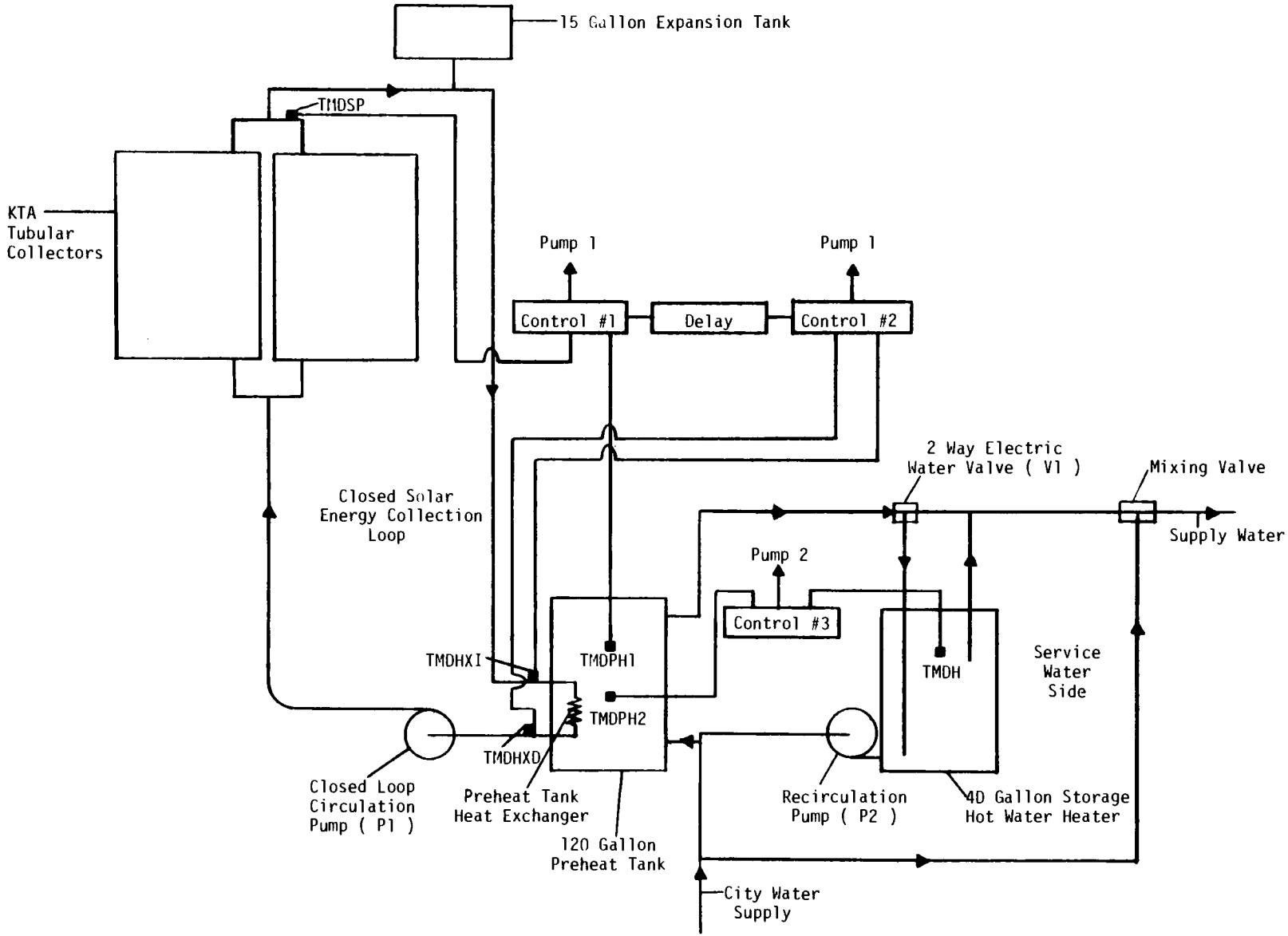

Figure 3.1 Forced Circulation, Solar Water Heating System - R.I.T. Energy House

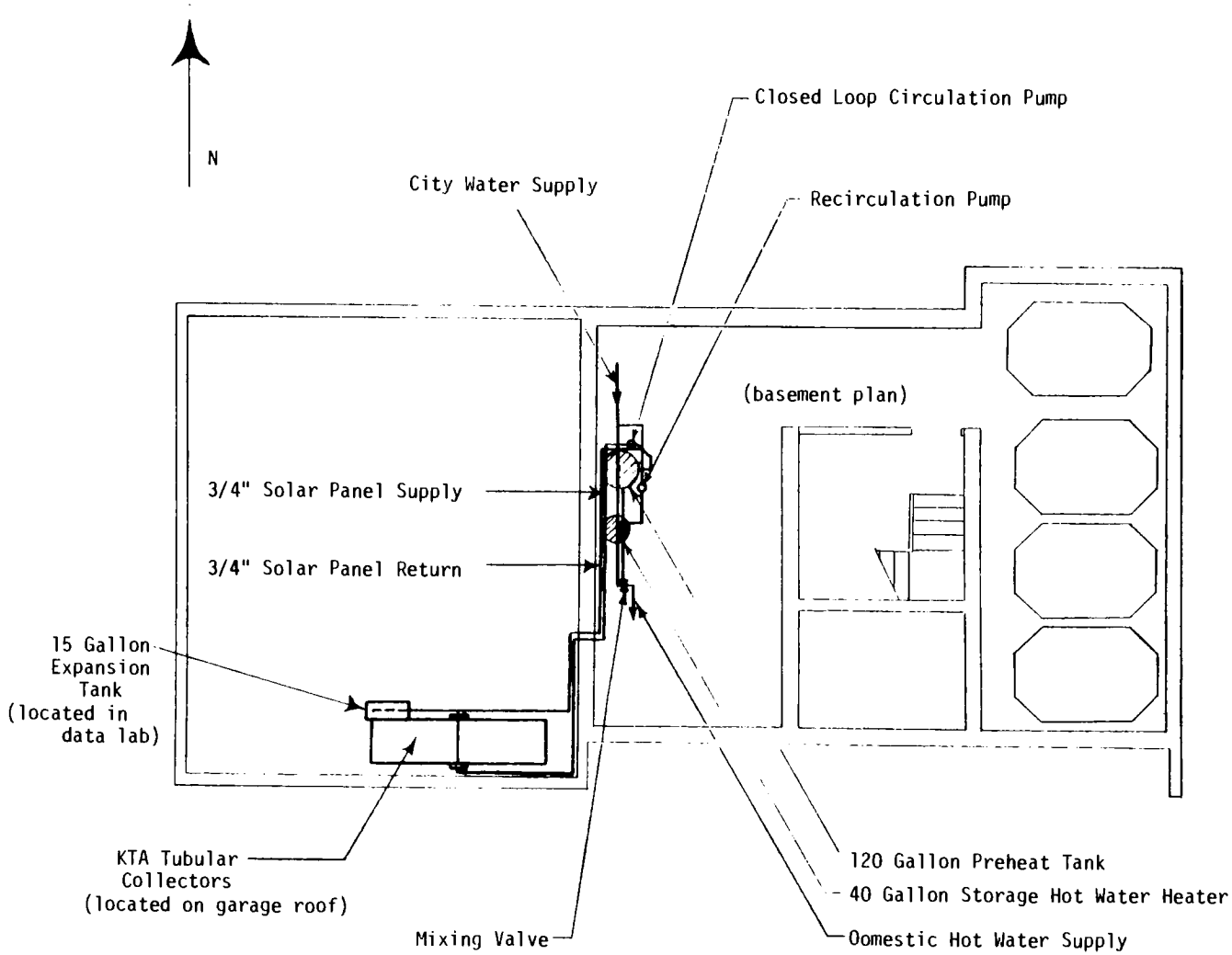

Figure 3.2 Actual Solar Water Heating System Layout - Plan View

These are mounted at a 60° tilt angle and face due south. Each collector consists of a parallel array of 40 tubular collection elements, each element consisting of a copper absorber tube with a selective coating and 2 glass cover tubes. The absorber and inner glass cover tube centers are concentric while eccentric with respect to the outer cover tube. The outer cover tube is reflectorized internally over its entire length in a semi-cylindrical fashion to provide a circular-cylindrical reflector 2 inches in diameter by 57 inches long. A schematic of a single tubular collection element along with an end cap is shown in Figure 3.3. The purpose of the end cap is to allow each tubular collection element to be hermetically sealed, thereby reducing losses. Also, provision has been made in the end cap seals for absorbing cover plate expansion and contraction. Additionally, each collector is composed of insulated headers into which the tubular collection elements are attached. Figure 3.4 is an individual collector layout with header locations and tubular collection elements shown. The headers are constructed so that parallel flow is established for each group of four tubular collection elements proceeding from the bottom of the collector to the top of the collector and series flow is established for these 10 groups of four elements each (10 x 4 = 40 elements/collector). The flow pattern for the two collectors in parallel is shown in Figure 3.5. A summary of collector materials and their properties is given in Table 3.1.

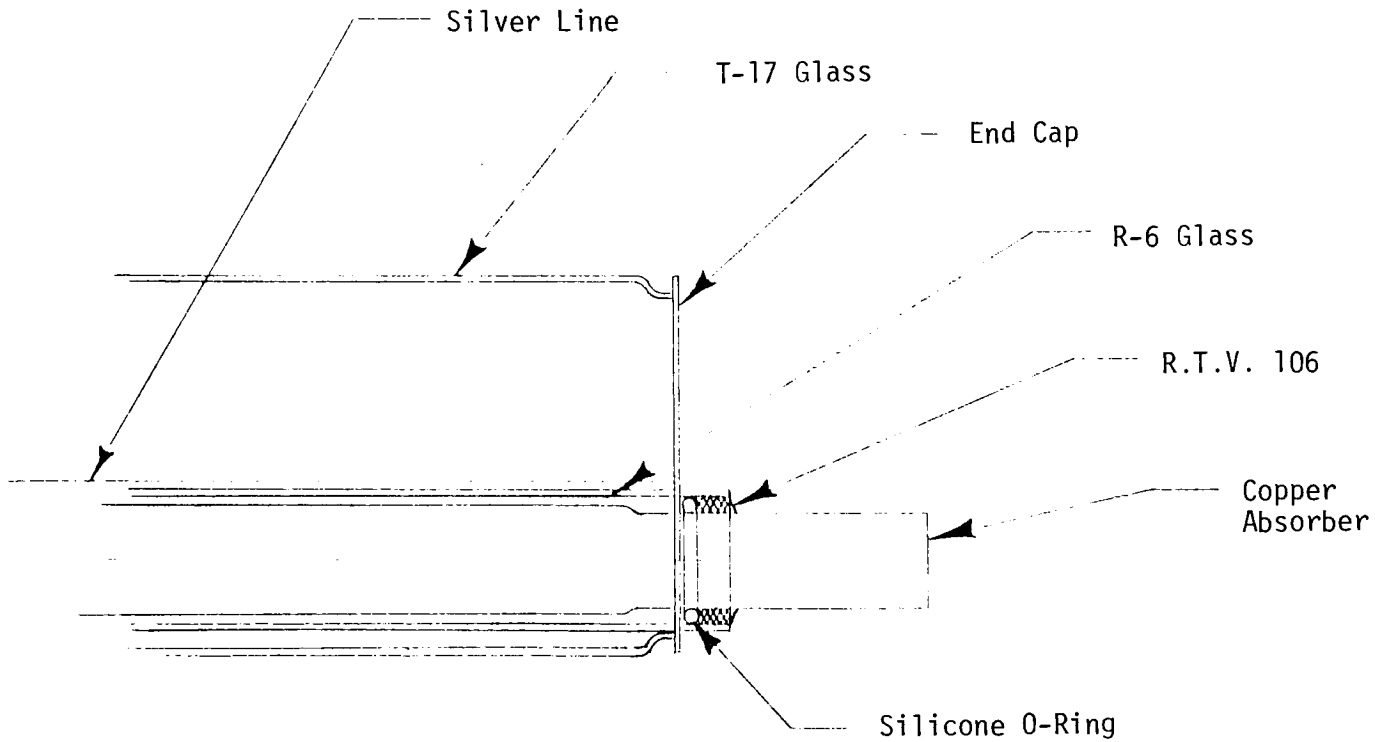

Figure 3.3 Single Tubular Collection Element Cross Section With End Plate

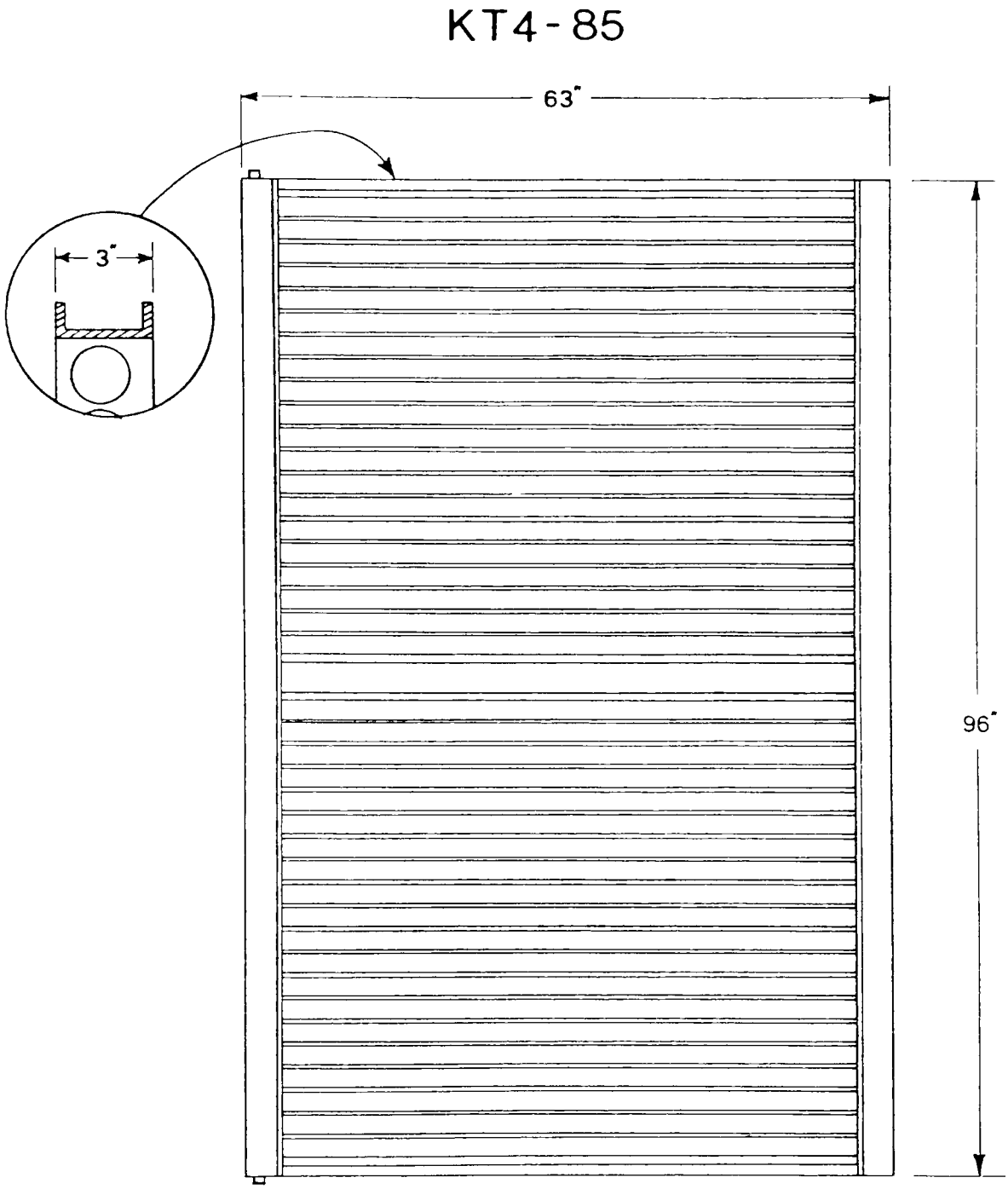

Figure 3.4 Single KTA Tubular Collector Layout

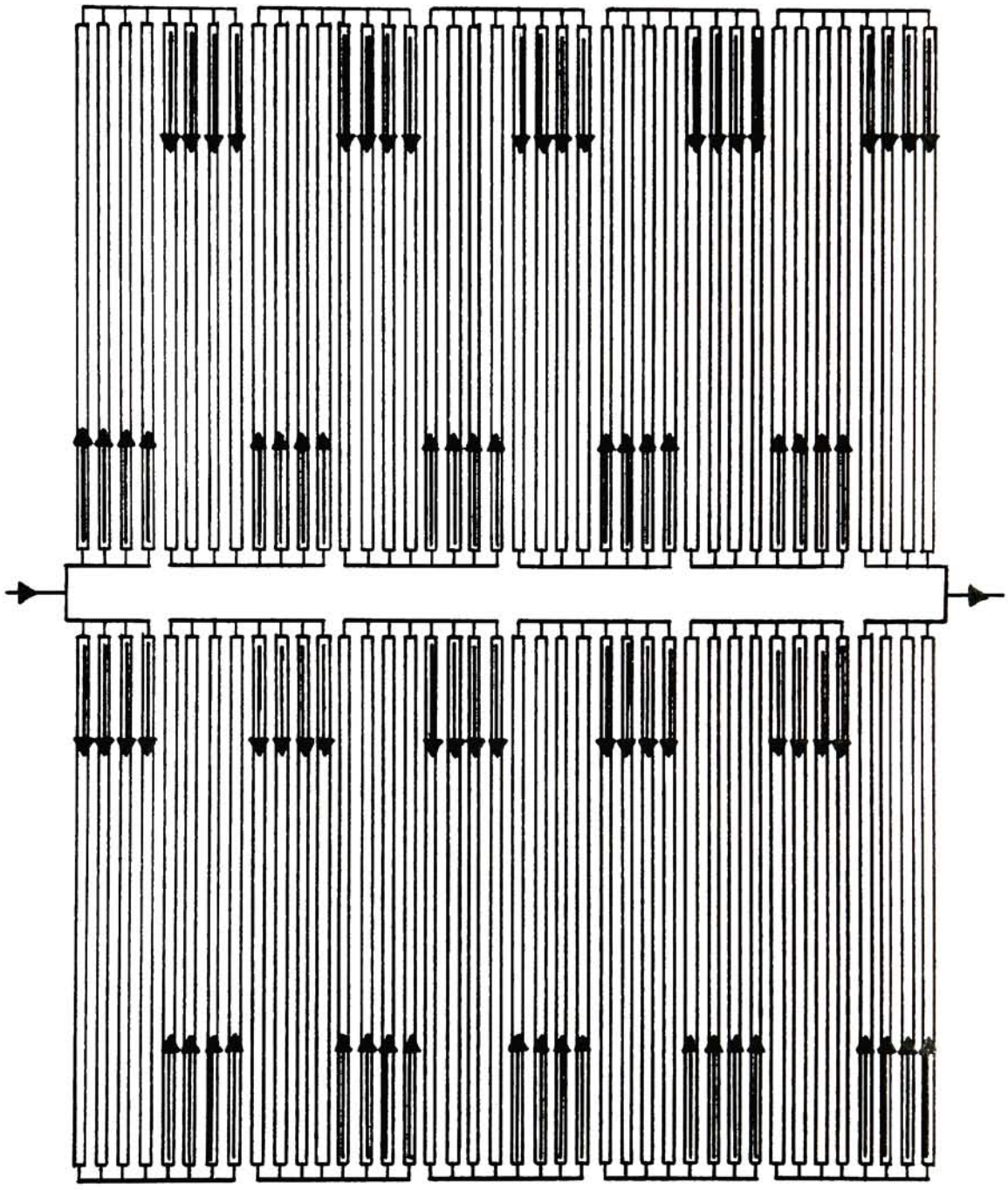

Figure 3.5 Flow Pattern For 2 KTA Tubular Collectors In Parallel

Table 3.1 - KTA Tubular Collector Materials and Properties

Model No: KT4-85

Quantity: 2

Outside Dimensions: 63" x 96" x 3" (160.02 x 243.84 x 7.62 cm)

Sealing System: -3M Company, high temperature, structural epoxy adhesive #2214

-General Electric RTV high temperature silicon rubber

Working Fluid: Water or water/glycol

Line Pressure: 125 psi max. (8.79 kg/cm^2)

Weight: 4.2 psf (20.51 kg/m^2)

Normal Operating Temperature: -25°F to 230°F (-32°C to 110°C)

Stagnation Temperature: 450°F (232°C)

Side Rails, End Caps: 6063-T5 Aluminum

Back Cover: 500-H-34 Aluminum

Effective Apperture Area per Collector: 31.67 ft^2 (2.94 m^2)

Plumbing Connections: Sealed with a high temperature silver brazing alloy

Absorber: -1/2" OD M-Type hard drawn copper tube

-selective coatings: black chrome

-absorptivity: 95%

-emissivity: 7%

-flow rates: 0.37 GPM to 1.46 GPM per collector at water temperature = 140°F (60°C)

-flow condition: laminar in all cases

Glass Cover Tubes: -008 soda-lime glass

-solar spectrum transmissivity: 92% at normal incidence

Table 3.1 - Cont.

-solar reflectivity: 4% at normal incidence

-infrared transmissivity: 1.6% at 5 microns

-density: 2.7 Grams/cm^3

Insulation: Isocyanurate Polyurethane foam tested for continuous usage at 300°F (149°C)

2. Expansion Tank - The expansion tank is a standard 15 gallon Adamson Flash tank with a sight glass attached.

3. Preheat Tank - The preheat tank is a 120 gallon water storage tank manufactured by the Electric Heater Company and contains a removable 3/4" copper tube heat exchanger built on location. The tank model number is C1205R-0 and the serial number is 07710332. It has been tested to 353 psig (24.8 kg/cm^2) and is designed for a working pressure of 150 psig (10.6 kg/cm^2).

4. Closed Loop Circulation Pump - The recirculation pump is a Grundfos Model No. UP26-64 variable speed circulator pump. It is rated at 1/12 hp., 3200rpm single phase, 60 cycle, 115 volts and 1.65 amps. It has built in overload protection. The flow rate varies from about 0.8 gpm (0.05 liters/sec) to about 2 gpm (0.13 liters/sec) and is controlled by a hand adjustment located on the underside of the pump. Previously, the closed loop circulation pump was a Bell and Gossett model as will be described for the recirculation application. It was replaced since it was not variable speed and attained a flow rate of 1 gpm (0.06 liters/sec).

This completes the description of the apparatus found in the closed solar energy collection loop. Turning to the service water side and again referring to Figure 3.1, the following apparatus is described:

1. Hot Water Tank - The hot water tank is a 40 gallon water storage tank with one heating element located near the top

and one heating element located near the bottom of the tank. Each element is rated at 4500 watts with the maximum power rating at any given time equal to 4500 watts (corresponding to either but never both elements on at any one time). The tank is manufactured by the A.O. Smith Company. The model number is Ken 40 and the serial number is 780T-G-88-40173. It has been tested to 300 psig (21.0 kg/cm^2) and is designed for a working pressure of 150 psig (10.6 kg/cm^2).

2. Recirculation Pump - A Bell and Gossett centrifugal pump number 106189 FU, series number 100 is used in this application. It is rated at 1/12 hp, 1725 rpm, single phase, 60 cycle, 115 volts, and 1.7 amps. It is thermally protected and is continuous rated up to 40°C. The flow rate generated by the pump is approximately 5 gpm (0.32 liters/sec). An identical pump in the closed loop application had a much slower flow rate due to the increased pump head in the closed loop.

3. Two Way Water Valve - This valve is manufactured by Honeywell and is controlled by a Honeywell Modutrol Motor rated at 24 volts, 60 hz, 1.06 amps, and 24 watts.

4. Mixing Valve - This valve is a watts 3/4" model number 70A.

Photographs of the apparatus described in this section are shown in Figures 3.6 through 3.13.

Figure 3.6. K.T.A. Tubular Collectors

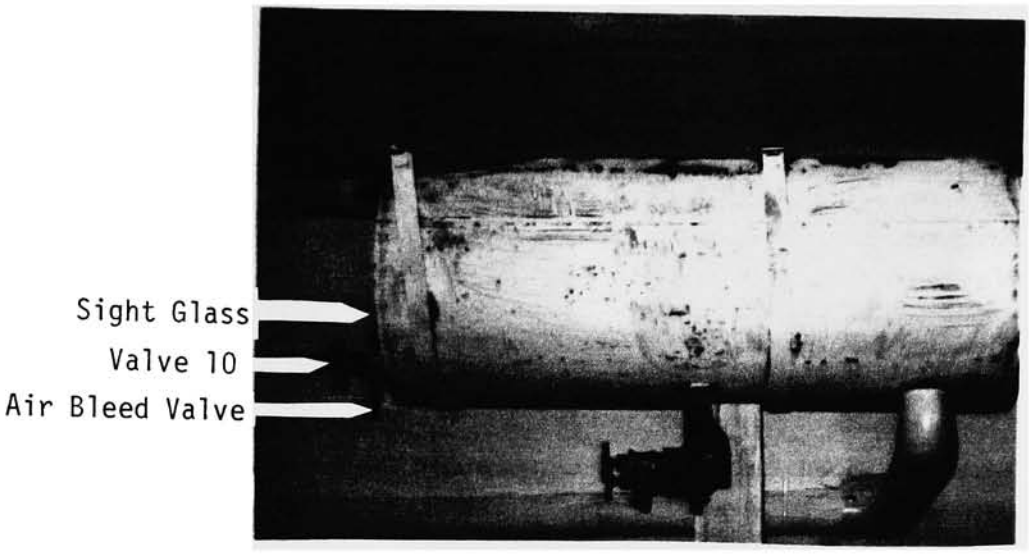

Figure 3.7. 15 Gallon Expansion Tank

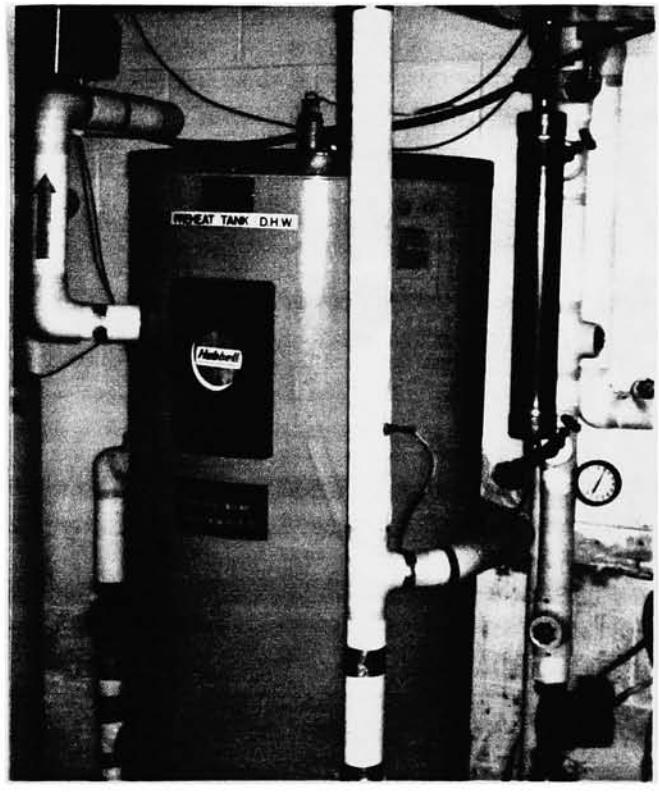

Figure 3.8. 120 Gallon Preheat Tank

Figure 3.9. Closed Loop Circulation Pump

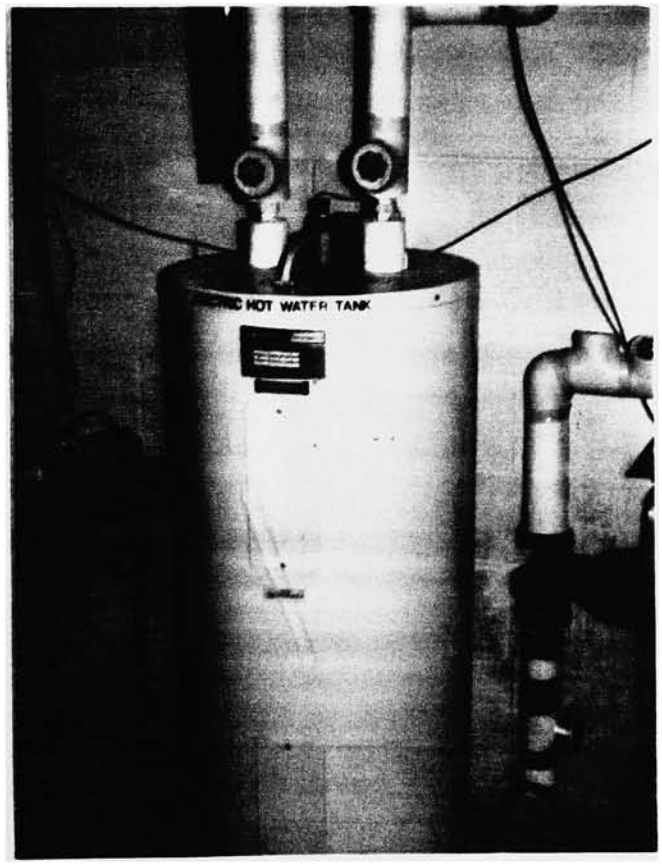

Figure 3.10. 40 Gallon Hot Water Tank

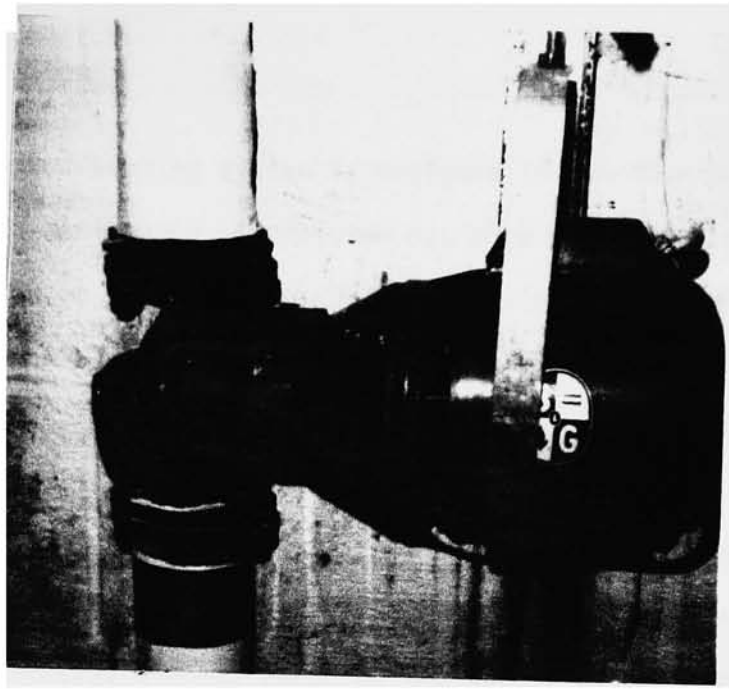

Figure 3.11. Recirculation Pump

Figure 3.12. 2 Way Water Valve

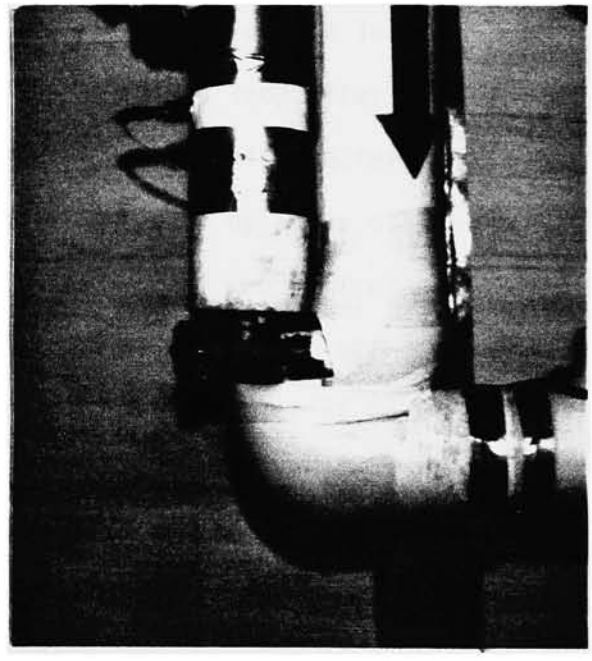

Figure 3.13. Mixing Valve

3.2 System Operation

The solar water heating system is designed to function both with and without solar assistance. Provision has also been made to allow solar heated water in the preheat tank to be switched with water in the storage hot water heater should the temperature difference become greater than 4°C. This provides a means of storing additional solar heated hot water. Should this provide hot water temperatures that are higher than desired, the mixing valve shown in Figures 3.1 and 3.13 will allow, when supply is required, the addition of city water at the hot water heater outlet thereby reducing the supply water temperature.

There are three differential controllers used to operate the solar water heating system and they are shown diagramatically in Figure 3.1. Controller #1 is used to initialize the solar energy collection loop while controller #2 is used to operate the solar energy loop after initialization. Controller #3 is used for the preheat-to-water heater recirculation. The three controllers sense temperature by means of thermistors located as shown in Figure 3.1. The purpose of two controllers for the solar energy collection loop is to prevent repeated on-off cycling of the closed loop circulation pump which could occur if only controller #1 was used. This would result due to the transient nature of temperature at sensor TMDSP until quasi-steady-state conditions are reached. Control is designed such that both automatic and manual operation is possible. For a complete control explanation, see Appendix 1. Also involved in system operation is the charging of the closed solar energy collection loop with the transfer fluid. The procedure used is given

in Appendix 2. The transfer fluid used is called Solar Winter Ban produced by the Camco Manufacturing Company of Greensboro, NC. Its ingredients are propylene glycol with food grade dipotassium hydrogen phosphate inhibitor and food grade colorant added. It is non-toxic and offers freeze protection to -55°F (-48°C) full strength.

3.3 Measuring Apparatus

In order to analyze the solar water heating system performance provision had to be made to monitor various system parameters. These include fluid temperatures, air temperatures, fluid flow rates, and insolation (INcoming SOLar radiATION) rates. The purpose of this section is to discuss the devices used to monitor these parameters and the reasons for their choice. Also covered is the instrumentation used to process, display, and record the signals from the monitoring devices as well as their accuracies.

3.3.1 Temperature Measurement

Figure 3.14 is a system schematic showing the location of all the temperature monitoring devices required in the experimental work to follow. The control sensors shown in Figure 3.1 are not included in this figure to simplify the schematic.

The fluid temperatures at the preheat tank heat exchanger inlet and outlet (T1 and T2) collector inlet and outlet (T3 and T4) and inside of the preheat tank (T5) were measured by resistance thermometer

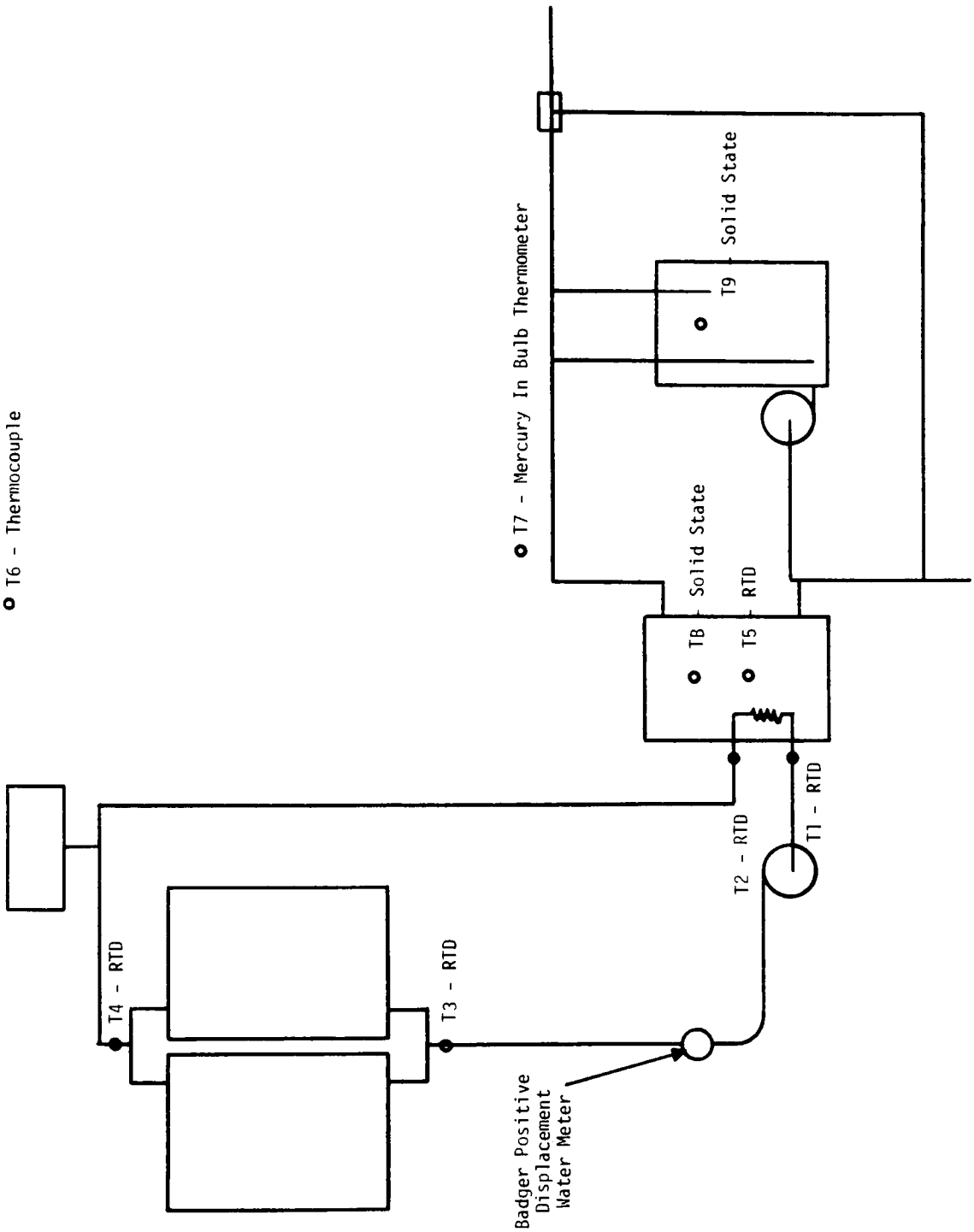

Figure 3.14 Forced Circulation, Solar Water Heating System - Instrumentation

elements (RTE) mounted in brass housings and supported by 1/8" compression fittings. The devices in conjunction with their brass housings are known as resistance temperature devices (RTD). The RTE's were purchased from RDF Corporation (model number EP-120) and mounted in brass housings by the author. Details on construction and installation are given in Appendix 3.

An RTE is a temperature-sensing transducer which operates on the principle of change in electric resistance of wire as a function of temperature. The elements utilized are made of high-purity platinum wire wound upon a ceramic core and encapsulated in aluminum oxide. Platinum elements were chosen because they resist contamination, are mechanically and electrically stable, and drift and error with age and use is negligible. The variation of resistance, R with temperature, T for most metallic materials can be represented by an equation of the form:

$$R = R_0 (1 + a_1 T + a_2 T^2 + \ldots + a_n T^n) \qquad (3.1)$$

where R_0 is the resistance at temperature T = 0. Figure 3.15, taken from Ref. 5, shows resistance vs. temperature curves for various RTD materials. R_0 values for the elements used are nominally 100Ω with a ± 2.0 Ω tolerance. For platinum elements two of the a constants are generally required for highly accurate work although quite respectable linearity can be achieved with one constant over limited ranges.

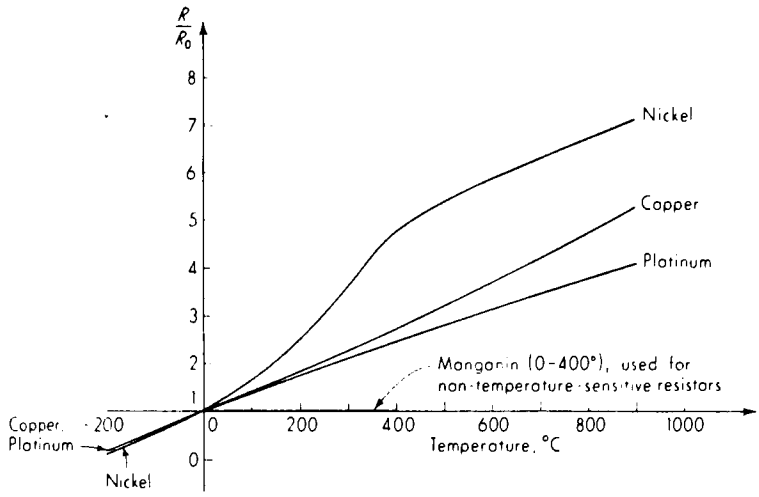

Figure 3.15 Resistance/Temperature Curves - R.T.D. Materials

For example [5], platinum is linear within ± 0.4 percent over the ranges -184 to -73°C and -73 to +149°C. ± 0.3 percent from -18 to 149°C ± 0.25 percent from -184 to -129°C, ± 0.2 percent from -18 to 93°C, and ± 1.2 percent from 260 to 816°C. For model number EP-120 platinum resistance elements, the temperature coefficient is 0.003915 ohm/ohm/°C over the range 0 to 100°C. In this work, however, two constants were obtained (see Appendix 3, RTD calibration) in order to achieve accuracies of ±0.1°C. The time constant of the RTD devices is about 5.5 sec in moving water (1 ft/sec). The flow rate in the system is approximately 0.7 ft/sec corresponding to a flow rate of 16 gpm.

Signal processing and display was done with a Fluke model 2180A RTD digital thermometer. The model 2180A is a portable, five digit RTD thermometer with 0.0° or 0.01° resolution. The instrument features:

1. Front panel switch selection of Fahrenheit or Celsius readings.
2. Switch selectable RTD inputs. Six RTD types plus a direct resistance measurement are possible.
3. Switch selectable input line voltage.
4. Dual-slope measurement techniques, under microcomputer control. 100 ms integration period, three readings per second.
5. Digital linearization of the RTD inputs. This is accomplished by a piecewise 4th order curve fit approximation under microcomputer control.

In the experimental work to follow (Section 5), readings were required at more than one point at the same time. This requires multiplexing capability which was provided by the use of two, two channel output Omega thermocouple selector switches. The reason for two selector switches was because 4 wire resistance thermometer elements were used. Since multiplexing capability is required, and also since each RTD has a different R_0 value, lead resistance error was accounted for in a different manner than would be employed if only one RTD was used. An explanation of how the digital thermometer determines temperature and how lead resistance effects are accounted for when one RTD is used is now given.

In operation, the digital thermometer maintains a constant, but adjustable, current through one set of wires (source wires) to and from the RTD. The other set senses the voltage drop across the RTD and transfers the signal to a comparator amplifier whose output voltage is proportional to the RTD resistance. The computer algorithm for the particular RTD type chosen now converts the voltage to a temperature. For any particular RTD type, the computer algorithm is constant i.e. a particular voltage level equals a particular temperature value and therefore to offset any lead resistance effects the current through the source wires is adjusted such that the proper voltage drop characterizing the measured temperature is across the RTD. This current is adjusted by a resistor on the input module. The calibration can be made at any temperature and is valid over the entire scale. This can be readily shown from Figure 3.15 and Ohm's Law. From Figure 3.15, for a given temperature:

$$R_1/R_{01} = R_2/R_{02} \tag{3.2}$$

where 1 and 2 indicate two RTD's of the same nominal rating but different actual R_o values due to tolerances.

From Ohm's Law:

$$V_1 = I_1 R_1 \tag{3.3}$$

where I_1 is constant.

Also: $V_2 = I_2 R_2$ (3.4)

again with I_2 constant but unequal to I_1. In order for the calibration to be valid over the entire scale, Eq. 3.3 must equal Eq. 3.4 over the range of R_1 and R_2. Equating Eq. 3.3 and Eq. 3.4 gives:

$$I_1 R_1 = I_2 R_2 \tag{3.5}$$

which is

$$I_2 = I_1 \frac{R_1}{R_2} \tag{3.6}$$

However, from Eq. 3.2: $$\frac{R_1}{R_2} = \frac{R_{01}}{R_{02}} \tag{3.7}$$

which substituted into Eq. 3.6 gives:

$$I_2 = I_1 \frac{R_{01}}{R_{02}} \tag{3.8}$$

which is constant for any value of R_1 and R_2.

Thus, by adjusting the resister on the input module, such that Eq. 3.8 is satisfied, V_1 will equal V_2 at any temperature and the lead effects will have been negated.

However, since five RTD's are used with each having a different lead length, as well as a different R_0 value, the calibration for one RTD will not be valid for the remaining RTD's. Therefore, each RTD

was calibrated separately with its leads and connections to the selector switches and digital thermometer the same as were used in the experimental work. The direct resistance measurement setting was used on the digital thermometer and twelve readings taken for each RTD at twelve known temperatures. From this data, the method of least squares for a quadratic curve fit was used to generate constants a_1 and a_2 for Eq. 3.1. The resistor setting on the input module was not adjusted during calibration or during subsequent testing. Having constants a_1 and a_2 and R_0 from calibration work, a measured R value at an unknown temperature readily allowed calculation of the unknown temperature. Since the resistor on the input module had not been adjusted, the selector switches could be multiplexed and accurate temperatures found since lead resistance effects were incorporated into constants a_1 and a_2. See Appendix 3, RTD calibration for additional calibration details. A photograph of the RTD's, selector switches, and digital thermometer is shown in figure 3.16.

Ambient temperature (T6, Figure 3.14) was measured by a type T copper-constantan thermocouple. The thermocouple was constructed from Omegaclad thermocouple wire with magnesium oxide insulation and 304 stainless steel sheathing. It was placed in a well-ventilated housing such that direct radiation of the sun could not fall on it and the housing mounted on the northeast corner of the east KTA tubular collector. The housing was constructed out of tin which has a low emissivity thereby reducing radiation effects. Figure 3.17 is a photograph of the housing and thermocouple in position. The thermocouple was chosen because of its rapid response time (it has a time constant of approximately 50 seconds in still air as opposed to 2.9 minutes for the RTD).

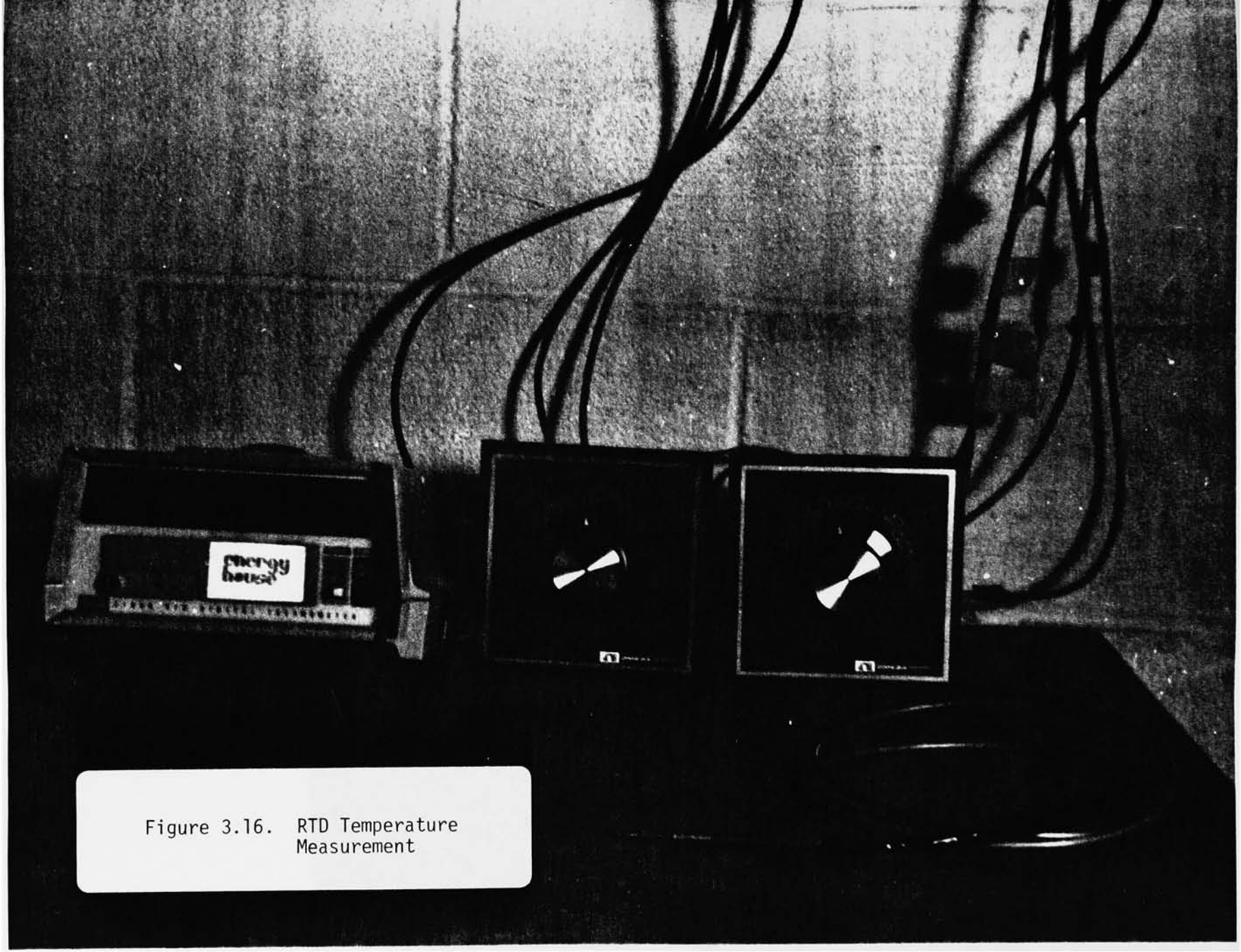

Figure 3.16. RTD Temperature Measurement

Figure 3.17. Thermocouple and Housing

Missing Page

Signal processing and display was done with a Fluke model 2190A thermocouple digital thermometer. The model 2190A is a portable, five-digit thermocouple with a resolution of 0.1°. It has a temperature range of -242°C to +2471°C. The instrument has the following features:

1. Front panel switch selection of Fahrenheit or Celsius readings.
2. Switch selectable thermocouple inputs. Seven thermocouple types are available.
3. Switch selectable input line voltage.
4. Dual-slope measurement techniques, under microcomputer control. 100 ms integration period, three readings per second.
5. Digital linearization of the thermocouple inputs. This is accomplished by a 4th order curve fit.
6. Automatic reference-junction compensation eliminating the need for an ice bath reference-junction.

Calibration was checked before experimentation by inserting the thermocouple in an ice water lag bath and adjusting R1 on the thermocouple input module through the rear access port until the correct temperature was displayed. Using this procedure, a maximum error of $\pm$ 0.2°C was obtained as stated by the instruction manual.

Ambient temperature (T7, Figure 3.14) of the basement was measured by a mercury in bulb thermometer whose description and accuracy is given in Appendix 3, part 3, RTD calibration.

The preheat tank (T8) and storage hot water heater tank water temperature (T9) were measured by National Semiconductor device LM134. The LM134 is a 3-terminal true floating current source temperature transducer with no separate power supply connections. This device provides a regulated, constant current with as little as 1 volt across its V+ and V- terminals (see Figure 3.18). The sense voltage across pins 1 and 3 used to establish operating current in the LM134 is 64 mv at 25°C and is directly proportional to absolute temperature (°K). The one external resistor (470 Ω) connection shown in Figure 3.18 generates a current with ≈ +0.33%/°C temperature dependence. Since current is proportional to temperature (125 μA to 170 μA over the range 0° to 100°C), series resistance in long wire runs do not affect accuracy, hence only two leads are required. The LM134 is guaranteed over a

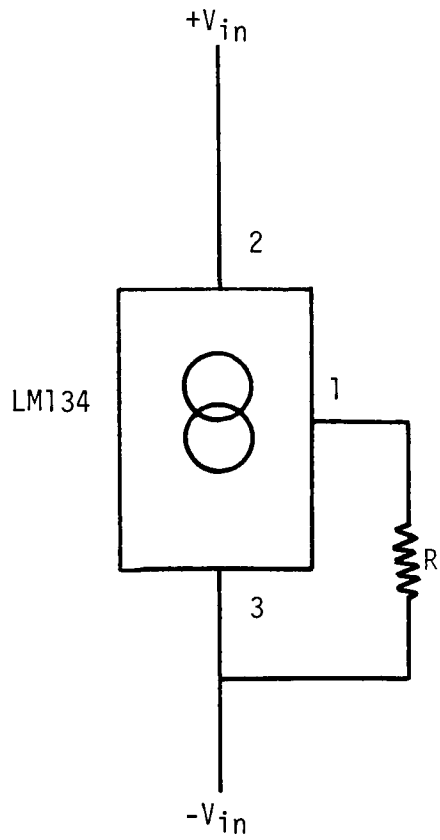

Figure 3.18 Basic Two-Terminal Current Source - LM134

temperature range of -55°C to +125°C and is hermetically sealed.

The LM134 devices with external resister were mounted in 1/8"O.D. thin-walled brass tubes with a brass plug soldered to the tube end. Since the LM134 is a floating current source, teflon heat shrink was used to isolate the sensor from the brass housing. Finally, the housing was backfilled with sand and sealed with epoxy. A check of each unit was made with a digital voltmeter to assure that the LM134 was isolated from the brass housing. The LM134 with resistor and brass housing will be identified as a solid state sensor.

An analog signal conditioning circuit board provided a voltage output from the temperature-dependent current generated by the solid state sensor. In addition, zeroing (offset) and spanning (gain) circuitry was also located on the analog board. This allowed for calibration of the particular sensor which is covered in Appendix 3. An active 2 pole filter effectively removed line noise.

Power requirements of the analog signal conditioning circuit board was met by a +25, -25V dc unregulated power supply which fed two onboard regulators giving a split ± 15V dc supply. This supply also powered the LM134 devices.

Signal display (a voltage directly relatable to temperature) was achieved using a Keithley 170 TRMS digital multimeter (D.M.M.). The input impedance is equal to 10 mΩ, Instrument accuracy is 0.04% of the reading plus one digit. The instrument was used during calibration and during experimentation.

Experimental work described in section 5.2 required a hard copy of the D.M.M. display. This was obtained using a Techni-Rite, Model TR-888 eight channel direct writing analog recorder. Writing is done by the use of a heated stylus (for each channel) which puts pressure on a heat-sensitive paper producing a trace. The recorder has eight chart speeds, from 0.5 mm/min to 100 mm/min. The Model TR-888 has eight plug-in signal conditioners: two-model TSC-801 signal conditioners and six model TSC-810 signal conditioners. Since only the model TSC-801 signal conditioner was used, it only will be described. The TSC-801 performs the dual function of providing calibrated amplification of signals and regulated power to the amplifier pen motor located in the recorder main frame. The input circuit is differential, balanced with respect to frame, and provides excellent common mode rejection. Calibrated zero suppression is provided. Eight active range settings are available, from 1 mv/div to 2 mv/div. Calibration procedures outlined in the operation manual were followed giving an accuracy of 0.25 div.

Figures 3.19 is a photograph of a solid state sensor, the analog signal conditioning circuit board, the unregulated power supply, the D.M.M., and the eight channel analog recorder. With the arrangement shown and by following the calibration procedure outlined in Appendix 3, a maximum error of $\pm$0.16°C was achieved. The solid state sensor was chosen because its output was more readily conditioned to allow for recording. In future work at Energy House, this capability will be available for RTD's and thermocouples. Also, the solid state device

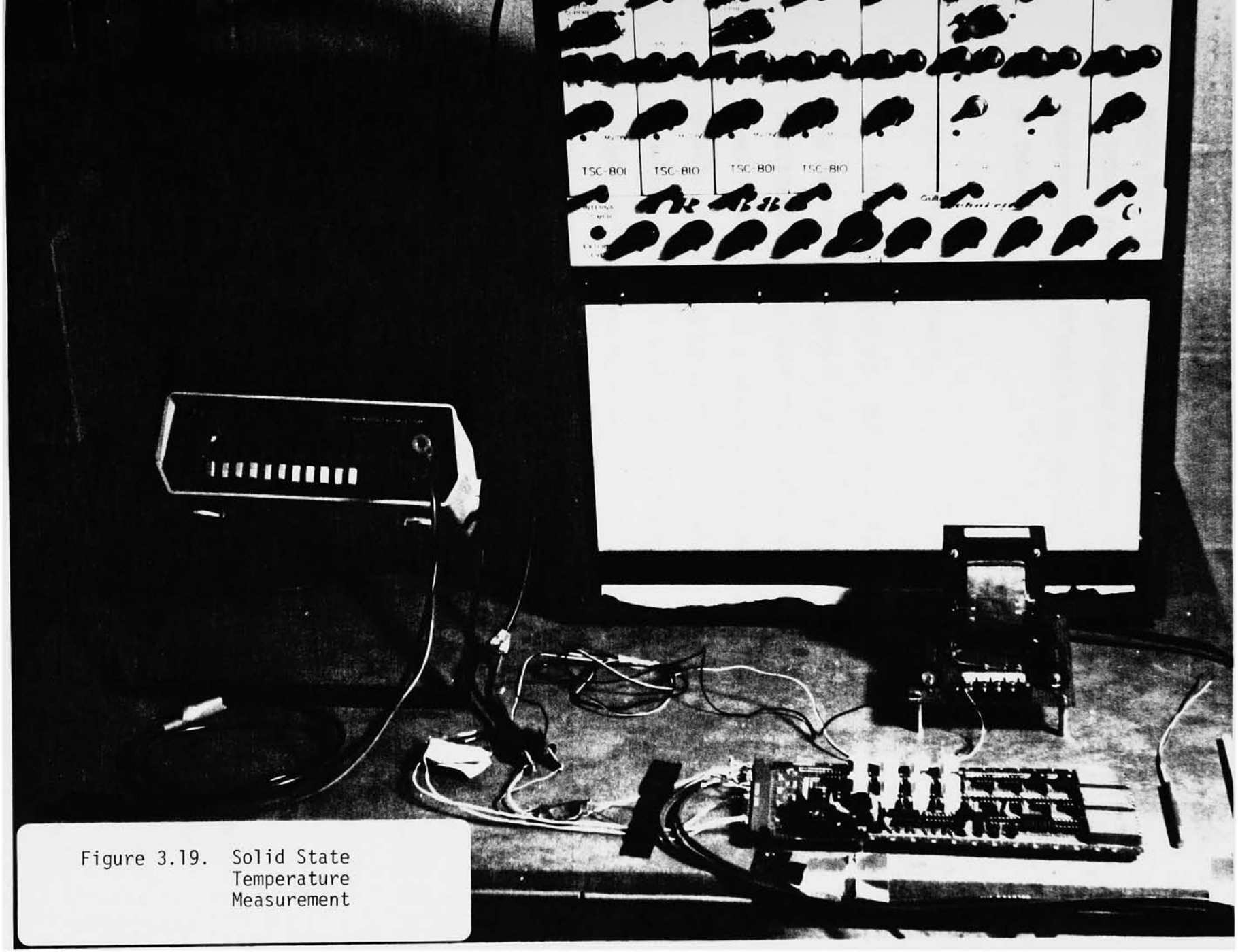

Figure 3.19. Solid State Temperature Measurement

only requires two leads as opposed to four by the RTD. It is to be noted that T8 and T9 shown on Figure 3.14 occupy the same location as TMDPH1 and TMDH in Figure 3.1 which is no problem since the experiments using T8 and T9 did not require the presence of TMDPH1 or TMDH.

3.3.2 Flow Measurement

Flow measurement was required in the closed solar energy collection loop as shown in Figure 3.14. A 5/8" by 3/4" model SCER-H positive displacement Badger water meter was used for this application. The model SCER-H features a bronze housing and a synthetic rubber disc capable of operation up to 250°F (121°C). In addition, the water meter has a magnetic drive system which eliminates the need for a packing gland. This operates by means of a four pole magnet located inside the water meter housing. The magnet rotates at the same rate of speed as the nutating synthetic rubber disc. This magnet then drives a magnet located in a removable gear train mounted on the water meter. The gear train in turn drives a digital register. The materials used for construction of the water meter permit either water or propylene glycol to be used as the monitored fluid.

Conventional monitoring of flow with the external gear train results in an integrated total flow rate. However, experimental work in Section 5.1 required instantaneous flow rates, hence another method of monitoring flow was used. A type TL170C Silicon Hall-Effect Switch in conjunction with an electromagnetically-operated digital counter was chosen. The TL170C is a low cost magnetically-operated electronic

switch that utilizes the Hall Effect to sense reversals in magnetic field direction. Briefly, the Hall Effect is the property of a semiconductor or conductor which, when exposed to a current and a perpendicular external magnetic field, gives rise to an orthogonal internal electric current due to the Lorentz force. As the magnetic field direction reverses, the internal current changes direction also. By internal signal conditioning in the TL170C, this reversal in current direction is outputed as a change in voltage level between 0.4V (low state) and 20V (high state). This voltage change from the TL170C then is used to drive the digital counter. Power was supplied to the TL170C and the digital counter by means of an RCA WP-703A constant voltage dc. power supply. Its output ranged from 0 to 20V dc. with the setting at 20V used to power the device and counter. The TL170C switch mounted directly on the outside of housing top was not activated by the four pole magnet so a groove 0.060 inches was milled from the cover and the device epoxied in position. Because the TL170C was recessed, the magnetic gear train could either be attached or removed depending on preference without hindering operation of the TL170C. To measure instantaneous flow rates, the digital counter reading was divided by the time required to accumulate it and from the calibration results of Appendix 4, the flow rate found. The four pole magnet resulted in two counts per revolution which when taken into account with the calibration technique gave an accuracy for flow rate measurements of $\pm$ 0.85% of the reading. How this result was arrived at as well as the calibration technique and procedure is found in Appendix 4. Figure 3.20 is a photograph of the configuration described above(digital counter not shown).

Figure 3.20. Part A - Flow Rate Monitoring Equipment

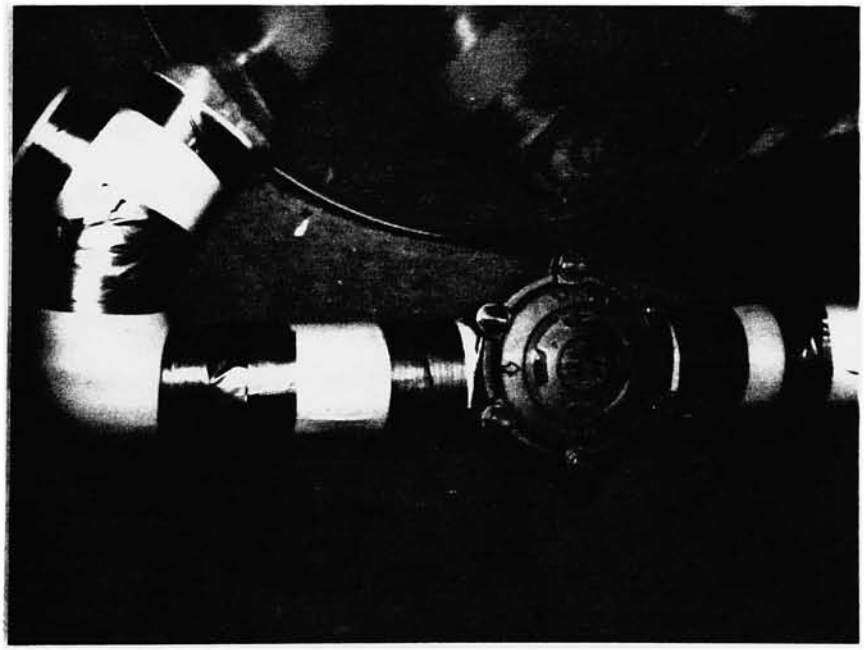

Figure 3.20. Part B - Water Meter

3.3.3 Insolation Measurement

Insolation data utilized for the work to be described in Section 7 were measured by two Eppley Black and White Model 8-48 pyranometers, two quantity integrators, Science Associates Catalog number 619, and two strip chart recorders, Science Associates Catalog number 619H. The data were collected beginning April 8, 1976 on both a horizontal surface and a tilted surface, 60° from the horizontal facing due south. The pyranometers are located on the southwest corner of the power lab roof of the Mechanical Engineering building. This location is approximately 1/2 mile from the Energy House. For the experimental work of Section 5, the output of the pyranometer on the tilted surface was recorded utilizing a Gould 110 strip chart recorder. The Gould 110 is a ten inch, multi-speed, two channel strip chart recorder, which utilizes a thermal writing technique. It was used in order to obtain more precise insolation measurements. Following calibration procedures outlined in the owner's manual, an accuracy of $\pm$ 0.1% was obtained. This represents the accuracy of the output of the pyranometer and does not exclude the possibility that the pyranometer itself is inaccurate. Using the Science Associates strip chart, however, for insolation values over 15 minute periods, accuracies of no better than 1 part in 30 were possible (assuming readibility of 1/2 langley with the highest total per 15 minute period approximately 15 langleys) or 3.3%. Therefore, by using the Gould 110, this inaccuracy is essentially eliminated and the total error is only the result of the pyranometer. This error is thought to be no larger than 5%.

4. COMPONENT MODELS

Each component of the solar water heating system can be mathematically described. With these formulations plus additional information on the nature of the system loads and the driving forces, it is possible to represent the thermal performance of the system. The purpose of this section is to derive the mathematical expressions describing the major components of the system, i.e., the KTA collectors, the preheat and hot water tank, and the heat exchanger.

4.1 KTA Collector Analysis

The derivations to follow parallel that of a flat plate collector. Since the flat plate derivation has been extensively covered in the literature [6], [7], [8] [9] with an excellent compilation given in Duffie and Beckman's Solar Energy Thermal Processes [10], it will not be given here. However, as important results are obtained, their correlation to flat plate results will be noted.

4.1.1 General Equation for Useful Heat Gain

Figure 4.1 is a control volume for a single tubular collector element. Assuming steady-state conditions, an energy balance on an elemental section dx yields

$$\Sigma \text{ losses} + \Sigma \text{ Gains} = 0 \tag{4.1}$$

where each can be expressed as:

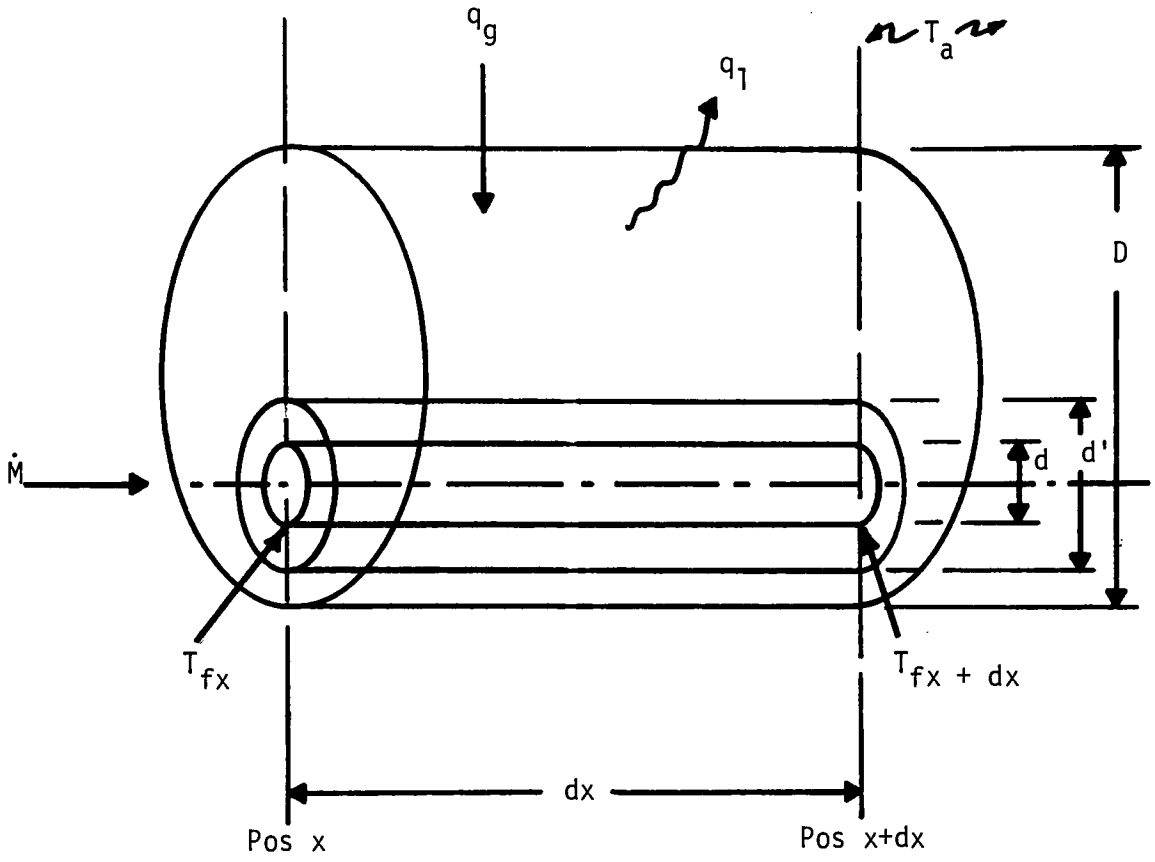

d = 1/2" O.D. (0.0127m) M-type hard drawn copper tube

d'= 3/4" O.D. (0.0191m) 008 soda-lime glass tube

D = 2" O.D. (0.0508m) 008 soda-lime glass tube

Figure 4.1 Tubular Collection Element Control Volume

$$\Sigma \text{ Losses} = -\pi \, D dx \, q_{\ell} - \dot{M} \, C_p \, (T_{fx} + d_x) \tag{4.2}$$

$$\Sigma \text{ Gains} = D \, dx \, q_g + \dot{M} \, C_p \, (T_{fx}) \tag{4.3}$$

The variable q_{ℓ} is the energy lost per unit area of the outer tube and the variable q_g is the net energy gain per unit aperture area. Equation 4.1 in terms of equations 4.2 and 4.3 becomes:

$$D \, dx \, (q_g - \pi q_{\ell}) + \dot{M} C_p \, (T_{fx} - T_{fx + dx}) = 0 \tag{4.4}$$

The right portion of the left hand side of equation 4.4 can be written as

$$\dot{M} C_p \, (T_{fx} - T_{fx + dx}) = -q_u \, D dx \tag{4.5}$$

where q_u is the useful energy gain per unit aperture area. Combining equations 4.4 and 4.5 gives:

$$q_u = q_g - \pi q_{\ell} \tag{4.6}$$

The variable q_g can be expressed as

$$q_g = (\tau\alpha)_e \, I_{eff} \tag{4.7}$$

where $(\tau\alpha)_e$ is the transmittance, absorptance product of the cover system and I_{eff} is the insolation per unit area over the aperture area which is either directly absorbed or backreflected by the

silvered portion of the outer cover tube to the absorber tube.

The variable q_ℓ can be expressed as

$$q_\ell = \frac{U_L \, \pi d \cdot dx}{\pi D \cdot dx} \left[\frac{T_{fx + dx} + T_{fx}}{2} - T_a \right] \tag{4.8}$$

where U_L is the overall heat transfer coefficient between the absorber tube and the surroundings. The numerator represents losses from the absorber tube and the denominator represents the fact that q_ℓ is per unit outer tube area which is the circumferential area of the aperture tube. Equation 4.8 becomes:

$$q_\ell = U_L \frac{d}{D} (T_{fx} - T_a) \tag{4.9}$$

where

$$\frac{T_{fx + dx} + T_{fx}}{2} \rightarrow T_{fx} \text{ as } dx \rightarrow 0$$

Substituting Equations 4.9 and 4.7 into Equation 4.6 gives:

$$q_u = (\tau\alpha)_e \, I_{eff} - U_L \frac{\pi d}{D} (T_{fx} - T_a) \tag{4.10}$$

Defining $q_{u/L} = q_u D$ gives

$$q_{u/L} = D[(\tau\alpha)_e \, I_{eff} - U_L \frac{\pi d}{D} (T_{fx} - T_a)] \tag{4.11}$$

This result is analogous to Equation 7.5.16 of Duffie and Beckman [10] except for the fact that F (the fin efficiency factor) and F' (the collector efficiency factor) are equal to 1. Since there are no fins between the absorber tubes, the fin efficiency must be 1. The collector efficiency factor is 1 if it is assumed the absorber tube is at the local fluid temperature. This is equivalent to saying that the resistance R_1 between the fluid in the absorber tube and the absorber tube is negligible compared to the addition of resistances in the thermal network. This is the case (see Section 4.1.4) with this resistance. The value of R_1 is approximately 3% of the resistance between the absorber tube and the first glass cover tube. Work by Beekley and Mather [11] supports this result.

4.1.2 Temperature Distribution in Flow Direction

The useful gain per unit of flow length as calculated from Equation 4.11 is ultimately transferred to the fluid. The fluid enters the collector at temperature T_{INC} and increases in temperature until at exit it is T_{OUTC}. Equation 4.5 can be rewritten:

$$q_u D dx = q_{u/L} dx = \dot{M} C_p (T_{fx + dx} - T_{fx}) \tag{4.12}$$

Dividing through by dx, finding the limit as dx approaches zero, and substituting Equation 4.11 for $q_{u/L}$ gives:

$$q_{u/L} = \dot{M} C_p \frac{dT_{fx}}{dx} = D[(\tau\alpha)_e I_{eff} - U_L \frac{\pi d}{D} (T_{fx} - T_a)] \tag{4.13}$$

rearranging gives:

$$\frac{dT_{fx}}{dx} + \frac{U_L \pi d}{\dot{M} C_p} T_{fx} = \frac{D}{\dot{M} C_p} [(\tau\alpha)_e I_{eff} + U_L \frac{\pi d}{D} T_a] \qquad (4.14)$$

Equation 4.14 is a first order nonhomogeneous differential equation which is solved as follows:

$$T_{fx} = T_c + T_p \qquad \text{Assume} \quad T_c = C_1 e^{rx} \qquad (4.15)$$

Upon substitution of Equation 4.15 into Equation 4.14 (with the right side of the equation set to zero), the following is obtained:

$$(r + \frac{U_L \pi d}{\dot{M} C_p}) C_1 e^{rx} = 0$$

$$r = \frac{-U_L \pi d}{\dot{M} C_p}$$

and

$$T_c = C_1 e^{\frac{-U_L \pi d}{\dot{M} C_p} x} \qquad (4.16)$$

Assume $T_p = A$ and substitute into Equation 4.14:

$$\frac{U_L \pi d}{\dot{M} C_p} A = \frac{D}{\dot{M} C_p} [(\tau\alpha)_e I_{eff} + U_L \frac{\pi d}{D} T_a]$$

$$A = \frac{D}{d} \frac{1}{\pi U_L} [q_g + U_L \frac{\pi d}{D} T_a]$$

where

$$q_g = (\tau\alpha)_e I_{eff}$$

from Equation 4.7.

$$A = \frac{q_g}{U_L} \frac{D}{d} \frac{1}{\pi} + T_a \qquad (4.17)$$

Now, $$T_{fx} = c_1 e^{\frac{-U_L \pi d}{\dot{M} C_p} x} + \frac{q_g}{U_L} \frac{D}{d} \frac{1}{\pi} + T_a \qquad (4.18)$$

Boundary Conditions

$$T_{fx} = T_{INC} \qquad \text{at} \quad x = 0 \qquad (4.19)$$

$$T_{fx} = T_{OUTC} \qquad \text{at } x = L \text{ (collector outlet)}$$

Equation 4.18 with the above boundary condition substituted in becomes:

$$T_{INC} = C_1 + \frac{q_g}{U_L} \frac{D}{d} \frac{1}{\pi} + T_a \qquad (4.20)$$

and rearranging,

$$C_1 = T_{INC} - \frac{q_g}{U_L} \frac{D}{d} \frac{1}{\pi} - T_a \tag{4.21}$$

Substitution of Equation 4.21 into Equation 4.18 gives after rearranging :

$$\frac{T_{fx} - T_a - \frac{q_g}{U_L} \frac{D}{d} \frac{1}{\pi}}{T_{INC} - T_a - \frac{q_g}{U_L} \frac{D}{d} \frac{1}{\pi}} = e^{\frac{-U_L \pi d}{\dot{M} C_p} x} \tag{4.22}$$

which is of the analogous form of Equation 7.6.3 of Duffie and Beckman [10].

Collector Heat Removal Factor

It is convenient to define a quantity that relates the actual useful energy gain to the energy gain if the whole collector were at the fluid inlet temperature. This is known as the collector heat removal factor.

$$F_R = \frac{\text{useful heat gain}}{\text{useful heat gain if whole collector is at fluid inlet temperature}}$$

The collector heat removal factor can be expressed as :

$$F_R = \frac{G C_p (T_{OUTC} - T_{INC})}{[q_g - U_L \frac{\pi d}{D} (T_{INC} - T_a)]} \tag{4.23}$$

where G = mass flow rate per unit aperture area, $\dot{M}/A_t$

$$F_R = \frac{G\ C_p\ D}{U_L\ \pi\ d}\left[\frac{T_{OUTC} - T_{INC}}{\frac{q_g}{U_L}\frac{D}{d}\ \frac{1}{\pi} - (T_{INC} - T_a)}\right] \tag{4.24}$$

or

$$F_R = \frac{G\ C_p\ D}{U_L\ \pi\ d}\left[\frac{\left(T_{OUTC} - T_a - \frac{q_g}{U_L}\frac{D}{d}\frac{1}{\pi}\right) - \left(T_{INC} - T_a - \frac{q_g}{U_L}\frac{D}{d}\frac{1}{\pi}\right)}{T_a - T_{INC} + \frac{q_g}{U_L}\frac{D}{d}\frac{1}{\pi}}\right] \tag{4.25}$$

or

$$F_R = \frac{GC_p}{U_L\pi}\frac{D}{d}\left[1 - \frac{\frac{q_g}{U_L}\frac{D}{d}\frac{1}{\pi} - (T_{OUTC} - T_a)}{\frac{q_g}{U_L}\frac{D}{d}\frac{1}{\pi} - (T_{INC} - T_a)}\right] \tag{4.26}$$

which, from Equation 4.22 with $T_{fx} = T_{OUTC}$ and x = L:

$$F_R = \frac{GC_p}{U_L\pi}\frac{D}{d}\left[1 - e^{-\left[\frac{U_L\ \pi}{G\ C_p}\frac{d}{D}\right]}\right] \tag{4.27}$$

Again, this result is of a form paralleling that of a flat plate which is given as Equation 7.7.4 of Duffie and Beckman [10].

Rewriting Equation 4.23 gives:

$$q_u = F_R[q_g - U_L\frac{\pi d}{D}(T_{INC} - T_a) \tag{4.28}$$

and

$$Q_u = q_u A_t = A_t F_R \left[q_g - U_L \frac{\pi d}{D} (T_{INC} - T_a)\right] \tag{4.29}$$

Collector Efficiency

Collector efficiency is defined as the useful energy collected divided by the maximum possible energy available. This can be expressed as follows:

$$\eta = \frac{\dot{M} C_p (T_{OUTC} - T_{INC})}{IDL} = \frac{\dot{M} C_p (T_{OUTC} - T_{INC})}{IA_t} \tag{4.30}$$

Substituting Equation 4.23 into the above expression gives:

$$\eta = \frac{A_t F_R \left[q_g - U_L \frac{\pi d}{D} (T_{INC} - T_a)\right]}{IA_t} \tag{4.31}$$

which becomes

$$\eta = \frac{F_R S}{I} - U_L \pi \frac{d}{D} \frac{(T_{INC} - T_a)}{I} F_R \tag{4.32}$$

or

$$\eta = F_R (\tau\alpha)_e \frac{I_{eff}}{I} - U_L \frac{\pi d}{D} \frac{(T_{INC} - T_a)}{I} F_R \tag{4.33}$$

Equations 4.29 and 4.33 represent the KTA tubular collector performance equations. They are similar in form to those derived for flat plate performance. The variables of these equations are now examined separately as they apply to the tubular collector.

4.1.3 Effective Insolation, I_{eff}

The development of this section follows that developed by Beekley and Mather [11] [2]. I_{eff} is the effective insolation on the aperture tube, defined on the basis of the aperture cross sectional area, A_t. It is based on aperture cross sectional area in order to be consistent with the work of Sections 4.1.1 and 4.1.2. If I is the insolation in the tilt plane of the collector, I_{eff} can be written [2] as:

$$I_{eff} = \Gamma I \qquad (4.34)$$

where Γ is defined as the enhancement factor. Substituting Equation 4.34 into Equation 4.33 gives:

$$\eta = F_R \left[(\tau\alpha)_e \Gamma - U_L \frac{\pi d}{D} \frac{(T_{INC} - T_a)}{I}\right] \qquad (4.35)$$

The enhancement factor can be calculated for the tubular collection elements by realizing that I_{eff} is made up of both directly intercepted beam and diffuse radiation and backreflected

beam and diffuse radiation. Further, $I = I_b + I_d$. Also, Γ_b and Γ_d can be defined [2] as follows:

$$I_{eff} = \Gamma_b I_b + \Gamma_d I_d \tag{4.36}$$

with the tube centerline axes oriented in an east-west direction. Dividing Equation 4.36 and I and substituting in Equation 4.34 gives:

$$\Gamma = \Gamma_b \frac{I_b}{I} + \Gamma_d \frac{I_d}{I} \tag{4.37}$$

In order to calculate Γ, the beam and diffuse enhancement factors must first be examined.

4.1.3.1 Beam Enhancement Factor, Γ_b

The beam enhancement factor can be written as [2];

$$\Gamma_b = \frac{g(\Omega)}{\cos \Omega} \frac{d}{D} + \rho\gamma(\Omega) \tag{4.38}$$

where the first part is the beam radiation directly absorbed by the absorber tube and the second part is the beam radiation reflected to the absorber tube. The incident angle relationships necessary for a complete understanding of the work to follow can be found in Appendix 5.

The terms of Equation 4.38 are defined below and will each be examined closer:

$g(\Omega)$ = shading factor (represents the fact that the absorber tube can be partially shaded from the sun by either adjacent tubes or its own silver backing),

$\cos \Omega$ = relates beam radiation measured on a tilted surface to that measured on the absorber tube,

ρ = reflectance of the silver backing of the aperture tube. It is the average of the spectral reflectance over the solar spectrum,

$\gamma(\Omega)$ = the fraction of the aperture area over which beam radiation is reflected to the absorber tube

$g(\Omega)$ - Shading Factor

From Appendix 5 for east-west mounted tubes, it is seen that the angle Ω can be both positive and negative. Therefore, the relationship for $g(\Omega)$ will be derived for both cases. Note also that glass absorptance, reflectance, and transmittance is not dealt with in this part.

a.) Case 1 - $\Omega > 0°$

The shading factor $g(\Omega)$ is equal to one when $\Omega \leq \Omega_s$ where Ω_s is an angle above which the absorber tube is not fully exposed to the sun. The angle Ω_s can be seen geometrically in Figure 4.2. From the figure:

$$\Omega_s = 90 - \theta - \gamma \qquad (4.39)$$

where: θ is positive measured C.W. from n_s
and γ is positive measured CCW from n (not to be confused with $\gamma(\Omega)$)
and Ω, Ω_s are positive measured CCW from n_s.

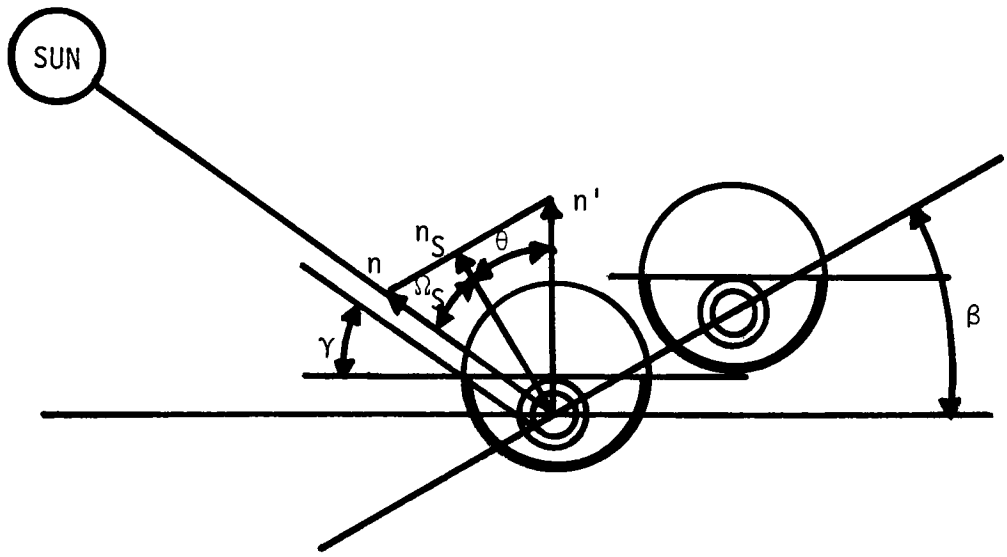

Figure 4.2 Shading Angle, Ω_S

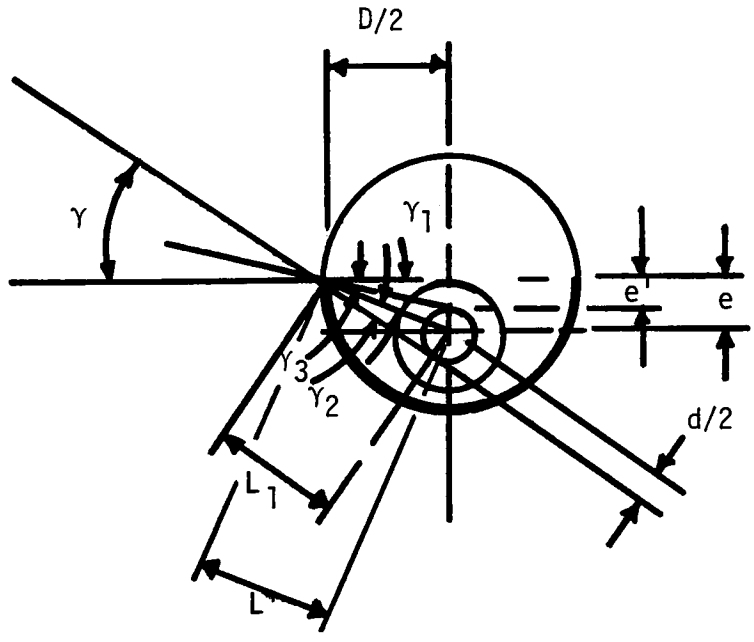

Figure 4.3 Collector Tube Geometric Angle, γ

In the figure, the sun is positioned such that any increase in Ω will result in a shading factor of less than one.

The angle θ is an orientation angle which depends on the tube rotational orientation. This angle was factory set and has been found to be equal to -10.8°. The angle γ is also a geometric angle. It is found from Figure 4.3 and is unchangeable. From the figure, it is seen that

$$\gamma = \gamma_1 + \gamma_2 \tag{4.40}$$

and

$$\gamma_1 = \text{Tan}^{-1} \frac{e}{D/2} \tag{4.41}$$

$$\gamma_2 = \text{Sin}^{-1} \frac{d/2}{L^1} \tag{4.42}$$

where

$$L^1 = \sqrt{(D/2)^2 + (e)^2} \tag{4.43}$$

for the KTA tubular collector: D = 2"

e = 1/2"

d = 1/2"

therefore:

$$\gamma = \text{Tan}^{-1}(1/2) + \text{Sin}^{-1}\frac{1/4}{\sqrt{1^2 + (0.5)^2}}$$

$$\gamma = 26.6 + 12.9 = 39.5°$$

From Equation 4.39, $\Omega_s = 90 - (-10.8) - 39.5 = 61.3°$

The shading factor $g(\Omega)$ is equal to zero for $\Omega \geq \Omega_{co}$ where Ω_{co} is the cutoff angle above which the tube is not exposed at all to the incoming beam radiation. From Figures 4.2 and 4.3:

$$\Omega_{co} = 90 - \theta - \gamma_3 \qquad (4.44)$$

and

$$\gamma_3 = \text{Tan}^{-1}\frac{e'}{D/2} \qquad \text{where } e' = e - \frac{d}{2} = 0.25$$

So:

$$\gamma_3 = 14.0°$$

with $\Omega_{co} = 90 - (10.8) - 14.0 = 86.8°$

Finally, $g(\Omega) = \frac{86.8 - \Omega}{25.5}$ (4.45)

for $\Omega_s < \Omega < \Omega_{co}$. This means that when the absorber tube is partially shaded, the shading factor is a linear function indirectly proportional to the amount of the projected absorber tube shaded.

In summary, the following results were obtained:

$$g(\Omega) = 1 \qquad \text{for } \Omega \leq 61.3° \qquad (4.46)$$

$$g(\Omega) = 0 \qquad \text{for } \Omega \geq 86.8° \qquad (4.47)$$

$$g(\Omega) = \frac{86.8 - \Omega}{25.5} \qquad \text{for } 61.3° < \Omega < 86.8° \qquad (4.45)$$

b) Case 2 - $\Omega \leq 0°$

When Ω is less than or equal to zero, there are three tube orientations possible which give rise to three sets of results for $g(\Omega)$. Figures 4.4, 4.5, and 4.6 show these three orientations which can be described as follows:

1. Figure 4.4 represents shading caused solely by the adjacent tube silver backing.

2. Figure 4.5 represents shading caused solely by the tube of interest with adjacent tubes having no shading effect.

3. Figure 4.6 represents a combination of the two cases described above.

Looking at Figures 4.4, 4.5, and 4.6, it is clear that for a

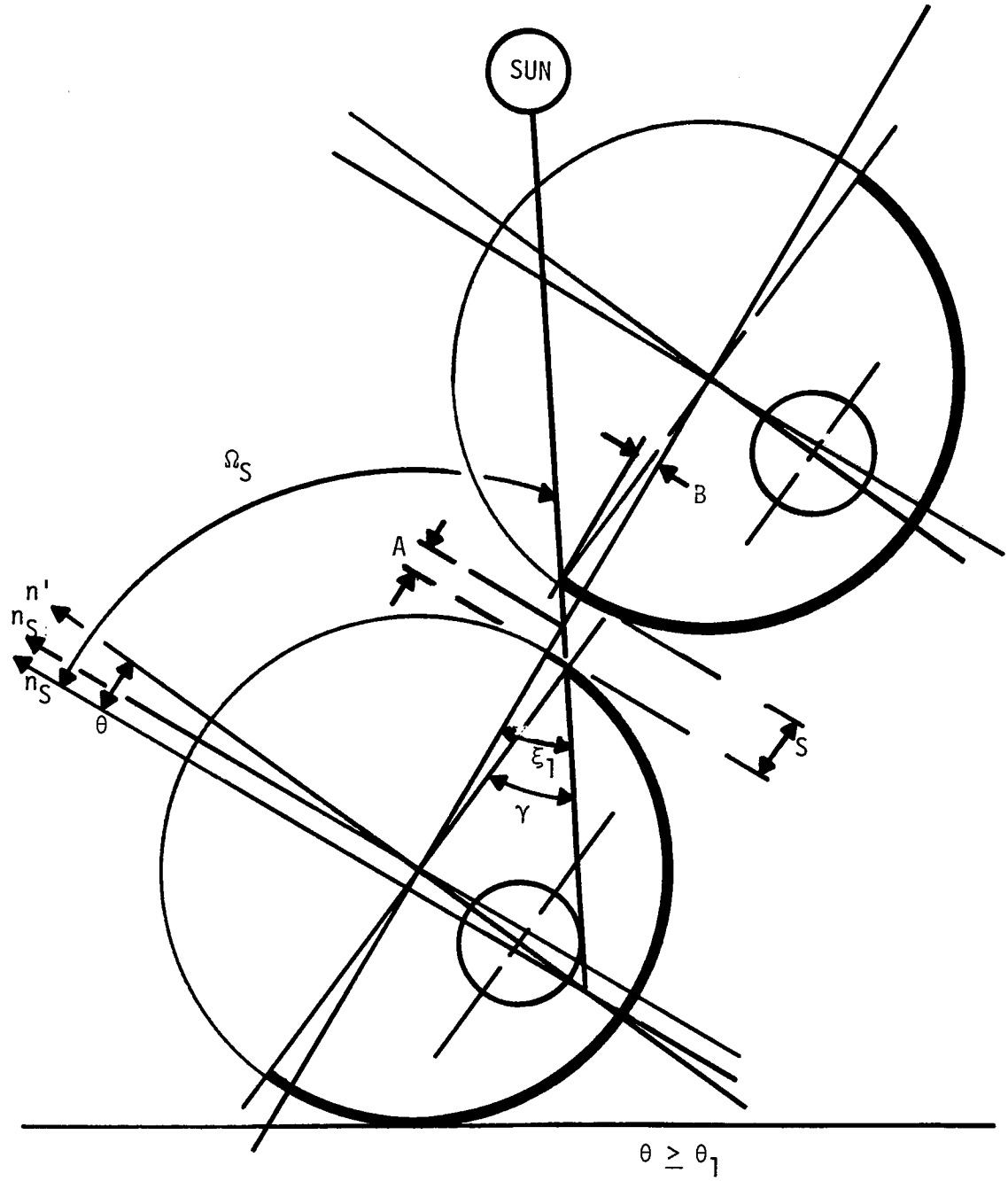

Figure 4.4 Tube Orientation 1 - Shading By Adjacent Tube

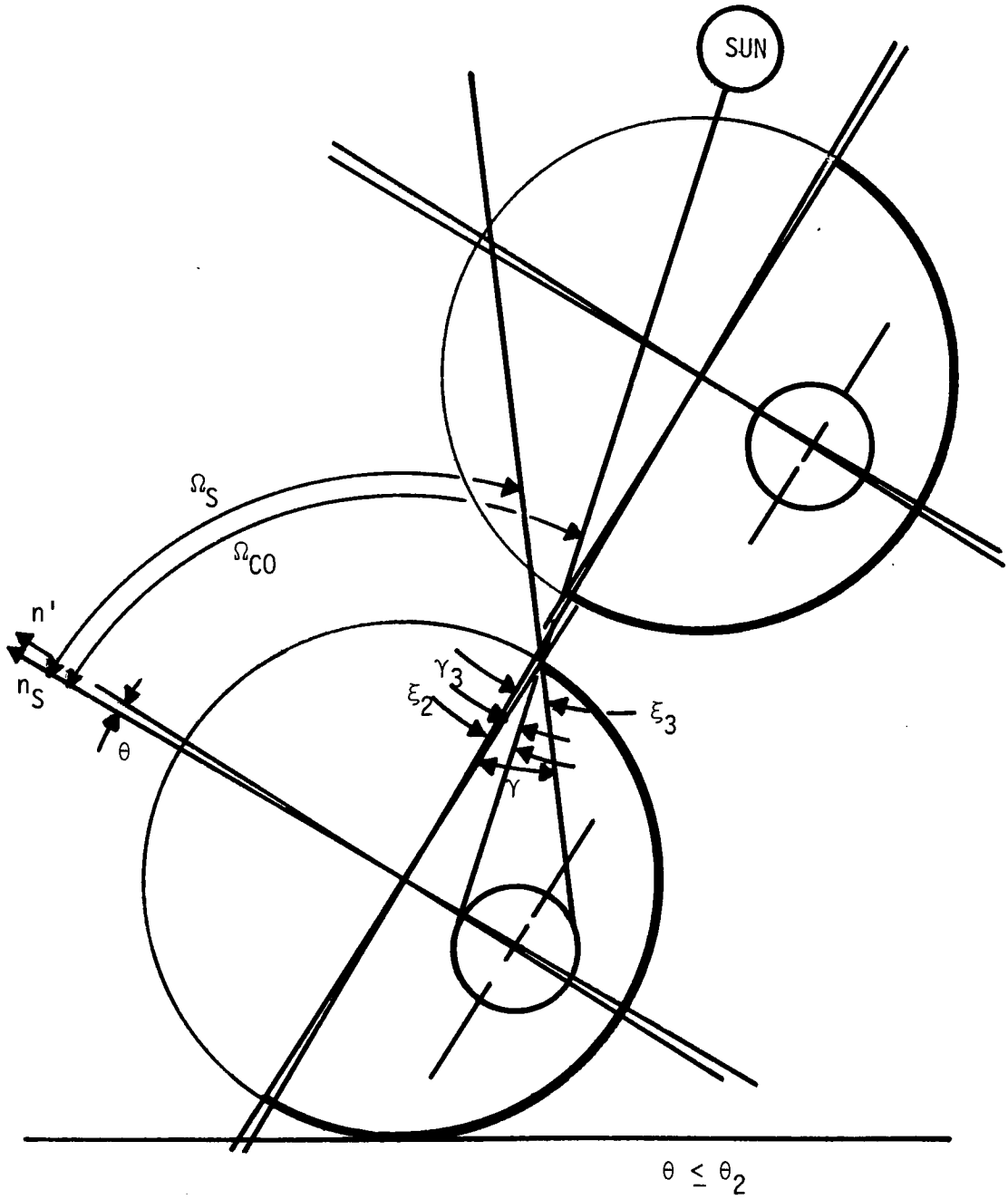

Figure 4.5 Tube Orientation 2 - Shading By Tube Of Interest

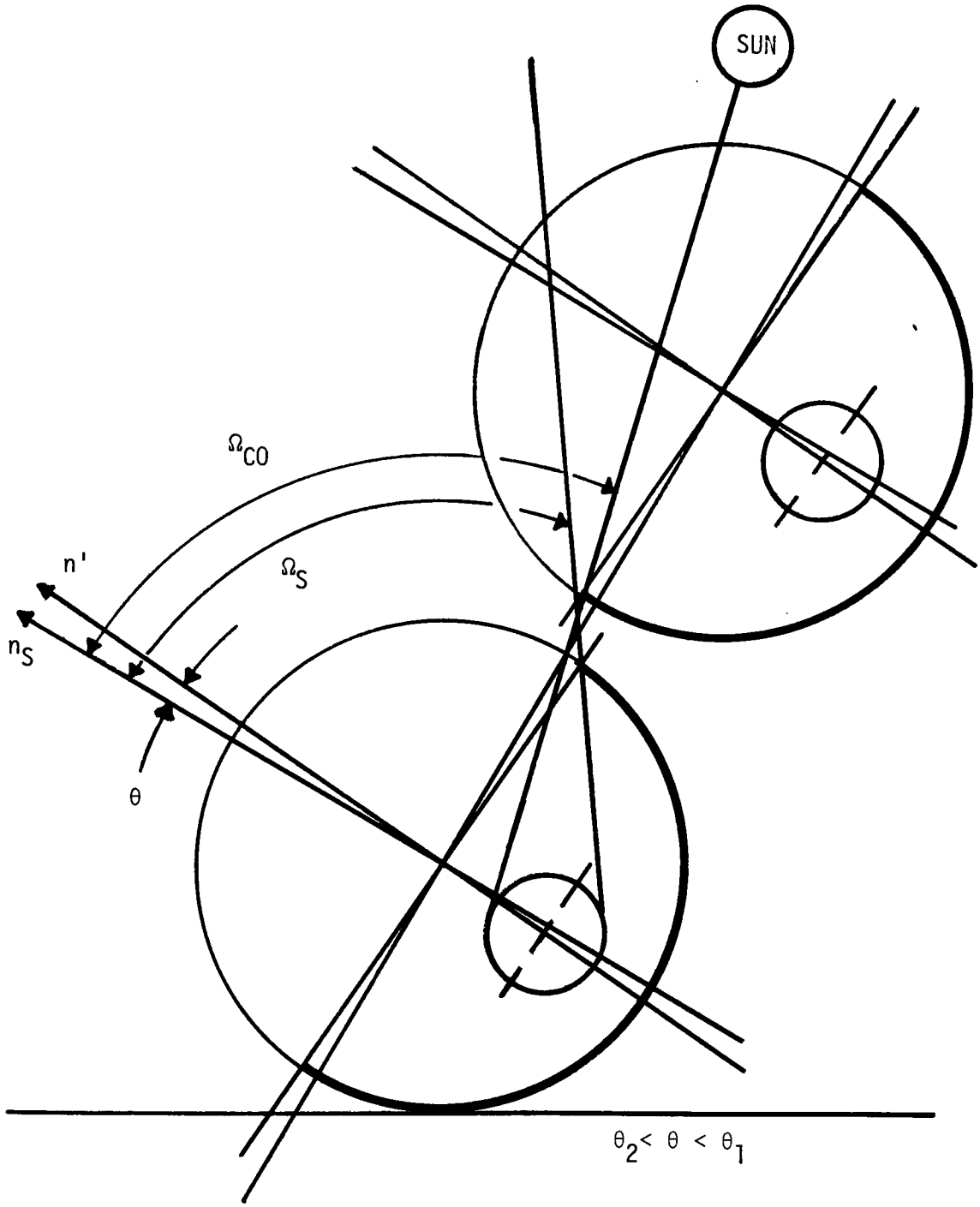

Figure 4.6 Tube Orientation 3 - Shading By Combination

given tube clearance S, the angle θ determines which of the cases above is appropriate. Therefore, the limiting values for θ will first be determined.

1) Orientation 1 - From Figure 4.4, if $\theta \geq \theta_1$, then orientation 1 is the case under consideration. Note that θ is positive measured CW from n_s. The angle θ_1 is found as follows:

From the figure,

$$\xi_1 = \gamma - \theta_1 \tag{4.48}$$

when $\theta = \theta_1$.

The angle γ was previously found and is shown in Figure 4.3. Also:

$$\text{Tan } \xi_1 = \text{Tan } (\gamma - \theta_1) = \frac{B}{A} = \frac{\frac{D}{2} \text{ Sin } \theta_1}{\frac{S}{2} + (\frac{D}{2} - \frac{D}{2} \text{ Cos } \theta_1)} \tag{4.49}$$

Simplification gives:

$$\text{Tan } (\gamma - \theta_1) = \frac{\text{Sin } \theta_1}{\frac{S}{D} + (1 - \text{Cos } \theta_1)} \tag{4.50}$$

Equation 4.50 is a transcendental function with an infinite number of roots. However, in the first quadrant, there is only

one solution for θ_1, when the known variables are substituted in.

For $\gamma = 39.5°$, $S = 9/32"$, and $D = 2"$, θ_1 equals 5.6°.

2) Orientation 2 - From Figure 4.5, if $\theta \leq \theta_2$, then orientation 2 is in effect. The angle θ_2 is found from Figure 4.5 in a similar manner as θ_1.

From the figure,

$$\xi_2 = \gamma_3 - \theta_2 \tag{4.51}$$

when $\theta = \theta_2$,

again where γ_3 was previously found and shown in Figure 4.3.

Also:

$$\text{Tan } \xi_2 = \text{Tan } (\gamma_3 - \theta_2) = \frac{B_1}{A} = \frac{\frac{D}{2} \text{ Sin } \theta_2}{\frac{S}{2} + (\frac{D}{2} - \frac{D}{2} \text{ Cos } \theta_2)} \tag{4.52}$$

which gives:

$$\text{Tan } (\gamma_3 - \theta_2) = \frac{\text{Sin } \theta_2}{\frac{S}{D} + (1 - \text{Cos } \theta_2)} \tag{4.53}$$

For $\gamma_3 = 14.0°$, $S = 9/32"$, and $D = 2"$, the solution for θ_2 in the first quadrant is 1.7°.

3) Orientation 3 - From Figure 4.6, if $\theta_2 \leq \theta \leq \theta_1$, then orientation 3 is in effect.

For the actual collector orientation, $\theta = -10.8°$. Therefore, orientation 2 represents the actual case. The

relationships describing the results for $g(\Omega)$ will be derived for orientation 2 while those for orientation 1 and 3 can be found in Appendix 6.

c) Orientation 2 - $g(\Omega)$ - $\theta \leq 1.7°$

The shading factor $g(\Omega)$ is equal to 1 when $|\Omega| \leq |\Omega_s|$ where $|\Omega_s|$ is the angle above which the absorber tube is not fully exposed to the sun. From Figure 4.5, $|\Omega_s|$ is equal to $90 - \xi_3 = 90\ (\gamma - \theta) = 90 - 39.5 + \theta = 50.5 + \theta$.

The shading factor $g(\Omega)$ is equal to 0 when $|\Omega| \geq |\Omega_{co}|$ where $|\Omega_{co}|$ is the angle above which the tube is not exposed at all to the sun. Again, from Figure 4.5, $|\Omega_{co}|$ is equal to $90 - \xi_2 = 90 - (\gamma_3 - \theta) = 90 - 14.0 + \theta = 76.0 + \theta$.

Finally, $g(\Omega) = \dfrac{76.0 + \theta - |\Omega|}{25.5}$ when $|\Omega_s| < |\Omega| < |\Omega_{co}|$.

This again states that when the absorber tube is partially shaded, the shading factor is a linear function indirectly proportional to the amount of the projected absorber tube shaded.

For $\theta = -10.8°$, the above results become:

$$g(\Omega) = 1 \qquad \text{for } |\Omega| \leq 39.7° \tag{4.54}$$

$$g(\Omega) = 0 \qquad \text{for } |\Omega| \geq 65.2° \tag{4.55}$$

$$g(\Omega) = \frac{65.2 - |\Omega|}{25.5} \qquad \text{for } 39.7° < |\Omega| < 65.2° \tag{4.56}$$

Table 4.1 gives the shading factors for the KTA tubular collectors at the midpoint of each month. Also indicated on the table is the equation used to calculate $g(\Omega)$.

Table 4.1 - Shading Factors

Month	δ	Ω	$g(\Omega)$	Eq. No.
January	-22.0°	5.0°	1.00	4.46
February	-12.5°	-4.5°	1.00	4.54
March	-2.5°	-14.5°	1.00	4.54
April	10.0°	-27.0°	1.00	4.54
May	17.5°	-34.5°	1.00	4.54
June	23.0°	-40.0°	0.99	4.56
July	22.5°	-39.5°	1.00	4.54
August	15.0°	-32.0°	1.00	4.54
September	4.0°	-13.0°	1.00	4.54
October	-9.0°	-8.0°	1.00	4.54
November	-18.0°	1.0°	1.00	4.54
December	-22.5°	5.5°	1.00	4.54

$\beta = 60°$ $\quad \ell = 43°$

Cos Ω

As was previously mentioned, $\cos\Omega$ relates beam radiation measured on a tilted surface to that measured on the absorber tube. This modification is required because the absorber tube is always

oriented toward the sun when not shaded (see Figure A5.4).

Since I_{eff} is based on aperture cross-sectional area (see Equation 4.29), the first term of Equation 4.38 has to be modified by d/D. This accounts for the fact that this term is only concerned with the absorber tube.

ρ - Reflectance

This parameter has previously been defined and for the silver backing of the KTA tubular collectors is taken equal to 0.94. This result is from page 169 of reference 12.

$\gamma(\Omega)$ - Reflection Factor

As was previously stated, $\gamma(\Omega)$ is the fraction of the aperture area over which beam radiation is reflected to the absorber tube. the absorber tube. If it is assumed that all rays incident on the silver backing are intercepted by the absorber tube, then the expression is [2]:

$$\gamma(\Omega) = \text{Cos } \theta - \frac{\frac{d}{D}\ g(\Omega)}{\cos\ \Omega} \qquad (4.57)$$

The first term of Equation 4.57, cos θ, is required since the area over which the beam portion I_b on the tilted surface acts is the projected aperture area. This is the net collection area when viewed from the perpendicular normal (n_s, Figure 4.2) of the tube bank. It is equal to A_t cos θ.

This first term, however, does not account for the fact that a certain amount of radiation cannot be reflected to the absorber tube since it will be directly intercepted by the absorber tube instead. Since the directly intercepted amount was previously accounted for in Equation 4.38, the second term of Equation 4.57 is required so that it is not incorporated twice.

In actuality, not all radiation which is incident on the silver backing is reflected to the absorber tube and indeed, the amount which is not can be a substantial portion of the total. To account for this, Equation 4.57 is modified and rewritten as:

$$\gamma(\Omega) = b\ (\cos\theta - \frac{\frac{d}{D}\, g(\Omega)}{\cos\Omega}) \qquad (4.58)$$

In practice, the parameter b would be determined by a ray trace for the ranges of θ and Ω considered. This would be done since the refraction characteristics of the glass tubes would complicate the analytical modeling of the concentrator optics necessary for determination of b. However, the analysis of the concentrator optics is greatly simplified when it is assumed that the direction of beam radiation is unchanged by passage through the cover tubes. Since the thickness of the cover tubes is quite small compared to the tube diameters, the effect of this assumption on the result for b is small.

Utilizing this simplification, the necessary equations describing the optics are now generated. Figures 4.7, 4.8, and 4.9 show the geometry of the outer cover tube and the absorber tube. The problem was

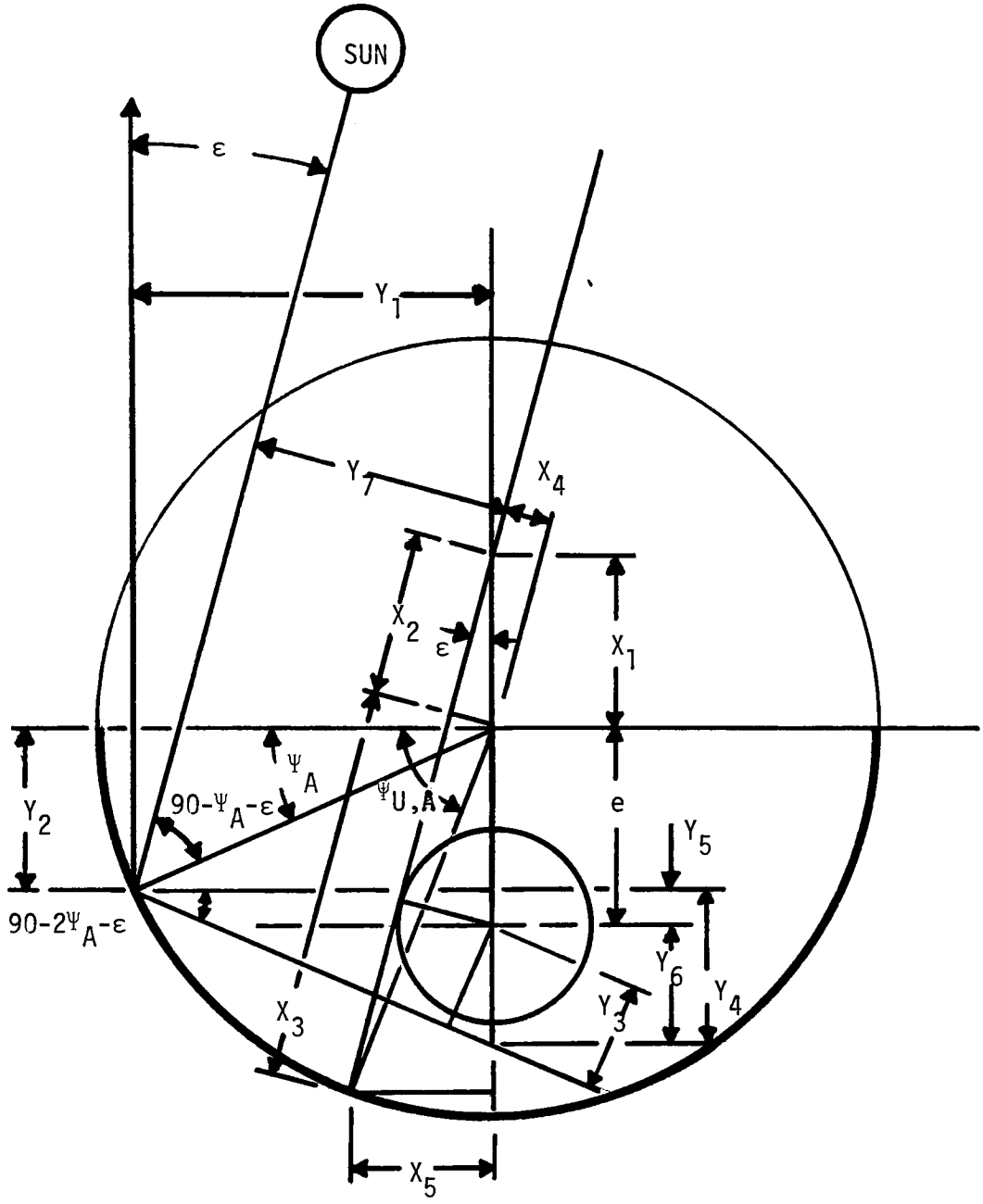

Figure 4.7 Reflection Factor, Parameter b, Part A

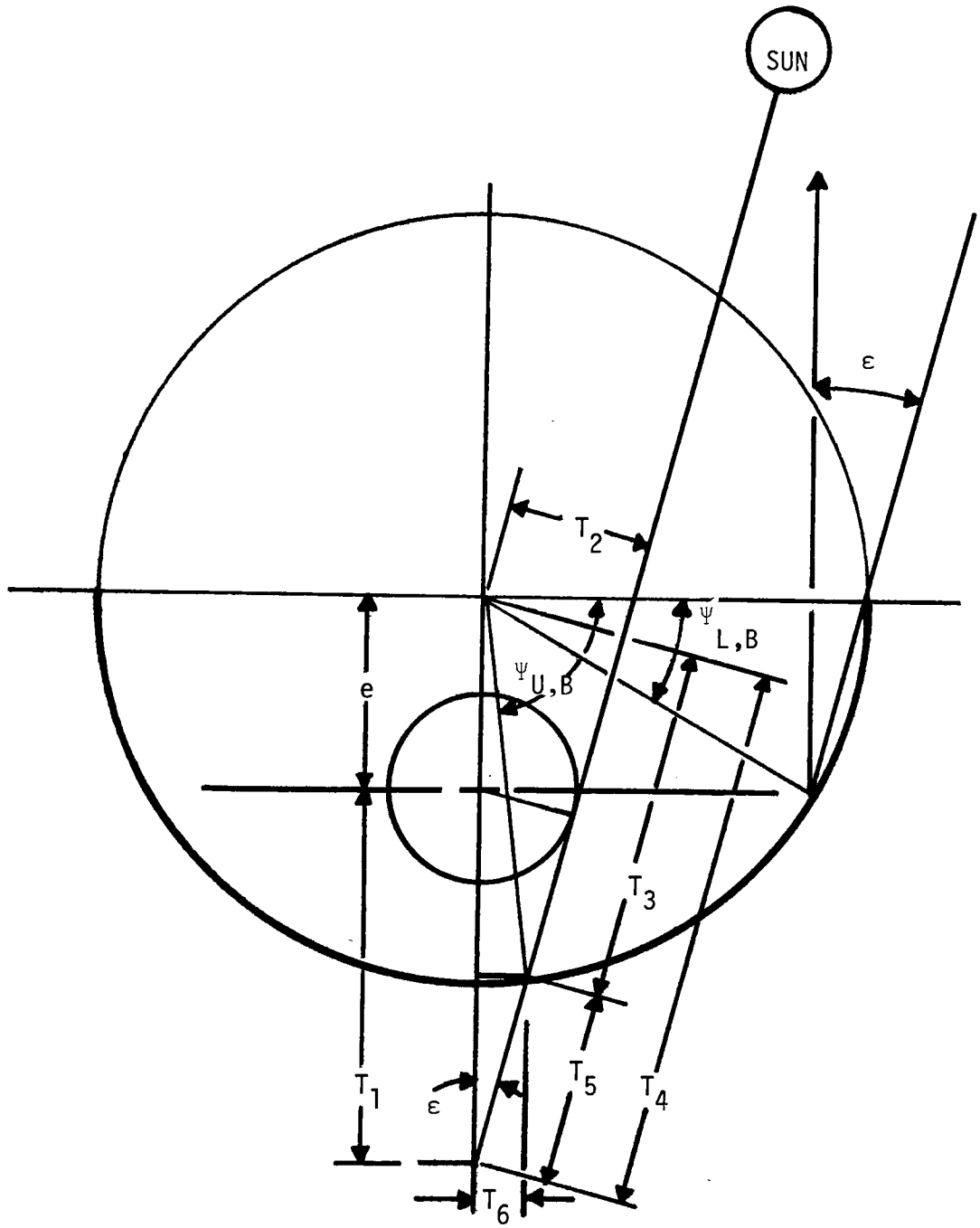

Figure 4.8 Reflection Factor, Parameter b, Part B - Limiting Angles

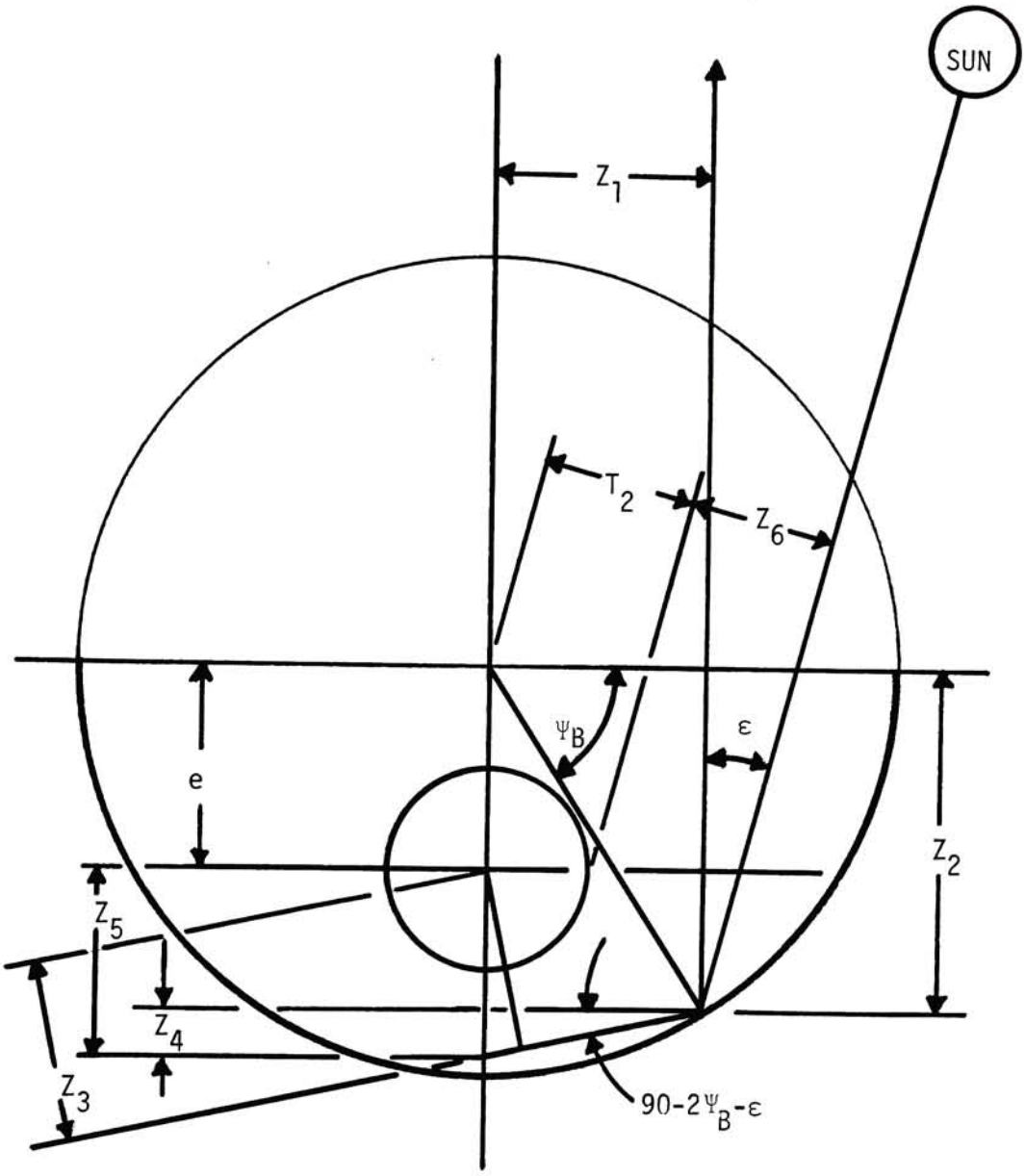

Figure 4.9 Reflection Factor, Parameter b, Part B - Projected Area Causing Reflection To Absorber Tube

separated into the two parts shown in the figures to further simplify the derivations.

The first step in the analysis is to determine the range of the angle Ψ over which the incoming beam radiation falls on the silver backing. For part A shown in Figure 4.7, the lower limit is obviously equal to 0° while the upper limit is calculated as follows:

$$X_1 = \frac{d/2}{\sin \varepsilon} - e \tag{4.59}$$

$$X_2 = X_1 \cos \varepsilon \tag{4.60}$$

$$X_4 = X_1 \sin \varepsilon \tag{4.61}$$

$$X_3 = \sqrt{(D/2)^2 - (X_4)^2} \tag{4.62}$$

$$X_5 = (X_3 + X_2) \sin \varepsilon \tag{4.63}$$

Finally, the upper limit of Ψ is found to be:

$$\Psi_{U,A} = 90 - \sin^{-1} \left(\frac{X_5}{D/2}\right) \tag{4.64}$$

For part B shown in Figure 4.8, the lower limit is

$$\Psi_{L,B} = 2\varepsilon \tag{4.65}$$

while the upper limit is calculated as follows:

$$T_1 = \frac{d/2}{\sin \varepsilon} \tag{4.66}$$

$$T_2 = (e + T_1) \sin \varepsilon \tag{4.67}$$

$$T_4 = (e + T_1) \cos \varepsilon \tag{4.68}$$

$$T_3 = \sqrt{(D/2)^2 - (T_2)^2} \tag{4.69}$$

$$T_5 = T_4 - T_3 \tag{4.70}$$

$$T_6 = T_5 \sin \varepsilon \tag{4.71}$$

Finally,

$$\Psi_{U,B} = 90 - \sin^{-1} \left(\frac{T_6}{D/2}\right) \tag{4.72}$$

As can be seen, these limiting angles depend on the angle ε.

Having the limiting values of Ψ, the next step is to calculate for each part the amount of the projected area perpendicular to the sun's rays over which beam radiation is reflected to the absorber tube. Note that the projected area of the absorber tube has been accounted for. For part A, this is done in the following manner.

For the range

$$\Psi_{L,A} \leq \Psi_A \leq \Psi_{U,A}$$

$$Y_1 = D/2 \cos \Psi_A \tag{4.73}$$

$$Y_2 = D/2 \sin \Psi_A \tag{4.74}$$

$$Y_4 = Y_1 \text{ Tan } (90 - 2\Psi_A - \varepsilon) \tag{4.75}$$

$$Y_5 = e - Y_2 \tag{4.76}$$

$$Y_6 = Y_4 - Y_5 \tag{4.77}$$

$$Y_3 = |Y_6 \cos (90 - 2\Psi_A - \varepsilon)| \tag{4.78}$$

Also,

$$Y_7 = D/2 \cos (\Psi_A + \varepsilon) - X_4 \tag{4.79}$$

The amount of the projected area over which beam radiation is reflected to the absorber tube is calculated from Equation 4.79 when the result of Equation 4.78 is less than or equal to d/2.

For part B, a similar approach is followed from Figure 4.9:

$$Z_1 = D/2 \text{ Cos } \Psi_B \tag{4.80}$$

$$Z_2 = D/2 \text{ Sin } \Psi_B \tag{4.81}$$

$$Z_4 = Z_1 \text{ Tan } (90 - 2\Psi_B + \varepsilon) \tag{4.82}$$

$$Z_5 = Z_2 - e + Z_4 \tag{4.83}$$

$$Z_3 = |Z_5 \text{ Cos } (90 - 2\Psi_B + \varepsilon)| \tag{4.84}$$

and

$$Z_6 = D/2 \text{ Cos } (\Psi_B - \varepsilon) - T_2 \tag{4.85}$$

over the range $\Psi_{L,B} \leq \Psi_B \leq \Psi_{U,B}$

Finally, b is calculated by dividing the areas found from Equations 4.78 and 4.75 over which the beam radiation is reflected to the absorber tube by the total projected area.

Note that the angle ε is actually equal to $|\theta+r|$ from Figure A5.4.

Equations 4.59 through 4.85 are readily programmable providing a quick method for evaluation of the parameter b for any angle ε. This was done and the calculations performed for the midpoint of each month for the actual collector configuration. The results are given in Table 4.2.

TABLE 4.2 - Reflection Factor, Parameter b

Month	δ	Ω	ε	Part A: Projected Area Which Reflects To Absorber Tube	Part A: Total Projected Area	Part B: Projected Area Which Reflects To Absorber Tube	Part B: Total Projected Area	Total Projected Area Which Reflects To Absorber Tube	Total Projected Area	b
Jan.	-22.0°	5.0°	5.8°	0.5407	0.7954	0.4494	0.6944	0.9901	1.4898	0.66
Feb.	-12.5°	-4.5°	15.3°	0.6068	0.8465	0.3615	0.5826	0.9683	1.4291	0.68
March	-2.5°	-14.5°	25.3°	0.6676	0.8678	0.2300	0.4404	0.8976	1.3082	0.69
April	10.0°	-27.0°	37.8°	0.5001	0.8466	0.0000	0.2337	0.5001	1.0803	0.46
May	17.5°	-34.5°	45.3°	0.4284	0.8088	0.0000	0.0980	0.4284	0.9068	0.47
June	23.0°	-40.0°	50.8°	0.3920	0.7695	0.0000	0.0000	0.3920	0.7695	0.51
July	22.5°	-39.5°	50.3°	0.3975	0.7735	0.0000	0.0041	0.3975	0.7776	0.51
Aug.	15.0°	-32.0°	42.8°	0.4479	0.8235	0.0000	0.1440	0.4479	0.9675	0.46
Sept.	4.0°	-13.0°	23.8°	0.6591	0.8667	0.2561	0.4632	0.9151	1.3299	0.69
Oct.	-9.0°	-8.0°	18.8°	0.6291	0.8578	0.3235	0.5355	0.9526	1.3933	0.68
Nov.	-18.0°	1.0°	9.8°	0.5695	0.8205	0.4143	0.6503	0.9838	1.4708	0.67
Dec.	-22.5°	5.5°	5.3°	0.5344	0.7919	0.4561	0.6995	0.9906	1.4914	0.66

$\theta = -10.8°$ $\ell = 43°$ $\beta = 60°$

Equation 4.58 is now evaluated for the midpoint of the months utilizing the results from Tables 4.1 and 4.2. The results are tabulated below.

Table 4.3. Reflection Factors

Month	Ω	$\gamma(\Omega)$
January	5.0°	0.48
February	-4.5°	0.50
March	-14.5°	0.50
April	-27.0°	0.32
May	-34.5°	0.32
June	-40.0°	0.34
July	-39.5°	0.34
August	-32.0°	0.32
September	-13.0°	0.50
October	-8.0°	0.50
November	1.0°	0.49
December	5.5°	0.48

θ = -10.8° d = 0.5 in. D = 2 in.

Having evaluated all the parameters of Equation 4.38, Γ_b can now be computed for the collector configuration at RIT Energy House. The results are given below.

Table 4.4 Beam Enhancement Factors

Month	Ω	$g(\Omega)$	$\gamma(\Omega)$	Γ_b
January	5.0°	1.00	0.48	0.70
February	-4.5°	1.00	0.50	0.72
March	-14.5°	1.00	0.50	0.73
April	-27.0	1.00	0.32	0.58
May	-34.5°	1.00	0.32	0.60
June	-40.0°	0.99	0.34	0.64
July	-39.5°	1.00	0.34	0.64
August	-32.0°	1.00	0.32	0.60
September	-13.0°	1.00	0.50	0.73
October	-8.0°	1.00	0.50	0.72
November	1.0°	1.00	0.49	0.71
December	5.5°	1.00	0.48	0.70

d = 0.5 in. D = 2 in. ρ = 0.94

4.1.3.2 Diffuse Enhancement Factor, Γ_d

As was the case for the beam component, the diffuse component of insolation is both directly intercepted by each absorber tube and indirectly intercepted from reflections off the silvered mirrow surface on the outer cover tube. If the apparent origin of the diffuse radiation is localized over a region of sky near the solar disk, it would be reasonable to treat the diffuse component as beam radiation and use the total insolation in place of the beam insolation in Equation 4.36.

If, at the other extreme, the diffuse component is distributed uniformly over the sky dome, as might be the case on a cloudy or hazy day, its contribution to the total insolation on the tube must be calculated separately. In the work that follows this assumption is used.

From Equation 4.36, the effective diffuse insolation intercepted by the absorber tube is,

$$I_{eff,d} = \Gamma_d I_d \tag{4.86}$$

Rewriting,

$$\Gamma_d = \frac{I_{eff,d}}{I_d} \tag{4.87}$$

where $I_{eff,d}$ is the amount of diffuse insolation intercepted by the absorber tube per unit aperture area.

The quantity, I_d is composed of two components: diffuse solar radiation and the solar radiation reflected from the ground which the tilted surface sees. If the ground reflected radiation is diffuse, then the expression for I_d is [13].

$$I_d = H_d \left(\frac{1 + \cos\beta}{2}\right) + (H_d + H_b) \left(\frac{1 - \cos\beta}{2}\right) \rho_g \tag{4.88}$$

where H_d and H_b are the diffuse and beam components of the insolation measured in the horizontal plane. The quantity, ρ_g, is the ground

reflectance and from Liu and Jordan [14] is taken to be 0.2 when there is no snow and 0.7 when there is snow cover.

In order to calculate $I_{eff,d}$, the relationship between radiation flux and intensity must first be established. Referring to Figure 4.10, the total radiation flux q passing through the area ΔA can be expressed as

$$q = \int_0^{\pi} \int_0^{\pi} I_N \sin \xi \sin \beta' \sin \xi d\xi d\beta' \qquad (4.89)$$

where $\sin \xi d\xi d\beta'$ is the elemental area on the hemisphere and $I_N \sin \xi \sin \beta'$ is the energy per unit time passing through the area ΔA from the area $\Delta A'$ on the hemisphere. Carrying out the integration of Equation 4.89 and assuming a uniform intensity distribution gives:

$$q = \pi I_N \qquad (4.90)$$

If however, instead of the limits of 0 to π for the angle β', they are replaced by β_1 and β_2, the integral becomes

$$q' = \int_{\beta_1}^{\beta_2} \int_0^{\pi} I_N \sin^2 \xi \sin \beta' d\xi d\beta' \qquad (4.91)$$

which is

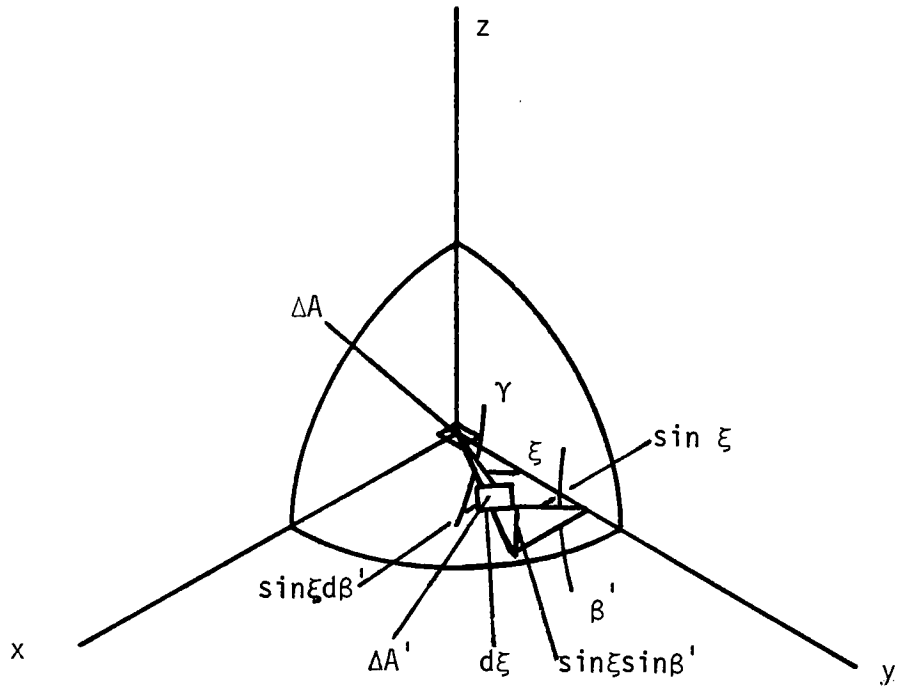

Incremental Area = $\sin\xi d\xi d\beta'$
Projection of $\Delta A'$ on $\Delta A = \sin\gamma = \sin\xi\sin\beta'$

Figure 4.10 Schematic of Radiation Flux on a Unit Sphere

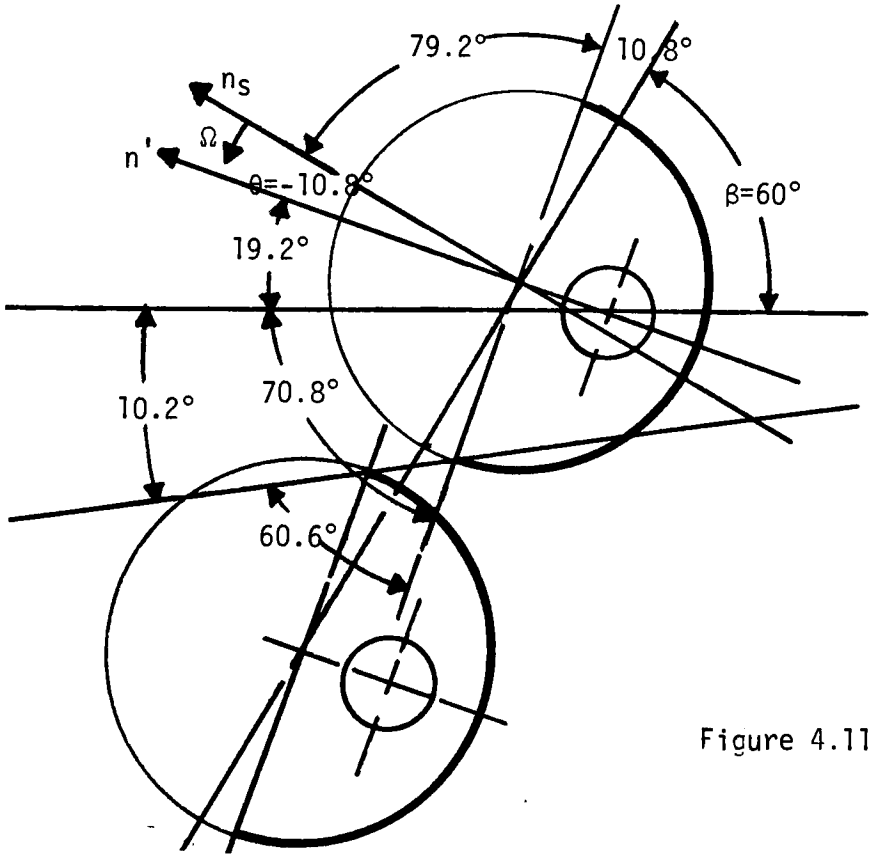

Figure 4.11 Determination of The Diffuse Enhancement Factor, Γ_d

$$q' = \frac{I_N \pi}{2} \left(-\cos\beta'\right) \Big|_{\beta_1}^{\beta_2} \tag{4.92}$$

or when Equation 4.90 is substituted in

$$q' = q \left(\frac{-\cos\beta'}{2}\right) \Big|_{\beta_1}^{\beta_2} \tag{4.93}$$

Equation 4.93 represents the source of the conversion factors given in Equation 4.88.

Having the relationships of Equations 4.91 and 4.93, an expression for $I_{eff,d}$ can now be given. Referring to Figure 4.11, $I_{eff,d}$ can be written as:

$$I_{eff,d} = \frac{H_d}{2} \int_0^{180-(\beta-\theta)} \Gamma_{b,s}(\beta') \sin\beta' d\beta' +$$

$$\frac{(H_d + H_b)\rho_g}{2} \int_{60.6°}^{\beta-\theta} \Gamma_{b,g}(\beta') \sin\beta' \, d\beta' \tag{4.94}$$

The first portion of the expression represents the diffuse insolation from the sky done intercepted by the absorber tube while the second part represents that portion intercepted by the absorber tube from the ground. The limits of integration on the second portion arise since the next lower tubular element in the array shades

the element under consideration from a portion of the ground dome. The lowest tube in the array would not be shaded in this manner but would instead be shaded by the collector wall. This effect is small and is neglected in this analysis.

The expressions $\Gamma_{b,s}$ and $\Gamma_{b,g}$ represent the percentage of the radiation intensity over the projected aperture area which is either directly absorbed or backreflected to the absorber tube. These factors are only functions of β' and not ξ. A variation of ξ only causes the axial location where the backreflected radiation hits the absorber tube to change. It does not affect the percentage of radiation which directly or indirectly hits the absorber tube. The expressions used to evaluate $\Gamma_{b,s}$ and $\Gamma_{b,g}$ are very similar to those used to evaluate Γ_b given by Equation 4.38. They are:

$$\Gamma_{b,s} = \Gamma_{b,g} = g(\Omega)\, d/D + \rho\gamma_{mod}(\Omega) \tag{4.95}$$

where:

$$\gamma_{mod}(\Omega) = b(1 - d/D\, g(\Omega)) \tag{4.96}$$

The differences in values for $\Gamma_{b,s}$ and $\Gamma_{b,g}$ result due to the evaluation of the expression over its appropriate angular range.

It is seen that the term cos Ω is not present in Equations 4.95 or 4.96 and the term cos θ is not present in Equation 4.96.

These terms in the previous work accounted for the fact that I_b measured in the collector plane was different from the beam radiation measured on the projected area and that measured on the plane formed by the two mirrowed edges of the outer cover tube. In Equation 4.94, both of these considerations are accounted for since the radiation is uniform and since the limits of integration are for the entire exposed area of the plane formed by the two mirrowed edges.

The integrals in Equation 4.94 were evaluated by utilizing the definition of an integral:

$$\int_0^{\beta-\theta} \Gamma_{b,s}(\beta') \sin\beta' d\beta' = \frac{\sum_{i=1}^{N} \Gamma_{b,s}(\beta_i') \sin\beta_i'}{N} \qquad (4.97)$$

$$\int_0^{\beta-\theta} \Gamma_{b,g}(\beta') \sin\beta' d\beta' = \frac{\sum_{i=1}^{N} \Gamma_{b,g}(\beta_i') \sin\beta_i'}{N} \qquad (4.98)$$

This approach was used since the parameter b in Equation 4.96 was previously calculated by use of a computer program for individual values of ε. Considerable care must be taken in utilizing the correct angular ranges in order to calculate $\Gamma_{b,s}$ and $\Gamma_{b,g}$ over the range of β'. These are given below and are obtained from Figure 4.11.

Skydome:

$$0 \leq \beta' \leq 109.2° \qquad 30° \geq \Omega \geq -79.2° \qquad 19.2° \geq \varepsilon \geq -90°$$

Ground dome:

$$60.6° \leq \beta' \leq 70.8° \quad 40.2° \geq \Omega \geq 30° \qquad 29.4° \geq \varepsilon \geq 19.2°$$

The relationships for $g(\Omega)$ are found from Equations 4.45, 4.46, and 4.47 when Ω is positive and from Equations 4.54, 4.55, and 4.56 when Ω is negative.

Evaluating Equations 4.97 and 4.98 over one degree increments gave the following result for Equation 4.94.

$$I_{eff,d} = \frac{H_d}{2}(0.303) + \frac{(H_d + H_b)\,\rho_g}{2}(0.663)$$

and

$$I_{eff,d} = H_d(0.152) + (H_d + H_b)\rho_g(0.332) \tag{4.99}$$

Now, the diffuse enhancement factor for the tubular collectors can be expressed by Equation 4.87 when Equations 4.88 and 4.99 are substituted in.

$$\Gamma_d = \frac{H_d(0.152) + \rho_g[0.332]) + H_b\rho_g[0.332]}{H_d(0.750 + \rho_g[0.250]) + H_b\rho_g[0.250]} \tag{4.100}$$

where $\beta = 60°$.

4.1.3.3 Enhancement factor, Γ

From Equation 4.37, the enhancement factor Γ can be written:

$$\Gamma = \frac{\Gamma_b I_b + \Gamma_d I_d}{I} \tag{4.101}$$

Equation 4.101 can be rewritten when Equation 4.99 is substituted in as:

$$\Gamma = \frac{\Gamma_b I_b + H_d(0.152) + (H_d + H_b)\rho_g(0.332)}{I_b + I_d} \tag{4.102}$$

In order to calculate Γ, I_b must now be expressed in terms of H_b which is the beam component of radiation measured on a horizontal surface. From Figure 4.12, it follows that $H_b = H_n \cos i_h$

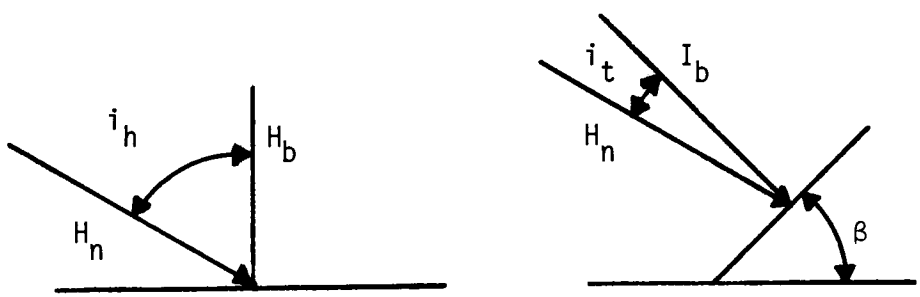

Figure 4.12 Radiation on Horizontal and Tilted Surfaces

and $I_b = H \cos i_t$. The ratio of radiation on the tilted surface, I_b, to that on the horizontal surface, H_b, is given in terms of the angles i_t and i_h and radiation normal to the beam, H_n, by:

$$R_b = \frac{I_b}{H_b} = \frac{H_n \cos i_t}{H_n \cos i_h} = \frac{\cos i_t}{\cos i_h} \tag{4.103}$$

The expression for cos i_t is found by Equations A5.6 of Appendix 5 while that for cos i_h is the same equation with $\beta=0$. That is, for a surface tilted directly toward the equator:

$$R_b = \frac{\cos(\ell-\beta)\cos\delta_s \cos h_s + \sin(\ell-\beta)\sin\delta_s}{\cos\ell \cos\delta_s \cos h_s + \sin\ell \sin\delta_s} \tag{4.104}$$

Substituting Equations 4.103 and 4.88 into Equation 4.102 gives:

$$\Gamma = \frac{\Gamma_b R_b H_b + H_d(0.152) + (H_d + H_b)\rho_g(0.332)}{R_b H_b + H_d(0.750) + (H_d + H_b)\rho_g(0.250)} \tag{4.105}$$

Let the ratio of diffuse radiation to total radiation on the horizontal surface (H_d/H_t) equal K. Then the ratio of beam radiation to total radiation on the horizontal surface (H_b/H_t) equals 1-K. Utilizing these results, Equation 4.105 can be rewritten as:

$$\Gamma = \frac{K(0.152 - \Gamma_b R_b) + \Gamma_b R_b + \rho_g(0.332)}{K(0.750 - R_b) + R_b + \rho_g(0.250)} \tag{4.106}$$

From Equation 4.106 is seen that Γ is a function of the following variables:

$$\Gamma = f(K, \Gamma_b, R_b, \rho_b) \tag{4.107}$$

It is desired to be able to calculate Γ for any hour corresponding to actual data collection measured by the pyranometers at RIT. To do this requires that the variables of Equation 4.107 be evaluated on an hour by hour basis. This would be extremely tedious and would be best handled by use of a digital computer. As an alternative to this approach, certain constraints are placed on Equation 4.106 to simplify its solution.

The variable Γ_b has previously been calculated for the midpoint of each month. It is seen from Table 4.4 that it is a weak function of the month of interest except between March and April and between August and September. These larger jumps occur due to the variations in the parameter b shown in Table 4.2 which are caused by the tube optics. The results for b are continuous, however, as would be expected and can be shown by utilizing the computer program with the angle ε changing in smaller increments. Therefore, use is made of the results of Table 4.4 in Equation 4.106 and Γ_b is assumed a constant for any given month.

The ground reflectance ρ_g has previously been stated to equal 0.2 for snow cover and 0.7 for no snow cover. This corresponds to November through March and April through October, respectively. Therefore, this variable is a constant for a given month.

The parameter R_b is expressed by Equation 4.104. The latitude, ℓ, and the collector tilt, β, are constants while the declination, δ_s , and hour angle, h_s, are not. When Γ_b is assumed constant

in a month, this is equivalent to saying that δ_s is constant in a given month. This assumption will again be used leaving R_b only a function of the declination at the midpoint of each month and the hour angle. While this assumption can result in an error of several percent in the result for R_b at the monthly extremes, its result on the error of the value for Γ is usually less than 1%.

Care must be taken in evaluating R_b since it is desired that the results of Equation 4.106 correspond to actual solar data taken at RIT. Since the pyranometers record data based on eastern standard time and the hour angle found in Equation 4.104 is based on solar time, an equation relating the two must be used. This can be found from Reference 15 and is:

$$\text{Solar time} = \text{Standard Time} + E + 4(L_{st} - L_{loc}) \qquad (4.108)$$

where E is the equation of time, shown in Figure 4.13, L_{st}

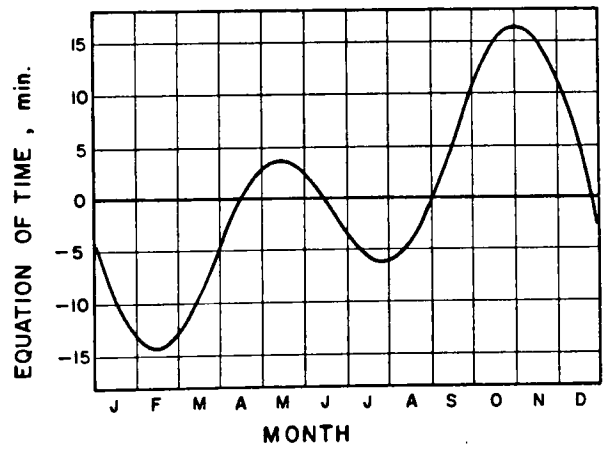

Figure 4.13 Equation of Time
(Source: Ref 15)

is the standard meridian for the local time zone, and L_{loc} is the longitude of the location in question, in degrees west. For the eastern time zone where Rochester is located, L_{st} is 75° while L_{loc} for Rochester is 78°W. Utilizing Equation 4.108 and Figure 4.13, the solar time and hour angles are determined corresponding to midpoints of eastern standard time hours. These results are given in Table 4.5. Note that the hour angles are positive before solar noon and negative after solar noon. Having obtained the hour angles, h_s, for the entire range of daylight hours, R_b can now be calculated. The results of these calculations are given in Table 4.6 with ℓ = 43° and β = 60°. The declination angles used correspond to those given in Table 4.2.

The ratio of diffuse radiation to total radiation, K, has been previously found [16] to be a function of the ratio, K_t, of the total radiation on a horizontal surface, H_t, to the extraterrestrial radiation on a horizontal surface, H_o. The correlation was based on measured values of both total and diffuse radiation on a horizontal surface at the Toronto Airport over the period September 1967 through August 1971. For each hour period, the ratios K_T and K were calculated. Then for each interval in K_T of 0.05, the corresponding values of K were averaged and these average values plotted against the value of K_T for the midpoint of the interval. In all, 12,704 hourly periods were used.

The extraterrestrial solar radiation on a horizontal surface for a given hourly period was calculated by integrating the following equation over the proper hour angle limits:

TABLE 4.5 - Solar Time and Hour Angle Conversions

EST Hour	Jan.	Feb.	March	April	May	June
5:30 am	5:08 103°	5:04 104°	5:09 102.8°	5:18 100.5°	5:21 99.8°	5:18 100.5°
6:30 am	6:08 88°	6:04 89°	6:09 87.8°	6:18 85.5°	6:21 84.8°	6:18 85.5°
7:30 am	7:08 73°	7:04 74°	7:09 72.8°	7:18 70.5°	7:21 69.8°	7:18 70.5°
8:30 am	8:08 58°	8:04 59°	8:09 57.8°	8:18 55.5°	8:21 54.8°	8:18 55.5°
9:30 am	9:08 43°	9:04 44°	9:09 42.8°	9:18 40.5°	9:21 39.8°	9:18 40.5°
10:30 am	10:08 28°	10:04 29°	10:09 27.8°	10:18 25.5°	10:21 24.8°	10:18 25.5°
11:30 am	11:08 13°	11:04 14°	11:09 12.8°	11:18 10.5°	11:21 9.8°	11:18 10.5°
12:30 pm	12:08 -2°	12:04 -1°	12:09 -2.2°	12:18 -4.5°	12:21 -5.2°	12:18 -4.5°
1:30 pm	1:08 -17°	1:04 -16°	1:09 -17.2°	1:18 -19.5°	1:21 -20.2°	1:18 -19.5°
2:30 pm	2:08 -32°	2:04 -31°	2:09 -32.2	2:18 -34.5°	2:21 -35.2°	2:18 -34.5°
3:30 pm	3:08 -47°	3:04 -46°	3:09 -47.2°	3:18 -49.5°	3:21 -50.2°	3:18 -49.5°
4:30 pm	4:08 -62°	4:04 -61°	4:09 -62.2°	4:18 -64.5°	4:21 -65.2°	4:18 -64.5°
5:30 pm	5:08 -77°	5:04 -76°	5:09 -77.2°	5:18 -79.5°	5:21 -80.2°	5:18 -79.5°
6:30 pm	6:08 -92°	6:04 -91°	6:09 -92.2°	6:18 -94.5°	6:21 -95.2°	6:18 -94.5°
7:30 pm	7:08 -107°	7:04 -106°	7:09 -107.2°	7:18 -109.5°	7:21 -110.2°	7:18 -109.5°

TABLE 4.5 - (continued)

EST Hour	July	Aug.	Sept.	Oct.	Nov.	Dec.
5:30 am	5:12 102°	5:14 101.5°	5:23 99.3°	5:33 96.8°	5:33 96.8°	5:24 99°
6:30 am	6:12 87°	6:14 86.5°	6:23 84.3°	6:33 81.6°	6:33 81.6°	6:24 84°
7:30 am	7:12 72°	7:14 71.5°	7:23 69.3°	7:33 66.8°	7:33 66.8°	7:24 69°
8:30 am	8:12 57°	8:14 56.5°	8:23 54.3°	8:33 51.8°	8:33 51.8°	8:24 54°
9:30 am	9:12 42°	9:14 41.5°	9:23 39.3°	9:33 36.8°	9:33 36.8°	9:24 39°
10:30 am	10:12 27°	10:14 26.5°	10:23 24.3°	10:33 21.8°	10:33 21.8°	10:24 24°
11:30 am	11:12 12°	11:14 11.5°	11:23 9.3°	11:33 6.8°	11:33 6.8°	11:24 9°
12:30 pm	12:12 -3°	12:14 -3.5°	12:23 -5.7°	12:33 -8.2°	12:33 -8.2°	12:24 -6°
1:30 pm	1:12 -18°	1:14 -18.5°	1:23 -20.7°	1:33 -23.2°	1:33 -23.2°	1:24 -21°
2:30 pm	2:12 -33°	2:14 -33.5°	2:23 -35.7°	2:33 -38.2°	2:33 -38.2°	2:24 -36°
3:30 pm	3:12 -48°	3:14 -48.5°	3:23 -50.7°	3:33 -53.2°	3:33 -53.2°	3:24 -51°
4:30 pm	4:12 -63°	4:14 -63.5°	4:23 -65.7°	4:33 -68.2°	4:33 -68.2°	4:24 -66°
5:30 pm	5:12 -78°	5:14 -78.5°	5:23 -80.7°	5:33 -83.2°	5:33 -83.2°	5:24 -81°
6:30 pm	6:12 -93°	6:14 -93.5°	6:23 -95.7°	6:33 -98.2°	6:33 -98.2°	6:24 -96°
7:30 pm	7:12 -108°	7:14 -108.5°	7:23 -110.7°	7:33 -113.2°	7:33 -113.2°	7:24 -111°

TABLE 4.6 - Ratio of Beam Radiation on a Tilted Surface to that on a Horizontal Surface

EST Hour	Jan.	Feb.	March	April	May	June	July	Aug.	Sept.	Oct.	Nov.	Dec.
6:30 am	-	-	-	0.132	-	-	-	-	0.619	-	-	-
7:30 am	-	6.517	1.585	0.735	0.509	0.366	0.343	0.543	1.037	2.349	7.092	-
8:30 am	5.579	2.472	1.451	0.917	0.721	0.593	0.587	0.767	1.133	1.852	2.975	4.635
9:30 am	3.152	2.092	1.410	0.999	0.827	0.713	0.714	0.873	1.173	1.700	2.461	3.023
10:30 am	2.600	1.845	1.391	1.040	0.883	0.778	0.783	0.929	1.190	1.636	2.149	2.579
11:30 am	2.402	1.778	1.383	1.059	0.909	0.809	0.816	0.955	1.200	1.611	2.070	2.423
12:30 pm	2.358	1.760	1.381	1.062	0.912	0.814	0.823	0.960	1.201	1.612	2.074	2.410
1:30 pm	2.436	1.783	1.385	1.050	0.893	0.794	0.806	0.946	1.194	1.640	2.161	2.533
2:30 pm	2.696	1.859	1.395	1.019	0.848	0.744	0.760	0.953	1.179	1.709	2.397	2.894
3:30 pm	3.451	2.043	1.418	0.957	0.761	0.650	0.672	0.832	1.146	1.876	3.085	4.067
4:30 pm	8.364	2.598	1.474	0.828	0.592	0.476	0.509	0.684	1.070	2.454	9.002	-
5:30 pm	-	11.508	1.699	0.484	0.208	0.119	0.179	0.342	0.808	-	-	-

$\ell = 43°$ $\beta = 60°$

$$\dot{H}_o = S_c E \cdot [\cos\ell\cos\delta_s\cos h_s + \sin\ell \sin\delta_s] \qquad (4.109)$$

The variable S_c is the solar constant which is the energy from the sun per unit time, received on a unit area of surface perpendicular to the radiation, in space, at the earth's mean distance from the sun. Its standard value has been found to be 1353 W/m^2. The variable E is the eccentricity correction factor for the solar constant. The quantity, $S_c \cdot E$, is given in Figure 4.14.

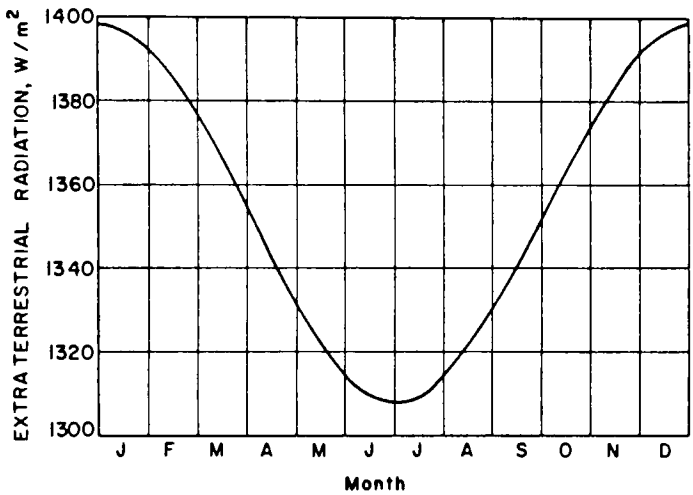

Figure 4.14 Extraterrestrial Radiation Variation (Source: Ref 17)

The correlation was first made with values of H_o calculated as described above and then with values of H_o calculated at the midpoint of the hour. No significant departure in the results was seen.

The correlation is shown graphically in Figure 4.15 as well as the correlation equations defining the ranges. This correlation

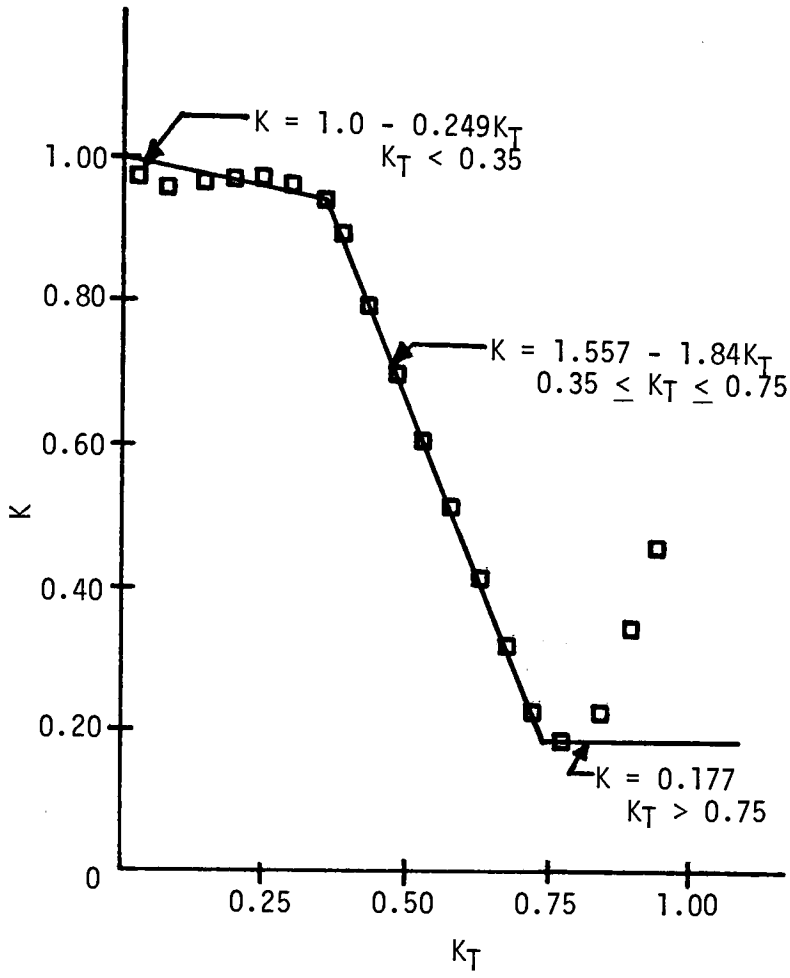

Figure 4.15 Plot of K vs K_T With Correlation Equations
(Source: Ref 16)

departs from that of Liu and Jordan [18] slightly. It is based however, on hourly values while Liu and Jordan's work is based on daily values.

Now, Equation 4.106 can be rewritten as

$$\Gamma = \frac{k_a^{\,1} + a^2}{k_a^{\,3} + a^4} \tag{4.110}$$

where

$$a^1 = 0.152 - \Gamma_b R_b, \tag{4.111}$$

$$a^2 = \Gamma_b R_b + \rho_g(0.332), \tag{4.112}$$

$$a^3 = 0.750 - R_b, \quad \text{and} \tag{4.113}$$

$$a^4 = R_b + \rho_g(0.250) \tag{4.114}$$

The values for a^1, a^2, a^3, and a^4 are given in Table 4.7 as well as the extraterrestrial radiation H_o for the given period. The quantity H_o is calculated using Figure 4.14, Equation 4.109, and the declinations corresponding to the midpoint of each month given in Table 4.2. H_o is given in langley's per hour.

TABLE 4.7 - Enhancement Factors a^1, a^2, a^3, a^4, and H_o

EST Hour	January	February	March	April	May	June
5:30 am	a^1=0.152 a^2=0.232 a^3=0.750 a^4=0.175 H_o=0	0.152 0.232 0.750 0.175 0	0.152 0.232 0.750 0.175 0	0.152 0.066 0.750 0.050 0	0.152 0.066 0.750 0.050 0	0.152 0.066 0.750 0.050 0
6:30 am	0.152 0.232 0.750 0.175 0	0.152 0.232 0.750 0.175 0	0.152 0.232 0.750 0.175 0	0.075 0.143 0.618 0.182 20.216	0.152 0.066 0.750 0.050 30.521	0.152 0.066 0.750 0.050 35.966
7:30 am	0.152 0.232 0.750 0.175 0	-4.540 4.925 -5.767 6.692 5.859	-1.005 1.005 -0.835 1.760 25.153	-0.274 0.493 0.015 0.785 41.470	-0.153 0.372 0.241 0.559 50.728	-0.082 0.301 0.384 0.416 55.329
8:30 am	-3.753 4.138 -4.829 5.754 12.467	-1.628 2.012 -1.722 2.647 26.216	-0.907 1.292 -0.701 1.626 42.237	-0.380 0.465 -0.167 0.967 60.830	-0.281 0.499 0.029 0.771 69.068	-0.228 0.446 0.157 0.643 72.968
9:30 am	-2.054 2.439 -2.402 3.327 28.863	-1.354 1.739 -1.342 2.267 43.588	-0.877 1.262 -0.660 1.585 59.475	-0.427 0.646 -0.249 1.049 76.978	-0.344 0.563 -0.077 0.877 84.291	-0.304 0.523 0.037 0.763 87.679
10:30 am	-1.668 2.052 -1.850 2.775 41.202	-1.176 1.561 -1.095 2.020 56.792	-0.863 1.248 -0.641 1.566 72.421	-0.451 0.670 -0.290 1.090 88.812	-0.378 0.596 -0.133 0.933 95.360	-0.346 0.564 -0.028 0.828 98.461
11:30 am	-1.529 1.914 -1.652 2.577 48.643	-1.128 1.513 -1.028 1.953 64.927	-0.858 1.242 -0.633 1.558 80.193	-0.462 0.681 -0.309 1.109 95.526	-0.393 0.612 -0.159 0.959 101.519	-0.366 0.584 -0.059 0.859 104.578
12:30 pm	-1.499 1.883 -1.608 2.533 50.680	-1.115 1.500 -1.010 0.875 67.440	-0.856 1.241 -0.631 1.556 82.263	-0.464 0.682 -0.312 1.112 96.664	-0.395 0.614 -0.162 0.962 102.351	-0.369 0.587 -0.064 0.864 105.614

TABLE 4.7 - Enhancement Factors, cont.

EST Hour	January	February	March	April	May	June
1:30 pm	-1.553 1.938 -1.686 2.611 47.173	-1.132 1.516 -1.033 1.958 64.159	-0.859 1.243 -0.635 1.560 78.488	-0.457 0.675 -0.300 1.100 92.146	-0.384 0.602 -0.143 0.943 97.797	-0.356 0.575 -0.044 0.844 101.498
2:30 pm	-1.735 2.120 -1.946 2.871 38.361	-1.186 1.571 -1.109 2.034 55.308	-0.866 1.251 -0.645 1.570 69.126	-0.439 0.657 -0.269 1.069 82.281	-0.357 0.575 -0.098 0.898 88.168	-0.324 0.543 0.006 0.794 92.511
3:30 pm	-2.264 2.648 -2.701 3.626 24.845	-1.319 1.703 -1.293 2.218 41.489	-0.883 1.268 -0.668 1.593 54.816	-0.403 0.621 -0.207 1.007 67.742	-0.305 0.523 -0.011 0.811 74.121	-0.264 0.482 0.100 0.700 79.265
4:30 pm	-5.703 6.087 -7.614 8.539 7.546	-1.719 2.103 -1.848 2.773 23.645	-0.924 1.308 -0.724 1.649 36.531	-0.328 0.547 -0.078 0.878 49.519	-0.203 0.422 0.158 0.642 56.612	-0.153 0.371 0.274 0.526 62.663
5:30 pm	0.152 0.232 0.750 0.175 0	-8.134 8.518 -10.758 11.683 2.992	-1.088 1.473 0.949 1.874 15.519	-0.129 0.347 0.266 0.534 28.854	0.027 0.191 0.542 0.258 36.835	0.076 0.143 0.631 0.169 43.836
6:30 pm	0.152 0.232 0.750 0.175 0	0.152 0.232 0.750 0.175 0	0.152 0.232 0.750 0.175 0	0.152 0.066 0.750 0.050 7.156	0.152 0.066 0.750 0.050 16.138	0.152 0.066 0.750 0.050 24.067
7:30 pm	0.152 0.232 0.750 0.175 0	0.152 0.232 0.750 0.175 0	0.152 0.232 0.750 0.175 0	0.152 0.066 0.750 0.050 0	0.152 0.066 0.750 0.050 0	0.152 0.066 0.750 0.050 4.703

TABLE 4.7 - Enhancement Factors, cont.

EST Hour	July	August	September	October	November	December
5:30 am	0.152 0.066 0.750 0.050 0	0.152 0.066 0.750 0.050 0	0.152 0.066 0.750 0.050 0	0.152 0.066 0.750 0.050 0	0.152 0.232 0.750 0.175 0	0.152 0.232 0.750 0.175 0
6:30 am	0.152 0.066 0.750 0.050 33.381	0.152 0.066 0.750 0.050 24.967	-0.300 0.518 0.131 0.669 13.841	0.152 0.066 0.750 0.050 0	0.152 0.232 0.750 0.175 0	0.152 0.232 0.750 0.175 0
7:30 am	-0.068 0.286 0.407 0.393 52.917	-0.174 0.392 0.207 0.593 45.545	-0.605 0.823 -0.287 1.087 35.221	-1.539 1.625 -1.599 2.399 20.862	-4.883 5.268 -6.342 7.267 7.528	0.152 0.232 0.750 0.175 0
8:30 am	-0.224 0.442 0.163 0.637 70.850	-0.308 0.527 -0.017 0.817 64.387	-0.675 0.893 -0.383 1.183 54.575	-1.181 1.400 -1.102 1.902 39.879	-1.960 2.345 -2.225 3.150 26.108	-3.093 3.477 -3.885 4.810 16.333
9:30 am	-0.305 0.523 0.036 0.764 85.959	-0.372 0.590 -0.123 0.923 80.208	-0.704 0.923 -0.423 1.223 70.584	-1.072 1.290 -0.950 1.750 55.325	-1.595 1.980 -1.711 2.636 41.200	-1.964 2.349 -2.273 3.198 31.681
10:30 am	-0.349 0.568 -0.033 0.833 97.212	-0.405 0.624 -0.179 0.979 91.930	-0.717 0.935 -0.440 1.240 82.156	-1.026 0.923 -0.440 1.240 66.149	-1.374 1.758 -1.399 2.324 51.775	-1.653 2.038 -1.829 2.754 42.735
11:30 am	-0.370 0.589 -0.066 0.866 103.845	-0.421 0.639 -0.250 1.005 98.755	-0.724 0.942 -0.450 1.250 88.504	-1.008 1.226 -0.861 1.661 71.611	-1.318 1.702 -1.320 2.245 57.112	-1.544 1.929 -1.673 2.598 48.745
12:30 pm	-0.375 0.593 -0.073 0.873 105.403	-0.424 0.642 -0.210 1.010 100.218	-0.725 0.943 -0.451 1.251 90.724	-1.009 1.227 -0.862 1.662 71.341	-1.321 1.705 -1.324 2.249 56.848	-1.535 1.919 -1.660 2.585 49.298

TABLE 4.7 - Enhancement Factors, cont.

EST Hour	July	August	September	October	November	December
1:30 pm	-0.364 0.582 -0.056 0.856 101.783	-0.416 0.634 -0.196 0.996 96.218	-0.720 0.938 -0.444 1.244 85.623	-1.029 1.247 -0.890 1.690 65.356	-1.382 1.767 -1.411 2.336 51.001	-1.621 2.006 -1.783 2.708 44.359
2:30 pm	-0.334 0.553 -0.010 0.810 93.229	-0.420 0.638 -0.203 1.003 87.028	-0.709 0.927 -0.429 1.229 73.801	-1.078 1.297 -0.959 1.759 54.065	-1.550 1.934 -1.647 2.572 39.969	-1.874 2.258 -2.144 3.069 34.264
3:30 pm	-0.278 0.496 0.078 0.722 80.325	-0.347 0.566 -0.082 0.882 73.275	-0.685 0.903 -0.396 1.196 59.776	-1.199 1.417 -1.126 1.926 38.237	-2.038 2.423 -2.335 3.260 24.504	-2.695 3.079 -3.317 4.242 19.700
4:30 pm	-0.174 0.392 0.241 0.559 63.951	-0.258 0.477 0.066 0.734 55.896	-0.629 0.848 -0.320 1.120 40.792	-1.615 1.833 -1.704 2.504 18.949	-6.239 6.624 -8.252 9.177 5.660	0.152 0.232 0.750 0.175 1.660
5:30 pm	0.037 0.181 0.571 0.229 45.222	-0.053 0.272 0.408 0.392 36.075	-0.438 0.656 -0.058 0.858 19.408	0.152 0.066 0.750 0.050 0	0.152 0.232 0.750 0.175 0	0.152 0.232 0.750 0.175 0
6:30 pm	0.152 0.066 0.750 0.050 25.415	0.152 0.066 0.750 0.050 15.163	0.152 0.066 0.750 0.050 0	0.152 0.066 0.750 0.050 0	0.152 0.232 0.750 0.175 0	0.152 0.232 0.750 0.175 0
7:30 pm	0.152 0.066 0.750 0.050 5.879	0.152 0.066 0.750 0.050 0	0.152 0.066 0.750 0.050 0	0.152 0.066 0.750 0.050 0	0.152 0.232 0.750 0.175 0	0.152 0.232 0.750 0.175 0

In order to use Table 4.7, the insolation level, H_t, at any given hour is divided by the corresponding extraterrestrial radiation giving K_T. From Figure 4.15, the proper correlation curve is used to determine K. Finally, Equation 4.110 is used to find the enhancement factor Γ.

I_{eff} can then be found by utilizing Equation 4.34.

4.1.4 Collector Loss Coefficient, U_L

The effectiveness of a solar collector is determined primarily by the amount of heat loss by the collector during operation. This heat loss governs the potential operating temperature of the collector and the level of insolation required in order for operation to be feasible. The heat loss is the product of the loss coefficient, loss area, and temperature difference. While the heat loss can be reduced by reducing any one of these terms, the loss coefficient is the term most readily made smaller by application of engineering and scientific techniques. In our collector, hermetically sealed tubes and a spectrally selective coating have been used to reduce the loss coefficient. The analysis of this section shows how the loss coefficient can be calculated.

From Equation 4.9;

$$q_\ell = \frac{U_L d}{D} (T_{fx} - T_a) \qquad (4.9)$$

and

$$Q_\ell = \pi D \ell q_\ell = U_L \, \pi d \ell (T_{fx} - T_a) \tag{4.115}$$

where $\pi d \ell = A_a$ = absorber tube total surface area.

So,

$$Q_\ell = A_a \, U_L \, (T_{fx} - T_a) \tag{4.116}$$

The loss coefficient is defined in terms of the absorber tube cross-sectional area.

4.1.4.1 Collector Tube Thermal Network

A sketch of the tubular element cross-section is shown in Figure 4.16. Heat flow is assumed to be by convection and conduction from temperature T_{fx} to T_{fx}' while from temperature T_{fx}' to T_{c1}, the heat loss is by convection and radiation. In Section 2, heat flow is more complicated due to the presence of the silver mirror over one-half of the inside of cover tube #2. In order to treat this problem, the enclosure can be separated into three parts and each part considered to be exchanging radiant energy with the remaining two parts. These three parts are cover tube #1 and the silvered and unsilvered portion of cover tube #2. Convective heat transfer will also occur between the three sections and hence must also be considered in the thermal network. Finally, heat loss occurs from cover tube #2 to ambient by radiation and convection. A thermal network showing the situation described above is shown in Figure 4.17. It is noted that the radiative

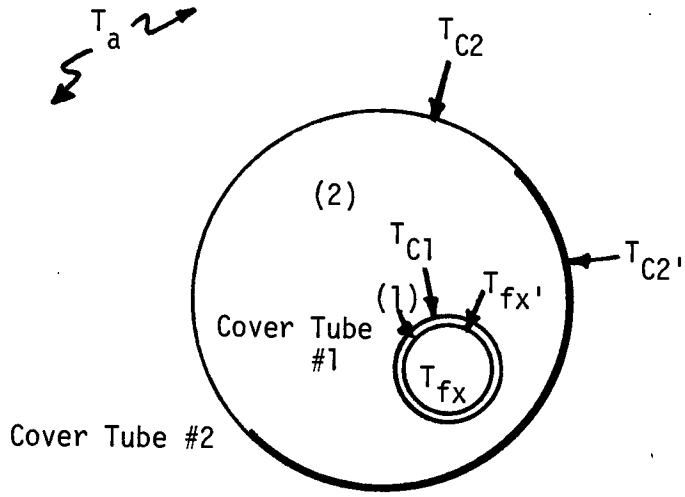

Figure 4.16 Loss Coefficient - Tube Cross Section

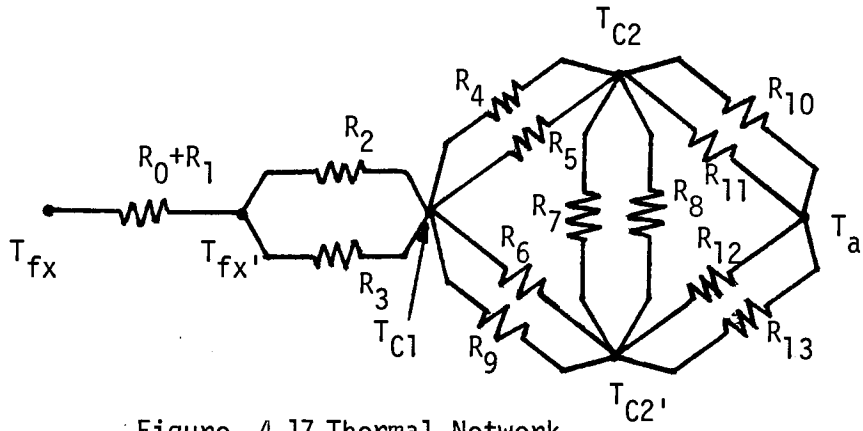

Figure 4.17 Thermal Network

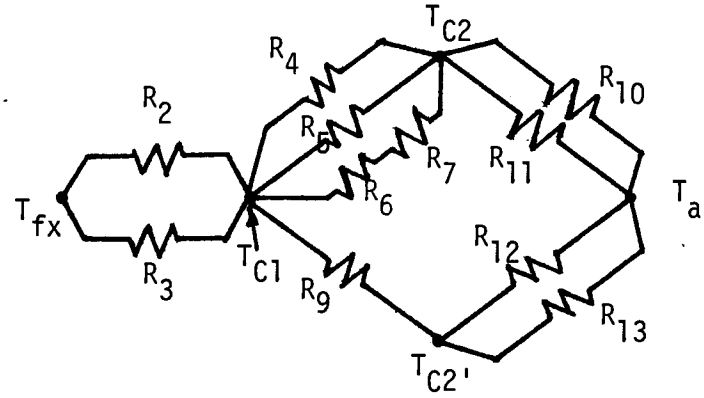

Figure 4.18 Simplified Thermal Network

resistances from T_{c2} and T_{c2}' to T_a incorporate the effective sky temperature which would be different from T_a. This will be discussed in more detail later.

Reduction of the thermal network shown in Figure 4.17 to a form similar to Equation 4.116 can be greatly facilitated by several simplifications. First, the magnitude of the series combination of convective resistance R_0 and conductive resistance R_1 will be very small compared to those of the rest of the network. Therefore, these resistances can be neglected and T_{fx}' set equal to T_{fx}. This assumption was later shown to be valid by calculating the magnitude of the series combination and comparing the result to the parallel combination of resistances R_2 and R_3. The result was less than 3 percent at a flow rate of 1 gpm. Second, the silvered portion of cover tube #2 can be considered to be a perfectly reflecting wall with an emittance of zero. This allows R_6 and R_7 to be treated as two series resistances unconnected to T_{c2}' since no heat will be absorbed or radiated by the silver mirror surface. Lastly, the convective heat transfer rate between the silvered and unsilvered portion of cover tube #2 will be small since the magnitudes of T_{c2} and T_{c2}' will be very close to one another. Therefore that portion of the network can be removed. The simplified thermal network is seen in Figure 4.18.

From Figure 4.18, the following simplifications are made:

$$R_1' = (h_{r,fx-c1} + h_{c,fx-c1})^{-1} = \left(\frac{1}{R_2} + \frac{1}{R_3}\right)^{-1} \quad (4.117)$$

$$R_2' = \left(\frac{h_{c,c1-c2}}{2} + h_{r,c1-c2}\right)^{-1} = \left(\frac{1}{2R_4} + \frac{1}{R_5} + \frac{1}{R_6+R_7}\right)^{-1} \quad (4.118)$$

$$R_3' = \left(\frac{h_{c,c1-c2'}}{2}\right)^{-1} = 2R_9 \quad (4.119)$$

$$R_4' = (h_{c,c2-a} + h_{r,c2-a})^{-1} = \left(\frac{1}{R_{10}} + \frac{1}{R_{11}}\right)^{-1} \quad (4.120)$$

$$R_5' = (h_{c,c2'-a} + h_{r,c2'-a})^{-1} = \left(\frac{1}{R_{12}} + \frac{1}{R_{13}}\right)^{-1} \quad (4.121)$$

Section heat balances can now be done for each portion of the network shown in Figure 4.18.

$$Q_{fx-c1} = A_a(T_{fx} - T_{c1})(h_{r,fx-c1} + h_{c,fx-c1}) \quad (4.122)$$

where

$$A_a = \pi d\ell$$

$$Q_{c1-c2} = A_{c1}(T_{c1} - T_{c2})\left(\frac{h_{c,c1-c2}}{2} + h_{r,c1-c2}\right) \quad (4.123)$$

where

$$A_{c1} = \pi d'\ell$$

$$Q_{c1\text{-}c2'} = A_{c1}(T_{c1} - T_{c2'})\left(\frac{h_{c,c1\text{-}c2'}}{2}\right) \tag{4.124}$$

$$Q_{c2\text{-}a} = A_{c2}(T_{c2} - T_a)(h_{c,c2\text{-}a} + h_{r,c2\text{-}a}) \tag{4.125}$$

where

$$A_{c2} = \frac{\pi D \ell}{2}$$

$$Q_{c2'\text{-}a} = A_{c2'}(T_{c2'} - T_a)(h_{c,c2'\text{-}a} + h_{r,c2'\text{-}a}) \tag{4.126}$$

where

$$A_{c2'} = A_{c2}$$

For steady state conditions,

$$Q_\ell = Q_{fx\text{-}c1} = Q_{c1\text{-}c2} + Q_{c1\text{-}c2'} = Q_{c2\text{-}a} + Q_{c2'\text{-}a} \tag{4.127}$$

Equation 4.122 can be rewritten as,

$$\frac{Q_\ell}{A_a}\frac{1}{(h_{c,fx\text{-}c1} + h_{r,fx\text{-}c1})} = (T_{fx} - T_{c1}) \tag{4.128}$$

Equations 4.123 and 4.124 can be rearranged and added giving,

$$\frac{Q_\ell}{A_a}\left(\frac{\left(\frac{A_a}{A_{c1}}\right)}{\left(\frac{\frac{h_{c,c1-c2'}}{2}}{\frac{T_{c1}-T_{c2}}{T_{c1}-T_{c2'}}}+\frac{h_{c,c1-c2}}{2}+h_{r,c1-c2}\right)}\right)=(T_{c1}-T_{c2}) \quad (4.129)$$

Following a similar approach, Equations 4.125 and 4.126 become,

$$\frac{Q_\ell}{A_a}\left(\frac{\left(\frac{A_a}{A_{c2}}\right)}{\left(\frac{h_{c,c2'-a}+h_{r,c2'-a}}{\frac{T_{c2}-T_a}{T_{c2'}-T_a}}+h_{c,c2-a}+h_{r,c2-a}\right)}\right)=(T_{c2}-T_a) \quad (4.130)$$

Now, Equations 4.128, 4.129, and 4.130 can be added giving,

$$Q_\ell\left[\frac{1}{h_{c,fx-c1}+h_{r,fx-c1}}+\left(\frac{A_a}{A_{c1}}\right)\frac{1}{\left[\frac{\frac{h_{c,c1-c2'}}{2}}{\frac{T_{c1}-T_{c2}}{T_{c1}-T_{c2'}}}+\frac{h_{c,c1-c2}}{2}+h_{r,c1-c2}\right]}\right.$$

$$\left.+\left(\frac{A_a}{A_{c2}}\right)\frac{1}{\left[\frac{h_{c,c2'-a}+h_{r,c2'-a}}{\frac{T_{c2}-T_a}{T_{c2'}-T_a}}+h_{c,c2-a}+h_{r,c2-a}\right]}\right]=A_a(T_{fx}-T_a) \quad (4.131)$$

Comparing Equation 4.131 to Equation 4.116 gives,

$$U = \left[\left(\frac{1}{h_{c,fx-c1} + h_{r,fx-c1}}\right) + \left(\frac{A_a}{A_{c1}}\right)\frac{1}{\left[\frac{\frac{h_{c,c1-c2'}}{2}}{\frac{T_{c1}-T_{c2}}{T_{c1}-T_{c2'}}} + \frac{h_{c,c1-c2}}{2} + h_{r,c1-c2}\right]}\right.$$

$$\left. + \left(\frac{A_a}{A_{c2}}\right)\frac{1}{\left[\frac{h_{c,c2'-a} + h_{r,c2'-a}}{\frac{T_{c2}-T_a}{T_{c2'}-T_a}} + h_{c,c2-a} + h_{r,c2-a}\right]}\right]^{-1} \qquad (4.132)$$

Finally, substitution of Equations 4.117 through 4.121 into 4.132 give,

$$U_L = \left[R_1' + \left(\frac{A_a}{A_{c1}}\right)\frac{1}{\frac{1}{R_3'}\left(\frac{T_{c1}-T_{c2'}}{T_{c1}-T_{c2}}\right) + \frac{1}{R_2'}} + \left(\frac{A_a}{A_{c2}}\right)\frac{1}{\left[\frac{1}{R_5'}\left(\frac{T_{c2'}-T_a}{T_{c2}-T_a}\right) + \frac{1}{R_4'}\right]}\right] \qquad (4.133)$$

4.1.4.2 Thermal Network Resistance Evaluation

In order to evaluate the resistances in Equation 4.133, the following simplifying assumptions are used:

1. all surfaces are gray (all radiative properties are independent of wavelength),
2. surfaces emit and reflect radiation in a diffuse manner (except silver mirror portion of cover #2),

3. the surface temperatures are uniform as indicated in Figure 4.16,
4. there is negligible absorption of solar energy by the covers with respect to the loss coefficient,
5. the glass covers are opaque to radiation emitted by surfaces of the tubular element.

The radiative resistance R_2 is equal to the inverse of the radiative heat transfer coefficient, $h_{r,fx-cl}$. For radiation between two surfaces [19],

$$h_{r,fx-cl} = \frac{\sigma(T_{fx} + T_{cl})\ (T_{fx}^2 + T_{cl}^2)}{\frac{1}{\varepsilon_a} + \frac{A_a}{A_{cl}}\left(\frac{1}{\varepsilon_{cl}} - 1\right)} \tag{4.134}$$

where the shape factor, F_{fx-cl}, equals 1.

The convective resistance R_3 is equal to the inverse of the convective heat transfer coefficient, $h_{c,fx-cl}$. From Kreith and Kreider [12], the following correlation is recommended for long annuli formed by concentric tubes,

$$N_u = \frac{h_c L}{K_f} = 0.135\left(\frac{R_a P_r}{1.36 + P_r}\right)^{0.278} \tag{4.135}$$

for $\quad 3.5 \leq \log_{10}\left(\frac{R_a P_r}{1.36 + P_r}\right) \leq 8.00$

and $$0.25 \leq \frac{r_o - r_i}{r_i} \leq 3.25$$

If $\log_{10}\left(\frac{R_a P_r}{1.36 + P_r}\right) \leq 3.0$, then [20]

$$N_u = \frac{h_c L}{K_f} = 1 \qquad (4.136)$$

The terms in Equations 4.135 and 4.136 are defined as follows:

L = annulus width, $d'/2 - d/2$, m

K_f = thermal conductivity of the fluid (evaluated at arithmetic mean of T_{fx} and T_{c1}), W/m°K

h_c = $h_{c,fx-c1}$, $W/m^2°K$

R_a = Raleigh number = $P_r \cdot G_r$

P_r = Prandtl number, $c_p\mu/K_f$ where c_p = specific heat, J/kg°K,

μ = absolute viscosity, $N \cdot sec/m^2$

G_r = Grashof number, $\rho^2 g\beta_T(T_{fx} - T_{c1})L^3/\mu^2$

where

ρ = fluid density, Kg/m^3

g = gravitational constant, 9.8 m/s^2

β_T = coefficient of expansion of the fluid in $°K^{-1}$ (for ideal gases, β_T equals the reciprocal of the absolute temperature, that is $\beta_T = 1/T$)(evaluated at arithmetic mean of T_{fx} and T_{c1}).

The convective resistances R_4 and R_9 from T_{c1} to T_{c2} and $T_{c2'}$ respectively, are determined utilizing the same correlations

as given by Equations 4.135 and 4.136. Kreith and Kreider recommend their use for eccentric annular areas for lack of better correlations at present. This method is equivalent to assuming a cover tube #2 uniform temperature of $T_{c2'}$ to find R_9. Again, since the temperature difference between T_{c2} and $T_{c2'}$ is small, the error introduced by this assumption will be small.

The radiative resistance between T_{c1} and T_{c2} is equal to the inverse of the radiative heat transfer coefficient, $h_{r,c1-c2}$. From Karlekar and Desmond [21] for an enclosure of three surfaces where one surface is a perfectly reflecting surface, the heat flow due to radiation is given by:

$$Q_{r,c1-c2} = \frac{A_{c1}\sigma(T_{c1}^4 - T_{c2}^4)}{\frac{1-\varepsilon_{c1}}{\varepsilon_{c1}} + \frac{[1/F_{c1-c2}][1/A_{c2}F_{c2-c2'} + 1/A_{c1}F_{c1-c2'}]}{1/A_{c1}F_{c1-c2} + 1/A_{c2}F_{c2-c2'} + 1/A_{c1}F_{c1-c2'}} + \left(\frac{A_{c1}}{A_{c2}}\right)\frac{1-\varepsilon_{c2}}{\varepsilon_{c2}}} \tag{4.137}$$

The radiative heat transfer coefficient, $h_{r,c1-c2}$, is obvious from Equation 4.137 and is given by

$$h_{r,c1-c2} = \frac{\sigma(T_{c1} + T_{c2})\,(T_{c1}^2 + T_{c2}^2)}{\frac{1-\varepsilon_{c1}}{\varepsilon_{c1}} + \frac{[1/F_{c1-c2}][1/A_{c2}F_{c2-c2'} + 1/A_{c1}F_{c1-c2'}]}{1/A_{c1}F_{c1-c2} + 1/A_{c2}F_{c2-c2'} + 1/A_{c1}F_{c1-c2'}} + \left(\frac{A_{c1}}{A_{c2}}\right)\frac{1-\varepsilon_{c2}}{\varepsilon_{c2}}} \tag{4.138}$$

To utilize Equation 4.138, the shape factors F_{c1-c2}, $F_{c2-c2'}$, and $F_{c1-c2'}$ must be found. From Figure 4.16,

$$F_{c1-c2} + F_{c1-c2'} = 1 \tag{4.139}$$

Also,

$$F_{c2\text{-}c2} + F_{c2\text{-}c1} + F_{c2\text{-}c2'} = 1 \tag{4.140}$$

The shape factor $F_{c1\text{-}c2}$ for diffuse radiation [22] is equal to the angle subtended by the hemisphere formed by the unsilvered portion of cover tube #2 with respect to centerpoint of cover tube #1 divided by 360°. From Figure 4.3, the angle is seen to be $2(90 - \gamma_1)$ or 126.80°.

$$F_{c1\text{-}c2} = \frac{126.80°}{360} = 0.352$$

From Equation 4.139, $F_{c1\text{-}c2'} = 0.648$

$F_{c2\text{-}c2}$ can be found by evaluating the following equation,

$$F_{c2\text{-}c2} + F_{c2\text{-}c1'} = 1 \tag{4.141}$$

where surface c1' is an imaginary plane separating outer cover tube #2 into semi-cylinders. From the reciprocity relationship,

$$A_{c2}\, F_{c2\text{-}c1'} = A_{c1'}\, F_{c1'\text{-}c2} \tag{4.142}$$

where $F_{c1'\text{-}c2} = 1$ and,

$$F_{c2\text{-}c1'} = \frac{A_{c1'}}{A_{c2}} = \frac{D}{\pi D/2} = \frac{2}{\pi}$$

From Equation 4.141, $F_{c2\text{-}c2} = 1 - 2/\pi = 0.363$.

$F_{c2\text{-}c1}$ in Equation 4.140 can likewise be evaluated from the reciprocity relationship,

$$A_{c2} F_{c2\text{-}c1} = A_{c1} F_{c1\text{-}c2} \tag{4.143}$$

and,

$$F_{c2\text{-}c1} = \frac{A_{c1}}{A_{c2}} F_{c1\text{-}c2} = \frac{9/16}{1} (0.352) = 0.198$$

Finally, from Equation 4.140,

$$F_{c2\text{-}c2'} = 1 - 0.363 - 0.198 = 0.439$$

Now, the second term in the denominator of Equation 4.138 can be evaluated,

$$\frac{\left(\frac{1}{0.352}\right)\left(\frac{1}{\pi D\ell/2 \cdot 0.439} + \frac{1}{\pi d'\ell \cdot 0.648}\right)}{\frac{1}{\pi d'\ell \cdot 0.352} + \frac{1}{\pi D\ell/2 \cdot 0.439} + \frac{1}{\pi d'\ell \cdot 0.648}} = 1.416$$

and Equation 4.138 becomes:

$$h_{r,c1\text{-}c2} = \frac{\sigma(T_{c1} + T_{c2})(T_{c1}^2 + T_{c2}^2)}{\frac{1}{\varepsilon_{c1}} + 0.416 + \left(\frac{A_{c1}}{A_{c2}}\right)\left(\frac{1-\varepsilon_{c2}}{\varepsilon_{c2}}\right)} \tag{4.144}$$

The convective resistances R_{10} and R_{12} from T_{c2} and T_{c2}' to ambient temperature T_a are equal to the inverse of the convective

heat transfer coefficients $h_{c,c2-a}$ and $h_{c,c2'-a}$, respectively. To determine these coefficients, a correlation by Whitaker [23] for flow across a cylindrical tube at a uniform temperature is used. The correlation is evaluated for the convective heat transfer coefficient at a wall temperature of first T_{c2} and then $T_{c2'}$ in order to determine R_{10} and R_{12}. Again, since the temperature difference between T_{c2} and $T_{c2'}$ is small, the resulting error introduced by the assumption will be small. The correlation is,

$$Nu_{ave} = \frac{h_c L}{K} = (0.4\ Re^{1/2} + 0.06\ Re^{2/3})Pr^{0.4} \left(\frac{\mu_\infty}{\mu_\omega}\right)^{1/4} \qquad (4.145)$$

for $0.67 < Pr < 300$

$10 < Re < 100{,}000$

and $0.25 < \left(\frac{\mu_\infty}{\mu_\omega}\right) < 5.2$

All properties in Equation 4.145 are evaluated at the free stream temperature T_a except μ_w which is evaluated at the surface temperature.

The radiative resistances R_{11} and R_{13} are equal to the inverse of the radiative heat transfer coefficients $h_{r,c2-a}$ and $h_{r,c2'-a}$. In the real case, radiative transfer will occur between the unsilvered portion of cover tube #2,adjacent tubes and the surroundings and also between the silvered portion of cover tube #2, adjacent tubes and the collector backing. Thus, assuming all surfaces behave as gray bodies, each radiative heat transfer coefficient would be determined by evaluation

of a three body enclosure. A much simpler and worst case approach would be to assume that the radiation exchange occurs between the tube and the sky about the entire circumference of cover tube #2. This procedure was utilized in reference 11 and enables the heat flow due to radiation to be written as

$$Q_{r,c2-a} = A_{c2}\ \varepsilon_{c2}\ \sigma(T_{c2}^{4} - T_{sky}^{4}) \tag{4.146}$$

and

$$Q_{r,c2'-a} = A_{c2'}\ \varepsilon_{c2'}\ \sigma(T_{c2'}^{4} - T_{sky}^{4}) \tag{4.147}$$

for the unsilvered and silvered portion of outer cover tube #2, respectively. T_{sky} is an equivalent sky temperature which accounts for the fact that the atmosphere is not at a uniform temperature and that the atmosphere radiates only in certain wavelength bands. To evaluate T_{sky}, the relationship [24]

$$T_{sky} = 0.0552\ T_a^{1.5} \tag{4.148}$$

is used. Both T_{sky} and T_a are in degrees Kelvin. The radiative heat transfer coefficients $h_{r,c2-a}$ and $h_{r,c2'-a}$ can now be written from Equations 4.146 and 4.147 noting that the denominators account for the fact that the losses are based on T_a and not T_{sky}.

$$h_{r,c2-a} = \frac{\varepsilon_{c2}\ \sigma\ (T_{c2}^{4} - T_{sky}^{4})}{(T_{c2} - T_a)} \tag{4.149}$$

$$h_{r,c2'-a} = \frac{\varepsilon_{c2'} \sigma (T_{c2'}^4 - T_{sky}^4)}{(T_{c2'} - T_a)} \qquad (4.150)$$

4.1.4.3 Evaluation of U_L

The loss coefficient U_L was evaluated for a variety of particular conditions utilizing the following approach. First, guesses were made for cover temperature T_{c1},T_{c2}, and $T_{c2'}$. Next, U_L was calculated from Equation 4.133 and the heat loss calculated from Equation 4.116. Having the heat loss, section heat balances were then used to back calculate T_{c1}, T_{c2}, and $T_{c2'}$. Equations 4.128, 4.129, and 4.130 were used for this step. If the computed and guessed cover temperatures agreed within convergence requirements (± 0.1° C for T_{c1} and ± 1.0°C for T_{c2} and $T_{c2'}$), then the loss coefficient computed was correct. If they did not agree within the specified limits, T_{c1}, T_{c2}, and $T_{c2'}$ were set equal to their new values and the procedure repeated until convergence was achieved. The surface emissivities values used for the calculations are

$$\varepsilon_a = 0.07$$

$$\varepsilon_{c1} = \varepsilon_{c2} = \varepsilon_{c2'} = 0.88$$

4.1.4.1 Loss Coefficient Results

The loss coefficient U_L was calculated for two ambient temperature extremes (-20°C and 40°C) at a wind velocity of 10 mph (4.47m/s). This speed was used since it is approximately the average wind speed in Rochester.

The results are given in Table 4.8 and plotted in Figure 4.19.

	T_a = -20°C	T_a = 40°C
Absorber Temperature (°C)	U_L W/m^2°C	U_L W/m^2°C
0	4.055	-
25	4.512	-
50	4.981	4.458
75	5.541	5.097
100	5.846	5.637

Table 4.8 Collector Loss Coefficient, U_L

Also shown is the loss coefficient referenced to the aperture area ($U_L \pi d/D$). From Figure 4.19 it is seen that the loss coefficient increases gradually with increasing operating temperatures. If the collector is operated at a modest temperature gain, U_L can be treated as a constant over this temperature range. Thus linear theory in heat balance equations can be used. U_L has been treated this way in my work.

4.1.5 Effective transmittance-absorptance product, $(\tau\alpha)_e$.

The effective transmittance absorptance-product is the percentage of radiation which is transmitted through the cover system and absorbed by the absorber tube. In order to calculate its value, the transmittance of the cover system can first be determined. For

Figure 4.19. Collector Loss Coefficient, U_L

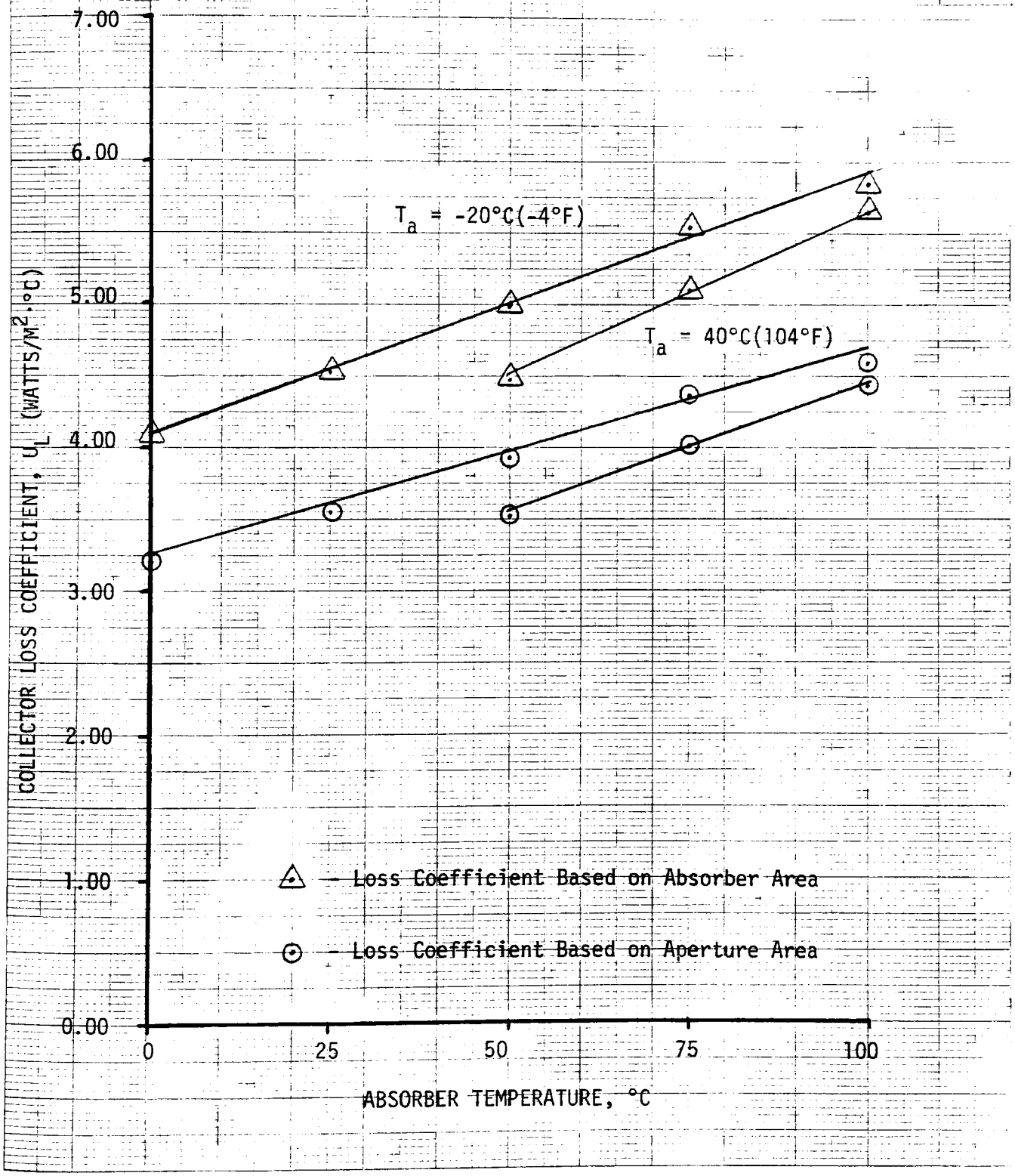

partially transparent surfaces, the sum of absorptance, reflectance and transmittance must be unity. Transmittance, like reflectance and absorptance, is a function of wavelength, angle of incidence of the incoming radiation, the refractive index, n, and the extinction coefficients, K, of the material. Strictly speaking, n and K are functions of wavelength but for most solar energy applications can be assumed to be independent of wavelength.

For a flat plate cover system, the determination of the transmittance of the cover system is a straightforward procedure as outlined in Chapter 6 of Duffie and Beckman. For nonpolarized radiation passing from medium 1 with a refractive index n_1, to medium 2 with a refractive index n_2, the reflectance is given by Fresnel as [25],

$$\rho = \frac{1}{2}\left[\frac{\text{Sin}^2(\theta_2 - \theta_1)}{\text{Sin}^2(\theta_2 + \theta_1)} + \frac{\tan^2(\theta_2 - \theta_1)}{\tan^2(\theta_2 + \theta_1)}\right] \qquad (4.151)$$

where θ_1 and θ_2 are the angles of incidence and refraction of the incoming radiation. The two terms in the brackets represent the reflection for each of the two components of polarization and hence Equation 4.151 gives the reflective nonpolarized radiation as the average of the two components. Snell's Law relates θ_1 and θ_2 to the indices of refraction. It is:

$$\frac{n_1}{n_2} = \frac{\sin\theta_2}{\sin\theta_1} \qquad (4.152)$$

Knowing n_1, n_2, and θ_1, θ_2 and ρ can easily be calculated.

In order to calculate the transmittance of a cover system, it must be remembered that there are two interfaces per cover present. Neglecting absorptance, it can be easily shown [25] that the transmittance of a single cover is:

$$\tau_{r,1} = \frac{1 - \rho}{1 + \rho} \tag{4.153}$$

For a multicover system, a similar analysis gives:

$$\tau_{r,n} = \frac{1 - \rho}{1 + (2n - 1)\rho} \tag{4.154}$$

For angles less than about 40°, the average reflectance as calculated by Equation 4.151 can be used above, for greater angles, each component must be considered separately.

The transmittance of radiation through a partially transparent media is also limited by absorption. From Beer's law, the transmittance due to absorption is;

$$\tau_a = e^{-KL} \tag{4.155}$$

where L is the actual path length of the radiation through the medium, and K is the absorption coefficient.

Finally, for τ_a approximately equal to one,

$$\tau = \tau_r \cdot \tau_a \tag{4.156}$$

which is always satisfied in solar energy applications.

The transmittance-absorptance product for a flat plate system can be calculated when it is realized that multiple reflections can occur due to the fact the absorber plate is not a perfect absorber. From reference

$$(\tau\alpha) = \frac{\tau\alpha}{1 - (1-\alpha)\,\rho_d} \tag{4.157}$$

where $(\tau\alpha)$ is the transmittance-absorptance product, τ is the transmittance of the cover system, α is the absorptance of the cover plate and ρ_d is the reflection of the cover plate for incident-diffuse radiation. It can be estimated by using the specular reflection of the cover system at an incidence angle of 60°.

When the cover system consists of cylindrical tubes, the calculation of $(\tau\alpha)_e$ becomes more complicated because the reflection losses must be integrated over different angles of incidence. At any single solar elevation angle, rays strike the cylindrical surface at all angles from normal incidence to grazing (0° to 90°). Because of this, reflection losses for a single cylindrical tube will be nearly twice those of a flat plate [26]. For example, if the collectors are normal to the sun, and the index of refraction of glass 1.52, the reflectance of the flat plate would be 0.043 (Equation 4.151) while that of the cylinder would be 0.07 corresponding to a transmittance of 0.92 (Equation 4.153) and 0.87 [26]. However, while the transmittance of a flat plate will

increase as the angular elevation of sun changes, the cylinder transmittance will remain essentially constant. This means that the value for the transmittance at solar noon is independent of the time of year for a tubular element. However, when the daily angular motion of the sun is considered, the reflection losses for a cylinder will increase as the angle between the sun's rays and the tube normal increases (angle i, Figure A5.3). The angle i at which this change becomes substantial is approximately 60° [27]. Evaluation of the angle i for the collector geometry at Energy House utilizing Equations A5.6 and A5.7 of Appendix 5 revealed that between the hours of 8:30 a.m. and 3:30 p.m. it did not exceed 60°. Since the greatest portion of usable solar energy is incident on the collector during this time, the value for the transmittance at angles of less than 60° will be used throughout the analysis. When calculating the transmittance, a simplification results when it is realized that the analysis need be made for only that portion of the cover system over which I_{eff} is measured. Since the incoming radiation which comprises I_{eff} is predominantly near normal incidence (i.e. that radiation at near grazing angles to the tube will not be a part of I_{eff} since it is generally not directly absorbed or backreflected to the absorber tube), the transmittance of the cover system can be approximated by calculating the transmittance of a two cover flat plate system with radiation at normal incidence. For a reflectance of 0.0434 per single air-glass interface, the transmittance of a two cover system is from Equation 4.154; $\tau_{r-2} = 0.85$. The transmittance due to absorptance can be calculated knowing that $K = 0.0878\ cm^{-1}$ and $L = 2(0.056\ in) = 0.2845\ cm$. From Equation 4.155, $\tau\alpha = 0.98$. The overall transmittance from Equation 4.156, is equal to 0.83. Finally,

the effective transmittance-absorptance product can be calculated from Equation 4.157 where $\alpha = 0.95$ and $\rho_d = 0.24$ with the result being $(\tau\alpha)_e = 0.80$.

One additional point which should be considered is that a significant portion of the reflected light from individual tubes will be captured by adjacent tubes. This is not the case for a flat plate collector as all reflected radiation can be considered lost. The actual percentage that is captured by adjacent tubes depends on the tube spacing and the position of the sun. While exact calculation of this value would be difficult, its effect would give a higher value for $(\tau\alpha)_e$ than given above. As the experimental work of Section 5 will show, the value for $(\tau\alpha)_e$ is indeed higher than that given above.

4.2 Tank Analysis

4.2.1 Energy Storage Capacity

The energy storage of a water storage unit operating over a finite temperature difference is given by;

$$Q_S = M_S C_{p,S} \Delta T \qquad (4.158)$$

where Q_S is the total heat capacity of the tank operating over a temperature range of ΔT with M_S kilograms of water.

For a nonstratified tank with both solar and auxiliary energy input, an energy balance gives the following result;

$$(M_S C_{p,S})\frac{dT_S}{dt} = Q_{TRAN} + Q_{AUX} - L - (UA)(T_S - T_{AMB}) \qquad (4.159)$$

where Q_{TRAN} is the rate of heat addition to the tank from the collector, Q_{AUX} is the rate of addition of auxiliary energy to the tank, L is the removal of energy from the tank due to usage and $(UA)(T_S - T_{AMB})$ is the loss of energy of the tank to the surroundings. Previous work by Klein [28] has shown this level of representation to be sufficient to accurately predict system performance. He has found for a particular system under study that the effect of using a thermal stratification model was to increase the fraction of the water heating load supplied by solar energy by 3%. Thus, use of a nonstratified model results in slightly conservative estimates of system performance. In addition, there is a computational benefit in using a nonstratified tank model. Based on these considerations, the nonstratified model is used. Equation 4.159 can now be applied to both the preheat tank and the hot water tank with nonapplicable terms removed.

From Figure 3.1, it is seen that energy from the KTA collectors is transferred to the preheat tank through a heat exchanger. The amount of energy transferred can be written as;

$$Q_{TRAN} = \dot{M} C_p (T_{OUTC} - T_{INC}) \qquad (4.160)$$

when the pipe losses are neglected. The collector outlet temperature

T_{OUTC} is found utilizing Equations 4.29 and 4.30 previously given for the collectors. The collector inlet temperature T_{INC} depends on several factors including the amount of surface available for heat transfer, the thermal conducitivity of the tube material, the amount of scaling on the heat exchanger, and the convective heat transfer coefficients on the inside and outside surface of the heat exchanger. If the overall heat transfer coefficient of the heat exchanger coefficient is assumed to be a constant, then the temperature difference from basic heat exchanger relationships [29] is found from:

$$\frac{T_{OUTC} - T_{INC}}{T_{OUTC} - T_{IWH}} = 1 - e^{-(U_h A)/(\dot{M} C_p)_c} \qquad (4.161)$$

where A is the area of the heat exchanger and $\dot{M} C_p$ is the heat capacity rate of the collector. Evaluation of the right side of Equation 4.161 will be done experimentally in Section 5.3.

For the preheat tank, Q_{AUX} is equal to zero while the removal of energy, L can be written as:

$$L = Q_{PRE} = \dot{M}_L C_{p,S}(T_{IWH} - T_{CW}) \qquad (4.162)$$

where T_{IWH} and T_{CW} are the fluid temperatures at the discharge and inlet of the preheat tank, respectively.

For the hot water tank, Q_{TRAN} is equal to zero while Q_{AUX} is equal to 16,200 kJ/hr when T_{IWH} is less than 140°F (60°C) (See Section 3.1.). The removal of energy can be written as:

$$L = Q_{HOT} = \dot{M}_L \, C_{p,S} \, (T_{OWH} - T_{IWH}) \qquad (4.163)$$

The environmental loss term remains to be examined.

4.2.2 Tank Loss Coefficient

The tank loss coefficient U in Equation 4.159 can be found experimentally for both the preheat tank and the hot water tank. In order to perform the analysis, the solution of Equation 4.159 in terms of the storage temperature T_S' must be obtained. For Q_{TRAN}, Q_{AUX}, and L equal to zero, Equation 4.159 becomes:

$$(M_S \, C_{p,S}) \, \frac{dT_S}{dt} = -UA(T_S - T_{AMB}) \qquad (4.164$$

where from Figure 3.14 T_{AMB} is measured at location T7 and T_S is measured at locations T5 and T9 for the preheat and hot water tank respectively. The right hand side of Equation 4.164 is equal to Q_{ENST} where T_S is T_{IWH} and to Q_{ENHW} where T_S is T_{OWH} for the preheat and hot water tank, respectively. Equation 4.164 can be rewritten as:

$$- \frac{dT_S}{dt} = \frac{UA}{M_S C_{p,S}} (T_S - T_{AMB}) = B(T_S - T_{AMB}) \qquad (4.165)$$

where

$$B = \frac{UA}{M_S C_{p,S}}$$

Solution of Equation 4.165 gives:

$$T_S = (T_{S,I} - T_{AMB})\, e^{-Bt} + T_{AMB} \qquad (4.166)$$

where $T_{S,I} = T_S$ at time $t = 0$. Equation 4.166 can be rewritten as:

$$\frac{T_S - T_{AMB}}{T_{S,I} - T_{AMB}} = e^{-Bt} \qquad (4.167)$$

The quantity 1/B is the time constant for the tank under consideration. It is the time required for the tank temperature to drop 63.2% of the initial difference between the tank temperature and the ambient temperature.

5. EXPERIMENTAL WORK

Several tests were performed utilizing the system described in Section 3 for the purpose of evaluating the parameters described in Section 4. For the collector, the loss coefficient, U_L, the effective transmittance-absorptance product $(\tau\alpha)_e$, and the collector heat removal factor F_R were evaluated. For the preheat and hot water tank, the loss coefficients U were evaluated while for the the heat exchanger, the loss coefficient-area product U_hA was found. Test descriptions and results are given in this section.

5.1 Collector Parameters

From Equation 4.29, the collector performance is given by:

$$Q_u = A_t F_R[(\tau\alpha)_e I_{eff} - U_L \frac{\pi d}{D} (T_{INC} - T_a)] \tag{4.29}$$

with the collector efficiency from Equation 4.35,

$$\eta = F_R \left[(\tau\alpha)_e \Gamma - U_L \frac{\pi d}{D} \frac{(T_{INC} - T_a)}{I}\right] \tag{4.35}$$

The heat removal factor is given by Equation 4.27;

$$F_R = \frac{GC_p}{U_L \pi} \frac{D}{d} \left[1 - e^{-[\frac{U_L}{G} \frac{\pi}{C_p} \frac{d}{D}]}\right] \tag{4.27}$$

5.1.1 Test #1 - U_L and F_R

For the case of no insolation, Equation 4.29 can be rewritten as,

$$Q_u = -A_t F_R U_L \frac{\pi d}{D} (T_{INC} - T_a) \tag{5.1}$$

Solving for $F_R U_L$ gives:

$$F_R U_L = \frac{-Q_u}{\frac{\pi d}{D} (T_{INC} - T_a) A_t} \tag{5.2}$$

where Q_u in this case is equal to energy lost by the collector. It is expressible as:

$$Q_u = -\dot{M} C_p (T_{OUTC} - T_{INC}) \tag{5.3}$$

giving;

$$F_R U_L = \frac{\dot{M} C_p (T_{OUTC} - T_{INC})}{\frac{\pi d}{D} (T_{INC} - T_a) A_t} \tag{5.4}$$

when substituted into Equation 5.2. By operating the collector at night, the right side of Equation 5.4 can be easily determined. F_R and U_L can then be calculated utilizing Equation 4.27 given above.

Following instrumentation procedures outlined in Section 3.3 temperatures were measured at locations T3, T4, and T6 indicated in

Figure 3.14 corresponding to T_{INC}, T_{OUTC}, and T_a, respectively in Equation 5.4. Flow measurement giving $\dot{M}$ was performed at the location indicated by the same figure. Measurements were made at three minute intervals. In order to verify the analytic results shown in Figure 4.19, the test was performed both during the summer and winter. Water was the transfer fluid in the summer while propylene glycol antifreeze was used in the winter. A time vs. temperature profile of the summer test is shown in Figure 5.1 while the winter results are shown in Figure 5.2. Observation of each figure shows initial unsteady response. After a short period of time, these characteristics disappeared. The initial unsteady condition is due to two factors. First, at the outset of each test, the tubular collection elements were approximately equal to the ambient temperature. Since the temperature of the fluid entering the elements was higher than ambient, a certain amount of time was necessary for the tubular collection elements to achieve a new equilibrium temperature. Also, the fluid itself was at different temperature levels depending on its location in the system and as a result, it had to come to a fully mixed condition before steady state conditions could be observed. From Figure 5.1, these effects become negligible in about 15 minutes while from Figure 5.2, a longer period of time elapses before steady conditions are observed. With these considerations in mind, the data was reduced for 15 minute intervals following the form of Equations 5.4 and 4.27. The final results are given in Table 5.1. The fluid temperature T_{WM} at the water meter was taken as the average of T1 and T3 shown in Figure 3.14. The fluid properties given for the summer run are those of water

Figure 5.1 Collector Time Vs Temperature Profile - Experimental Calculation of F_R and U_L - Summer

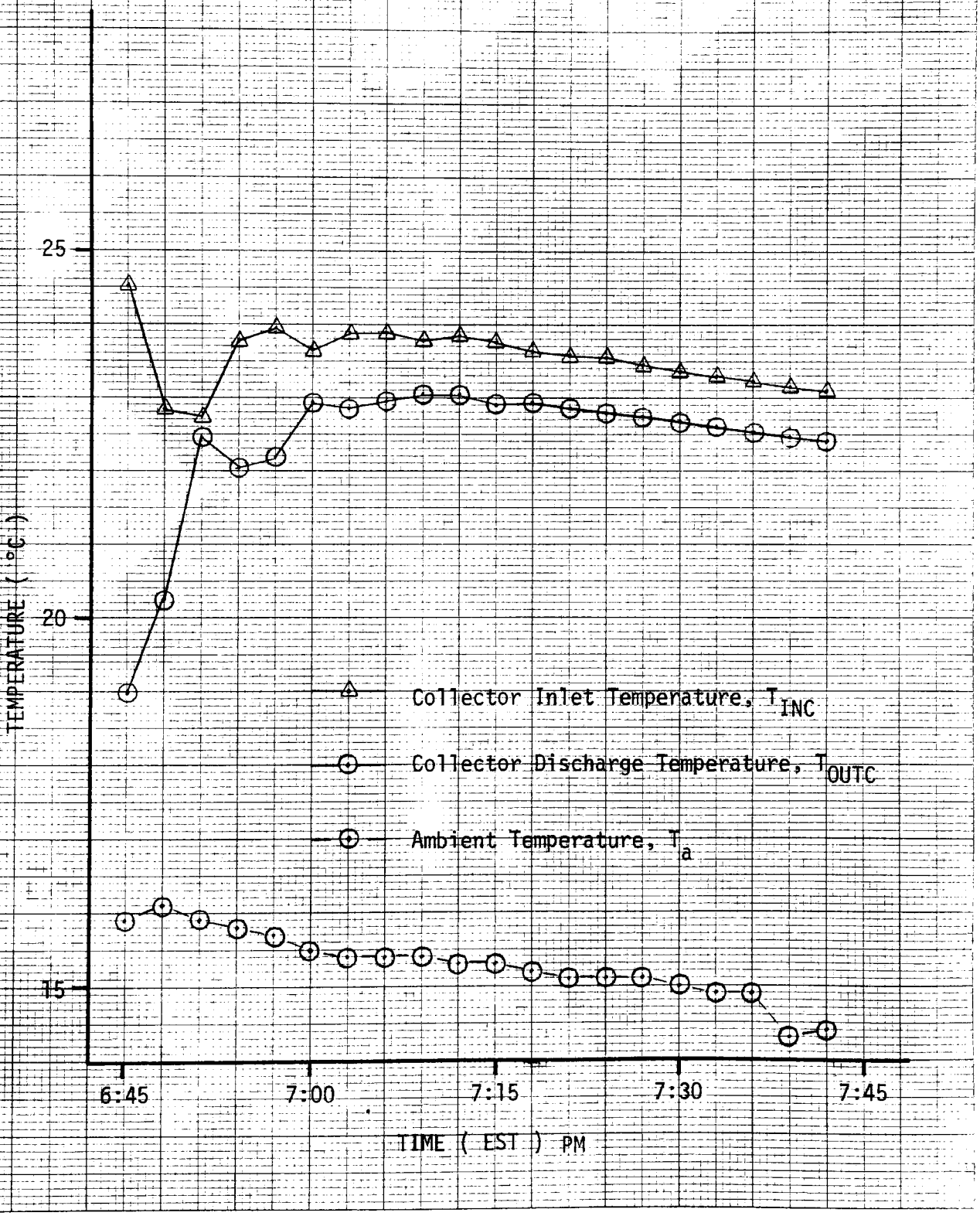

Figure 5.2 Collector Time Vs Temperature Profile - Experimental Calculation of F_R and U_L - Winter

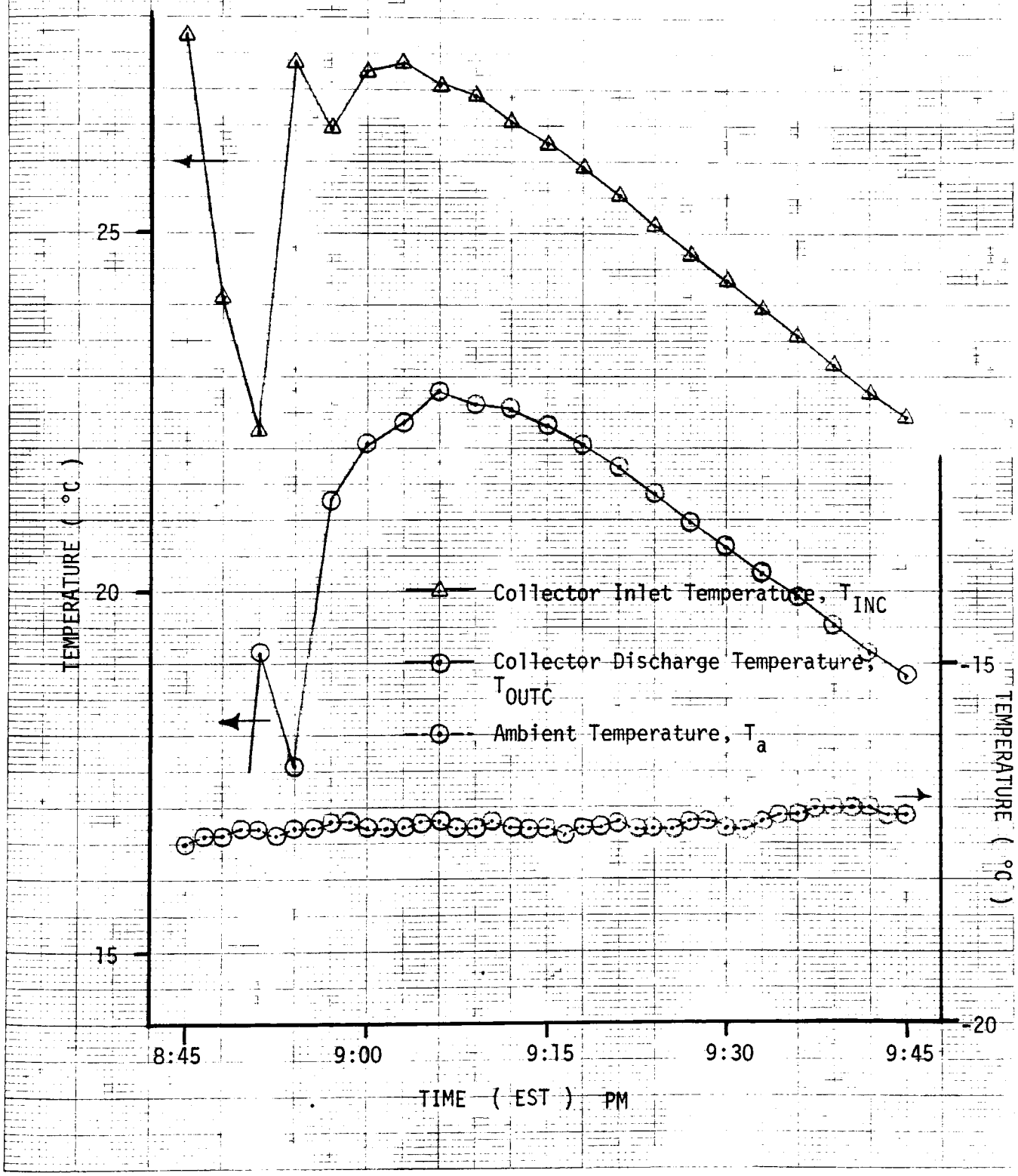

Figure 5.2 Continued

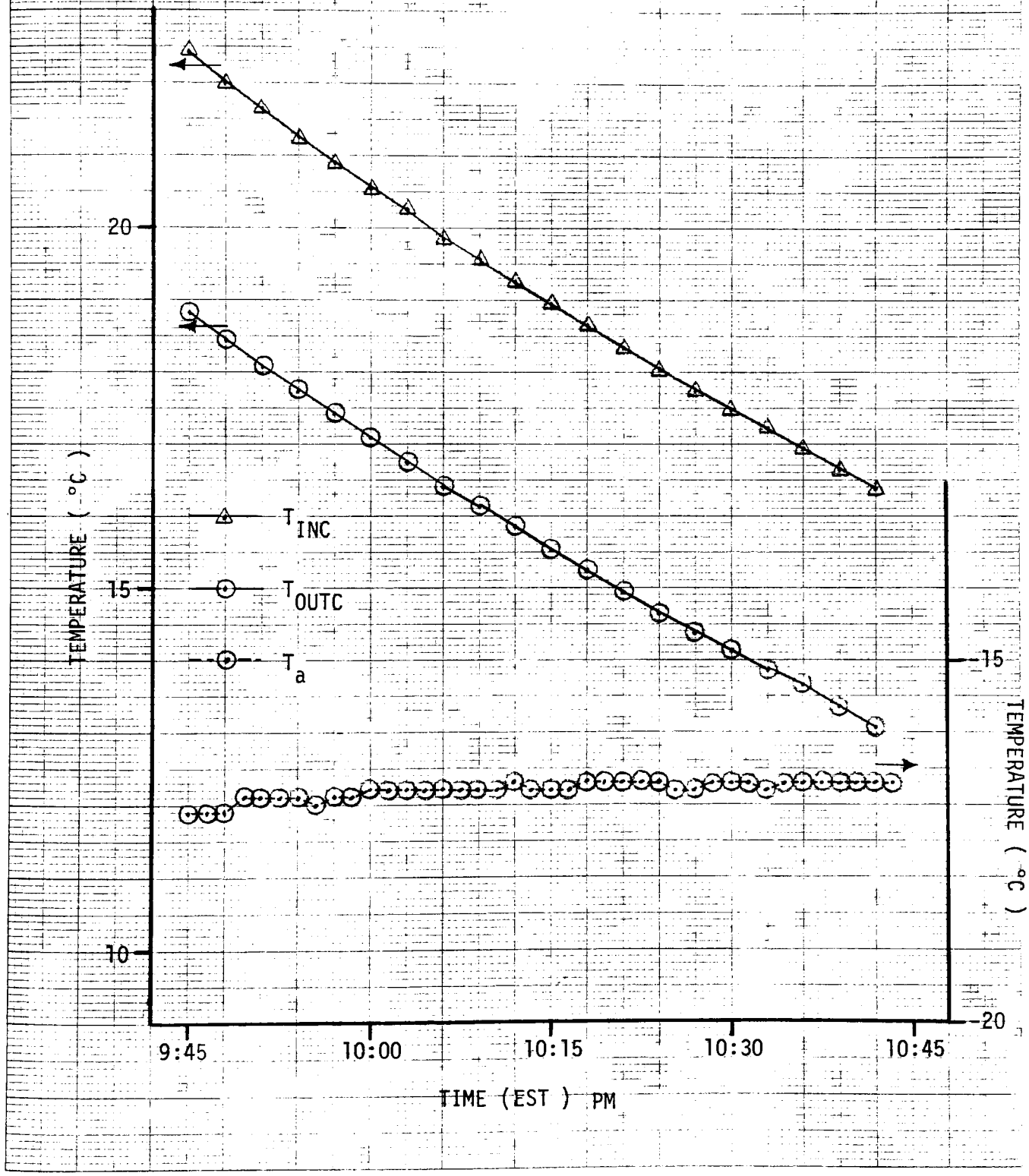

while for the winter run they are for propylene glycol antifreeze.

Time	$F_R U_L$ (W/m^2°K)	U_L (W/m^2°K)	F_R
6:45 - 7:00 pm.	19.08	23.01	0.83
7:00 - 7:15 pm.	6.09	6.42	0.95
7:15 - 7:30 pm.	5.45	5.71	0.95
7:30 - 7:45 pm.	4.98	5.20	0.96
7:21 - 7:36 pm.	5.17	5.41	0.96

Date of Test: October 1, 1979
Transfer fluid: water

Table 5.1 Date Reduction for U_L and F_R. - Run 1

Time	$F_R U_L$ (W/m^2°K)	U_L (W/m^2°K)	F_R
8:45 - 9:00 pm.	18.38	36.63	.76
9:00 - 9:15 pm.	6.78	7.16	.95
9:15 - 9:30 pm.	5.84	6.11	.96
9:45 - 10:00 pm.	5.60	5.88	.95
10:00 - 10:15 pm.	5.57	5.85	.95
10:15 - 10:30 pm.	5.55	5.84	.95
10:30 - 10:45 pm.	5.45	5.79	.95

Date of Test: February 29, 1980
Transfer Fluid: Propylene Glycol Antifreeze (Solar Winter Ban)

Table 5.1 Data Reduction for U_L and F_R - Run 2

5.1.2 Test #1 - Results

The results of both the summer and winter runs are shown in Figure 5.3. Also shown are the analytic results previously found. As can be seen in the figure, the analytical results are about 20-25% lower than the experimental results. This difference is primarily due to not considering the header losses in the analytic work previously described. While this term could be analytically defined, it appears from the experimental results that this is not necessary. From Figure 5.3, it is seen that good correlation of experimental winter data is achieved by using the same equation form as was used to describe the analytic results with only a change in the intercept. Only one point clearly does not conform to the curve. However, this is understandable in that this point represents data from 9:15 - 9:30 pm. and steady state conditions were still being established. Thus, no effort was made to further analyze these losses. Only one experimental data point is shown for summer. From Figure 5.1, steady conditions only existed for a short period of time resulting in limited data. In order to get additional data, the test would have had to be extended for a long period of time since the collector inlet temperature changed very slowly. Rather than this, an extrapolated curve fit through the point was made. This is shown in Figure 5.3.

Another smaller cause of the difference between the analytic and experimental results is that the RTD's measuring T_{INC} and T_{OUTC} were located approximately three feet from the actual inlet and outlet of the collectors. This was unavoidable as the inlet and outlet piping

Figure 5.3 Experimental Collector Loss Coefficient, U_L

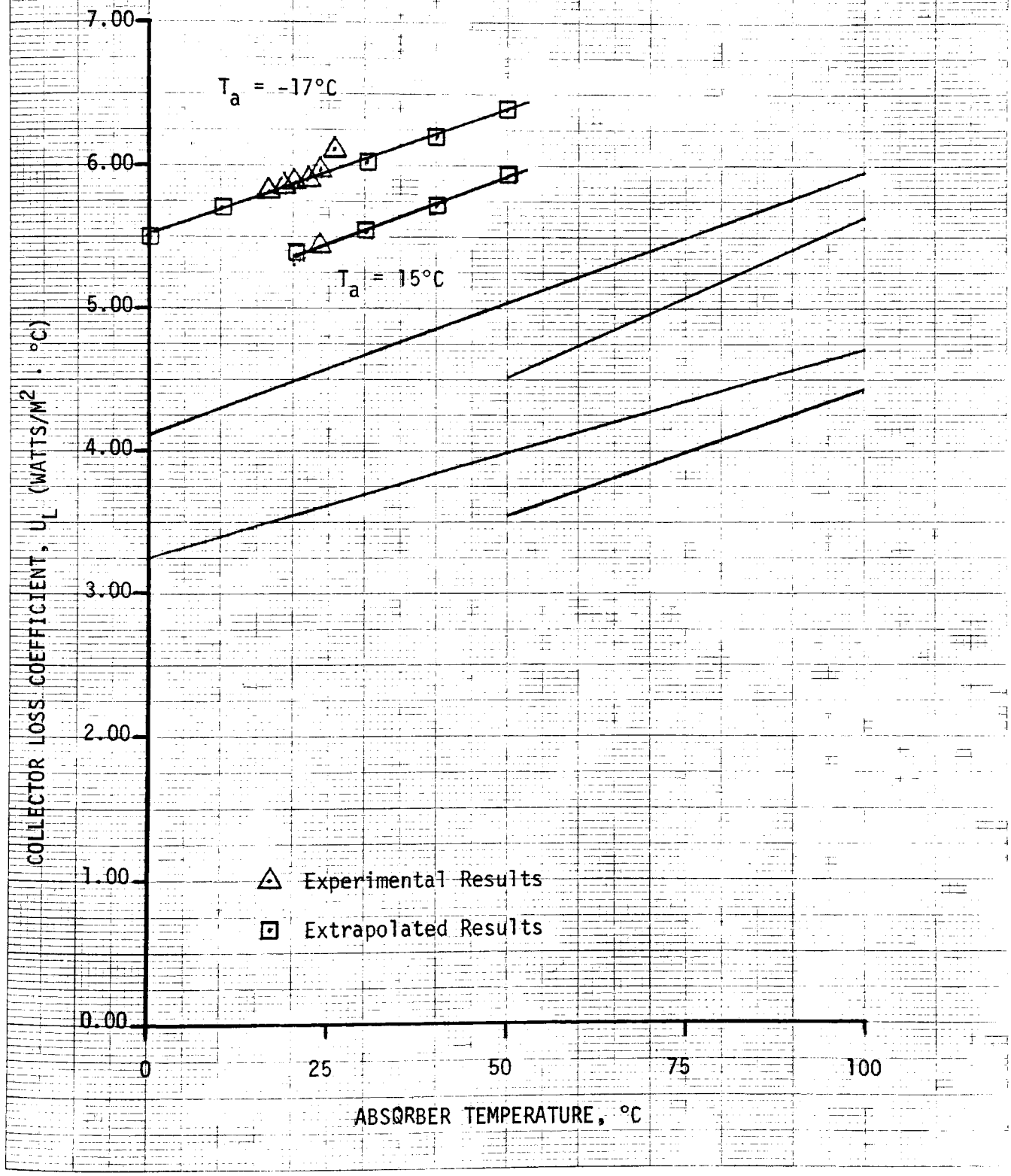

diverged and converged from one pipe to two and back to one as shown schematically in Figure 3.1. The entire three feet of pipe at the inlet and outlet of the collectors was insulated.

The heat removal factor F_R is easily found from Equation 4.27 and Figure 5.3 and is given in Section 7.1.1.

5.1.3 Test #2 - $(\tau\alpha)_e$

The effective transmittance-absorptance product can be determined from Equation 4.29 when the losses from the collector are negligible. For this case, Equation 4.29 can be rewritten as:

$$Q_u = A_t F_R (\tau\alpha)_e I_{eff} \tag{5.5}$$

or simplifying in terms of $(\tau\alpha)_e$:

$$(\tau\alpha)_e = \frac{Q_u/A_t}{F_R I_{eff}} \tag{5.6}$$

Since the collector efficiency η equals $\frac{Q_u/A_t}{I}$

and $\Gamma = \frac{I_{eff}}{I}$, the final result is:

$$(\tau\alpha)_e = \frac{\eta}{F_R\Gamma} \tag{5.7}$$

Equation 5.7 describes the behavior of the collectors when the collector inlet temperature T_{INC} is equal to T_a. While under normal operating conditions this was not the case with T_{INC} being larger than T_a, it was achieved for this test by the following procedure. First the electric resistance tank shown in Figure 3.1 was removed from the service water loop such that city water leaving the preheat tank went directly to supply. This was achieved by disconnecting the recirculation pump (Pump 2, Figure 3.1) and activating the 2-way electric water valve (V1) by the #3 controller manual override switch. City water was then allowed to flow through the preheat tank at a controlled rate by means of a globe valve located to the right of the mixing valve shown in Figure 3.1. This flow rate was adjusted during the test such that the heat removed from the heat exchanger gave rise to a collector inlet temperature equal to the outdoor ambient temperature. Again, following instrumentation procedures described in Section 3.3.1, temperatures were measured at locations T3, T4, and T6 indicated in Figure 3.14 corresponding to T_{INC}, T_{OUTC}, and T_a, respectively. Flow measurement was performed at the location shown in the same figure. In addition, the insolation rate on a tilted surface was measured by an Eppley Black and White pyranometer and recorded by a Gould 110 strip chart recorder as described in Section 3.3.3. Insolation on a horizontal surface was also measured by pyranometer but recorded by a Science Associates strip chart recorder.

The test was performed on September 27, 1979 with data being taken at 3 minute intervals between 10:45 am. and 1:00 pm. and between 2:00 pm. and 3:00 pm. Eastern Standard Time. The climatic conditions were bright sunshine except near the end of the test when some light cloudiness was experienced. The collect time vs. temperature profile is shown in Figure 5.4. Insolation values on the tilt plane of the collector integrated over 15 minute intervals are also indicated. Reduction of the data was carried out following the form of Equation 5.7. This is shown in Table 5.2. Again, this reduction was performed over 15 minute intervals. The enhancement factor Γ was calculated following the procedure outlined in Section 4.1.3.

5.1.4 Test #2 - Results

From Table 14, the average value of $(\tau\alpha)_e$ is .90. This does not include the final three time periods since unsteady conditions occurred during this time. Examination of the results shows that $(\tau\alpha)_e$ did not vary substantially during the test. This was expected since the angle between the sun's rays and the tube normal was always less than 60° during the test.

5.1.5 Test #3 - Normal Running Condition

As a final check of the parameters found in the first two tests, a third test was completed. The collectors were operated under normal conditions resulting in data that was reduced in

Figure 5.4 Collector Time Vs Temperature Profile - Experimental Calculation of $(\tau\alpha)_e$

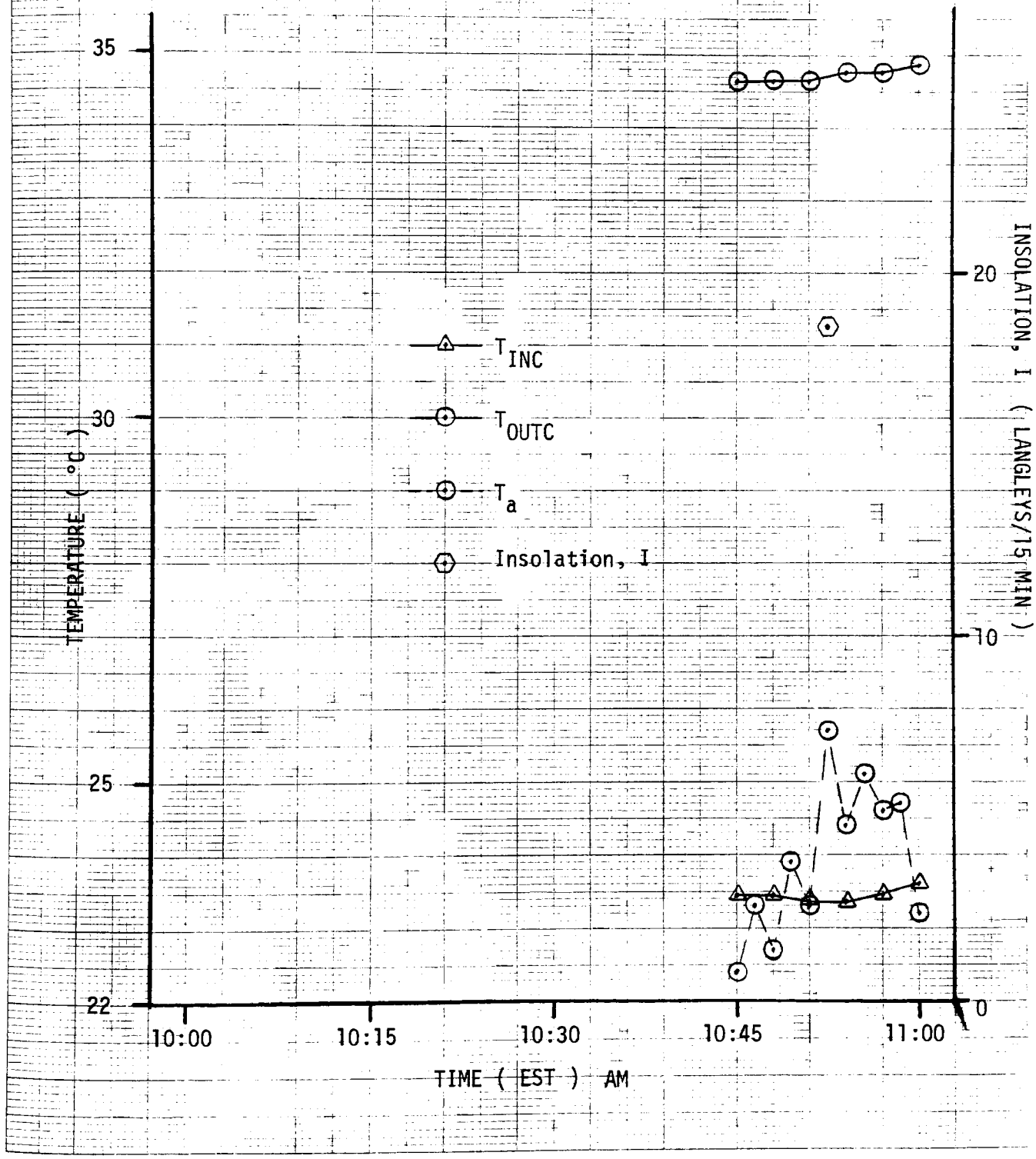

Figure 5.4 Continued

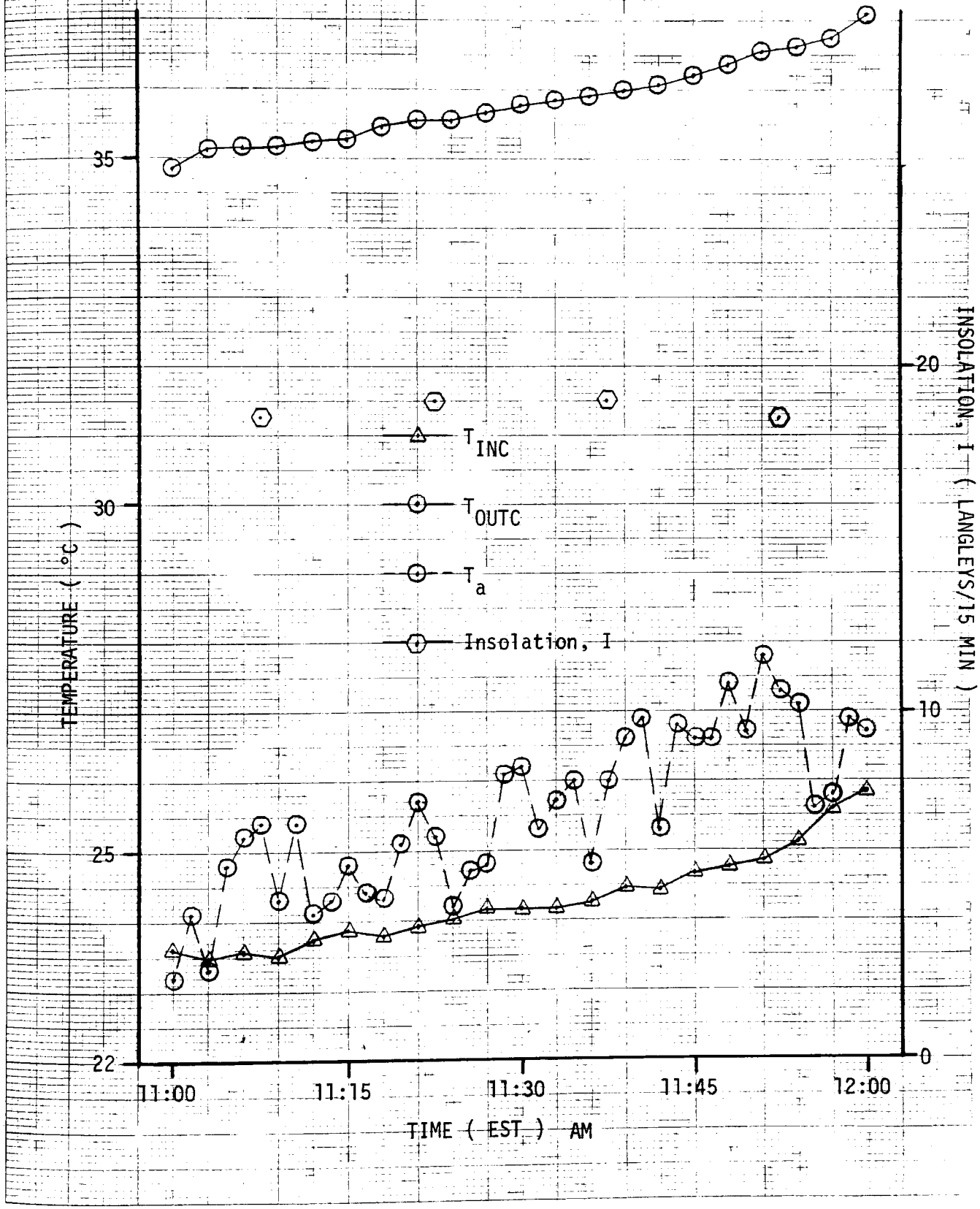

Figure 5.4 Continued

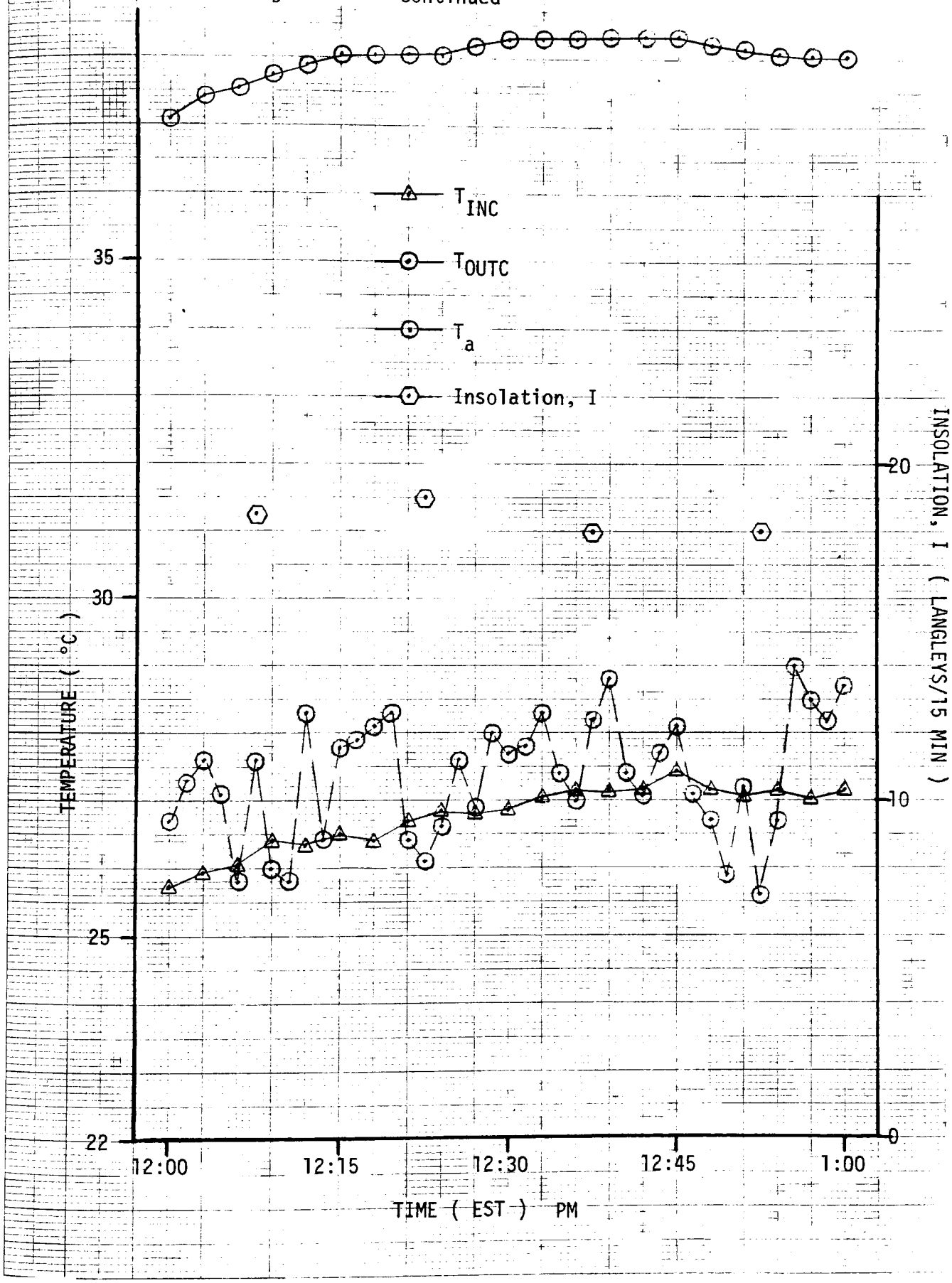

Figure 5.4 Continued

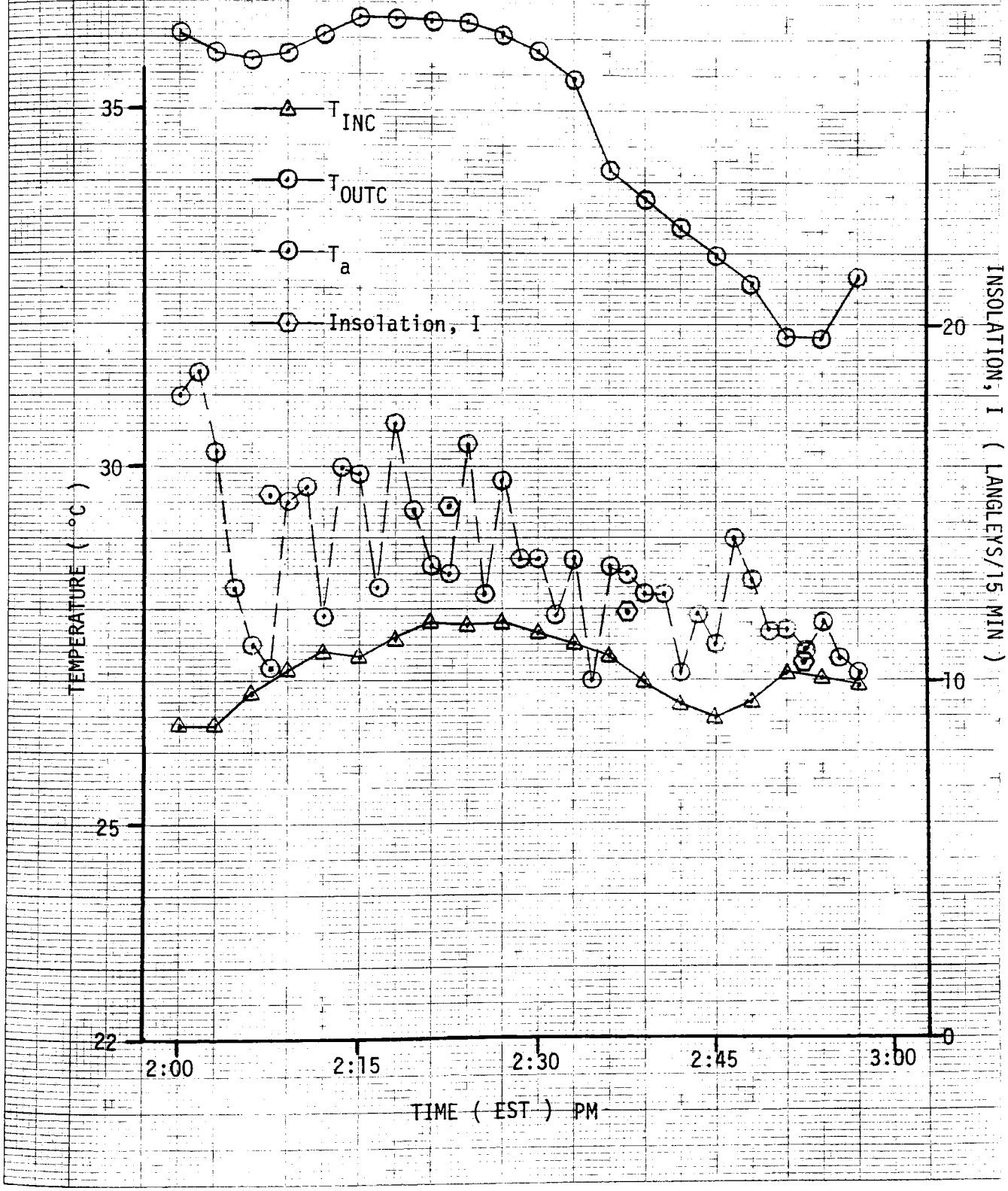

Time (EST)	$I(kJ/m^2$ 15 min)	$\eta(Q_u/A_t/I)$	$H_t(\frac{Langleys}{hr})$	Γ	F_R	$(\tau\alpha)_e$	
10:45 - 11:00 am.	760	0.62	62	0.70	0.96	0.92	
11:00 - 11:15 am.	765	0.63	68	0.70	0.96	0.94	
11:15 - 11:30 am.	780	0.62	68	0.70	0.96	0.92	
11:30 - 11:45 am.	790	0.61	68	0.70	0.96	0.90	
11:45 - 12:00 am.	795	0.60	68	0.70	0.96	0.89	
12:00 - 12:15 pm.	790	0.60	76	0.70	0.96	0.89	
12:15 - 12:30 pm.	790	0.60	76	0.70	0.96	0.89	
12:30 - 12:45 pm.	785	0.60	76	0.70	0.96	0.89	
12:45 - 1:00 pm.	780	0.59	76	0.70	0.96	0.88	
2:00 - 2:15 pm.	645	0.59	66	0.70	0.96	0.88	
2:15 - 2:30 pm.	630	0.57	66	0.70	0.96		unsteady conditions
2:30 - 2:45 pm.	500	0.60	66	0.68	0.96		
2:45 - 3:00 pm.	450	0.53	66	0.62	0.96		

Date of test: September 27, 1979
Transfer fluid: water

$(\tau\alpha)_e$ = .90 [average]

Table 5.2 Data Reduction $(\tau\alpha)_e$

accordance with Equation 4.29. The test was performed from 10:00 to 11:00 a.m. Eastern Standard Time on September 11, 1979. Data was collected in the same manner as has been previously described. Water was the transfer fluid. A time vs. temperature profile of the collector and ambient temperatures is given in Figure 5.5. Reduction of the data is shown in Table 5.3.

Results

The results of this test as well as the first two are shown plotted in Figure 5.6. The two curves were drawn as follows. First, the intercept value $F_R(\tau\alpha)_e\Gamma$ was obtained from Test #2 and plotted. It is equal to 0.60 from Table 5.2. Next, the loss coefficient for summer and winter was obtained from Figure 5.3. A value of 5.94 $W/m^2°C$ was used for winter while a value of 5.68 $W/m^2°C$ was used for summer. These values correspond to an ambient temperature of -2.2°C and 23.3°C, respectively. An absorber temperature of 40°C was used in both cases. The loss coefficients were computed by linear interpolation of the experimental results. The loss coefficient values were then multiplied by $\pi d/D$ giving the slope of the efficiency curve. The curves were then drawn through the intercept value with the proper slope. Finally, the results from test #3 were plotted. Good correlation with the summer efficiency curve is noted.

Figure 5.5. Collector Time Vs Temperature Profile - Normal Operating Conditions

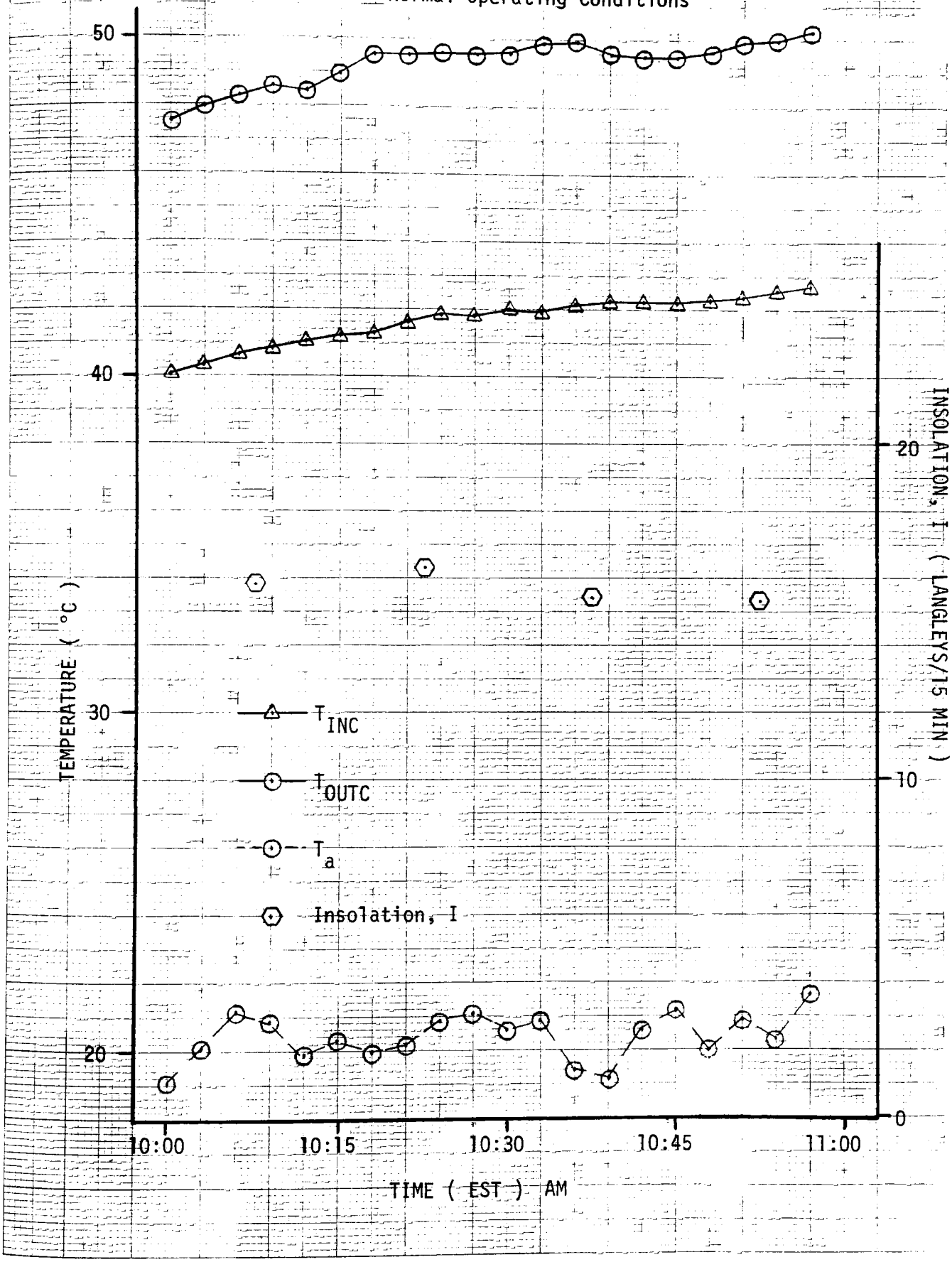

Time (EST)	$I(kJ/m^2\ 15min)$	$\eta(Q_u/A_t/I)$	$\frac{T_{INC} - T_a}{I}$ $(\frac{°C\ m^2}{W})$
10:00 - 10:15 am.	663	0.48	0.0277
10:15 - 10:30 am.	683	0.48	0.0278
10:30 - 10:45 am.	644	0.48	0.0308
10:45 - 11:00 am.	641	0.48	0.0304

Date of test: September 11, 1979

Transfer fluid: water

Table 5.3 - Data Reduction for Normal Conditions

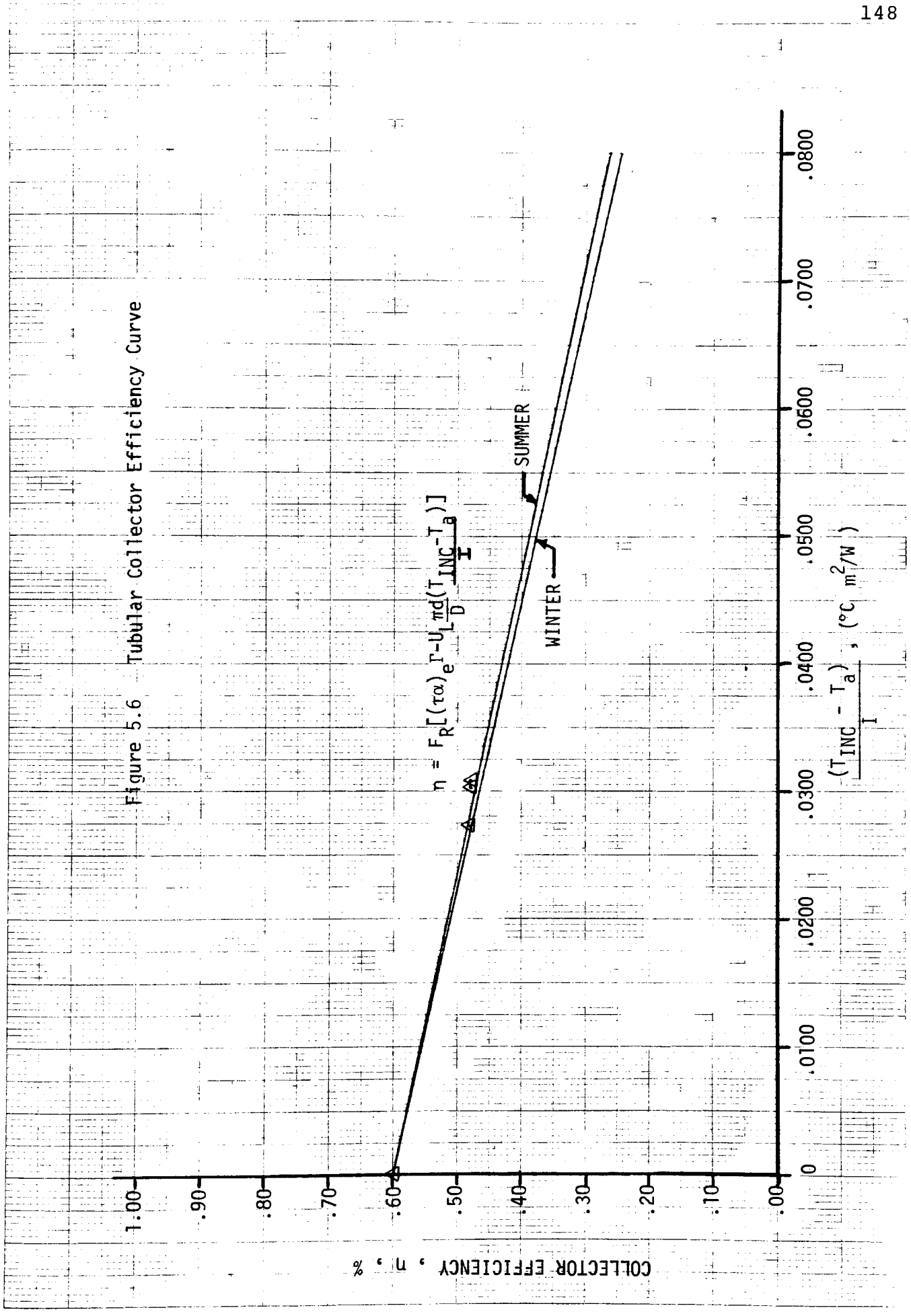
Tubular Collector Efficiency Curve
$\eta = F_R[(\tau\alpha)e^{\Gamma} - U_L\frac{\pi d}{D}(\frac{T_{INC}-T_a}{I})]$
SUMMER
WINTER
COLLECTOR EFFICIENCY , η , %
1.00
.90
.80
.70
.60
.50
.40
.30
.20
.10
.00
0
.0100
.0200
.0300
.0400
.0500
.0600
.0700
.0800
$\frac{(T_{INC} - T_a)}{I}$, (°C m^2/W)

5.2 Tank Parameters

5.2.1 Test Description

The tank loss coefficients are calculated by reducing experimental data according to Equation 5.8;

$$\frac{T_S - T_{AMB}}{T_{S,I} - T_{AMB}} = e^{-Bt} \tag{5.8}$$

where

$$B = \frac{UA}{M_S C_{p,S}}$$

Two tests were performed for both the 120 gallon preheat tank and the 40 gallon hot water tank. The first test was approximately 7 hours in length and enabled a prediction for the time constant B^{-1} to be made. Since the values of B^{-1} were found to be substantially greater than 7 hours, a second test of a much greater duration was performed. This insured that all initial nonsteady conditions were eliminated. Both tests were performed as follows. First, the two tanks were isolated from the remainder of the system. This was done by manually closing the globe valves located at the supply water pipe leaving the hot water tank and at the city water pipe entering the preheat tank. Next, the #3 controller was manually activated allowing the water to circulate between the two tanks. During this time auxiliary heat was supplied to the hot water tank thus raising the temperature of the 160 gallons of water in both tanks.

Once both tanks reached a temperature substantially above the surrounding ambient temperature, the #3 controller was manually turned off and the two tanks depressurized by bleeder valves located at the top of each tank. In addition, auxiliary heat input was eliminated. The two control thermistors labeled TMDPH1 and TMDH in Figure 3.1 were now removed from the top of each tank. These locations correspond to T8 and T9 shown in Figure 3.14. Two solid state sensors were now calibrated as indicated in Appendix 3 and then inserted into the tanks. Finally, tank temperatures were recorded by the eight channel analog recorder giving time vs. temperature data.

5.2.2 Test Results

For the preheat tank, the experimental data of test #1 is shown in Figure 5.7 while the data in reduced form is shown in Figure 5.8. In both figures, T_{IWH} corresponds to the preheat tank storage temperature which is equal to the hot water tank inlet temperature (T_{IWH}) for a nonstratified preheat tank. The data in Figure 5.8 is curve fit by the method of least squares with the time constant B^{-1} found to be 162 hours.

For the hot water tank, the corresponding experimental data is given in Figures 5.9 and 5.10. In both figures, T_{OWH} corresponds to the hot water tank storage temperature which is equal to the supply water temperature for a nonstratified hot water tank. The data is again fit by the method of least squares with the time constant equal to 74 hours.

Figure 5.7. Preheat Water Temperature Vs Time Profile - Experimental Calculation of U - Test 1

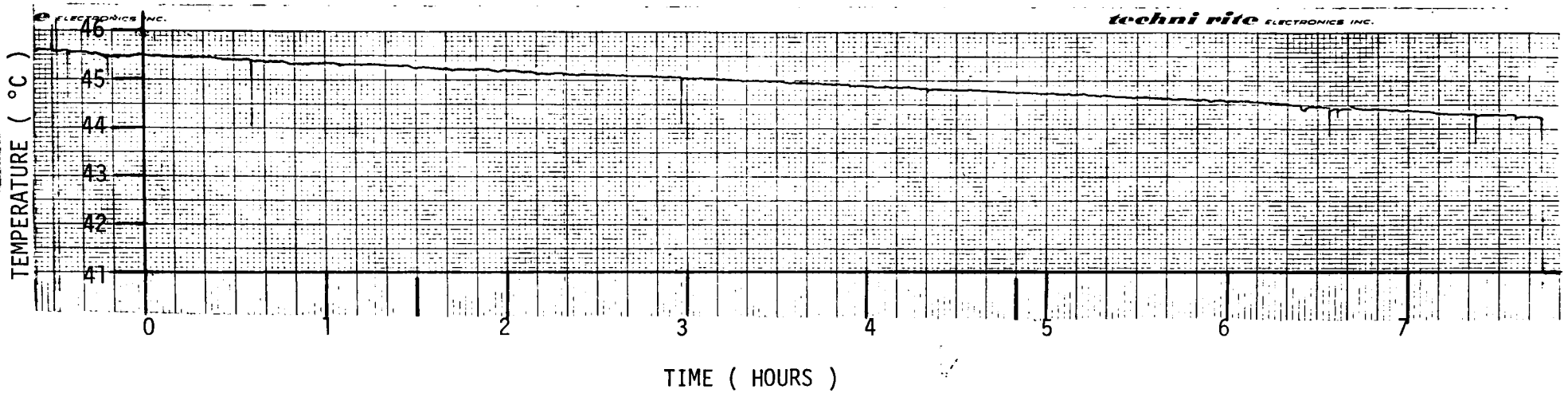

$T_{IWH,I}$ = 45.5°C
T_{AMB} = 19.4°C
T_{FINAL} = 44.24°C
TIME: 12:29 AM - 8:13 AM, 11/3/79
STRIP CHART INFORMATION: 10MV/DIV = 0.1°C/DIV
(5°C/FULL SCALE)
41°C NULLED OUT
TEMPERATURE OF TANK WATER MEASURED BY SOLID STATE DEVICE LM-134 (ADJUSTABLE CURRENT SOURCE)
AMBIENT AIR TEMPERATURE MEASURED BY MERCURY IN BULB THERMOMETER

Figure 5.8 — Reduction of Preheat Tank Data - Experimental Calculation of U - Test 1

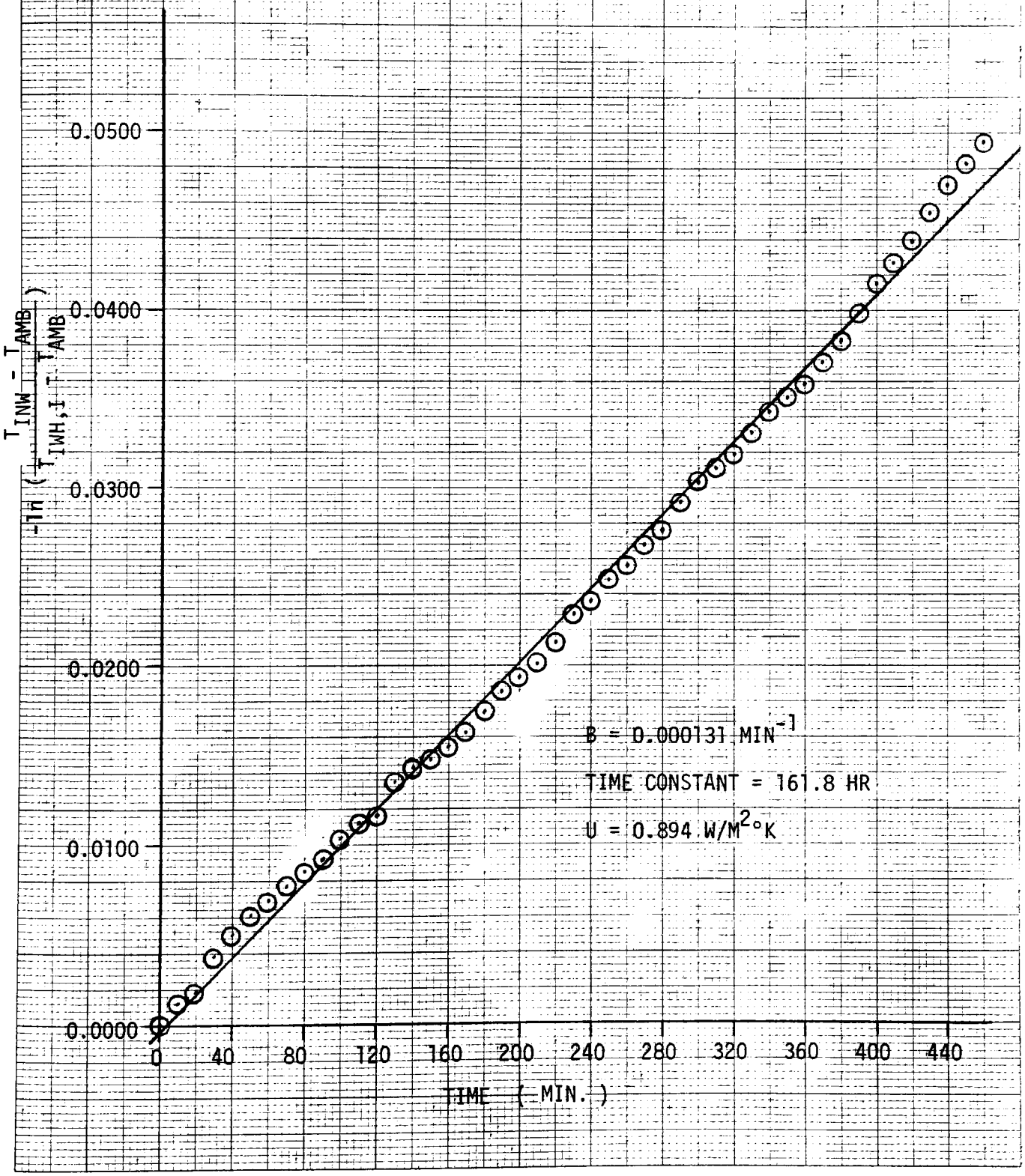

Figure 5.9 Hot Water Temperature Vs Time Profile - Experimental Calculation of U - Test 1

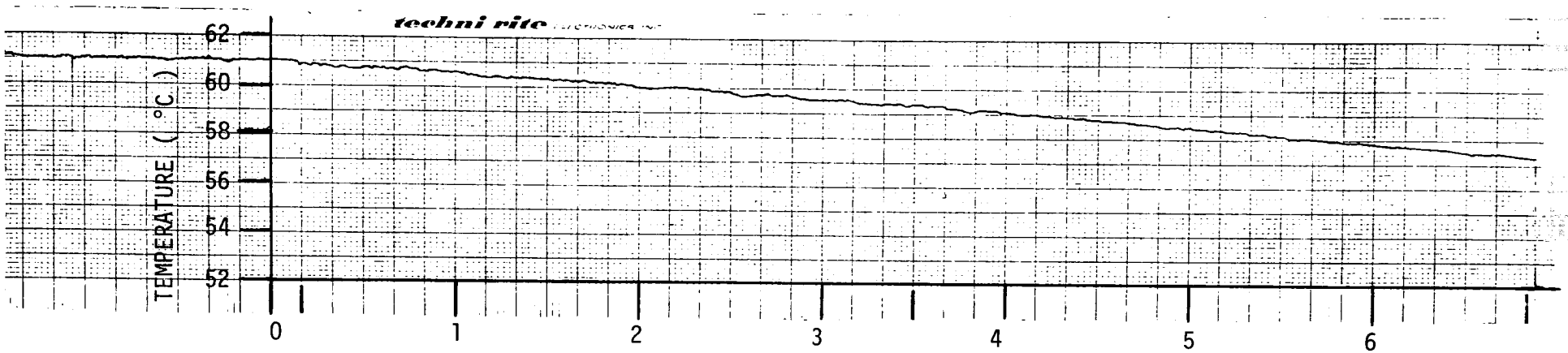

$T_{OWH,I}$ = 61°C

T_{AMB} = 19.4°C

T_{FINAL} = 57.25°C

TIME: 11:41 PM - 6:34 AM, 10/30 - 10/31/79

STRIP CHART INFORMATION: 20MV/DIV = 0.2°C/DIV

(10°C/FULL SCALE)

52°C NULLED OUT

TEMPERATURE OF TANK WATER MEASURED BY SOLID STATE DEVICE LM-134 (ADJUSTABLE CURRENT SOURCE)

AMBIENT AIR TEMPERATURE MEASURED BY MERCURY IN BULB THERMOMETER

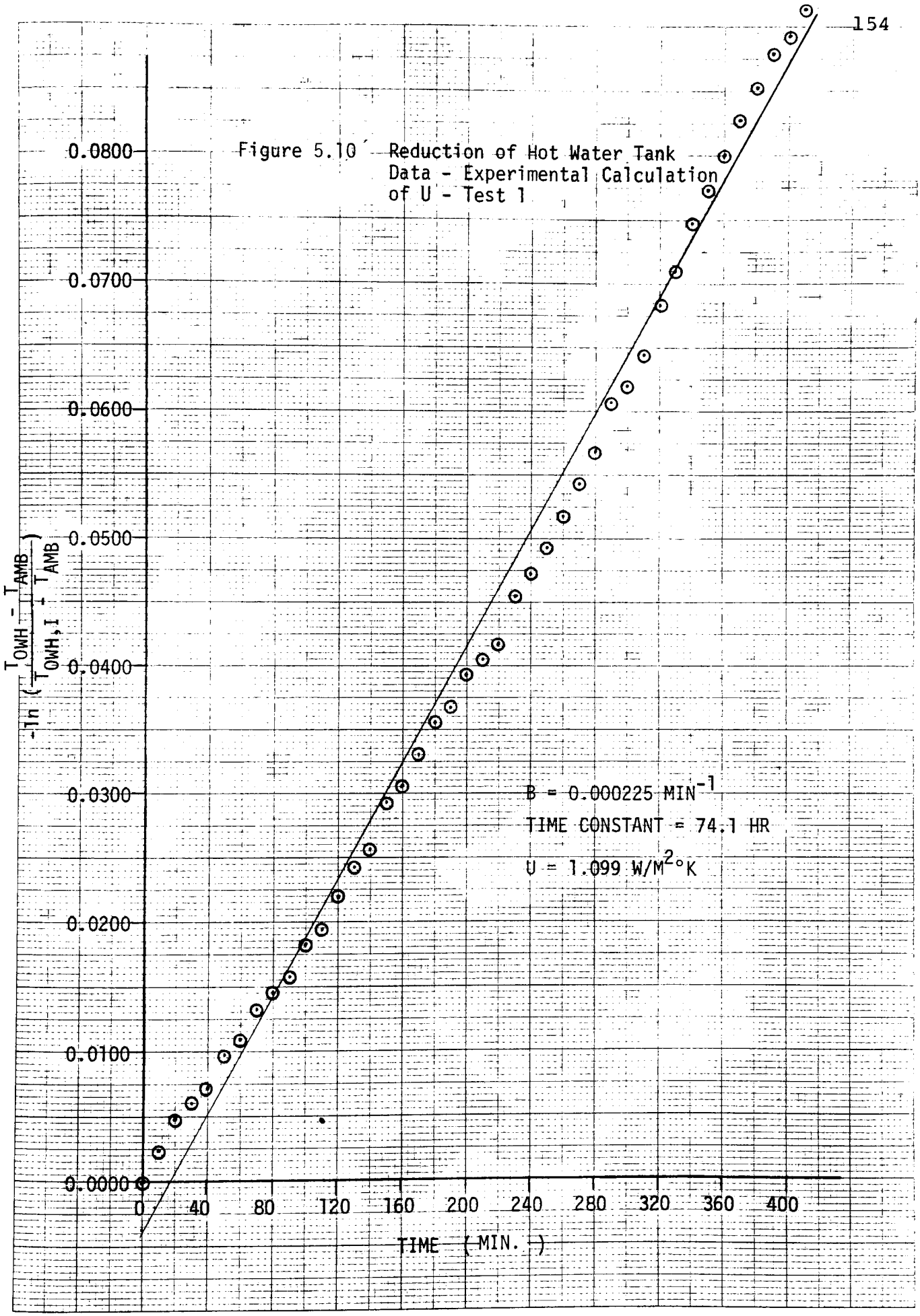

Figure 5.10 Reduction of Hot Water Tank Data - Experimental Calculation of U - Test 1

The experimental data for the preheat tank for test #2 is shown in Figure 5.11 and in reduced form in Figure 5.12. Likewise Figures 5.13 and 5.14 show the data for the hot water tank. In both cases, the experiment ran for approximately 66 hours. From test #2, the loss coefficients for each tank are found to be:

$$U \text{ preheat tank} = 1.099 \text{ W/m}^2\text{°K}$$

$$U \text{ hot water tank} = 1.157 \text{ W/m}^2\text{°K}$$

5.3 Heat Exchanger Loss Coefficient-Area Product

In order to calculate the heat exchanger loss coefficient-area product U_hA, Equation 4.161 must be evaluated. This can be done experimentally by measuring T_{OUTC}, T_{INC}, and T_{IWH} and calculating the left hand side of the equation. The quantity U_hA can then be found knowing the mass flow rate $\dot{M}$ and the specific heat C_p of the collector fluid. During test #2, which was performed in order to find $(\tau\alpha)_e$, the preheat tank temperature T_{IWH} was also measured. This was done by utilizing an RTD in location T5 shown in Figure 3.14. Results from that test give a value of $\left(T_{OUTC}-T_{INC}\right)/\left(T_{OUTC}-T_{IWH}\right)$ equal to .5. This value was calculated between 2:00 and 2:30 pm. Substituting the mass flow rate $\dot{M}$ equal to .066 kg/s and the specific heat C_p equal to 4.1793×10^3 J/kg°K into Equation 4.161 give a result for U_hA equal to 191.2 W/°K. While this result is a function of temperature, it can be shown* that for variations of $\left(T_{OUTC}-T_{INC}\right)/\left(T_{OUTC}-T_{IWH}\right)$

*See Appendix 7.

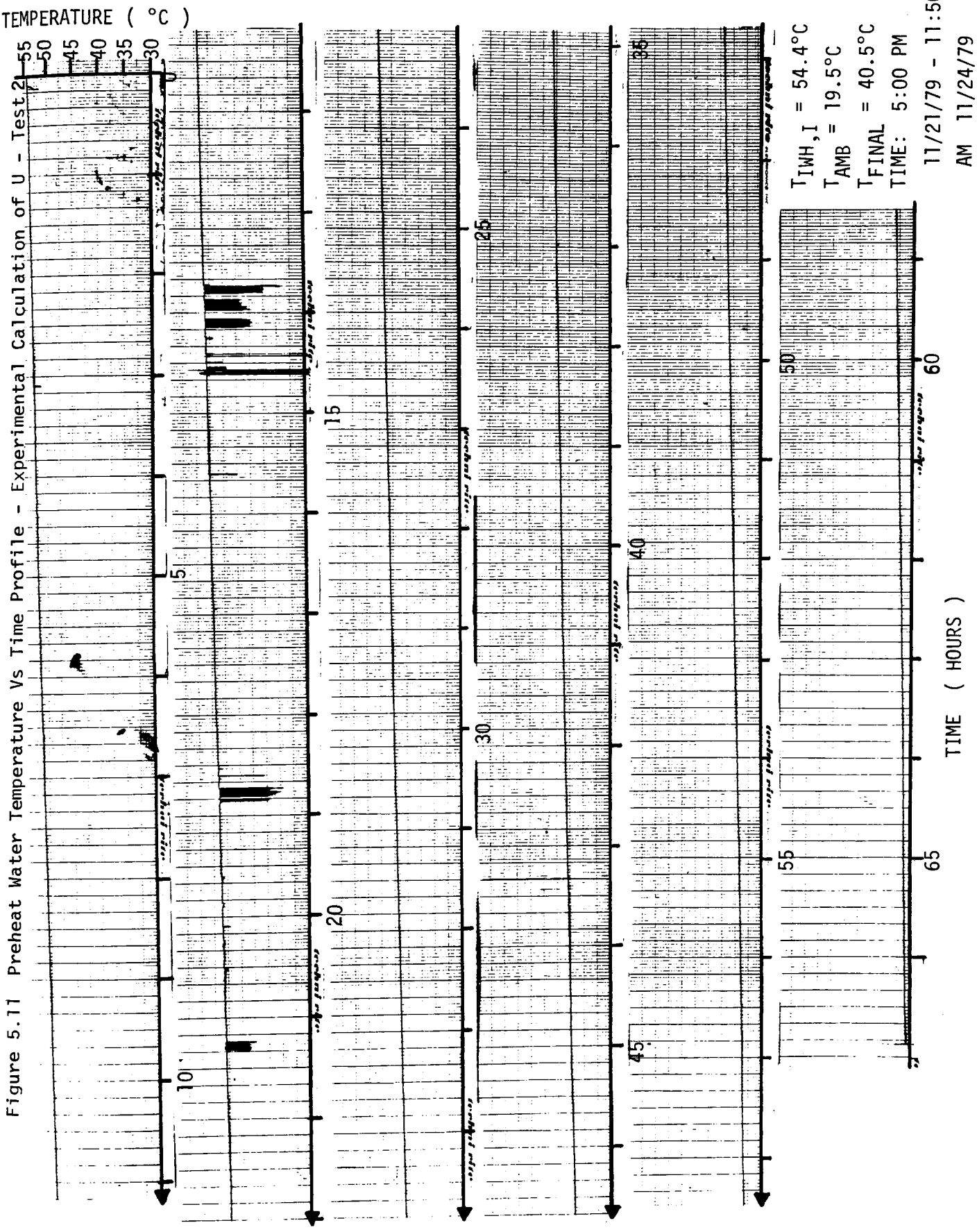

Figure 5.11 Preheat Water Temperature Vs Time Profile - Experimental Calculation of U - Test 2

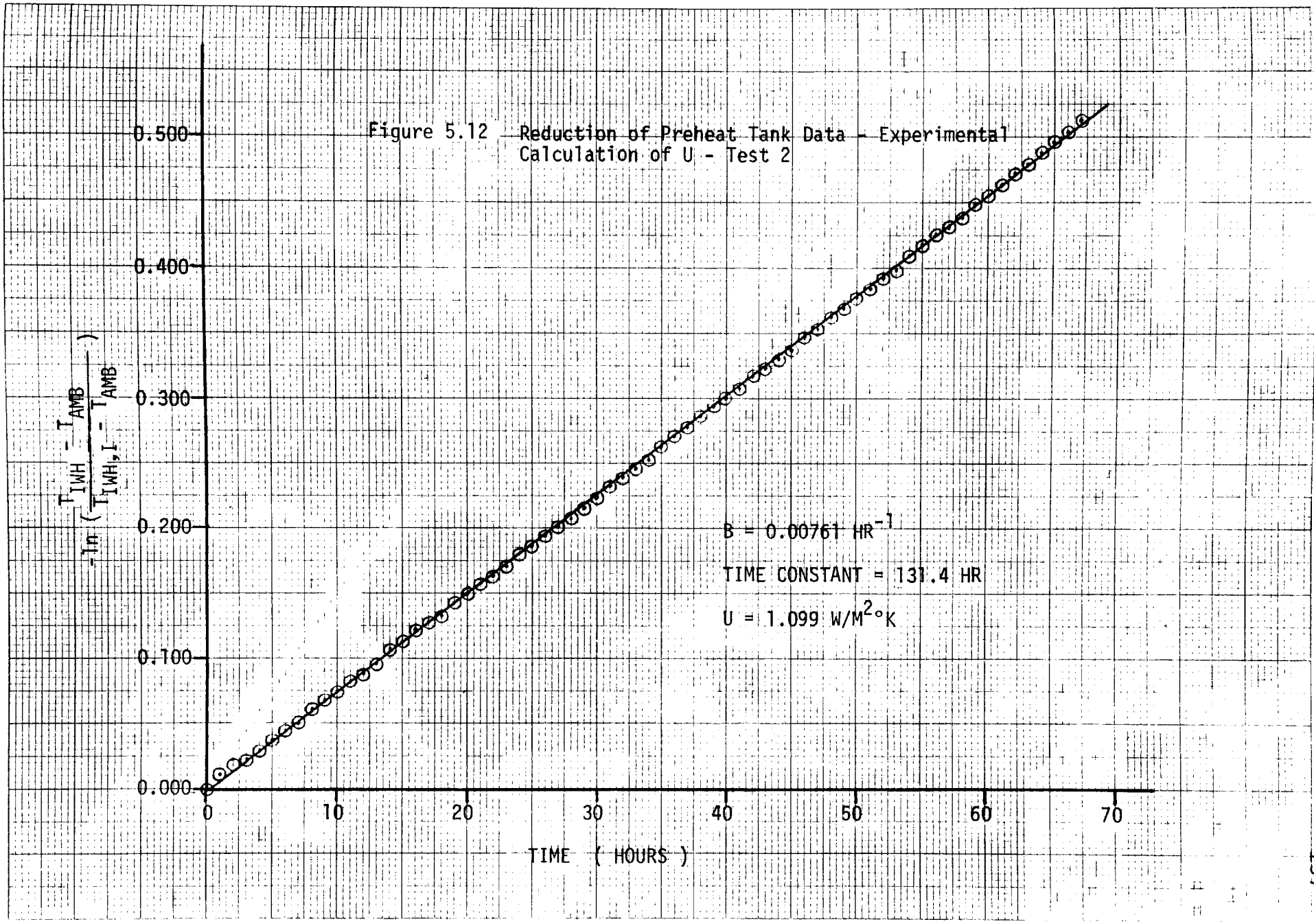

Figure 5.12 Reduction of Preheat Tank Data - Experimental Calculation of U - Test 2

Figure 5.13 Hot Water Temperature Vs Time Profile - Experimental Calculation of U - Test 2

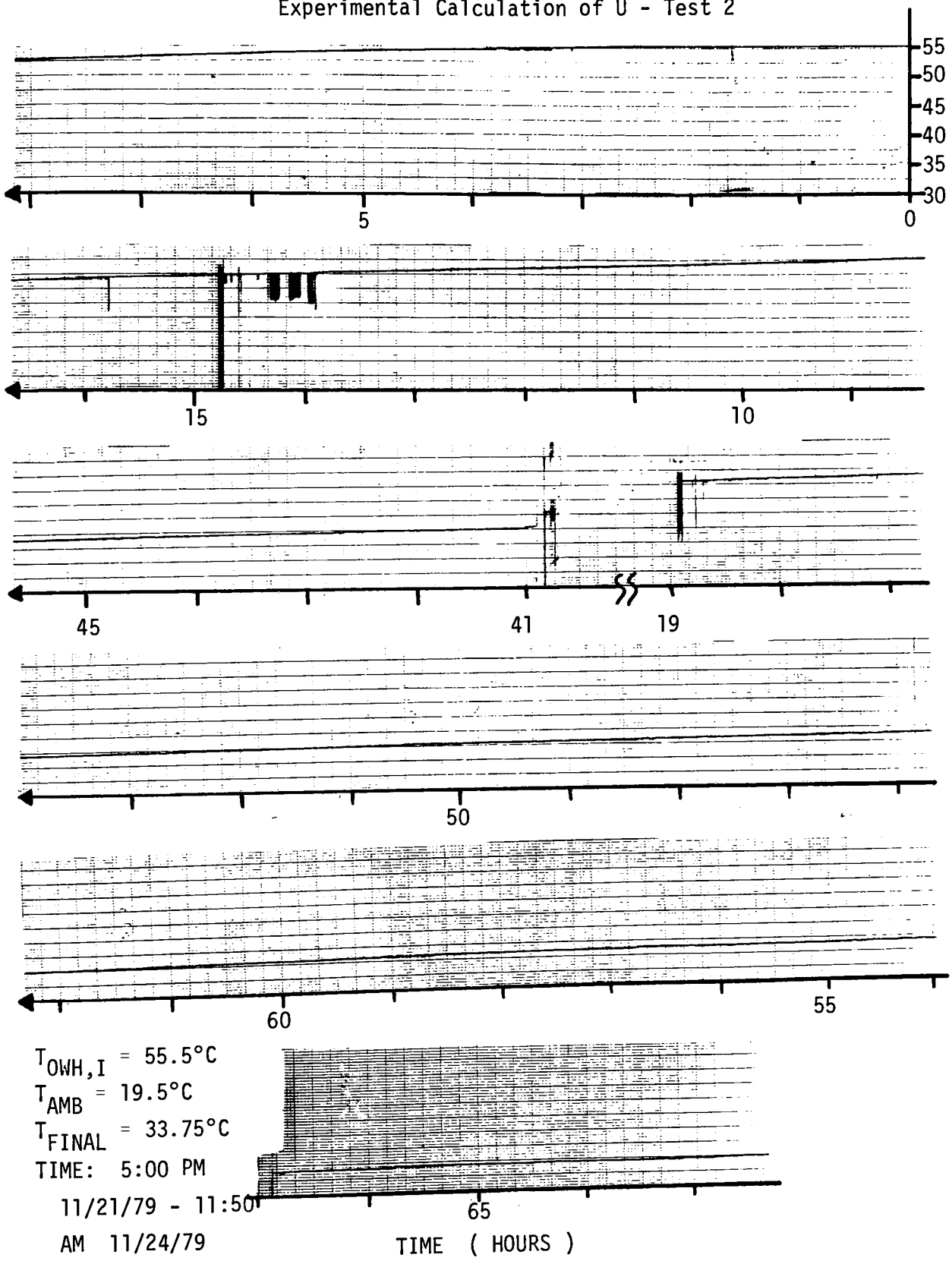

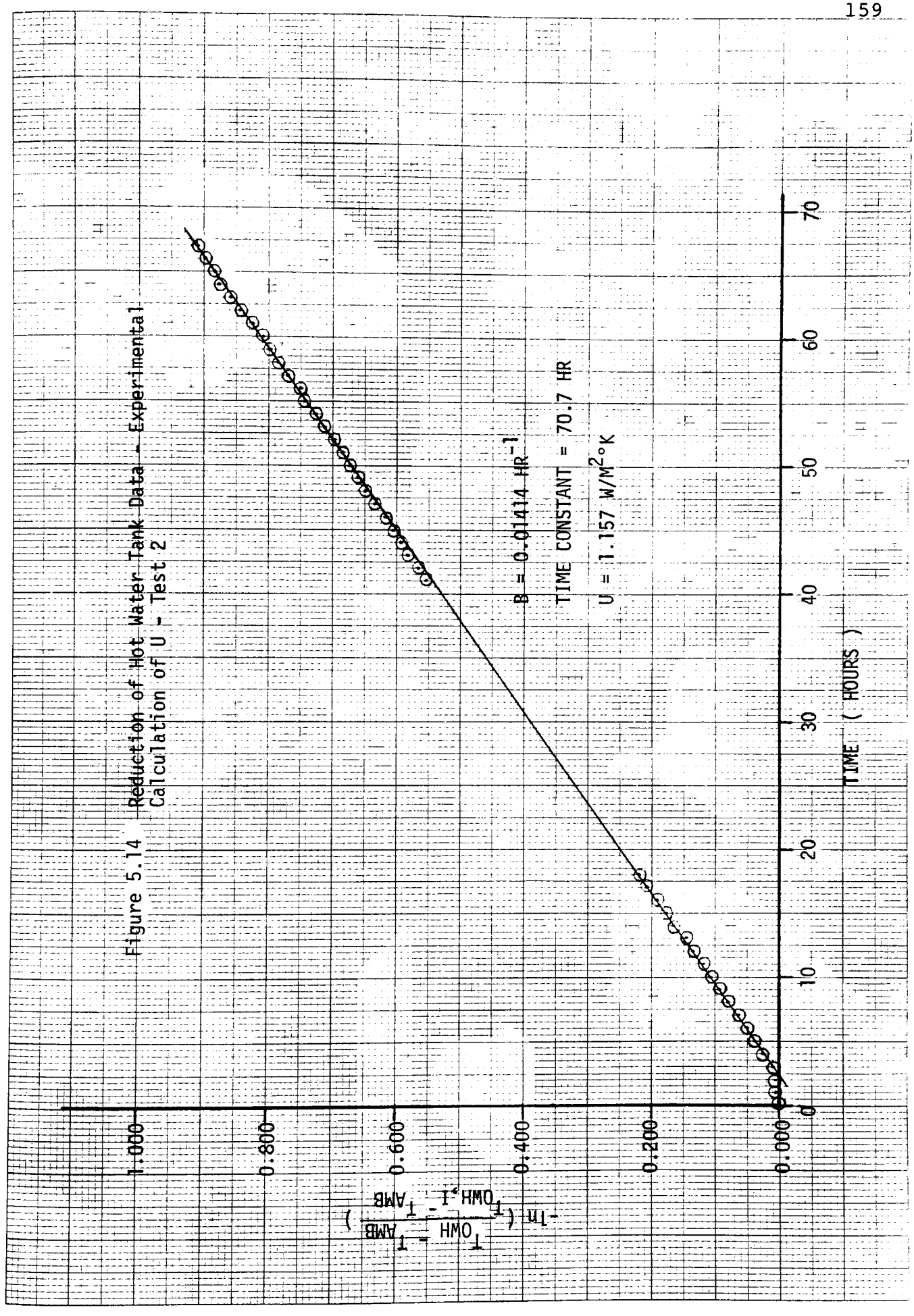
Reduction of Hot Water Tank Data - Experimental
Calculation of U - Test 2
B = 0.01414 HR⁻¹
TIME CONSTANT = 70.7 HR
U = 1.157 W/M²°K
-ln ((T_OWH - T_AMB) / (T_OWH,1 - T_AMB))
TIME (HOURS)
1.000
0.800
0.600
0.400
0.200
0.000
0
10
20
30
40
50
60
70

Figure 5.14

of between .4 and .6, the ratio of heat collected to the maximum amount collectable by the collector only varies by 8%. Since this is the case, the results given above are used in later work.

6. TRNSYS DESCRIPTION

6.1 General Description

As has been previously demonstrated (Sections 3 and 4), the domestic hot water system at RIT is modular in nature, i.e. it consists of a number of identifiable interacting components which can be either mathematically or empirically defined. This characteristic is very common to solar energy systems, hence, simulation models for these systems can be formulated by connecting models of each of the system components. This modular approach is used in the general transient system simulation program TRNSYS.

In the TRNSYS program, solar energy system components are described by individual FORTRAN subroutines. These subroutines, listed in Table 6.1, comprise a library of equipment models available to the user for system simulation. If a particular component is not available in the library, the user can supply his own. These subroutines may be fairly complex, as the case for the multinode storage tank or quite simple as is the case for a constant flow rate pump. For some hardware, analytical modeling is impractical as a mathematical model may be very difficult to develop or expensive to use in a lengthy simulation. In addition, a user may want to simulate a system that includes a particular piece of hardware for which he has measured performance data. In these cases, the component model may be empirically defined by relations obtained from curve-fitting either theoretical or measured performance characteristics. An example of such an empirical model is the TYNSYS absorption air conditioner subroutine (TYPE 7).

TABLE 6.1 - TRNSYS Library - Version 7.3

1	Collector	Uses Hottel-Whillier-Bliss equations for collector performance. Mode 1: all collector parameters are assumed constant. Mode 2: loss coefficient is calculated as function of conditions. Mode 3: cover transmission is calculated as function of angle. Mode 4: combination of Modes 2 and 3.
2	Differential Controller	Outputs 0 or 1 depending upon difference in two input signals.
3	Pump	Fixed flow rate pump (on or off).
4	Liquid Storage Tank	N-section model of liquid thermal storage tank.
5	Heat Exchanger	Counter, parallel or cross-flow heat exchanger.
6	Auxiliary Heater	On-off heater with set temperature and deadband.
7	Space Load and Air Conditioner	Simple house load calculated by energy per unit time per unit temperature difference method with built-in absorption air conditioner and cooling tower.
8	Three-Stage Room Thermostat	For use in controlling combined heating and air conditioning systems.
9	Card Reader	Reads data from cards or mass storage (usually weather data).
10	Packed Bed Energy Storage Tank	N-section model of packed bed thermal storage unit
11	Tee, Flow Mixer, Damper	Flow controllers for air or water.
12	Space Heating Load	Simple energy per unit time per unit temperature difference load, with Mode 1: parallel auxiliary. Mode 2: series auxiliary. Mode 3: no auxiliary. Mode 4: no auxiliary with thermal lag.

TABLE 6.1 - TRNSYS Library - Version 7.3 (contd.)

13	Relief Valve	"Dumps" energy to maintain temperature below specified maximum.
14	Time Dependent Forcing Functions	Permits time varying data to be introduced into simulation (usually periodic).
15	Algebraic Operations	Permits algebraic operation using Reverse Polish notation.
16	Solar Radiation Processor	Estimates beam and diffuse radiation on surface of any orientation from total radiation on horizontal surface.
17	Wall	Components that can be used to model buildings, which include the effects of thermal capacity infiltration, fenestration, etc.
18	Roof	
19	Room and Basement	
20	Heat Pump	Water or air source using manufacturer's performance data.
21	Liquid Collector-Storage Subsystem	Combined performance of a flat plat solar collector, a heat exchanger, a liquid storage tank, a relief valve, a controller and pumps.
22	Air Collector-Storage Subsystem	Analogous to TYPE 21 except a flat plate air solar collector is used.
23	Domestic Water Heating Subsystem	Common reoccuring subsystem consisting of a preheat tank that supplies solar preheated water to an auxiliary heater.
24	Integrator	Integrates any quantity with respect to time (not used to solve differential equations).
25	Printer	Prints desired information in easy-to-read format.
26	Plotter	Plots information in line printer.

6.2 System Model Construction

Once all of the components of a system are available, the next step is to construct a system information flow diagram. An information flow diagram is a schematic representation of the flow of information among the system components. Each component is represented by a box with arrows directed in and arrows directed out. Arrows directed into the box represent information required to describe the component while arrows out of the box represent information calculated by the algebraic or differential equations describing the component. This diagram is shown in Figure 6.1 for the system shown in Figure 6.2. The system represented in Figure 6.2 is analogous to that of Figure 3.1 except that the heat exchanger is modeled separate from the preheat tank. This was done since a heat exchanger within a tank was not available in the current TRNSYS library. By properly defining the heat exchanger parameters as well as the heat exchanger pump parameters, the system performance of Figure 6.2 is identical to that of Figure 3.1. More will be said concerning this in Section 7.1.3. Not included in the TRNSYS model is the recirculation portion of the system since it was seldom in operation. As is seen in Figure 6.1, each component is identified by a user given unit number and a TRNSYS specified type number. These identifiers are used in constructing the model for computer implementation. The inputs to units 11, 12, 13, and 14 are given in terms of two numbers. The first is the unit number of the component from where the information is coming and the second number is the position of the information at the output of the particular component.

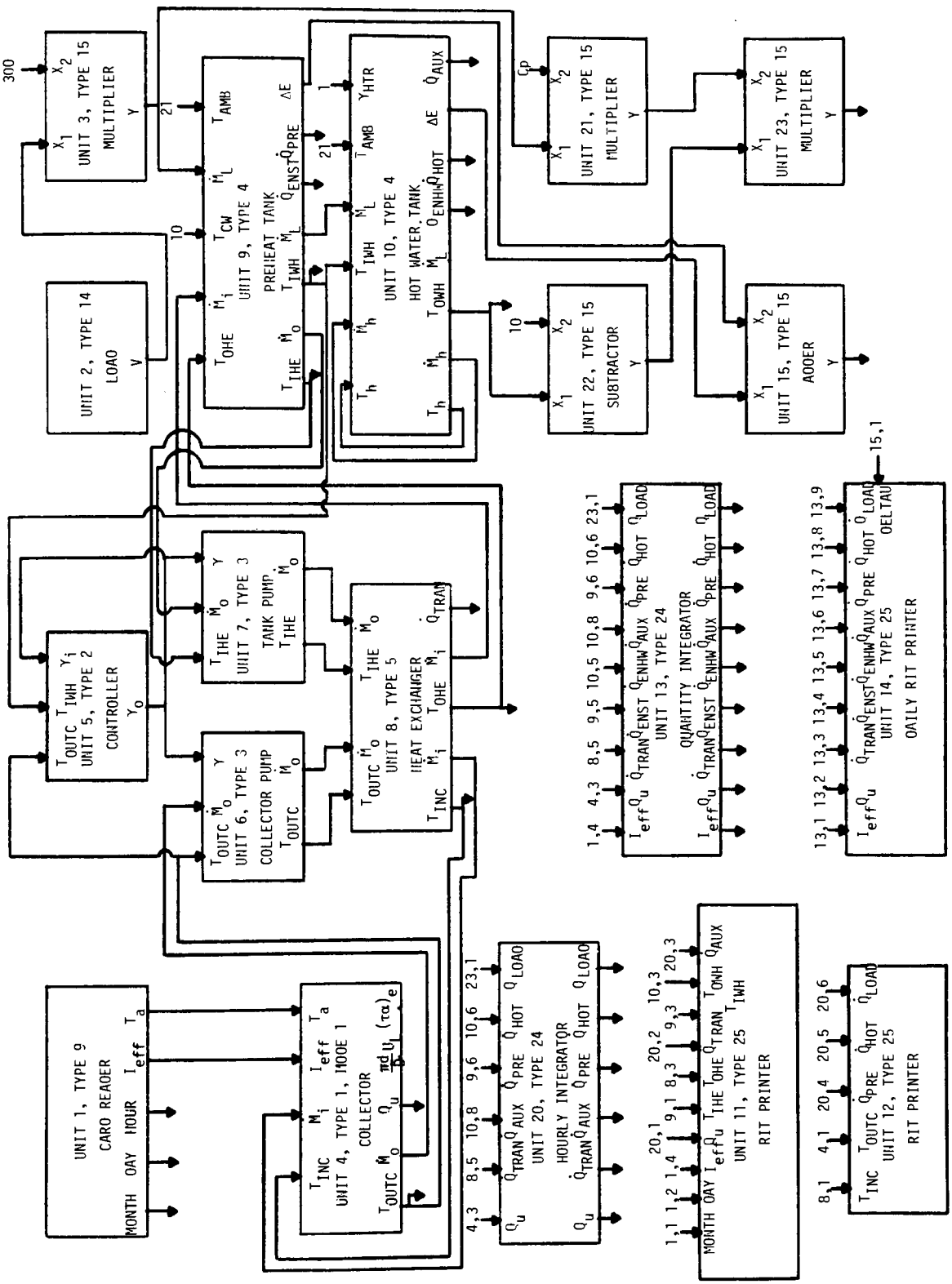

Figure 6.1 System Information Flow Diagram

Missing Page

Missing Page

Missing Page

Missing Page

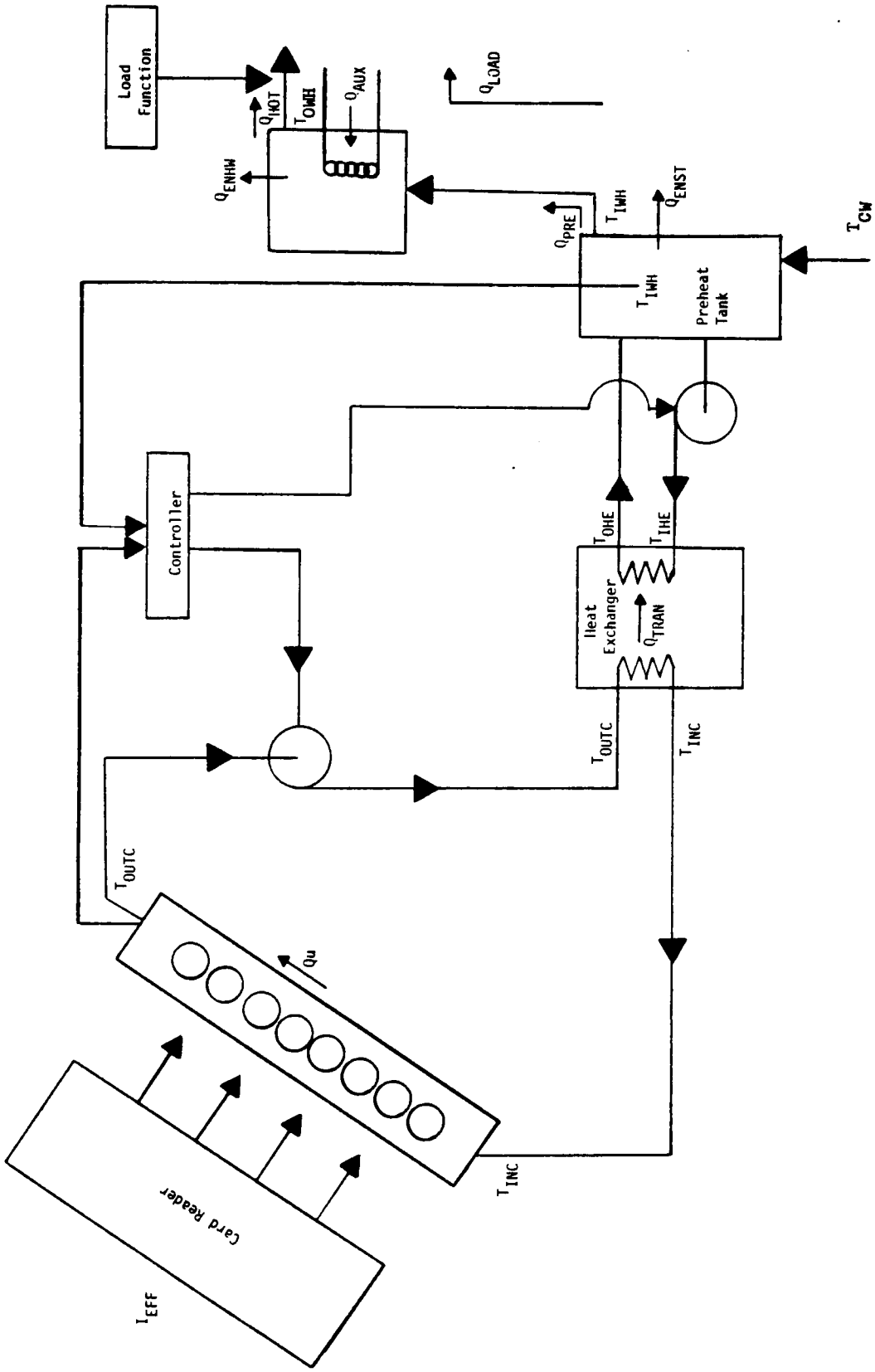

Figure 6.2 System Schematic - TRNSYS Simulation

7. OPERATION OF THE TRNSYS SYSTEM

In order to perform a computer simulation of the solar water heating system, the parameters describing the performance of the various components of the system have to be defined. In addition, the nature of the domestic hot water requirements as well as the climatological input to the system must be specified. It is the purpose of this section to give these quantities.

7.1 Parameter Definitions

7.1.1 Tubular Collector

The tubular collector performance is given by Equation 4.29:

$$Q_u = A_t F_R \left[(\tau\alpha)_e I_{eff} - U_L \frac{\pi d}{D} (T_{INC} - T_a)\right] \qquad (4.29)$$

where: A_t = total projected aperture area of the collector system, m^2

F_R = collector heat removal factor (Equation 4.27)

$(\tau\alpha)_e$ = effective transmittance-absorptance product of the collector

I_{eff} = effective insolation on the aperture tube defined on the basis of the aperture cross sectional area, kJ/m^2hr (Equation 4.34)

U_L = overall heat transfer coefficient between the absorber and surroundings, $W/m^2°C$

T_{INC} = inlet temperature of the collector, °C

Q_u = useful energy gain, kJ/hr

Since this equation is slightly different from the standard flat plate performance equation, the parameters are modified such that the flat plate equation is usable. This is done as follows.

Projected Aperture Area

For a flat plate collector, the area is the net absorber area of the collector. However, for the tubular collector, A_t is equal to:

$$A_t = (\text{No. of collectors})(\frac{40 \text{ passes}}{\text{collector}})(\frac{57 \text{ in.}}{\text{pass}})(2 \text{ in. width})$$

$$A_t = (2)\ (40)\ (57)\ (2) = 9120 \text{ in}^2 = 5.883 \text{ m}^2$$

Obviously, this does not include the area between each collector tube. Therefore, the projected aperture area for the tubular collector is less than the total panel area.

Overall Heat Transfer Coefficient

Two valves were used for U_L for the simulation corresponding to January and June climatic conditions. These valves were obtained from Figure 5.3 and as previously stated in Section 5.1.1, are equal to:

$$U_L = 5.94 \text{ W/m}^2\text{°C} \quad \text{(January - Ambient temperature of -2.2°C)}$$

$$U_L = 5.68 \text{ W/m}^2\text{°C} \quad \text{(June - Ambient temperature of 23.3°C)}$$

In order to use these valves in the computer simulation, they had to be multiplied by the quantity $\pi d/D$ seen in Equation 4.29. Performing this multiplication and putting the results in units of $kJ/HRm^2°C$ gives:

$$\frac{\pi d}{D} U_L = 4.665 \text{ W/m}^2\text{°C} = 16.795 \text{ kJ/hrm}^2\text{°C} \quad \text{(January)}$$

$$\frac{\pi d}{D} U_L = 4.461 \text{ W/m}^2\text{°C} = 16.060 \text{ kJ/hrm}^2\text{°C} \quad \text{(June)}$$

The units are used to maintain consistency in the program.

Collector Heat Removal Factor

From Equation 4.27, F_R was easily determined. Using a value of C_p of 3.446×10^3 J/kg°K for the propylene glycol antifreeze misture at 40°C and a value of the volumetric flow rate equal to 1.0 gal/min, it was found to be:

$$F_R = 0.94 \quad \text{(January)}$$

$$F_R = 0.95 \quad \text{(June)}$$

The values of C_p and the mass density for the propylene glycol antifreeze mixture were obtained from the vendor.

Effective Transmittance-Absorptance Product

The value of $(\tau\alpha)_e$ was found experimentally. Its value is .90. This result was used in both the summer and winter simulation.

7.1.2 Flat Plate Collector - Nonselective and Selective Surface

In addition to the tubular collectors, two other collector configurations were simulated. One is a flat plate collector with a nonselective surface while the second is a flat plate collector with a selective surface. The various operating parameters describing their behavior were chosen so as to correspond to readily available commercial collectors. This was done by surveying manufacturer's data for many collectors. The parameters found in this manner include the transmittance.absorptance produce ($\tau\alpha$), the collector loss coefficient U_L, and the collector efficiency factor, F'. The remaining parameters required such as the net absorber area, fluid specific heat, and fluid flow rate were chosen so as to correspond to the operating conditions for the existing system. A summary of the parameters used in the computer simulation for all three collector types is in Table 7.1.

7.1.3 Heat Exchanger

As was previously stated in Section 6.2, the heat exchanger is modeled spearate from the preheat tank since a heat exchanger within a tank is not available in the TRNSYS version used for the analysis. To insure that this representation of the heat exchanger simulates the actual system, it is necessary to insert an additional pump in the model as shown in Figure 6.2. This pump enables the fluid heated in the heat exchanger by the collector fluid to be transferred to the preheat tank. This pump as well as the collector pump is activated by the controller when the collector outlet temperature T_{OUTC} is sufficiently greater than the preheat tank water temperature T_{IWH}.

TABLE 7.1 Collector Operating Parameters

Parameter	Tubular	Flat Plate-Selective	Flat Plate-Nonselective
1. $(\tau\alpha)$	.90	.73	.76
2. τ	.95	.81	.81
3. α	.95	.90	.94
4. U_L	16.8 kJ/hrm^2°C ($U_L \frac{\pi d}{D}$ - Jan.) 16.1 kJ/hrm^2°C ($U_L \frac{\pi d}{D}$ - June)	15.8	20.4
5. F'	1.0	.95	.95
6. $\dot{M}$	246 kg/hr(A)(B)	246	246
7. C_p	3.446 kJ/kg°C(A)	3.446	3.446
8. A	5.883 m^2	6.711	6.711
9. G	41.82 kg/m^{2}hr	36.66	36.66
10. F_R	.95	.90	.88

(A) Propylene glycol antifreeze at 40°C, (B) 1.0 gpm

The heat exchanger model available is a zero capacitance sensible heat exchanger modeled in the parallel, counter, or crossflow mode, or as a constant effectiveness device which is independent of the system configuration. The constant effectiveness mode was chosen since the heat capacitance of the collector fluid during operation is essentially constant. For the heat exchanger shown in Figure 6.2, the effectiveness can be expressed as:

$$E = \frac{T_{OUTC} - T_{INC}}{T_{OUTC} - T_{IHE}} \tag{7.1}$$

However, since the preheat tank is modeled as unstratified, the heat exchanger temperature T_{IHE} is equal to the preheat tank water temperature T_{IWH} and the effectiveness can be written as:

$$E = \frac{T_{OUTC} - T_{INC}}{T_{OUTC} - T_{IWH}} = 1 - e^{-(U_h A)/(\dot{M} C_p)c} \tag{7.2}$$

from Equation 4.161. It is obvious that the effectiveness found experimentally in Section 5.3 is equal to that given by Equation 7.2. However, a value of E = .5 cannot be used directly in TRNSYS when it is remembered that this value was found experimentally for the case of water as the transfer fluid in the collector whereas normal winter operation is performed with propylene glycol antifreeze as the transfer fluid. The effectiveness is calculated for this case using the values of $U_h A$ found experimentally and the heat capacity of the propylene glycol antifreeze. When these values are substituted into Equation 7.2, the effectiveness E is found to be .56. This value was used for both summer and winter simulations since the use of water as a transfer fluid was only temporary with the propylene glycol antifreeze now used exclusively.

Two further points are of interest to note before considering the tank parameters. The first is that even though the effectiveness increases as a result of switching to a transfer fluid of propylene glycol antifreeze, the amount of heat transferred across the heat exchanger decreases for a given set of values of T_{OUTC}, T_{IWH}, and U_hA. This can be shown quite easily. For example, consider the following case.

Given:

$U_hA = 191.2\ W/°K$

$T_{OUTC} = 40°C$

$T_{IWH} = 10°C$

$(\dot{M}C_p)_c = 285.5\ W/°K$ (water at 40°C, 1 gpm)

From Equation 7.2, E = .49 and $T_{INC} = 25°C$. Also, from Equation 4.160, $Q_{TRAN} = 4{,}181\ W$. Now, if propylene glycol antifreeze is substituted for water, $(\dot{M}C_p)_c$ becomes equal to 235.5 W/°K and E = .56. The collector inlet temperature T_{INC} is now found to be 23°C and $Q_{TRAN} = 3{,}928\ W$.

The second point is that TRNSYS calculates Q_{TRAN} based on that branch of the heat exchanger which has the smallest specific heat/mass flow rate product. Thus it was important to specify the collector side specific heat as that of the propylene glycol antifreeze. Since the cold side represents water from the preheat tank, it was given a value of specific heat equal to that of water.

7.1.4 Preheat and Hot Water Tank

Several parameters are required by TRNSYS for the mathematical model of the preheat and hot water tank. These include the following:

1. tank volume
2. tank height
3. specific heat of fluid
4. fluid density
5. loss coefficient between tank and environment
6. ambient temperature of surrounding air.

In addition, the auxiliary energy input and setpoint temperature of the thermostat is required for the hot water tank. The values used for these parameters are given in Table 7.2. The loss coefficients used are one-half those as found in Section 5.2 and represent the existing tanks with 2 inches of additional insulation.

7.2 Load Requirements

As is shown in Figure 6.1, the domestic hot water demand is modeled by use of a type 14 time depend forcing function. This routine allows periodic time varying data (in this case, load requirements) to be introduced into the simulation. Although domestic hot water demand is subject to a high degree of variation from day to day and from house to house, it is impractical to use anything but a repetitive daily profile in a simulation. Inputed by use of this routine is a normalized daily mass flow rate

TABLE 7.2 - Tank Parameters

		Preheat Tank	Hot Water Tank
1.	Volume, (m^3)	.454	.151
2.	Height, (m)	1.626	1.181
3.	Fluid Specific Heat, (kJ/kg°C)	4.178**	4.178**
4.	Fluid Density, (kg/m^3)	994.6**	994.6**
5.	Tank Loss Coefficient, U ($kJ/hrm^2°C$)	1.978***	2.082***
6.	Surrounding Air Temperature T_{AMB}(°C)	69.8	69.8
7.	Auxiliary Energy Input,	-	16,200*
8.	Thermostat Setpoint Temperature, (°C)	-	60*

* See Section 3.1

** Water Temperature of 40°C

*** Corresponds to existing tanks with 2" of added insulation.

profile developed by a Rand Corporation Survey for a "typical residence (Figure 7.1) [30]. Then by multiplying this normalized daily mass flow rate profile by the total daily demand, instantaneous values of hot water are obtained. The data was input in this manner to allow flexibility in the magnitude of hot water demand. In this work, a total daily demand of 300 kg was used. This corresponds to approximately 20 gallons per day per person for a family of four.

7.3 Climatological Input Data

Climatological data is input to the simulation by use of the card reader shown in Figures 6.1 and 6.2. As in indicated in

Figure 7.1 Daily Normalized Mass Flow Rate Profile
Type 14 Time Dependent Forcing Function

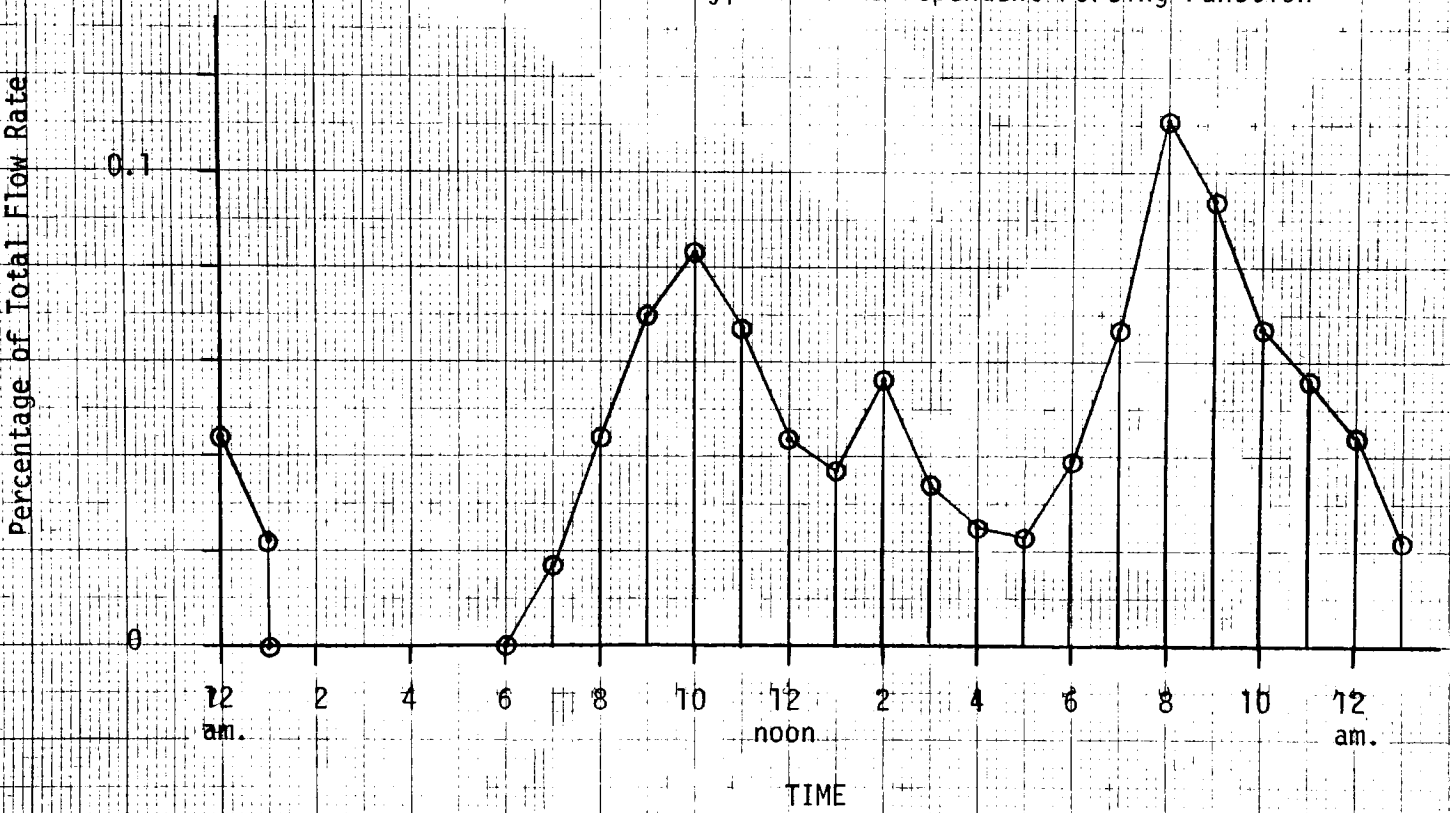

Figure 6.1, input data required includes month, day, hour, insolation on a tilted surface, and outside ambient temperature. Insolation data for the simulations performed was taken from the results of three years of data acquisition from the pyranometers mounted on the RIT Engineering building. In order to avoid inputing three years of data on an hour by hour basis, an alternate method was employed. Two simulations were performed for each collector configuration; one using June insolation data and the other using January insolation data. The data used for June and January were for those months of the three years available that most closely matched the three year average; averages in this context meaning monthly daily averages. The results of the two simulations were then averaged to give an average yearly performance efficiency which is defined as the percentage of domestic hot water load being met by solar energy. For January, data from 1978 was used while for June, data from 1977 was used. Since simulations were performed using both flat plate and tubular collectors, two sets of insolation data had to be input. The first was for the flat plate simulation and represented insolation data as measured by the tilted pyranometer. The second was for the tubular collector simulation and hence required an input of the effective insolation, I_{eff} as given by Equation 4.34. This data was obtained following the procedure given in Section 4.1.3. Finally, the outside ambient temperature data was obtained from the Rochester National Weather Service office for the two months. This data is directly input to the program and represents three hour averages. A listing of a portion of the climatological data is given in Figure 7.2. This data shown is

modified for use in a tubular collector simulation. Each column represents, from left to right respectively: month, day, hour, effective insolation, and outside ambient temperature.

Month	Day	Hour	I_{eff}	T_a
1.0	18.0	1.0	.0	25.0
1.0	18.0	2.0	.0	25.0
1.0	18.0	3.0	.0	25.0
1.0	18.0	4.0	.0	25.0
1.0	18.0	5.0	.0	25.0
1.0	18.0	6.0	.0	23.0
1.0	18.0	7.0	.0	23.0
1.0	18.0	8.0	1.6	23.0
1.0	18.0	9.0	4.5	24.0
1.0	18.0	10.0	7.2	24.0
1.0	18.0	11.0	9.9	24.0
1.0	18.0	12.0	10.8	24.0
1.0	18.0	13.0	8.1	24.0
1.0	18.0	14.0	5.6	24.0
1.0	18.0	15.0	2.4	24.0
1.0	18.0	16.0	.5	24.0
1.0	18.0	17.0	.0	24.0
1.0	18.0	18.0	.0	24.0
1.0	18.0	19.0	.0	24.0
1.0	18.0	20.0	.0	24.0
1.0	18.0	21.0	.0	23.0
1.0	18.0	22.0	.0	23.0
1.0	18.0	23.0	.0	23.0
1.0	19.0	24.0	.0	23.0
1.0	19.0	1.0	.0	23.0
1.0	19.0	2.0	.0	23.0
1.0	19.0	3.0	.0	22.0
1.0	19.0	4.0	.0	22.0
1.0	19.0	5.0	.0	22.0
1.0	19.0	6.0	.0	21.0
1.0	19.0	7.0	.0	21.0
1.0	19.0	8.0	2.4	21.0
1.0	19.0	9.0	5.4	23.0
1.0	19.0	10.0	12.5	23.0
1.0	19.0	11.0	11.1	23.0
1.0	19.0	12.0	11.4	26.6
1.0	19.0	13.0	8.7	26.0
1.0	19.0	14.0	5.4	26.0
1.0	19.0	15.0	1.9	28.0
1.0	19.0	16.0	.5	28.0
1.0	19.0	17.0	.0	28.0
1.0	19.0	18.0	.0	26.0
1.0	19.0	19.0	.0	28.0
1.0	19.0	20.0	.0	28.0
1.0	19.0	21.0	.0	26.0
1.0	19.0	22.0	.0	26.0
1.0	19.0	23.0	.0	26.0
1.0	20.0	24.0	.0	25.0

Figure 7.2 January Climatological Data (Day 18 and 19)

8. ECONOMIC ANALYSIS

In order to determine the feasibility of solar energy domestic hot water systems today, they must be examined from an economic standpoint. While it is clearly evident that these systems work in the scientific sense, it is not clearly apparent if they are economically competitive with the various conventional alternatives. The purpose of this section is to present an approach currently used [31] to perform this analysis. Actual application of the technique is performed in Section 9.

8.1 Economics of Solar Energy Heating

The most commonly accepted method used today to evaluate solar energy systems is known as the life cycle cost method. In this method all future costs are reduced to the common basis of present worth, that is, the amount of money that would have to be invested today to insure that the necessary funds are available in the future to meet all of the expenses. Included in these expenses besides fuel costs are mortgage payments for the equipment, property taxes, income taxes, and insurance and maintenance costs. The present worth of the costs of each alternative, both solar and nonsolar, would be determined and that alternative which has the lowest present worth cost would be selected. The cash flows of each alternative must be discounted since money has a time value due to inflation and a market discount rate which is defined as the after tax return on the best alternative investment.

While in the most general case each alternative would be evaluated in the manner described above, it is obvious that this need not be done. A simpler approach which would generate the same information (i.e. which system is most economical) is based on the concept of solar savings. Clearly stated, it is only necessary to evaluate costs that are not common to both the solar and nonsolar system. For instance, in both a solar and nonsolar domestic hot water system, a hot water tank as well as a good portion of the service water plumbing is common to both systems. In this case, the present worth of the costs involved with these components would be the same for each system and would cancel each other out in a comparison. In equation form, the solar savings are [31]:

$$\begin{aligned}\text{Solar savings} = {} & \text{Fuel savings} - \text{Extra mortgage payment} - \\ & \text{Extra insurance} - \text{Extra maintenance} - \\ & \text{Extra property tax} - \text{Operating cost} + \\ & \text{Tax savings}\end{aligned} \tag{8.1}$$

The income tax savings for a residence are:

$$\begin{aligned}\text{Tax savings} = {} & \text{Tax rate} \times [\text{Extra interest} + \text{Extra property tax}] \\ & + \text{Tax credits}\end{aligned} \tag{8.2}$$

In order to evaluate Equations (8.1) and (8.2), it is first necessary to be able to predict future costs in any particular year. Two situations can occur. First, costs may be anticipated to change in a regular manner through the period of the analysis. The most

common assumption is that the costs of Equations (8.1) and (8.2) inflate or deflate at a fixed rate per year. This situation gives rise to simplified inflation-discount functions which facilitate the various calculations by eliminating detailed year by year calculations. Second, the costs may vary in an irregular manner in which case the calculations have to be performed on a year by year basis and then discounted back to the present. If, however, these costs are not too irregular, then simplified methods can be applied.

If the costs are regularly varying, then Equations (8.1) and (8.2) can be written symbolically in one equation as:

$$C_T = FLc_f \left(\frac{E_f}{\eta_f} - E_o\right) - (AC_{ca}+C_{ci}) \left\{E_{mp} + E_{in} + E_m + E_{pt}\right\}$$

$$+ (AC_{ca} + C_{ci})(t) \left\{E_{\ell i} + E_{pt}\right\} + (AC_{ca} + C_{ci})(t_c) \qquad (8.3)$$

where:

- A is the collector area, m^2
- C_{ca} is the solar system area dependent cost per unit collector area, $\$/m^2$
- C_{ci} is the solar system area independent cost, \$
- C_T is the solar savings of the particular system under study for the life of the system.
- c_f is the first year fuel cost per unit of delivered heat, \$/GJ

E_f is an economic factor which accounts for fuel inflation rate and market discount rate

E_{in} is an economic factor which accounts for insurance rate and market discount rate

$E_{\ell i}$ is an economic factor which accounts for mortgage interest rate and market discount rate

E_m is an economic factor which accounts for inflation rate of maintenance cost and market discount rate

E_{mp} is an economic factor which accounts for downpayment, mortgage interest rate, and market discount rate

E_o is an economic factor which accounts for inflation rate of operating cost and market discount rate

E_{pt} is an economic factor which accounts for property tax rate and market discount rate

F is the fraction of annual heat load provided by the solar system

L is the annual heating load of the building or domestic hot water heater including hot water tank losses, GJ/year

t is the effective income tax rate of the owner

t_c is the tax credit rate available

η_f is the efficiency of the solar backup furnace

The economic factor E_f is the sum of annual compounded inflation factors discounted annually to present worth. The present worth of the sum of an annuity over a lifetime of N years, inflated at a constant rate and discounted at a constant rate, can be written as:

$$P/X\ (N,\ i,\ d) = \frac{(1+d)^N - (1+i)^N}{(1+d)^N\ (d-i)} \qquad \text{for } d \neq i \qquad (8.4)$$

and

$$P/X\ (N, i, d) = N/(1+i) \qquad \text{for } d = i \tag{8.5}$$

where:

P is the present value of an annuity over N years

X is the first year cost

d is the discount rate

i is the general inflation rate

N is the years of analysis or life of the system

The notation (N, i, d) after P/X indicates that the value of P/X refers to values of N, i, and d, placed in the appropriate terms of Equations (8.4) and (8.5). The economic factor E_f can be written as:

$$E_f = P/X\ (N, i_f, d) \tag{8.6}$$

The economic factors E_{in}, E_m, E_o, and E_{pt} are only slightly more complicated than E_f and can be written as follows:

$$E_{in} = C_{in}\ P/X\ (N, i, d) \tag{8.7}$$

$$E_m = C_m\ P/X\ (N, i, d) \tag{8.8}$$

$$E_o = C_o \; P/X \; (N, \; i, \; d) \tag{8.9}$$

$$E_{pt} = C_{pt} \; P/X \; (N, \; i, \; d) \tag{8.10}$$

where:

C_{in} is the extra insurance cost as a fraction of the investment

C_m is the extra maintenance cost as a fraction of the investment

C_o is the extra operating cost as a fraction of the cost of the energy supplied by the solar collector

C_{pt} is the extra property tax cost as a fraction of the investment

The economic factors $E_{\ell i}$ and E_{mp} are more complicated and can be expressed as:

$$E_{\ell i} = (1-J) \left\{ \frac{P/X \; (N_m, o, d)}{P/X \; (N_m, o, i_m)} - \frac{P/X \; (N_m, i_m, d)}{P/X \; (N_m, \; i_m, \; o)} \right\} \tag{8.11}$$

and

$$E_{mp} = J + (1-J) \left\{ \frac{P/X \; (N_m, o, d)}{P/X \; (N_m, o, i_m)} \right\} \tag{8.12}$$

where

J is the downpayment as a fraction of the investment

N_m is the term of the mortgage

This completes the general approach used in evaluating different solar energy systems. For a given solar energy system, Equation 8.3

is used to calculate the solar savings. The system giving the highest solar savings is the most economical. If all solar systems give rise to negative solar savings, then the conventional system used in the comparison is more economical.

8.2 Economic Analysis Parameters

To utilize the result of Section 8.1, the parameters of Equation 8.3 must be known. It is the purpose here to give the parameter values used in the economic analysis of Section 9. Most of the parameters were obtained from the workshop manual on Technical, Economic and Legal Considerations for Evaluating Solar Heating 8uildings for Lenders, Appraisers, Insurers, and Tax Consultants. The manual was prepared by Solar Energy Applications Laboratory of Colorado State University at Fort Collins, Colorado in March of 1979 and sponsored by the U.S. Department of Energy. In addition, current fuel costs were obtained from a study conducted by Michael Lints of the RIT Department of Mechanical Engineering. Collector costs, both area dependent and area independent, are evaluated from manufacturers information on various equipment and are broken into the two categories following the approach outlined in the manual given above. Labor costs are included in these costs. Table 8.1 summarizes these values.

TABLE 8.1 Economic Analysis Parameters

Parameter	Value
1. Annual mortgage interest rate, i_m	10%
2. Term of mortgage, N_m	20 years
3. Down payment (as fraction of investment), J	20%
4. Property tax rate (as fraction of investment), C_{pt} (by N.Y.S. law, not required for first 15 years)	1.33%
5. Effective income tax bracket (state + federal - state x federal), t	46%
6. Insurance tax rate (as fraction of investment), C_{in}	.5%
7. Maintenance cost rate (as fraction of investment), C_m	.5%
8. Operating cost as a fraction of solar supplied energy, C_o	1%
9. General inflation rate per year, i	16%
10. Fuel inflation rate per year, i_f	20%
11. Discount rate (after tax return on best alternate investment), d	18%
12. Term of economic analysis, N	20 years
13. State and federal tax credit, t_c	55% (15% - state) (40% - federal)
14. Electric cost, c_f	13.88 \$/GJ (5¢/KWHR)
15. Natural gas cost, c_f	3.79 \$/GJ (40¢/therm)
16. Oil cost, c_f	6.82 \$/GJ (72¢/therm)
17. Electric furnace efficiency, η_f	100%
18. Natural gas furnace efficiency, η_f	65%
19. Oil furnace efficiency, η_f	65%

TABLE 8.1 Contd.

20. Tubular collector area dependent costs, C_{ca}	224\$/m^2
21. Flat plate nonselective and selective surface area dependent costs, C_{ca}	240\$/m^2(two covers) 200\$/m^2(one cover)
22. Tubular, flat plate nonselective and selective surface area independent, C_{ci}	2000\$
23. Energy load, L	25.13 GJ/year
24. Collector area, A	6.7 m^2

9. DESCRIPTION OF RESULTS

9.1 Results of Storage/Hot Water Tank Study

From the experimental work of Section 5.2, the loss coefficients of the storage and hot water tanks in their delivered condition were found to be 1.1 and 1.2 $W/m^2 °K$, respectively. These values correspond to an insulation valve of R5. This result corresponds to the findings of the second year of New England Electric's solar water heating test program. Considering the 40 gallon hot water tank, the continuous heat loss in this condition amounts to approximately 90 watts. This represents 10% of the total domestic hot water load when 80 gallons per day are delivered from a city temperature of 10°C to a service water temperature of 60°C. Upgrading the insulation on the hot water tank from R5 to R10 by adding 2 inches of insulation will result in an annual savings of apprximately $20 assuming the cost of electricity to be 5¢/kWhr. For natural gas the savings would be $8.40 and for oil $15.10 assuming energy costs as shown in Table 8.1.

9.2 Simulation Results

Following the procedure outlined in Section 7.3, the system average yearly performance efficiency was found for the solar domestic hot water system at RIT utilizing the K.T.A. tubular collectors. In addition, the same system configuration with flat plate selective and nonselective surface collectors was simulated. Results indicated that the most efficient configuration was the flat plate selective surface collector system at 36% followed by the flat plate nonselective surface collector

system at 34%. The tubular collector system configuration was the least efficient at 25%. The poor performance of the tubular collector system configuration is the result of the lower collector efficiency of the tubular collectors. This is caused by a lower effective collection area, a larger loss coefficient, and tube optics which further limit insolation from reaching the collector absorber tubes.

A companion study [32] which simulated the system for an entire year utilizing climatological data input on an hour by hour basis showed the flat plate selective surface collector system configuration to have an efficiency of 42%. Thus, the simplified procedure given in Section 7.3 correlates well with the more extensive simulation. Of the configurations simulated in the study indicated, the most efficient was obtained using a flat plate selective surface collector tilted 35° from the horizontal toward the south and having one cover plate. The efficiency of this system was found to be 47%.

9.3 Solar System Economic Analysis Results

Following the procedure outlined in Section 8.1 and utilizing the parameters given in Section 8.2, a present worth analysis of the K.T.A. tubular collector system configuration was performed. An analysis was also done for the flat plate selective surface collector configuration with two covers and also for the optimum configuration of the companion study previously cited. For each system, the analysis was performed considering the auxiliary heat being supplied by electricity, natural gas, and oil. Also, each calculation was performed with and without

tax credits considered. The results are given in Table 9.1.

TABLE 9.1 Economic Analysis Results - Solar Savings Present Worth, $

System	Auxiliary Energy Fuel: Electric, With Tax Credits	Electric, Without Tax Credits	Natural Gas, With Tax Credits	Natural Gas, Without Tax Credits	Oil, With Tax Credits	Oil, Without Tax Credits
1. Tubular Collector System	1200	-725	200	-1725	790	-1135
2. Flat Plate Selective Surface. N = 2 Tilt Angle = 60°	1950	-37	508	-1480	1347	-638
3. Flat Plate Selective Surface. N = 1 Tilt Angle = 35°	2750	912	870	-968	1965	127

From Table 9.1 several conclusions can be drawn. First, when choosing a collector type for a D.H.W. application in Rochester and the surrounding region, one should not choose a tubular collector, but a flat plate selective surface collector. In all cases, the solar savings present worth for the tubular collector system configuration is less than that of flat plate selective surface collector system configurations. Also, the importance of the fuel type used to generate auxiliary heat is obvious. It is most beneficial to install a solar system if the hot water tank uses electricity followed by oil and finally natural gas. The contribution of tax credits to the economic benefit of installing a solar-assisted domestic hot water system can also be seen. It is not advisable to install any of the systems studied if

tax credits are not available and the hot water tank uses natural gas for auxiliary heat.

10. CONCLUSIONS

Based on the work completed in this study, the following conclusions can be made:

1. The tubular collectors analyzed showed inferior performance compared to both nonselective and selective surface flat plate collectors of equivalent area.

2. The poor performance of the tubular collectors is due to (i) poor optical characteristics of the collector tubes resulting in a reduced effective aperture and (ii) the fact that the tubes are not evacuated.

3. Evacuation of the tubular collectors would result in system performance that is slightly better than that of the system using selective surface flat plate collectors.

4. The life cycle cost analysis indicates that supplemental solar heating is cost effective if one uses electric resistance or oil for domestic water heating.

5. If natural gas is used to heat water for domestic use, conversion to solar heating is only marginally cost effective.

6. The cost effectiveness of the systems studied are dependent on the availability of tax credits. Without state and federal tax credits, supplemental solar heating is only

marginally cost effective when one uses electric resistance for domestic water use and not cost effective when one uses oil or natural gas.

7. Substantial energy savings can be realized by upgrading the insulation of delivered hot water tanks. For hot water tanks similar to the one of this study, losses can be cut in half by adding 2" of insulation.

Recommendations

1. Replace the tubular collectors with selective surface flat plate collectors.

2. Insulate the hot water tank and the preheat tank (2" of insulation will cut the losses in half in both cases).

3. In future experimental work, the sole use of RTD devices is recommended. They were found to be more repeatable and accurate than the solid state devices. They also are easier to calibrate.

4. A study should be undertaken to determine the optimum load usage profile which results in the highest system yearly efficiency.

Missing Page

REFERENCES

1. Workshop Manual on Technical, Economic and Legal Considerations for Evaluating Solar Heated Buildings For Lenders, Appraisers, Insurers, and Tax Consultants prepared by Solar Energy Applications Laboratory, Colorado State University, Fort Collins, Colorado. Sponsored by the U.S. Department of Energy. Pl.1, March 1979.

2. Mather, G.R., Beekley, D.C., "Performance of An Evacuated Tubular Collector Using Non-Imaging Reflectors", Proceedings of Sharing the Sun Conference, Vol. 2, p. 64, 1976.

3. Cobble, M.H., Smith, P.R., "Optimal Overall Efficiency for a Solar Radiation Collector Utilizing a Two Fluid Rankine Cycle to Generate Electrical Power", Inst. of Environmental Science Annual Technical Meeting, pp.308-313, 1976.

4. Besant, R.W., Winn, B.C., "Cost Effective Solar Heating of Houses with Seasonal Storage of Energy", Joint Conference of the International Solar Energy Society, Vol. 4, pp. 409-424, 1976.

5. Doeblin, E.O., Measurement Systems-Application and Design, McGraw-Hill, Inc., New York, p. 532, 1975.

6. Hottel, H.C., Woertz, B.B., "Performance of Flat-Plate Solar Heat Collectors", ASME Transactions, Vol. 64, p. 91, 1942.

7. Hottel, H.C., Whillier, A., "Evaluation of Flat-Plate Collector Performance", Transactions of the Conference on the Use of Solar Energy, Vol. 2, Part 1, p. 74, University of Arizona Press, 1958.

8. Bliss, R.W., "The Derivation of Serveral 'Plate-Efficiency Factors' Useful in the Design of Flat-Plate Solar-Heat Collectors", Solar-Energy, Vol. 3, No. 4, p. 55, 1959.

9. Whillier, A., "Design Factors Influencing Collector Performance", Low Temperature Engineering Applications of Solar Energy, ASHRAE, New York, 1967.

10. Duffie, J.A., Beckman, W.A., Solar Energy Thermal Processes, Wiley, New York, Chap. 7, 1974.

11. Beekley, D.C. Mather, G.R., "Analysis and Experimental Tests of a High Performance, Evacuated Tubular Collector", DOE/NASA CR-150874 1979.

12. Kreith, F., Kreider, J.F., Principles of Solar Engineering, McGraw-Hill, Inc. New York, p. 59, 1978.

13. Duffie, J.A., Beckman, W.A., Solar Energy Thermal Processes, Wiley, New York, p. 54, 1974.

14. Liu, B.Y.H., Jordan, R.C., "A Rational Procedure For Predicting the Long-Term Average Performance of Flat-Plate Solar-Energy Collectors", Solar Energy, Vol. 7, No. 2, p. 53, 1963.

15. Duffie, J.A., Beckman, W.A., Solar Energy Thermal Processes, Wiley, New York, p. 19, 1974.

16. Orgill, J.F., Hollands, K.G.T., "Correlation Equation for Hourly Diffuse Radiation on a Horizontal Surface", Solar Energy, Vol. 19, p. 357, 1977.

17. Duffie, J.A., Beckman, W.A., Solar Energy Thermal Processes. Wiley, New York, p. 9, 1974.

18. Liu, B.Y.H., Jordan, R.C., "The Interrelationship and Characteristic Distributuion of Direct, Diffuse and Total Radiation", Solar Energy, Vol. 4, No. 3, p. 1, 1960.

19. Duffie, J.A., Beckman, W.A., Solar Energy Thermal Processes, Wiley, New York, p. 77, 1974.

20. Lobo, P.C., Kluppel, R.P., de Araujo, S.R., "Performance of An Annular Cylindrical Solar Collector", Heliotechnique and Development Proc. of Int. Conf., Dhahram, Saudi Arabia, Nov. 2-6, 1975, Publ. by Dev. Anal. Assoc., Cambridge, Mass., Vol. 1, p. 233, 1976.

21. Karlekar, B.V., Desmond, R.M., Engineering Heat Transfer, West Publishing Co., New York, p.237, 1977.

22. Siegel, R., Howell, J.R., Thermal Radiation Heat Transfer, McGraw-Hill Inc., New York, 1972.

23. Karlekar, B.V., Desmond, R.M., Engineering Heat Transfer, West Publishing Co., New York, p.402, 1977.

24. Swinbank, W.C., "Long-Wave Radiation From Clear Skies", Quart. J. Roy. Meterol. Soc., Vol. 89, 1963.

25. Duffie, J.A. Beckman, W.A., Solar Energy Thermal Processes, Wiley, New York, p. 133, 1974.

26. Speyer, E., "Solar-Energy Collection with Evacuated Tubes", ASME Transactions, J. Engr. Power, Vol. 86, p. 270, 1965.

27. Mather, G.R., Beekley, D.C., "Long-Term Average Performance of the Sunpack Tubular Collector".

28. Klein, S.A. "A Design Procedure for Solar Heating Systems", Ph.D. Thesis, University of Wisconsin, Madison, 1976.

29. Duffie, J.A., Beckman, W.A., Solar Energy Thermal Processes, Wiley New York, pp. 134-135, 1974.

30. Mutch, J.J., "Residential Water Heating, Fuel Consumption, Economics, and Public Policy", RAND Report R1498, (1974).

31. Beckman, W.A., Klein, S.A., Duffie, J.A., Solar Heating Design by the F-Chart Method, Wiley, New York, 1977.

32. Wojciechowski, P.H., Nye, A.H., Jurusik, D., Wendt, P., "Cost/Benefit Analysis of Solar Domestic Hot Water Systems for Rochester, New York", Department of Mechanical Engineering, Rochester Institute of Technology, Rochester,New York, December 1980.

33. Benedict, R.P., Fundamentals of Temperature, Pressure, and Flow Measurements, Wiley, New York, p.158, 1977.

34. Hill, J.H., Streed, E.R., Kelley, G.E., Geist, J.C., Kusuda, T., "Development of Proposed Standards for Testing Solar Collectors and Thermal Storage Devices", NBS Technical Note 899, February, p. 145, 1976.

35. Wylie, C.R., Advanced Engineering Mathematics, McGraw-Hill, Inc., New York, p.508, 1978.

36. Benedict, R.P., Fundamentals of Temperature, Pressure, and Flow Measurements, Wiley, New York, p. 198, 1977.

37. Kreith, F., Kreider, J.F., Principles of Solar Engineering, Mc-Graw Hill, Inc., New York, p.58, 1978.

APPENDIX 1 - SOLAR WATER HEATING CONTROL SYSTEM

Figure A1.1 is a schematic of the solar water heating system control logic while Figure A1.2 is a photograph of the control panel located in the northwest corner of the basement at Energy House. These figures along with Figure 3.1, which shows the sensors locations in the system, will be referenced in the explanation that is to follow. This will be indicated by parenthesis with the proper figure number inside, for example, see Figure A1.1 will be indicated by: (A1.1).

As previously described, there are three differential controllers used to operate the solar water heating system.

Controller #1 senses the temperature of the collector and preheat storage tank via sensors TMDSP and TMDPH1 (3.1), respectively. When the collector temperature becomes significantly greater than the preheat tank temperature (typically 7°C greater), the controller energizes relay K1 (A1.1, A1.2). This causes the Normally Open (N.O.) contacts of K1 in the 24 VAC circuit to close and initialize the time delay relay, TDK1, which then begins its timing operation. Relay K5 is also energized through a set of N.O. K1 contacts and the Normally Closed (N.C.) TDK1 contacts. With K5 energized, relay K4 is de-energized and the pump, P1, is turned on through the K1 N.O. and K4 N.C. contacts. This condition persists independent of the state of controller #2 until TDK1 times out (TDK1 N.C. contacts open).

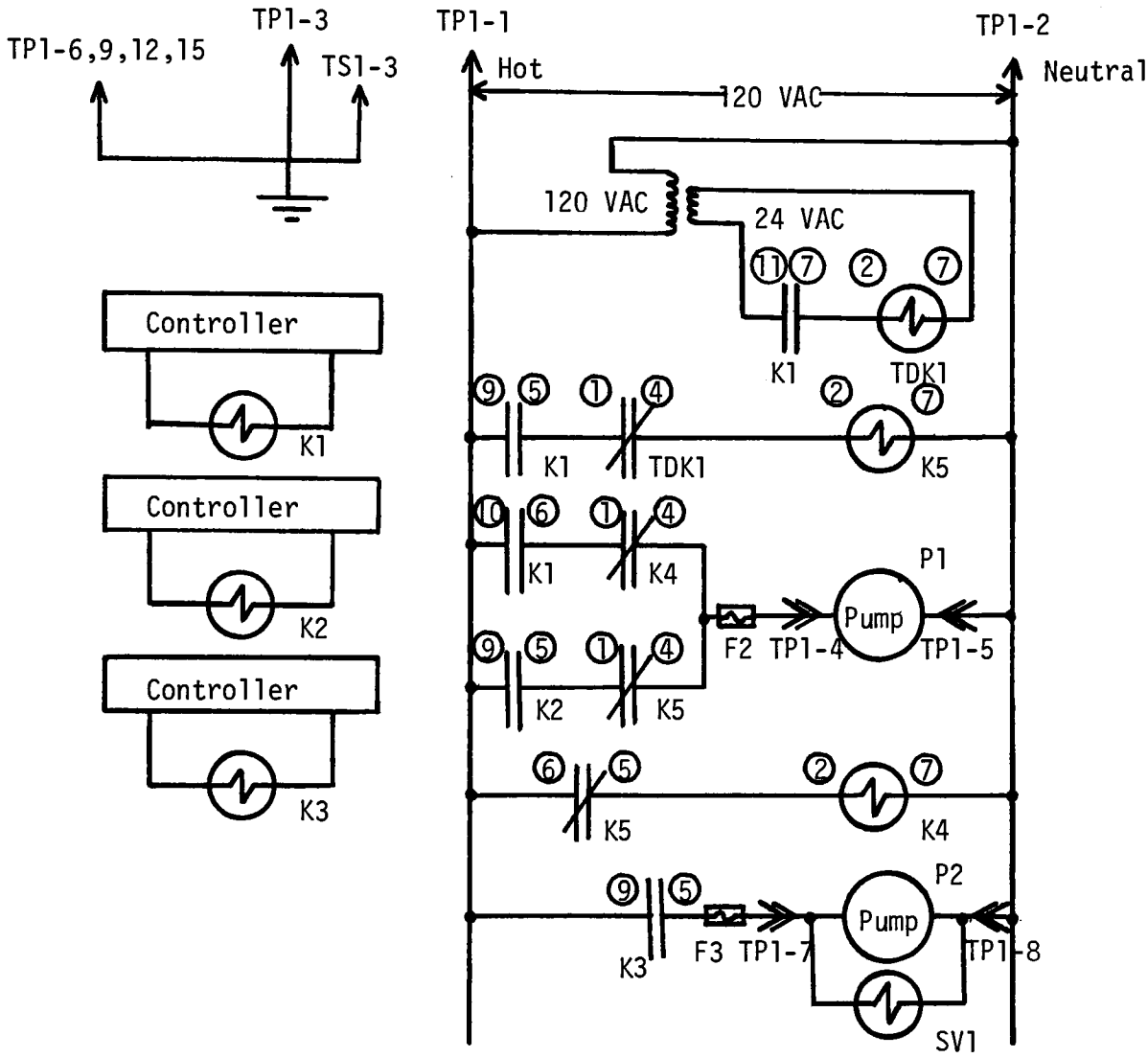

Notes:

1. ⓝ designates pin n of the indicated relay.
2. The purpose of K4 is to eliminate the interruption of pump power during controller crossover.
3. TDK1 - P & B CHB-38-30003 1-180 sec. time delay
   K1,K2,K3 - P & B KHU-17012-12v 4PDT
   K4,K5 - P & B KAP-11A-120V DPDT
4. Relay contacts are always shown in the de-energized state; ie, the state that they would be in if no power was applied to the panel.

Figure A1.1 Solar Water Heating System Control Logic Schematic

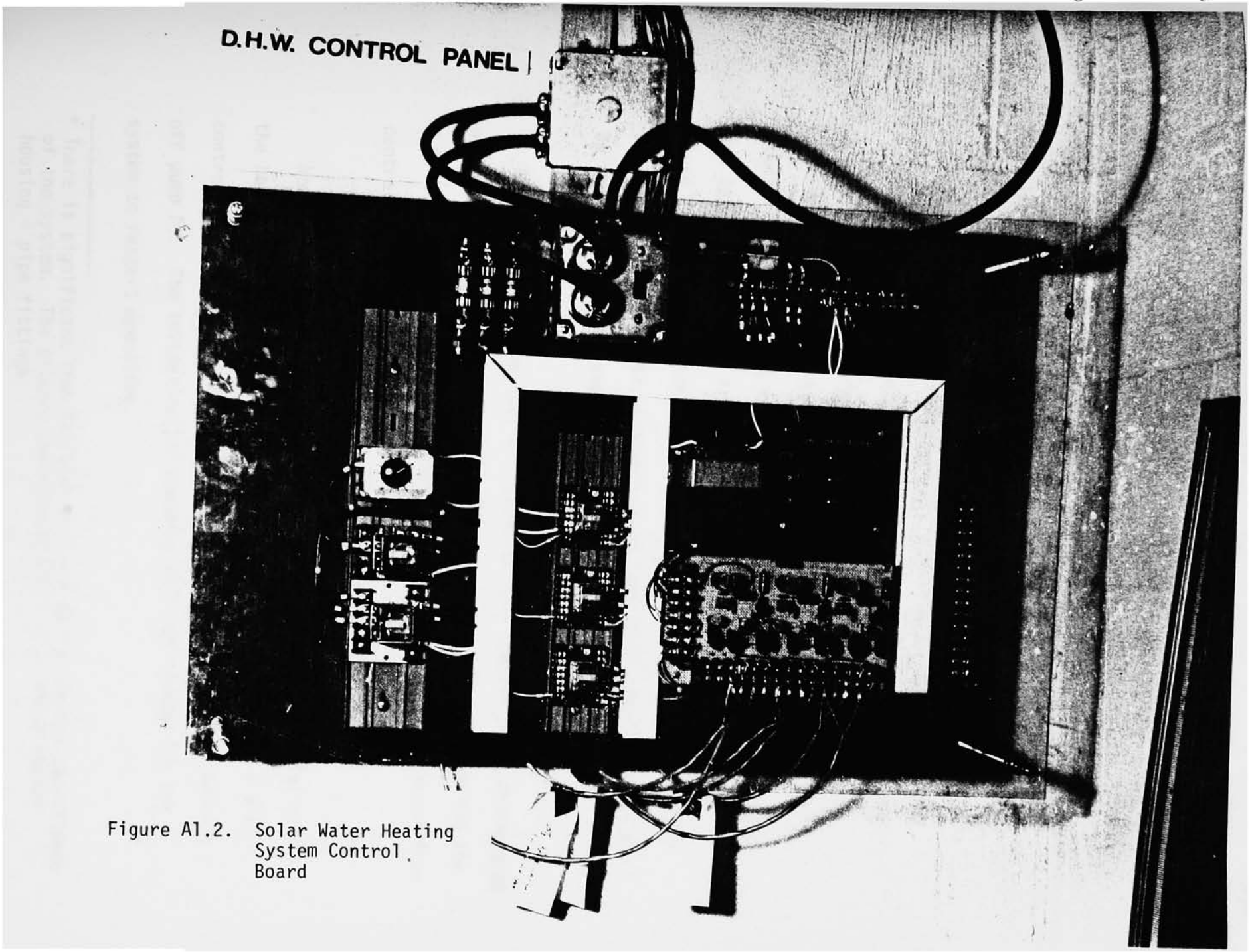

Figure A1.2. Solar Water Heating System Control Board

Controller #2 senses the temperature of the inlet and outlet of the collection loop-to-preheat tank heat exchanger via sensors TMDHXI and TMDHXO, respectively. Shortly after controller #1 has initialized the collection loop, the warm fluid from the collector has reached the heat exchanger. Since this fluid is warmer than the water in the preheat tank, heat transfer will take place and consequently the temperature of the heat exchanger outlet (TMDHXO) will be lower than the heat exchanger inlet (TMDHXI). When this temperature difference becomes significant (typically $\geq$ 4°C), controller #2 energizes K2. This is to occur within the time period set by TDK1.* When K2 is energized, its N.O. contacts close but cause no action since the N.C. K5 contacts are open (K5 is energized during the time interval, see above. At this point the controller can be thought to have "prepared" for the timing out of TDK1.

When TDK1 times out, its N.C. contacts open causing K5 to de-energize which causes K4 to re-energize. When the N.C. K4 contacts open and the N.C. K5 contacts close, the control of pump P1 has been transferred from controller #1 to controller #2.

When the temperature difference between the inlet and outlet of the heat exchanger (TMDHXI - TMDHXO) becomes low (typically $\leq$ 1.5°C) controller #2 will turn off de-energizing K2 and consequently turning off pump P1. The initialization sequence must now reoccur for the system to restart operation.

---

* There is significant time lag ($\sim$ 1 min) due to the thermal capacitance of the system. The primary contributor seems to be brass sensor housing + pipe fittings.

Note that controller #1 should shut off before controller #2 as required to re-initialize. The reasoning is as follows. After the pump has operated for a few minutes, the temperature being sensed by TMDPH1 (preheat tank temperature) is very close to the temperature being sensed by TMDHXO (heat exchanger outlet temperature). The collector temperature obviously must drop before the heat exchanger inlet temperature drops due to the time lag in the system. This should ensure that controller #1 will shut off before controller #2 shuts off. Also a higher temperature difference is needed to keep controller #1 on (typically 3°C).

Controller #3 senses the temperature of the preheat tank and the hot water heater tank via sensors TMDPH2 and TMDH, respectively. When the perheat tank temperature becomes significantly greater than the hot water heater tank temperature (typically 4°C greater), the controller energizes relay K3. The closing of the N.O. K3 contacts begins water circulation between the two tanks by energizing pump P2 and valve V1. The controller will shut off when the temperature difference becomes small (typically 2°C).

The capability to easily simulate and/or override each of the controllers has been included to allow for simple experimentation and system debugging. The manual override/automatic switches are located in the center right portion of the control panel. The switches are labeled 1, 2, and 3 for their respective controllers and each has three positions; on (left) - simulates the controller-on state, off (center) - simulates the controller-off state, auto (right) - allows the controller to operate automatically by using its temperature

sensors. Note that manual operation of the collection loop pump can be accomplished by using only the #2 switch.

APPENDIX 2 - Charging the Solar Energy Collection Loop

The solar energy collection loop can either be operated with water (summer operation only) or a non-freezing transfer fluid (summer or winter). The purpose of this appendix is to describe suitable procedures to charge the loop with either water or a non-freezing transfer fluid.

Water

1. Drain the system entirely. This can be done by first draining the largest portion of the system through the shot feeder valves No. 2 and No. 4 (see Figure A2.1.) and by finally removing the plug at the inlet of the perheat tank heat exchanger (see Figure A2.2).

2. Close valves 2 and 4 and reinstall the preheat tank heat exchanger inlet plug.

3. Open the valves from the city water line and allow the system to pressurize to approximately 20 psig as read by the pressure gage at the circulation pump discharge (see Figure A2.1).

4. Bleed the valve located at the top of the collectors on the garage roof to allow air to escape from the high point of the system.

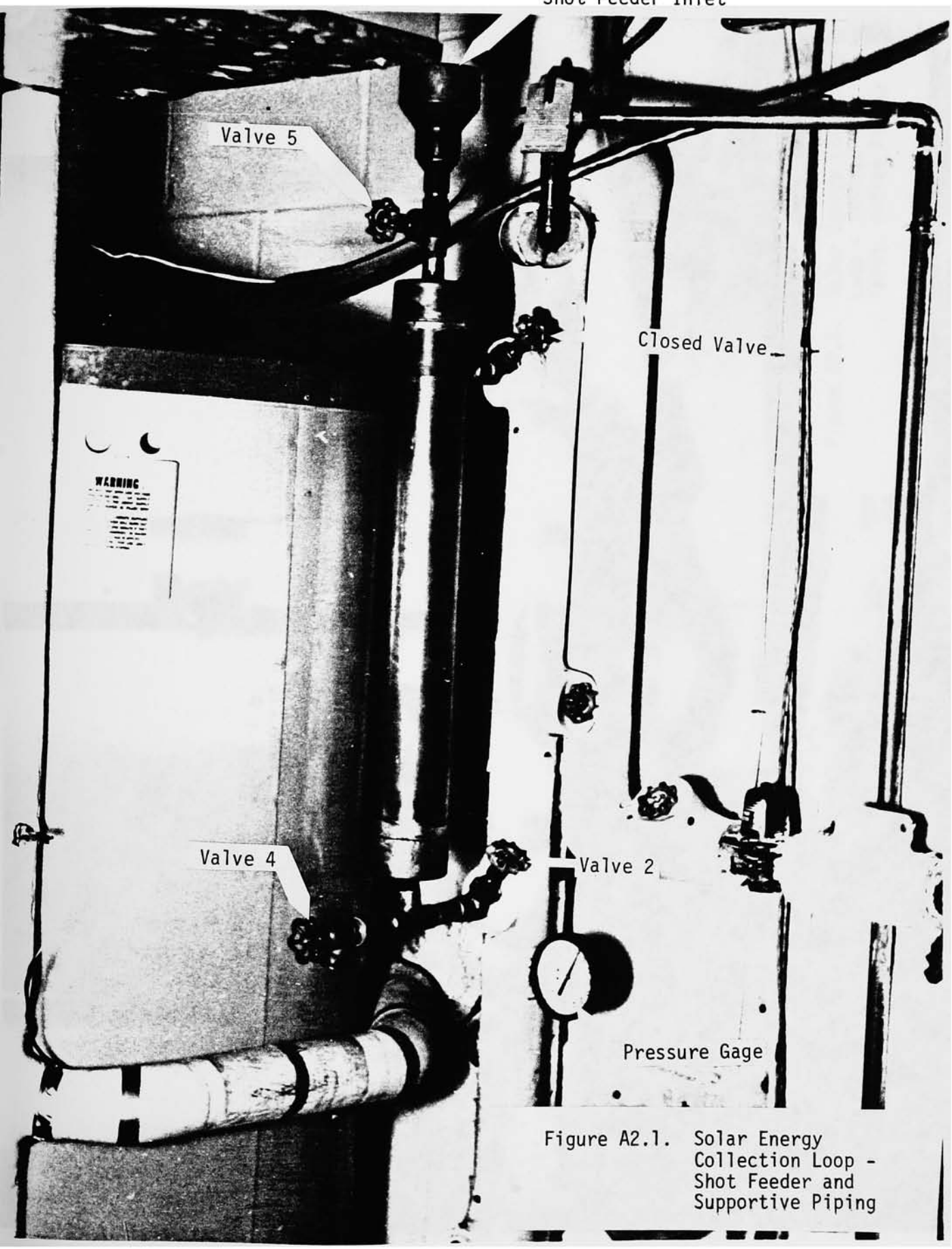

Figure A2.1. Solar Energy Collection Loop - Shot Feeder and Supportive Piping

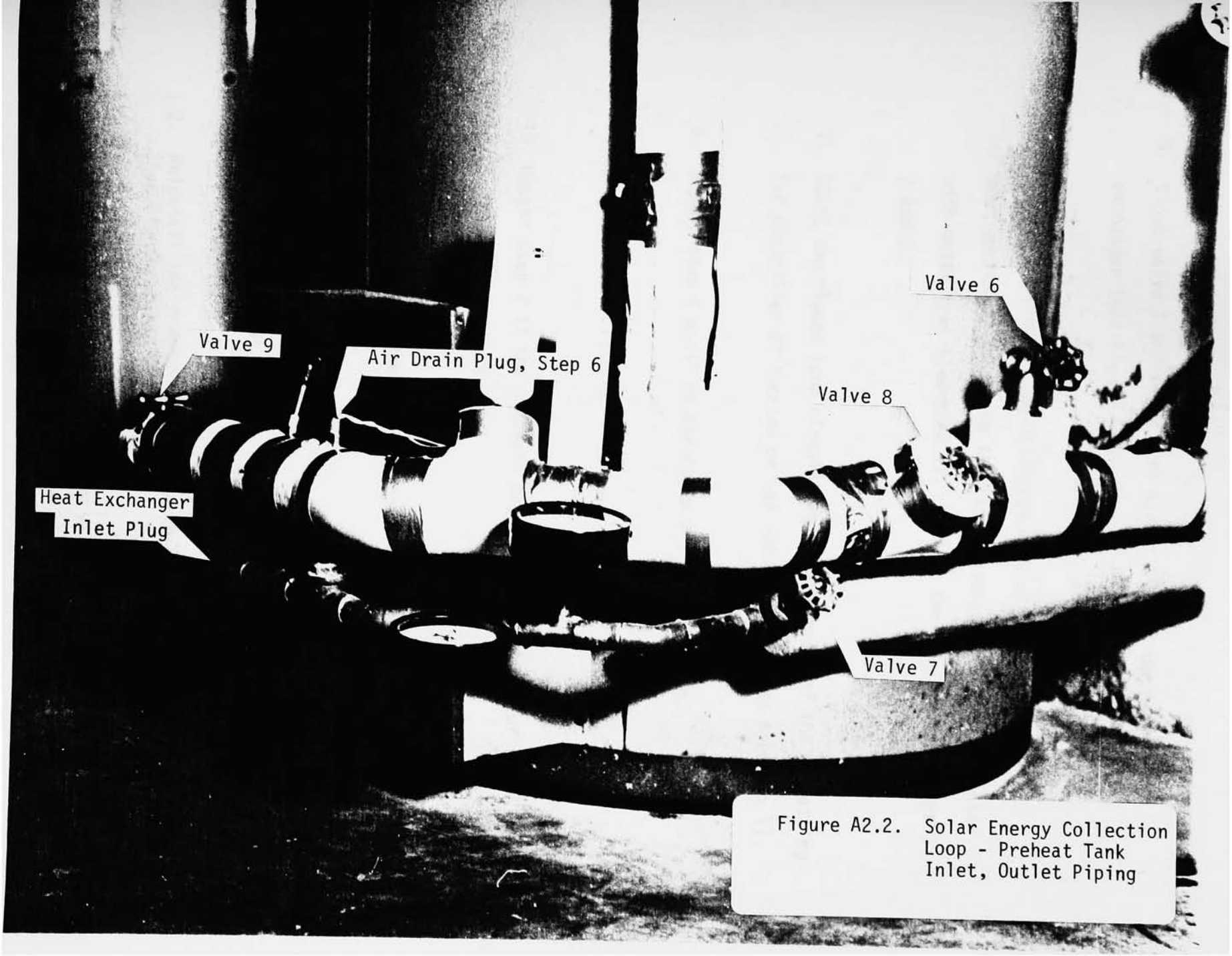

Figure A2.2. Solar Energy Collection Loop - Preheat Tank Inlet, Outlet Piping

5. Close valve 7 and valve 8 at either side of the heat exchanger (see Figure A2.2).

6. Remove the plug on the discharge side of the preheat tank heat exchanger and allow the air to escape. Fill this opening with water (see Figure A2.2). Replace the plug. Open valves 7 and 8.

7. Start the closed loop circulation pump by means of the on setting for controller #2 located on the control board (see Appendix 1).

8. Repeat step 4 until no air comes out of the system.

9. Shut off controller #2.

10. Repeat step 3 if the pressure gage at the discharge of the pump is less than 20 psig.

The system is now charged with water.

Non-freezing Transfer Fluid

1. Same as step 1 for water.

2. Reinstall the preheat tank heat exchanger inlet plug. Close valve 2. (See Figure A2.1.)

3. Connect hose 1 (Figure A2.3) from valve 4 to valve 6 (Figures A2.1 and A2.2).

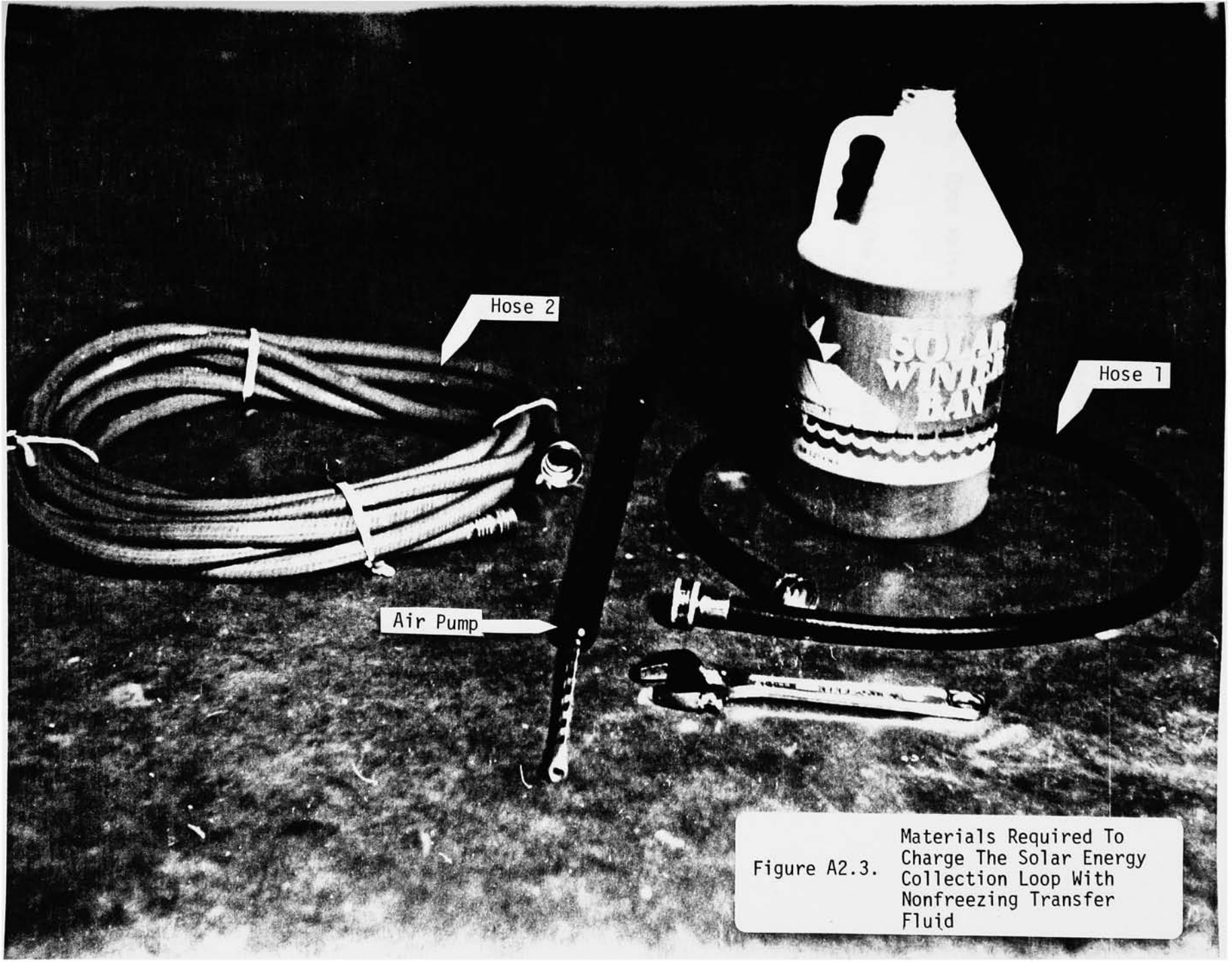

Figure A2.3. Materials Required To Charge The Solar Energy Collection Loop With Nonfreezing Transfer Fluid

4. Open valves 5 and 6.

5. Connect hose 2 (Figure A2.3) from valve 9 (Figure A2.2) to the inlet of the shot feeder (Figure A2.1).

6. Open valve 9 and close valve 8.

7. Fill the shot feeder with fluid until it is full.

8. With an assistant, place controller #2 in the on position while feeding fluid into the shot feeder. Continue until replacement fluid is made up entirely by that from hose 2. The shot feeder holds approximately 1 gallon while the system holds approximately 6 gallons.

9. With an assistant again, shut controller #2 off and at the same time, close valve 9.

10. Close valve 10 (Figure 3.7) on the expansion tank.

11. Start controller #2 and feed approximately 6 gallons of fluid into the system for a total of 12 gallons.

12. While performing step 11, have an assistant bleed the valve at the expansion tank (Figure 3.7).

13. Stop controller #2.

14. Drain the shot feeder, hose 1, and hose 2 into suitable containers.

15. Close valve 7 (valve 8 is closed, step 6).

16. Repeat step 6 as outlined for water except using the non-freezing transfer flud.

17. Utilizing the pump shown in Figure A2.3, pressurize the expansion tank until 20 psig is recorded at the pump discharge pressure gage.

18. Open valve 10. The fluid should rise approximately halfway up the sight glass.

19. Start controller #2.

20. Repeat step 4 as outlined for water.

21. Stop controller #2.

22. If the pressure gage at the pump discharge is less than 20 psig, repeat step 17.

This completes the charging procedure for the non-freezing transfer fluid.

APPENDIX 3 - Temperature Measurement

RTD Construction and Installation

Figure A3.1 shows a resistance thermometer element, a complete RTD sensor, and installation parts. The RTE housing was constructed of 1/8" and 1/4" outer diameter thin walled brass tubing. The RTE (0.100" diamter) is located in the 1/8" diameter section of tubing. The end cap was machined out of 1/8" diameter brass rod and soldered to the 1/8" diameter tubing. The 1/8" to 1/4" bushing was machined out of 1/4" diameter brass rod and attached by soldering. The housing was checked for leaks by subjecting it to approximately 40 psig and submerging it in water. Soldered wire connections with heat shrink preceded the installation of the element in the brass housing. Finally, the housing was backfilled with sand and sealed with epoxy.

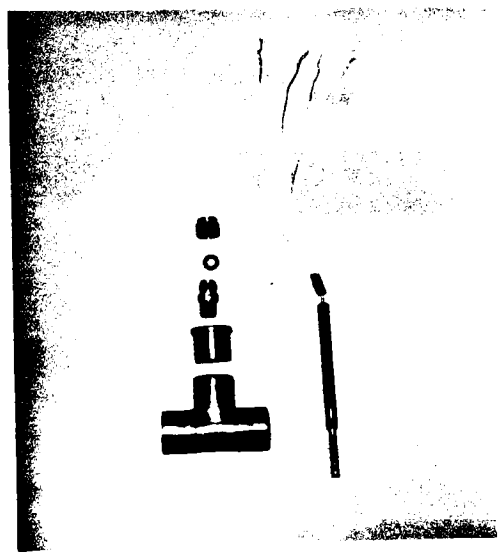

Figure A3.1 RTD Details and Installation

Installation was achieved by mounting the RTD's in 1/8 male thread N.P.T. brass compression fittings with N674-70 O rings used in place of brass ferrules. This allowed the RTD's to be easily installed and removed without damaging them. It was found that tightening the compression fittings hand tight adequately secured the RTD's. The compression fittings were located in specially machined brass plugs which were in turn soldered in a tee fitting. Finally the tee's were located in appropriate positions in the system as shown in Figure 3.14. This installation description is valid for all RTD locations except No. 5. Here, the RTD was mounted in a compression fitting as described above with the difference being that the compression fitting was then attached to a copper tube mounted on a flange which was bolted to the preheat tank. This is the same position as occupied by the thermistor TMDPH2 shown in Figure 3.1 which is used in conjunction with controller #3 to activate the recirculation loop. It was removed for certain aspects of the experimental work.

RTD Calibration

The following procedure was used to calibrate the RTD's:

1. Establish ice point temperature - Ice point temperature was established by freezing a quart of deionized water almost to a solid block while leaving a small quantity of unfrozen water in the center of the block into which the RTD's were inserted. Atmospheric pressure variations from 28.5 to 31 in Hg affect the ice point temperature by less than 0.001°F [33].

2. Using the fluke digital thermometer, R_0 was measured for each RTD. A time of 80 seconds (8 time constants) was allowed for the readings to stabilize. As noted before,all calibration work was performed with each RTD in its experimental configuration.

3. Establish accuracy of mercury in bulb thermometer - A Fisher Scientific Company #15-043A total immersion thermometer with a range of 1°C to 51°C and 0.1°C divisions was used. Total immersion means that the thermometer indicates the correct temperature when just that portion of the thermometer containing the liquid is exposed to the temperature being measured. The thermometer used was checked by measuring the ice point temperature and indicated a temperature of 0.00°C. The smallest scale division of the thermometer is not to exceed 2-1/2 times the specified precision [34]. Therefore, the thermometer is precise to ± 0.04°C.

4. Obtain eleven additional resistance/temperature readings - A model 2300 environmental test chamber located in the physics section of the science building was used to this step. It was made by Delta Design, Incorporated and has a test volume of 10.5 liters (20.3 x 25.4 x 20.3 cm). A 140 CFM centrifugal blower with baffling provides an evenly distributed vertical air flow pattern throughout the test chamber. Dual 20 Ω Nichrome elements provides heating capability up to 315°C while liquid nitrogen provides cooling to -184°C. The resetability is ± 0.15°C and control deviation from setpoint is ± 0.05°C. The five RTD's were placed in the center of of test chamber attached to the thermometer stem such that all the RTD's and the thermometer end measured the same temperature. Five

resistance readings were taken at each temperature setting as well as the thermometer temperature. Adequate time was allowed between oven settings to insure that the RTD's were measuring the oven temperature. The time constant in air for the RTD probe is 2.9 minutes. Table A3.1 gives the results of parts 3 and 4 described above.

5. Find constants a_1 a_2 for each RTD - The data generated in step 4 was fit to the quadratic

$$R = R_o (1 + a_1 T + a_2 T^2) \tag{A3.1}$$

by utilizing the method of least squares. This is achieved by minimizing the sum of the squares of the deviations of the actual data from the quadratic expression. Performing the math and utilizing Cramer's Rule [35] gives the following results:

$$a_1 = \frac{|D_1|}{|J|} \tag{A3.2}$$

$$a_2 = \frac{|D_2|}{|J|} \tag{A3.3}$$

where

$$|D_1| = \begin{vmatrix} \Sigma(T_i R_i) - R_o \Sigma(T_i) & R_o \Sigma(T_i^3) \\ \Sigma(T_i^2 R_i) - R_o \Sigma(T_i^2) & R_o \Sigma(T_i^4) \end{vmatrix} \tag{A3.4}$$

Table A3.1 - Temperature, Resistance Characteristics of Five RTD Probes

Test #	Temperature (°C)	RTD Probe # - Resistance 1	2	3	4	5
1	0.00	99.47	99.77	99.83	99.93	99.97
2	24.72	109.18	109.53	109.58	109.70	109.74
3	26.50	109.88	110.22	110.28	110.40	110.44
4	30.80	111.56	111.91	111.97	112.09	112.13
5	34.55	113.02	113.37	113.43	113.54	113.58
6	37.33	114.08	114.44	114.51	114.63	114.67
7	38.80	114.66	115.02	115.08	115.20	115.25
8	39.52	114.98	115.34	115.40	115.52	115.57
9	43.08	116.34	116.70	116.77	116.89	116.93
10	43.48	116.50	116.87	116.93	117.05	117.09
11	48.16	118.31	118.69	118.75	118.87	118.91
12	49.30	118.76	119.14	119.20	119.32	119.37

$$|D_2| = \begin{vmatrix} R_o\Sigma(T_i^2) & \Sigma(T_iR_i) - R_o\Sigma(T_i) \\ R_o\Sigma(T_i^3) & \Sigma(T_i^2R_i) - R_o\Sigma(T_i^2) \end{vmatrix} \quad \text{(A3.5)}$$

and

$$|J| = \begin{vmatrix} R_o\Sigma(T_i^2) & R_o\Sigma(T_i^3) \\ R_o\Sigma(T_i^3) & R_o\Sigma(T_i^4) \end{vmatrix} \quad \text{(A3.6)}$$

with i a free index ranging from 1 to 12. Application of Equations A3.2 through A3.6 gives a_1 and a_2 for the five RTD's. These are given in Table A3.2.

Table A3.2 - RTD Constants a_1 and a_2

RTD Probe #	R_o	a_1	a_2
1	99.47	.003965	-6.4545×10^{-7}
2	99.77	.003969	-6.6040×10^{-7}
3	99.83	.003965	-6.1391×10^{-7}
4	99.93	.003971	-7.3126×10^{-7}
5	99.97	.003969	-6.9547×10^{-7}

6. Determine T = f(R) from part 5 - From the quadratic equation,

$$T = \frac{-a_1/a_2 - \sqrt{(a_1/a_2)^2 - 4\,(R_o - R)/(R_o a_2)}}{2} \qquad \text{(A3.7)}$$

From this expression, measurement of R is then readily converted to its actual temperature. This completes RTD calibration

Uncertainty in RTD Measurement

Uncertainty is introduced in the calibration procedure by the fact that there is uncertainty in the measured value of temperature. These uncertainties can be quantified as due to the following causes:

a) Thermometer precision equal to ± 0.04°C (from part 3 above)

b) Setpoint deviation on oven equal to ± 0.05°C

c) Uncertainty in fluke digital thermometer reading. Assuming ± 0.01 Ω precision, application of A3.7 gives a ± 0.03°C precision.

If one assumes that these uncertainties are each expressed with the same odds, then the overall uncertainty having the same odds is [36]:

$$W_R = [(0.04)^2 + (0.05)^2 + (0.03)^2]^2$$

$$W_R = 0.07°C$$

where W_R is the overall uncertainty.

As a check on the results of the above procedure, the five RTD's were placed along with the thermometer in an isolated box and allowed to come to steady state. The results show a maximum difference between the calculated temperature and measured temperature of 0.07°C. These results are given in Table A3.3.

Table A3.3 - RTD Temperature Check

RTD Probe #	R	Tcal(°C)	Tmeans(°C)	Difference(°C)
1	108.51	23.01	23.05	.04
2	108.85	23.02	23.05	.03
3	108.91	23.02	23.05	.03
4	109.01	22.98	23.05	.07
5	109.06	23.00	23.05	.05

Finally, the data used to calculate the time constants for the RTD's is shown in Figures A3.2, A3.3, and A3.4 for moving water, still water, and still air. The time constants were calculated based on a first-order model of the RTD and its surroundings.

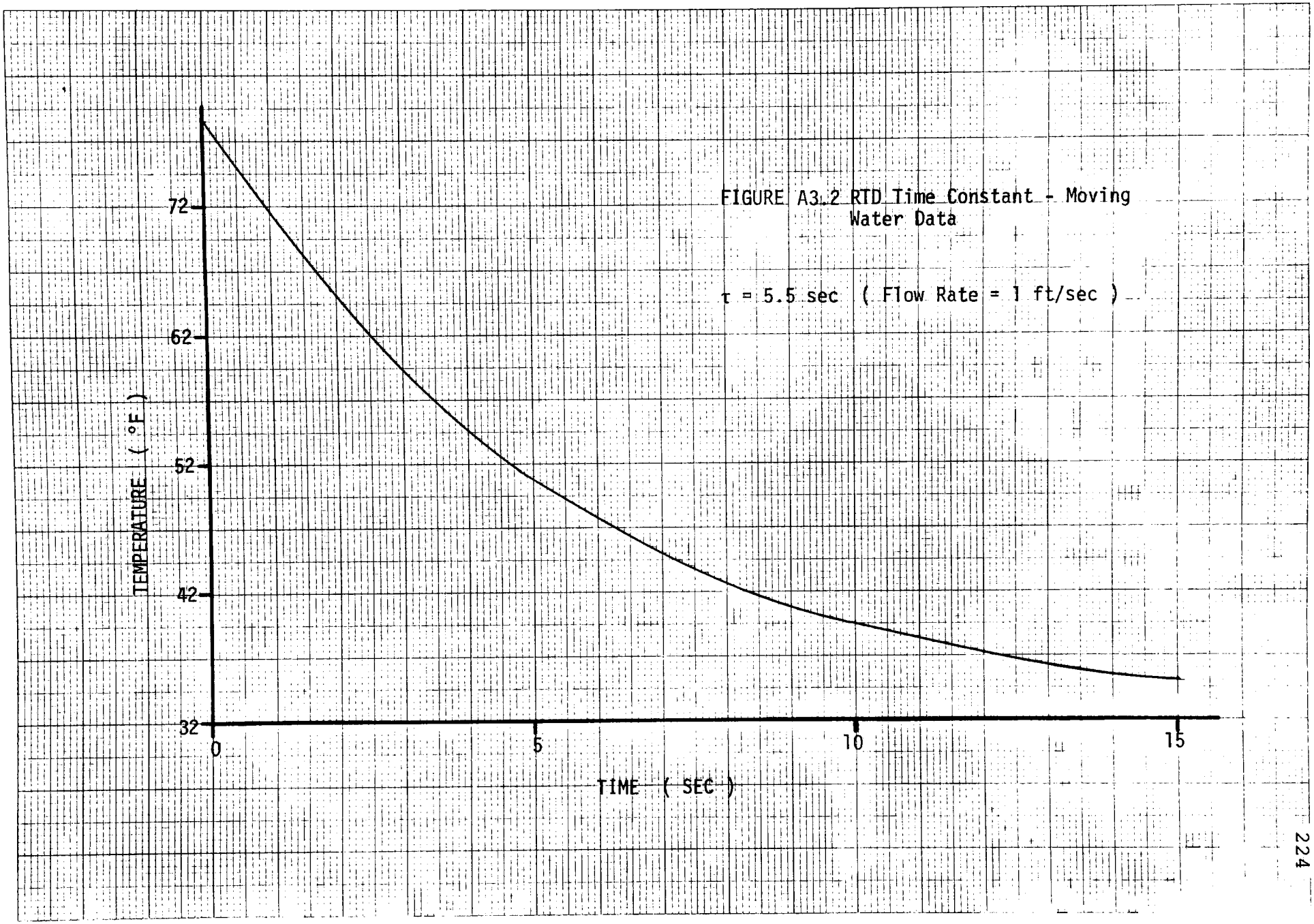

FIGURE A3.2 RTD Time Constant - Moving Water Data

τ = 5.5 sec (Flow Rate = 1 ft/sec)

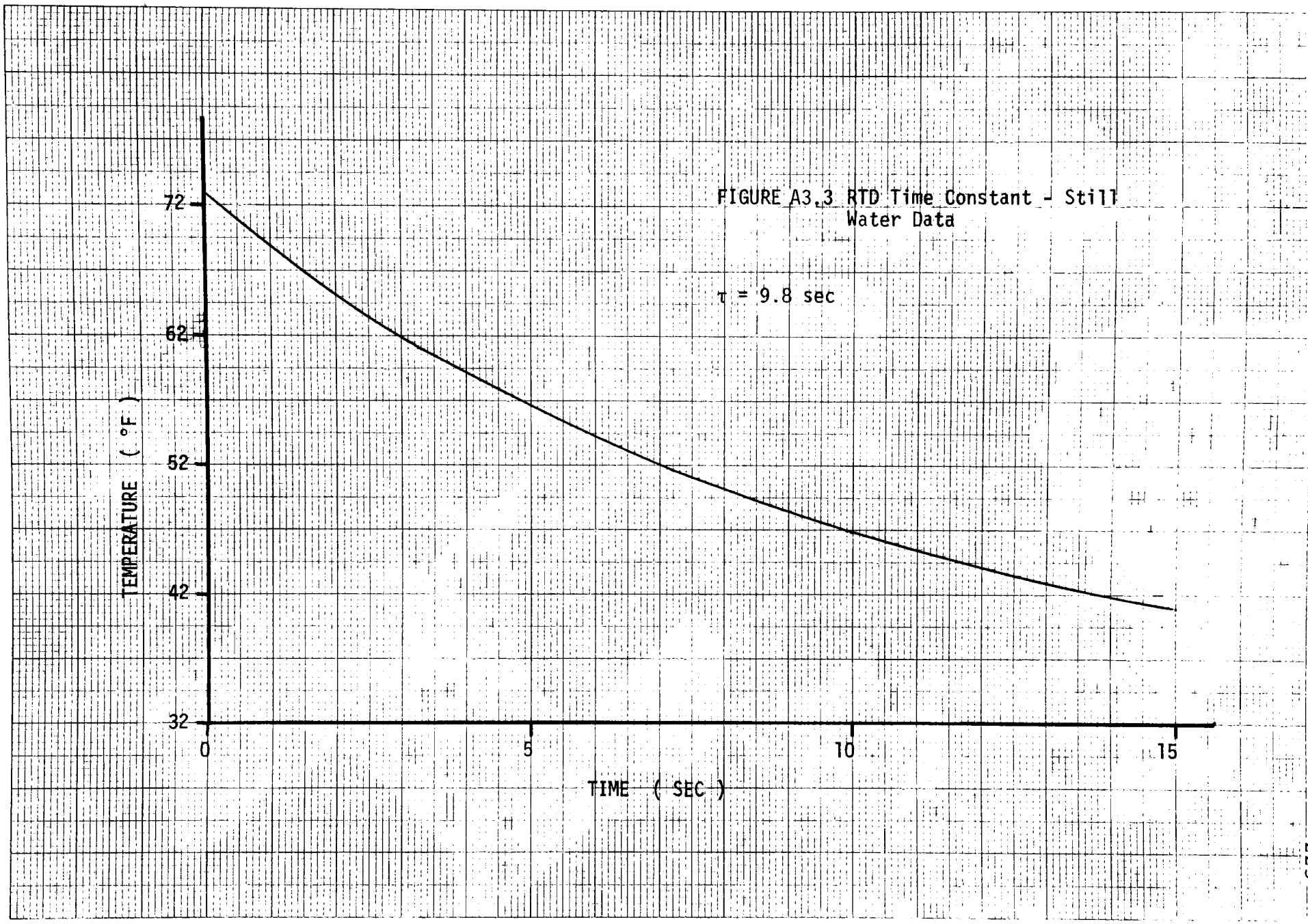

FIGURE A3.3 RTD Time Constant - Still Water Data

τ = 9.8 sec

FIGURE A3.4 RTD Time Constant - Still Air Data

τ = 2.9 min

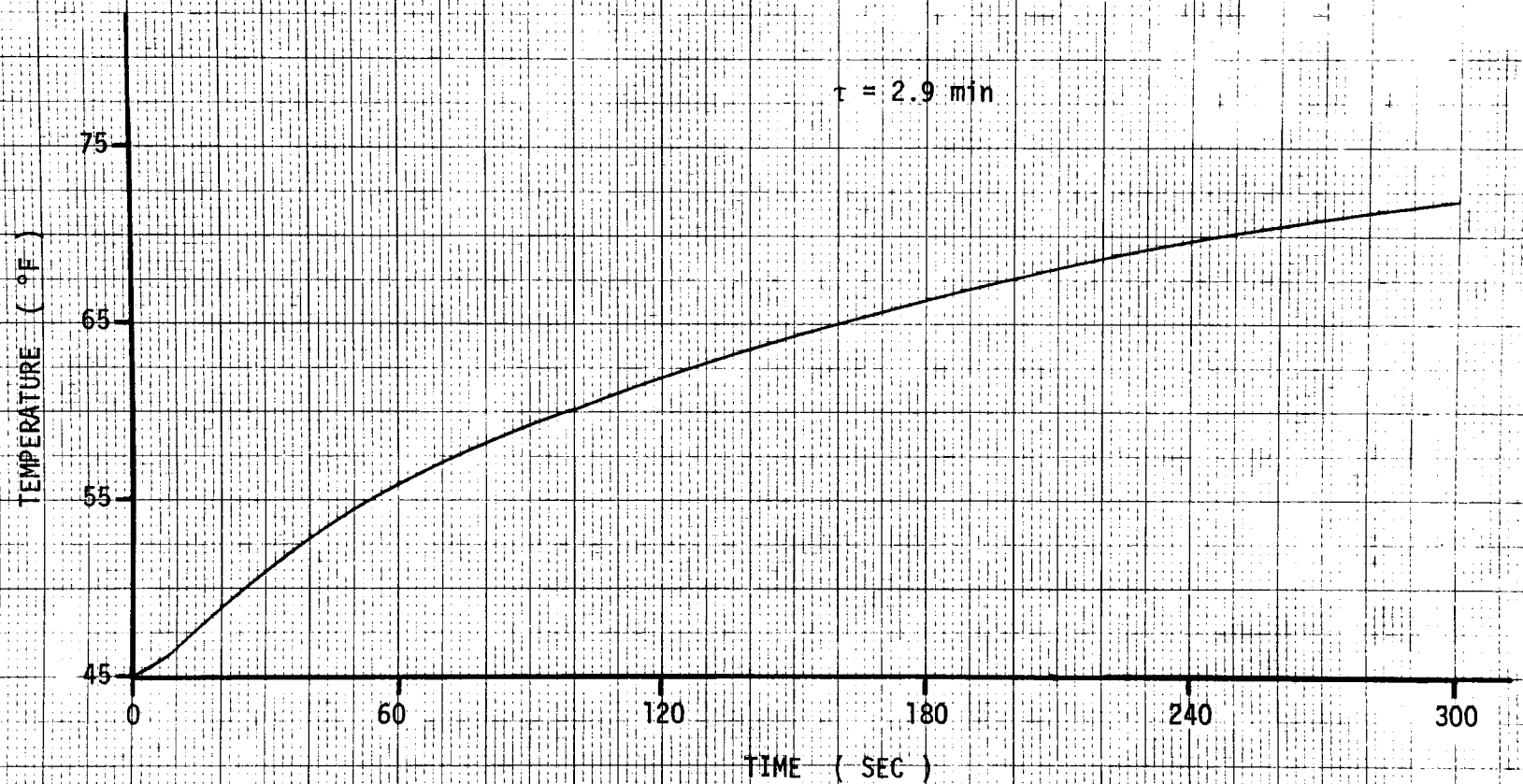

Solid State Calibration

The calibration of the solid state sensors was achieved as follows:

1. Determine the zero temperature and span required for the solid state sensor. Care must be taken such that the analog board output is between 0 and 15V for the range of temperatures experienced. The zero setpoints can be set anywhere between -25°C and +75°C while the span setting ranges from a minimum of 40°C (15V/40°C = 375 mv/°C) to a maximum limited only by the temperature capabilities of the device, i.e. the maximum would be 125 °C (upper temperature limit of device) - (-25°C)(lowest zero setting) = 150°C (15V/150°C = 100 mv/°C).

2. Make all connections as shown in Figure A3.5. Note that the analog signal conditioning board has provision for up to eight solid state sensors.

3. Set DMM to 'DC', 'Volts', '20V'. connect black (-) lead to 'Gnd' test point and red (+) lead to the appropriate signal output point (output corresponding to input solid state device occupies).

4. Establish zero point temperature and place solid state sensor with mercury in bulb thermometer in bath. A thermos is recommended since its time constant is much larger than

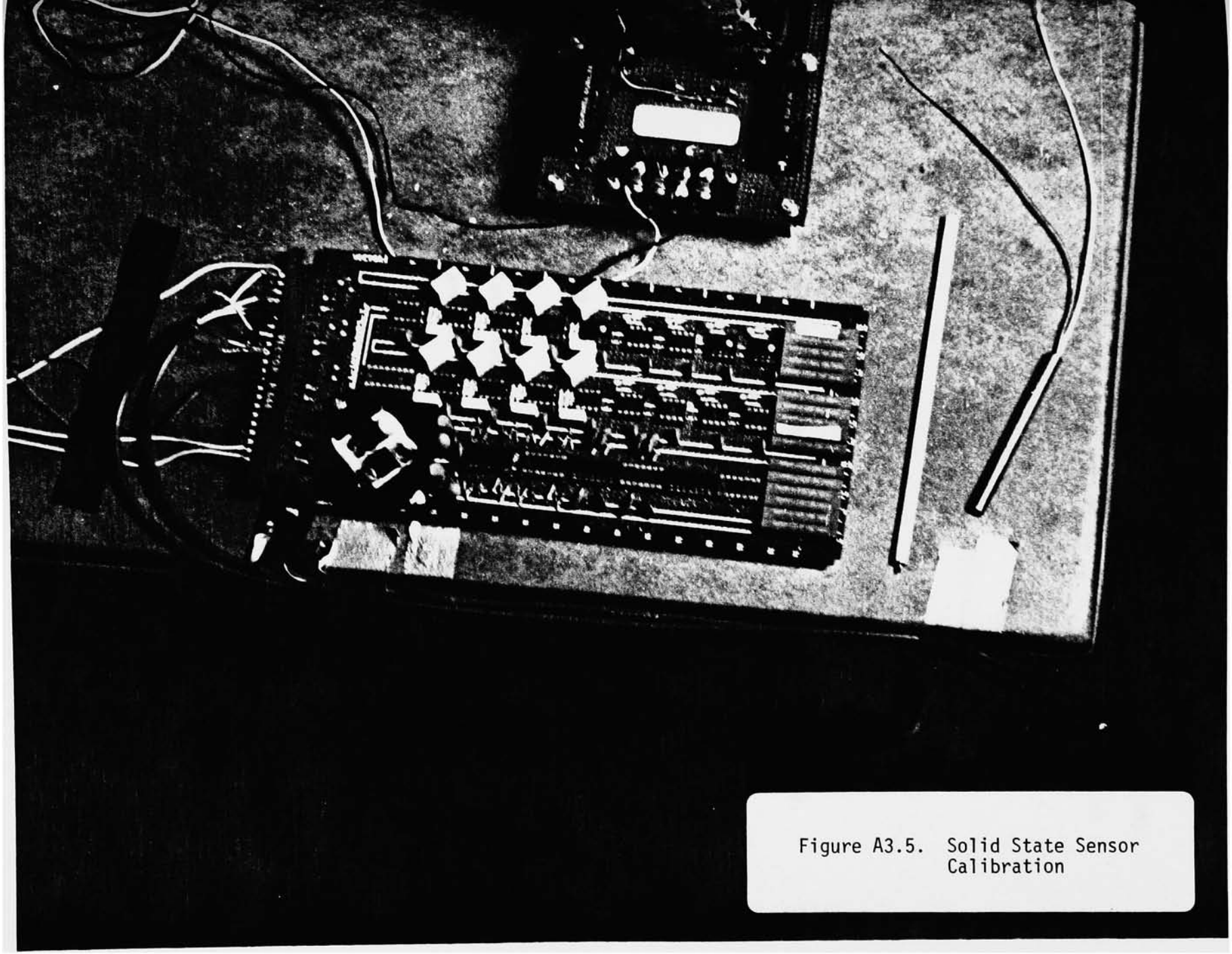

Figure A3.5. Solid State Sensor Calibration

that of the solid state sensor. Allow DMM reading to stabilize. A period of 55 seconds (nine time constants in still water) will assure that the output is less than 0.01% in error from the actual value.

5. Set 'zero' trim pot until DMM reads 0 V.

6. Establish a span temperature by use of a thermos. Place solid state sensor with thermometer in bath. Allow readings to stabilize. From thermometer reading, calculate DMM setting (span required, step 1, times thermometer reading).

7. Set 'span' trim pot until DMM reads value calculated in step 6.

This completes the solid state sensor calibration. Figures A3.6 and A3.7 are the data used to calculate the time constants for the solid state sensor in moving water and still water, respectively. The time constants were calculated as previously described for the RTD's.

Uncertainty in Solid State Temperature Measurements

Uncertainty in temperature measurement using the solid state devices is due to the following causes:

1. Thermometer precision equal to ± 0.04°C.

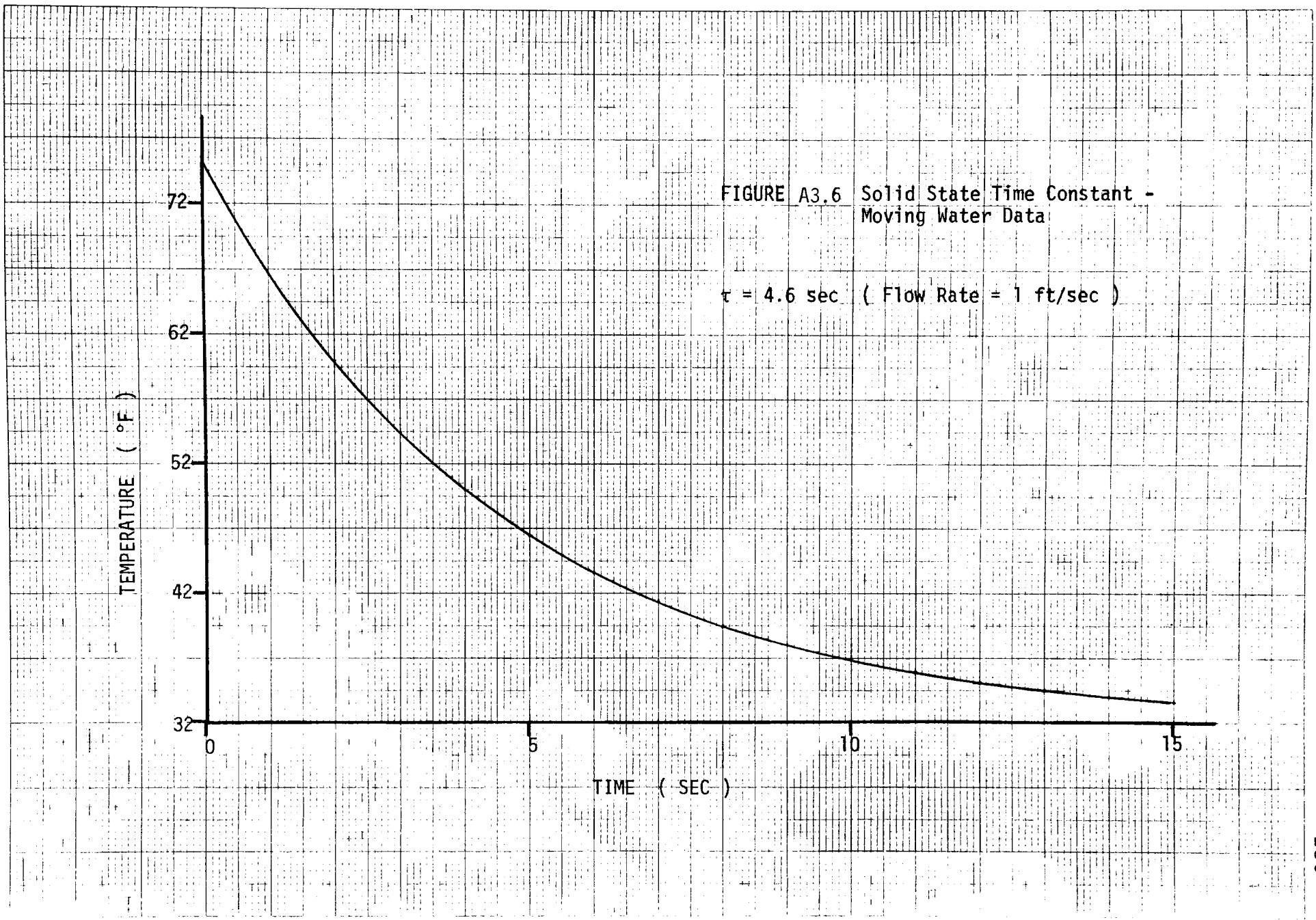

FIGURE A3.6 Solid State Time Constant - Moving Water Data

τ = 4.6 sec (Flow Rate = 1 ft/sec)

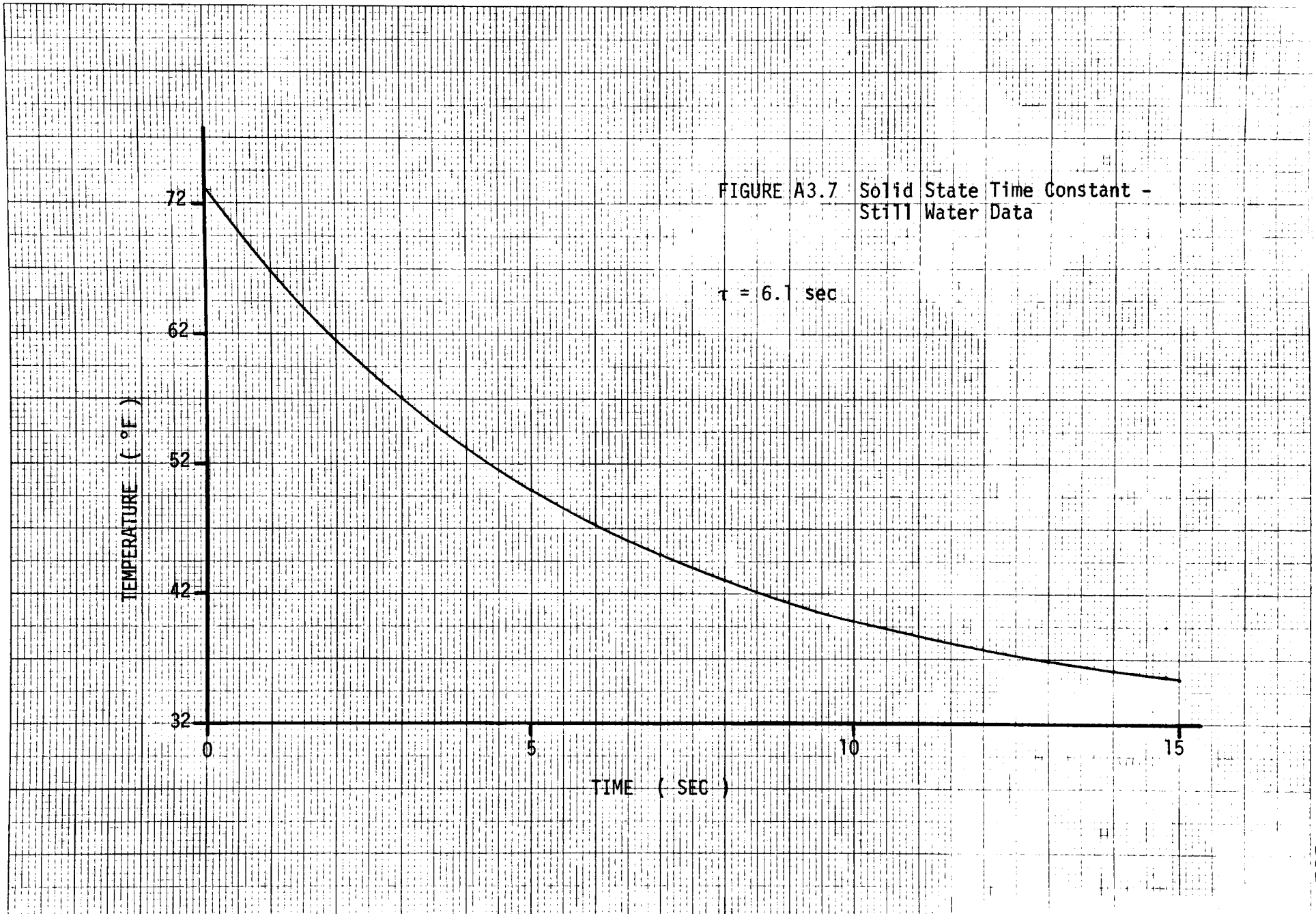

FIGURE A3.7 Solid State Time Constant - Still Water Data

τ = 6.1 sec

2. DMM uncertainty equal to 0.04% reading plus one digit. From Section 5.2, the DMM will read 2.400 V at 60°C for a zero setpoint of 0°C and a 4.00 MV/0.1°C span for the hot water tank. The DMM uncertainty is equal to (0.0004)(2.400) + 0.001 = 0.002V. This is equal to an uncertainty of ± 0.05°C.

3. Analog recorder uncertainty of 0.25 div. For a setting of 0.5°C/div for the hot water tank, an uncertainty of ± 0.13°C is found.

Parts 2 and 3 above represent the worst case for the experimental work of Section 5.2.

The overall uncertainty is [36].

$$W_R = [(0.04)^2 + (0.05)^2 + (0.13)^2\ ]^{1/2}$$

$$W_R = 0.14°C$$

where W_R is again the overall uncertainty.

APPENDIX 4 - Water Meter Calibration

Calibration Procedure

The positive displacement Badger water meter was calibrated using the constant head water system located inthe Mechanical Engineering power lab. The procedure used is described as follows:

1 The water meter was mounted in the constant head tank discharge piping. A dial thermometer was inserted in the discharge coupling. The TL170C switch, digital counter, and power supply was in monitoring position.

2. The constant head tank was filled with water at 68°F (20°C)*. Water was continuously allowed to enter the tank during all tests so that a constant head was always maintained.

3. It was determined that the calibration would be performed for flow rates between 0.8 gpm and 5.0 gpm. Flow rate was adjusted by means of a globe valve such that calibration increments of $\approx$ 0.5 gpm were obtained.

4. At each calibration setting, three tests were performed for the purpose of repeatability.

*Calibration was done at one temperature. According to specifications, the calibration curve generated in this section is valid up to 200 °F (93°C). Since the water meter location is after the heat exchanger, it is improbable that fluid temperatures will reach this level.

5. For each test, 100.0 pounds of water were collected. Knowing the time required and the water temperature, the actual flow rate was calculated. This was compared to the digital counter reading divided by time which gave a calibration point.

6. This data was then plotted resulting in Figure A4.1. This completes calibration. To utilize the curve, the digital counter was operated for three minutes and the resultant pulse total divided by three minutes. Figure A4.1 then gave the flow rate in gpm.

Flow Measurement Uncertainty

Uncertainty is introduced by the following factors:

1. Reference gpm reading used for calibration,
2. Digital pulse reading during calibration.

The reference gpm reading used for calibration is calculated from the following equation:

$$\text{reference gpm} = \frac{w(7.479)}{\rho(T)t} \qquad \text{(A4.1)}$$

where w = weight of water collected, pounds,

$\rho(T)$ = density of water at temperature, T, lb/ft^3,

t = time required to collect the water, minutes.

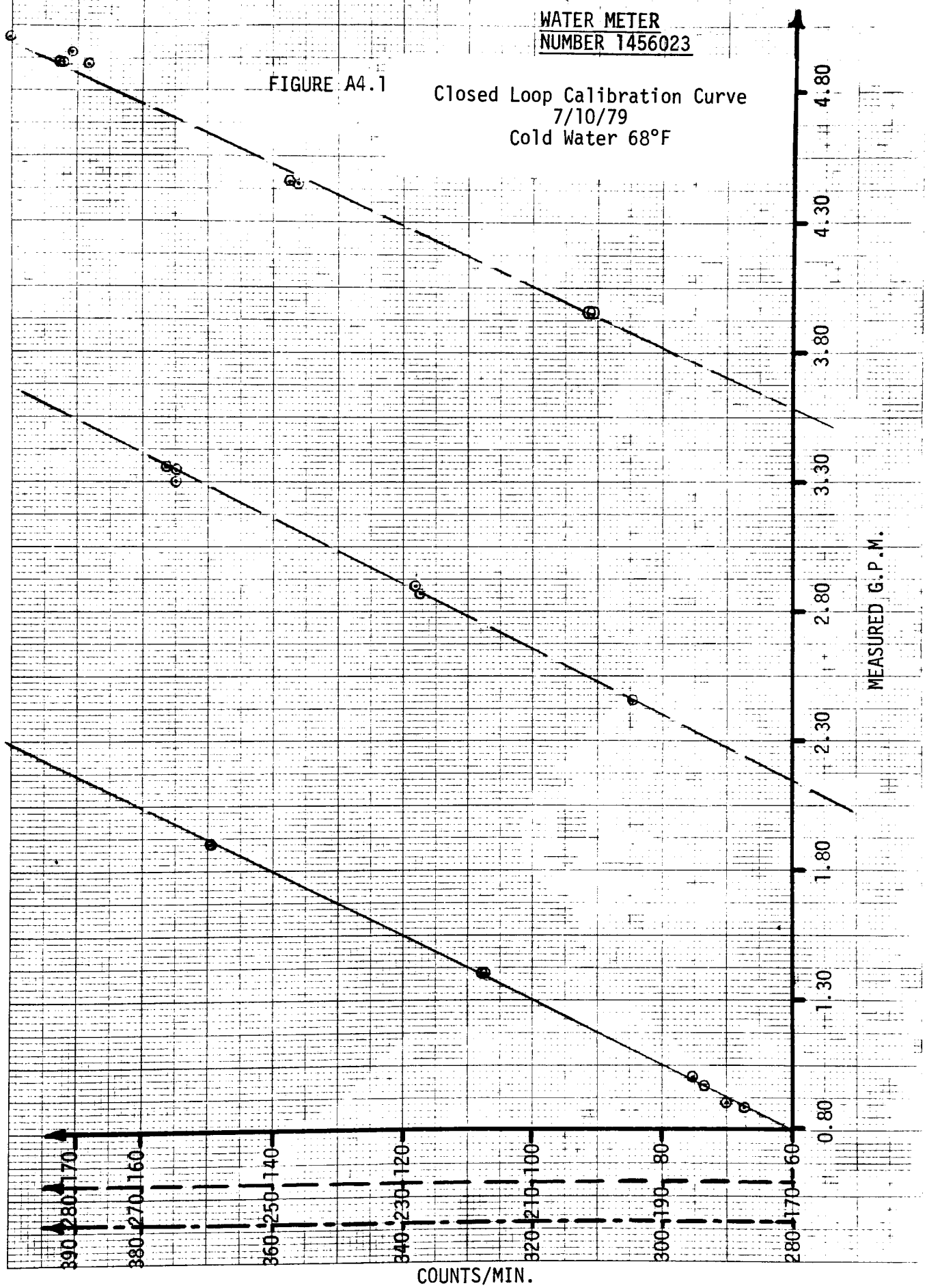
WATER METER
NUMBER 1456023
Closed Loop Calibration Curve
7/10/79
Cold Water 68°F
MEASURED G.P.M.
0.80
1.30
1.80
2.30
2.80
3.30
3.80
4.30
4.80
COUNTS/MIN.
390 280 170
380 270 160
360 250 140
340 230 120
320 210 100
300 190 80
280 170 60

FIGURE A4.1

The following errors can be assigned to the parameters in the above equation:

T ($\pm$ 1.0°C)

w ($\pm$ 0.5 lb)

t ($\pm$ 1.0 second = $\pm$ 1/60 minute)

$\rho(T)$ ($\pm$ 0.02 lb/ft^3)

To calculate the overall uncertainty, the following equation [36] is used:

$$W_R = \left[\left(\frac{\partial F}{\partial \rho} W_\rho\right)^2 + \left(\frac{\partial F}{\partial t} W_t\right)^2 + \left(\frac{\partial F}{\partial w} W_w\right)^2\right]^{1/2} \qquad \text{(A4.2)}$$

where

W_R = uncertainty of result,

W_ρ = uncertainty of density, 0.02 lb/ft^3,

W_t = uncertainty of time, 1/60 minute,

W_w = uncertainty of the weight of water, 0.5 lb.

The partials shown in Equation A4.2 can be evaluated from Equation A4.1 as follows:

$$\frac{\partial F}{\partial \rho} = \frac{-7.479w}{\rho(T)^2 t} \; ; \; \frac{\partial F}{\partial t} = \frac{-7.479w}{\rho(T) t^2} \; ; \; \frac{\partial F}{\partial w} = \frac{7.479}{\rho(T) t} \qquad \text{(A4.3, A4.4, A4.5)}$$

From observation of Equations A4.3, A4.4, and A4.5, it is obvious that as $\rho(T)$ and t get smaller, the overall uncertainty will rise.

Therefore, as a worst case analysis, assume a 5.0 gpm flow rate at 176°F (80°C) fluid temperature. With w equal to 100 lbs and $\rho(T) = 60.81\ lb/ft^3$, this results in a nominal t of 2.46 minutes from Equation A4.1. Substitution of these values into Equations A4.3, A4.4, and A4.5 and subsequently into Equation A4.2 gives the following results:

$W_R = \pm 0.042$ gpm with the reference gpm = 5.0gpm

or expressed in a percentage, 5 gpm $\pm$ 0.84%.

The digital pulse counter results in 1 pulse per 0.0125 gallon of fluid. If an error of $\pm$ 1 pulse is assumed possible in a test, then the maximum error in gallon per minute is

$$\frac{0.0125}{2.46} = \pm 0.005 \text{ gpm}$$

or again expressed as a percentage, 5 gpm $\pm$ 0.10%.

The overall uncertainty is equal to $[0.042^2 + 0.005^2]^{1/2} = 0.0423$ gpm or $\pm$ 0.85% of the reading. For a flow rate between 0.8 gpm and 2 gpm, this corresponds to an uncertainty of $\pm$ 0.007 gpm and $\pm$ 0.017 gpm, respectively.

APPENDIX 5 - Incident Angle Relationship

In order to perform the analysis outlined in Section 4.1, expressions for the incident angle on a tubular collector surface are required. For completeness, two cases are examined in this section, north-south tube orientation and east-west tube orientation. However, the KTA tubular collectors are oriented in an east-west fashion, thus the relevant results of this section are those for case 2.

Case 1 North-South Tube Orientation

Figure A5.1 shows a collector tube in a north-south orientation at a tilt angle, β and latitude, ℓ. The sun is at a declination, δ_s and hour angle, h_s. Defining i as the angle between a line collinear with the sun's rays and the outer normal to the tube lying in the plane formed by the tube centerline and a line collinear with the sun's rays, it can be expressed as [12]:

$$\cos i = \left\{1 - [\sin(\beta-\ell)\cos\delta_s \cosh_s + \cos(\beta-\ell)\sin\delta_s]^2\right\}^{1/2} \qquad \text{A5.1)}$$

Also, from Figure A5.1 , Ω is defined as the projected incident angle. It is the angle between the south facing tube normal (in the northern hemisphere) and the outer normal to the tube lying in the plane formed by the tube centerline and a line collinear with the sun's rays. This angle is shown in Figure A5.2. This is expressed as:

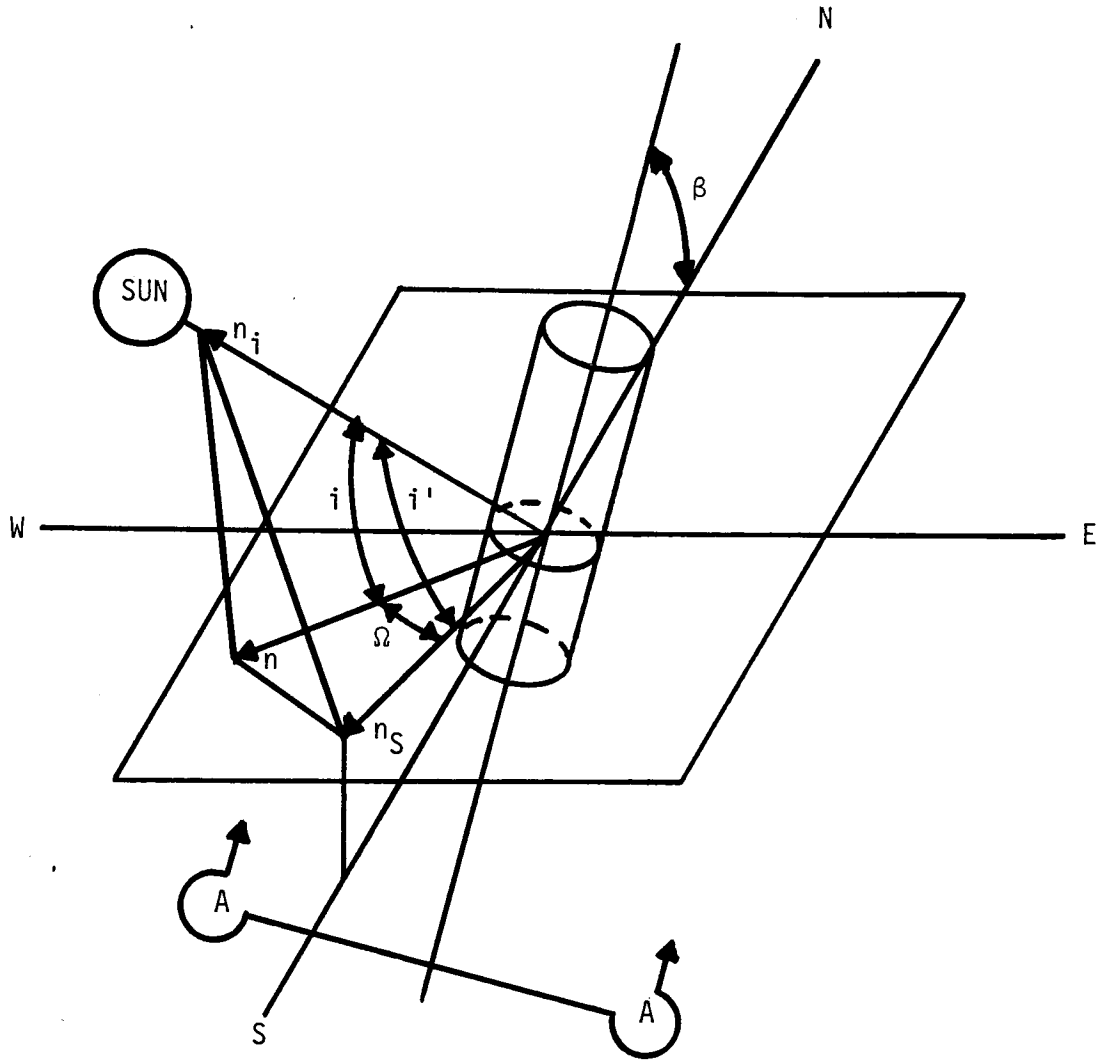

Figure A5.1 North-South Tube Orientation

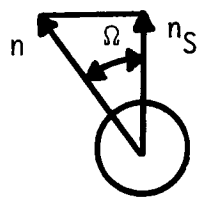

Figure A5.2 Section A-A, Projected Incident Angle, Ω

$$\text{Cos } \Omega = \frac{\cos(\ell-\beta)\cos\delta_s\cosh_s + \sin(\ell-\beta)\sin\delta_s}{\left\{1 - [\sin(\beta-\ell)\cos\delta_s\cosh_s + \cos(\beta-\ell)\sin\delta_s]^2\right\}^{1/2}} \qquad \text{(A5.2)}$$

The numerator of Equation A5.2 represents the expression for the cosine of the incident angle, i', between a line collinear with the sun's rays and the south facing tube normal. This is the same expression as that for a flat plate collector since its outer normal is the same as the south facing tube normal [37]. The denominator is as defined in Equation A5.1. Equation A5.2 can be shown to be correct when Figure A5.1 is examined. From the figure, the following expressions are found:

$$\cos i = \frac{n}{n_i} \qquad \text{(A5.3)}$$

$$\cos i' = \frac{n_s}{n_i} \qquad \text{(A5.4)}$$

$$\cos \Omega = \frac{n_s}{n} \qquad \text{(A5.5)}$$

but from Equation A5.2, $\cos \Omega = \frac{\cos i'}{\cos i}$ and substituting in Equations A5.3, A5.4, and A5.5 gives:

$$n_s/n = (n_s/n_i)/n/n_i = n_s/n$$

which are equal.

Case 2 East-West Tube Orientation

Figure A5.3 shows a collector tube in an east-west orientation while Figure A5.4 is a Section A-A indicated in Figure A5.3. The angle i is as defined for Case 1. The remaining angles are defined as follows:

1. Ω is the projected incident angle. It is the angle between the south facing normal (n_s) of the tube bank (in northern hemisphere) and the outer normal (n) to the tube lying in the plane formed by the tube centerline and a line collinear with the sun's rays (see Figure A5.4). It is defined as positive when measured CCW from n_s.

2. θ is the angle between the south facing normal (n_s) of the tube bank (in northern hemisphere) and the tube normal (n') perpendicular to a plane formed by the two mirrow-glass interfaces (see Figure A5.4). It is defined as positive when measured CW from n_s.

3. i_t is the angle between a line collinear with the sun's rays (n_i) and the south facing normal (n_s) of the tube bank (in northern hemisphere) (see Figure A5.3).

The angle i_t is expressed [37] as:

$$\cos i_t = \cos(\ell-\beta)\cos\delta_s\cosh_s + \sin(\ell-\beta)\sin\delta_s \qquad (A5.6)$$

while the angle Ω is

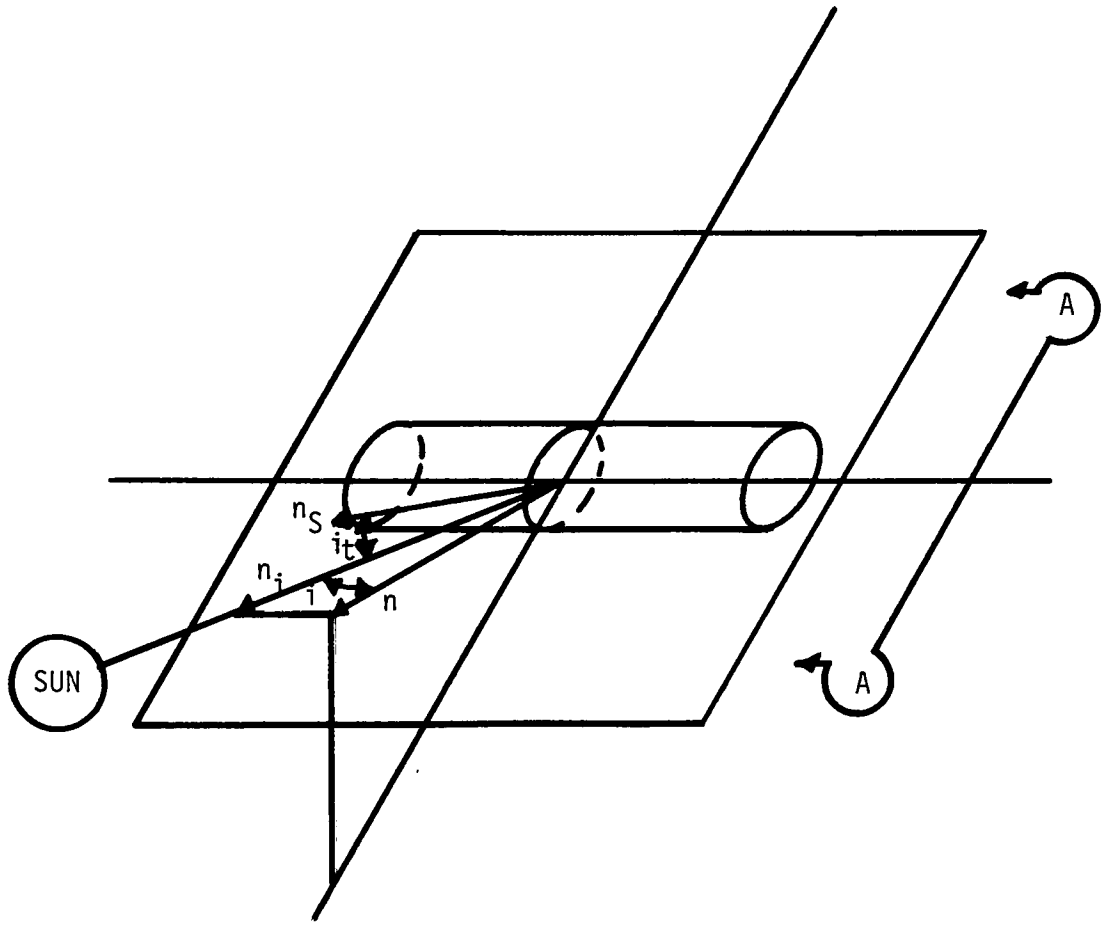

Figure A5.3 East-West Tube Orientation

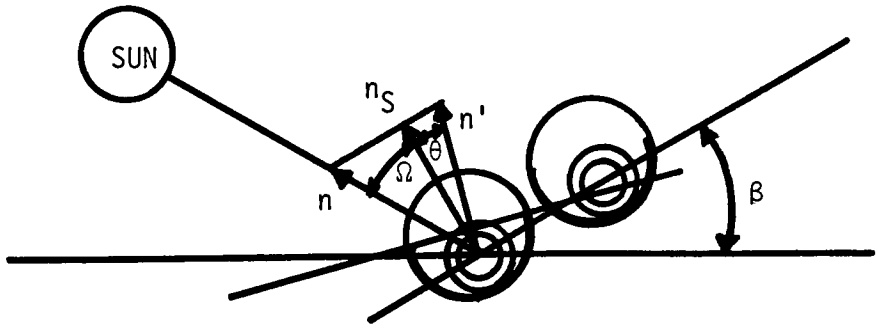

Figure A5.4 Section A-A, Projected Incident Angle, Ω

$$\cos \Omega = \cos(\ell-\beta)\cos\delta_s + \sin(\ell-\beta)\sin\delta_s \qquad \text{(A5.7)}$$

since Ω is equal to i_t when the hour angle h_s is equal to zero. The angle Ω is shown positive in Figure A5.4 but it can be negative also. This can be seen when Equation A5.7 is rewritten as:

$$\cos \Omega = \cos(\ell-\beta-\delta_s) \qquad \text{(A5.8)}$$

or

$$\Omega = \ell-\beta-\delta_s \qquad \text{(A5.9)}$$

APPENDIX 6 - Additional Shading Factor Relationships

The shading factor relationships for orientations 1 and 3 for case 2 ($\Omega < 0$) will be given here.

Orientation 1 - $\theta \geq 5.6°$

The parameter $g(\Omega) = 1$ when $|\Omega| \leq |\Omega_s|$. From Figure A6.1, $|\Omega_s|$ is found as follows. First,

$$|\Omega_s| = 90 - \xi \tag{A6.1}$$

with

$$\xi = \gamma_5 + \gamma_4 - \theta \tag{A6.2}$$

The angles γ_4 and γ_5 are found next.

$$\gamma_5 = \tan^{-1}\left(\frac{f+e}{g}\right) \tag{A6.3}$$

$$\gamma_4 = \tan^{-1}\left(\frac{d}{2L_2}\right) \tag{A6.4}$$

Also:

$$f = (D + S)\sin\theta \tag{A6.5}$$

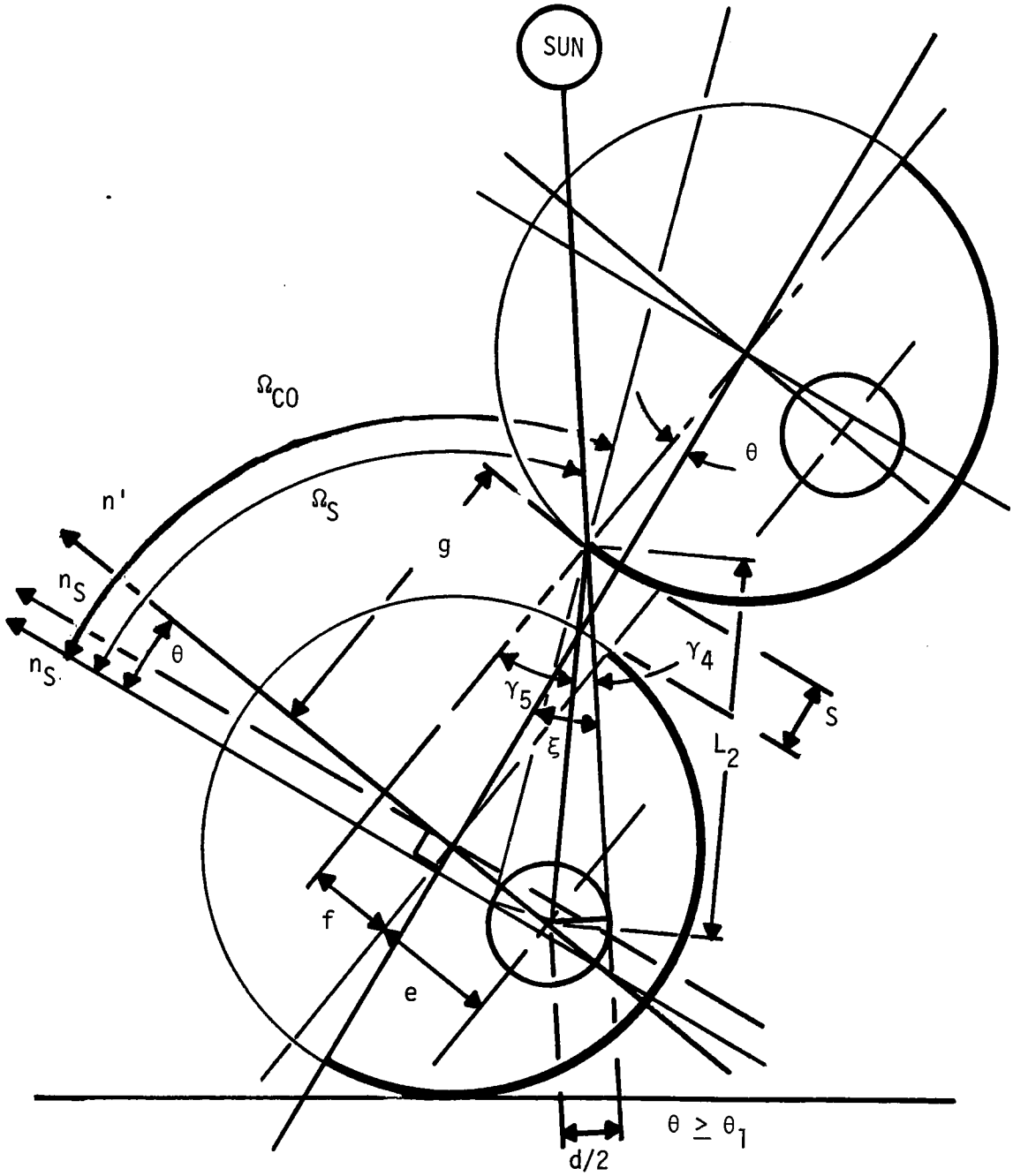

Figure A6.1 Tube Orientation 1 - Geometric Layout

and

$$g = (D + S)\cos\theta - D/2 \qquad \text{(A6.6)}$$

Finally,

$$L_2 = (g^2 + (f+e)^2)^{1/2} \qquad \text{(A6.7)}$$

where e is as previously shown in Figure 4.3. $|\Omega_s|$ can now be evaluated by first finding the results of Equations A6.5, A6.6, and A6.7 and substituting these back into Equations A6.3 and A6.4. These results are in turn substituted into Equation A6.2 and finally $|\Omega_s|$ found from Equation A6.1.

The parameter $g(\Omega) = 0$ when $|\Omega| \geq |\Omega_{co}|$. The angle $|\Omega_{co}|$ is shown on Figure A6.1 and can be easily calculated. The procedure is exactly the same as that used to determine $|\Omega_s|$ except in Equation A6.2 γ_4 is subtracted instead of added.

$$|\Omega_{co}| = 90 - \xi \qquad \text{(A6.8)}$$

and

$$\xi = \gamma_5 - \gamma_4 - \theta \qquad \text{(A6.9)}$$

γ_5 and γ_4 are determined using Equations A6.3 through A6.7.

In addition, $g(\Omega) = \dfrac{|\Omega_{co}| - |\Omega|}{|\Omega_{co}| - |\Omega_s|}$ when $|\Omega_s| < |\Omega| < |\Omega_{co}|$.

Finally, summarizing for orientation 1 ($\theta \geq 5.6°$):

$$g(\Omega) = 1 \qquad \text{for } \Omega \leq |\Omega_s| \tag{A6.10}$$

$$g(\Omega) = 0 \qquad \text{for } \Omega \geq |\Omega_{co}| \tag{A6.11}$$

$$g(\Omega) = \frac{|\Omega_{co}| - |\Omega|}{|\Omega_{co}| - |\Omega_s|} \quad \text{for } |\Omega_s| < |\Omega| < |\Omega_{co}| \tag{A6.12}$$

where $|\Omega_s|$ and $|\Omega_{co}|$ are determined from Equations A6.1 and A6.8, respectively.

Orientation 3 - $1.7° \leq \theta \leq 5.6°$

The parameter $g(\Omega) = 1$ when $|\Omega| \leq |\Omega_s|$. $|\Omega_s|$ can be calculated in the same manner as was done for orientation 2 (see Section 4.1.3.1). From Figure 4.5, $|\Omega_s|$ equals $90 - \xi_3 = 90 - (\gamma - \theta) = 90 - 41.2 + \theta = 48.8 - \theta$.

Also, $g(\Omega)$ when $|\Omega| \geq |\Omega_{co}|$. $|\Omega_{co}|$ is calculated exactly as is shown above in Equation A6.8 and A6.9.

Finally, $g(\Omega) = \dfrac{|\Omega_{co}| - |\Omega|}{|\Omega_{co}| - |\Omega_s|}$ for $|\Omega_s| < |\Omega| < |\Omega_{co}|$

This result neglects the fact that the absorber tube shading is caused by both the tube of interest and the adjacent tube as $|\Omega|$ increases. However, the resulting error is small since the tubes are close together compared to the distance from the shading edges to the absorber tube. Equations A6.10, A6.11, and A6.12 represent the same results for orientation 3 except $|\Omega_s|$ and $|\Omega_{co}|$ are calculated as described above.

APPENDIX 7 - Evaluation of Heat Exchanger Performance

The description of the preheat heat exchanger to follow is based on steady state conditions. As was mentioned in Section 4, this provides a sufficient description of system performance. Figure A7.1 is a schematic of only the collectors and the preheat tank. The amount of energy collected Q_u can be written from Equation 4.29 of Section 4 as:

$$Q_u = A_t F_R[(\tau\alpha)_e I_{eff} - \frac{U_L \pi d}{D} (T_{INC} - T_a)] \qquad (A7.1)$$

In addition, the energy collected can be written:

$$Q_u = \dot{M} C_p (T_{OUTC} - T_{INC}) \qquad (A7.2)$$

Defining the heat exchanger effectiveness E as:

$$E = \frac{T_{OUTC} - T_{INC}}{T_{OUTC} - T_{IWH}} \qquad (A7.3)$$

the energy transferred Q_T can be written:

$$Q_T = E \dot{M} C_p (T_{OUTC} - T_{IWH}) \qquad (A7.4)$$

For steady conditions:

$$Q_T = Q_u \qquad (A7.5)$$

Also,

$$T_{INC} = T_{OUTC} - \frac{Q_u}{\dot{M} C_p} \tag{A7.6}$$

and

$$T_{IWH} = T_{OUTC} - \frac{Q_T}{E\dot{M} C_p} \tag{A7.7}$$

Substituting Equation A7.7 into Equation A7.6 and setting $Q_T = Q_u$ gives:

$$T_{INC} = T_{IWH} + \frac{Q_T}{\dot{M} C_p} \left(\frac{1 - E}{E}\right) \tag{A7.8}$$

Rewriting Equation A7.1 with Equation A7.8 substituted in gives:

$$Q_u = A_t F_R \left[(\tau\alpha)_e I_{eff} - \frac{U_L \pi d}{D} \left(T_{IWH} - T_a + \frac{Q_T}{\dot{M} C_p} \left[\frac{1-E}{E}\right] \right) \right] \tag{A7.9}$$

which when simplified becomes

$$Q_u = \frac{I_{eff}(\tau\alpha)_e - U_L \frac{\pi d}{D} (T_{IWH} - T_a)}{\frac{1}{A_t F_R} + \frac{U_L \pi d}{\dot{M} C_p D} \left[\frac{1 - E}{E}\right]} \tag{A7.10}$$

The energy collected will be a maximum when E = 1 which results in the smallest value of the denominator. Denoted this amount as Q_{max} gives:

$$Q_{max} = \frac{I_{eff}(\tau\alpha)_d - U_L \frac{\pi d}{D} (T_{IWH} - T_a)}{\frac{1}{A_t F_R}} \tag{A7.11}$$

Thus when E = 1, $T_{INC} = T_{IWH}$.

The ratio of the energy collected to the maximum amount of energy collectable is:

$$\frac{Q_u}{Q_{max}} = \left[1 + \frac{A_t F_R U_L \pi d}{\dot{M} C_p D} \left(\frac{1 - E}{E} \right) \right]^{-1} \qquad \text{(A7.12)}$$

Equation A7.12 can be plotted for different values of E. This is done in Figure A7.2. From the figure, it is seen that for values of E greater than .2, the variation in heat collected divided by the maximum amount collectable is only 20%. In particular, for variations of E between .4 and .6, this change is only 8%. Thus, failure to evaluate E accurately results in only a small overall system performance error.

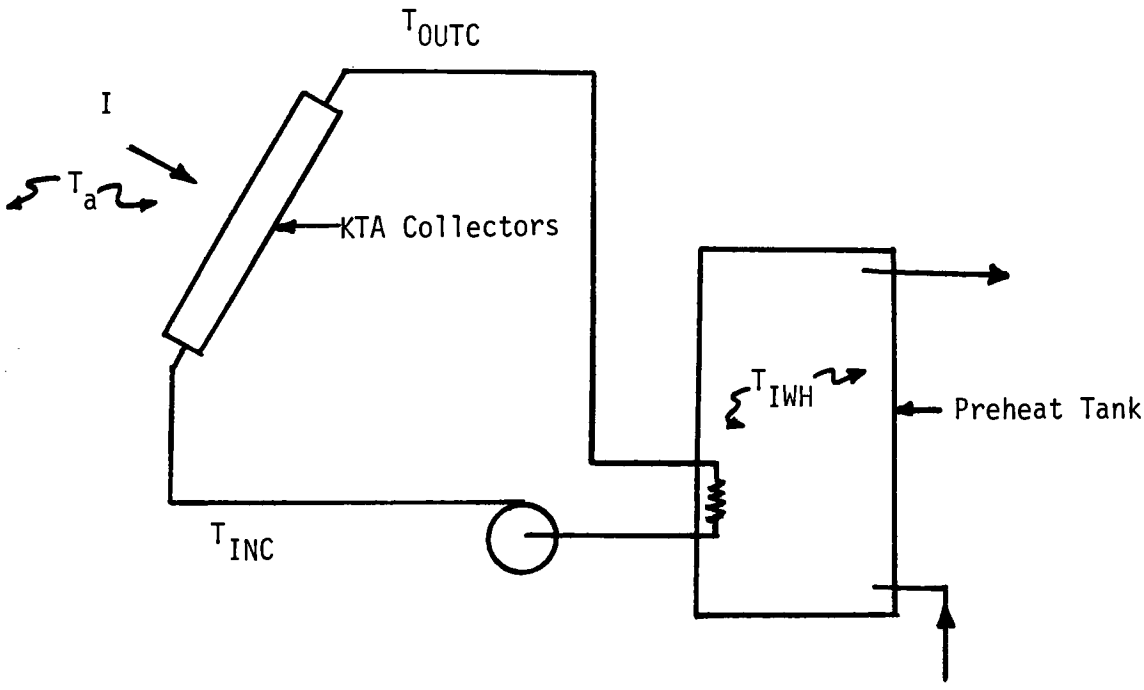

Figure A7.1 Collector, Preheat Schematic

Figure A7.2 - Ratio of Collected Energy to Maximum Amount Collectable